Vrije Universiteit Brussel
Faculty of Science and Bio-Engineering Sciences
Interuniversity Institute for High Energies
and Theoretische Natuurkunde

# Gravitino production at colliders

Thesis submitted in partial fulfilment of the requirements
for the award of the degree of Doctor of Science by

**Bettina Oexl**

**Jury members:**

| | |
|---|---|
| Prof. Dr. Ben Craps, *Supervisor* | VUB, TENA |
| Prof. Dr. Kentarou Mawatari, *Supervisor* | VUB, TENA and IIHE |
| Prof. Dr. Catherine de Clercq, *Chairperson* | VUB, IIHE |
| Prof. Dr. Steven Lowette, *Secretary* | VUB, IIHE |
| Prof. Dr. Francis Berghmans | VUB, B-Phot |
| Prof. Dr. Riccardo Argurio | Université Libre de Bruxelles |
| Directeur de Recherche Dr. Dirk Zerwas | Laboratoire de l'accélérateur linéaire Orsay |

September 21, 2014

# Contents

# Preface

The standard model (SM) of particle physics is a theory that describes the fundamental matter particles and the interactions among them. It is an extremely successful theory, in the sense that it predicts the outcome of many experiments with high precision. With the recent discovery of a new boson [1, 2] that might be identified with the Brout-Englert-Higgs boson (or $H$-boson for short) of the SM [3, 4], all the predicted particles of the SM have been experimentally confirmed. The scalar field is responsible for giving mass to gauge fields by a mechanism which was proposed by Brout and Englert [5] as well as Higgs [6] in 1964. The importance of this theoretical prediction and the experimental confirmation is emphasized by the award of the 2013 Nobel Prize in physics.

Besides strengthening the SM, the discovery of the $H$ boson has reinforced a need for new physics, since the scalar particle in the SM is unstable against quantum corrections and requires either unnatural fine-tuning or physics beyond the standard model (BSM). As well as theoretical motivations, there exist experimental observations that demand BSM physics. For example, matter as we know it constitutes less than 5% of the energy density in the universe and about 25% is so-called dark matter. This dark matter can not be explained within the particle content of the SM. Further experimental evidence for new physics comes e.g. from the observations of neutrino oscillations, which imply that neutrinos are massive, while in the SM neutrinos are massless.

There exists a variety of extensions of the SM, each of which addresses one or more of the questions for new physics. In this work, we focus on supersymmetric (SUSY) theories, which assume a symmetry between bosons and fermions. Each SM particle receives a partner, with spin differing by 1/2. SUSY theories offer an attractive solution to the above mentioned naturalness problem, and might also provide a potential dark matter candidate. In a perfect SUSY world, the SUSY particles would have the same masses as the corresponding SM particles. However, this has not been observed experimentally, so SUSY must be broken. As a result, the SUSY particles have to be heavier than the SM particles. Although we do not know the values of the masses, to solve the naturalness problem, one expects at least some of these particles to lie in the TeV range, which is in the reach of current and future particle colliders.

The lightest SUSY particle (LSP) can be a potential dark matter candidate, since a symmetry protects it from decaying into SM particles. In order to constitute dark matter, it is assumed that the LSP is electrically neutral and interacts only weakly with ordinary matter. Therefore, in collider experiments, the LSP will escape the detection and give rise to a missing energy ($\not{E}$) signal.

A typical and widely studied LSP candidate is the lightest neutralino. On the other hand, another interesting LSP candidate is the gravitino, and such scenarios have not yet been fully explored. The gravitino is the spin 3/2 superpartner of the graviton, arising in SUSY theories once gravity is included. Since its mass is related to the energy scale at which SUSY is broken, the gravitino can be very light up to very heavy, depending on the details of the theory. The gravitino interactions are highly suppressed, such that processes involving gravitinos are often negligible in collider experiments. However, if the gravitino is very light, its interactions are enhanced and may become strong enough

to give rise to an observable signal. In this work, we investigate potential signatures of very light gravitinos at current and future colliders.

We proceed in our phenomenological studies on gravitino production at colliders as follows. Starting from the mathematical description of a theory in the form of a Lagrangian, we compute the cross section for a given scattering process. The cross section expresses the probability for the process to happen, and may vary with the collision energy, the masses of the involved particles or other parameters. We also investigate distributions, which give e.g. the probability to find a certain particle in a given angular region, or with a specific momentum. Having understood how a signature changes for different model parameters and phase space points, the signal events are simulated as they would show up in a detector. The outcome can be compared to the data delivered by experiment. Our goal is to extract information about the valid parameter space of the theory, and to guide experimental searches on where to look for new physics.

Simulation tools are indispensable to facilitate the aforementioned procedure of comparing a theory to experimental data. One of the emphases of this thesis is the development and validation of tools related to gravitino production at colliders through the phenomenological studies.

We investigate light gravitino production at two different types of particle colliders, that is lepton colliders and hadron colliders. We start by analysing potential signatures at electron-positron ($e^+e^-$) colliders, especially at the International Linear Collider (ILC), foreseen to be built in Japan in the near future. We focus on the mono-photon+$\not{E}$ signal. We discuss the characteristics and parameter dependence of signatures arising from two different types of production processes, and compare the expected rates and distributions for selected parameter choices to SM background. We also investigate the mono-electron+$\not{E}$ signal arising from gravitino production in $e^-\gamma$ collisions, which are an option at an $e^+e^-$ collider.

Having understood the features of signatures arising from gravitino production at lepton colliders, we turn to hadron colliders. We focus on the Large Hadron Collider (LHC), a collider of 27 km circumference situated at the CERN laboratory (European Organization for Nuclear Research) in Switzerland. The LHC started its run in 2010 and collides two proton beams with high center-of-mass energies of 7 and 8 TeV. After the discovery of the $H$ boson by the two main experiments ATLAS and CMS, the purpose lies more in the search for new physics. We study the jets+$\not{E}$ and mono-photon+$\not{E}$ signals one can expect from light gravitinos at the LHC. We choose different benchmark scenarios that exemplify the different possible final state signatures, and analyse the resulting distributions. Further on, we interpret an existing dataset in terms of our theory.

We find that current and future colliders may be able to explore the parameter space chosen around our benchmark points. If an excess over the SM background is observed in the future data of the LHC or ILC, we show how to extract information on the parameters of our theory by simple final state observables. On the other hand, if no deviation from the SM expectations is found, our studies can be used to set bounds on

the parameters, such as e.g. the gravitino mass, which can be translated into the SUSY breaking scale. By interpreting a data set delivered by the 2012 LHC run in terms of our theory, we put a lower bound on the gravitino mass which extends existing bounds from similar searches.

The thesis is divided into two parts. In the first part, we review the theoretical background needed for studying gravitino production at colliders. In the second part, we present the collider phenomenology of very light gravitinos.

The first part starts with an abstract of the SM in Chapter 1. In Chapter 2, the basics of SUSY are introduced. The gravitino enters the theory when the global SUSY theory is promoted to a local theory, as shown in Chapter 3. We explain and illustrate the fact that we can calculate scattering processes involving light gravitinos by using the goldstino formalism thanks to the gravitino-goldstino equivalence theorem.

In the second part, after a brief recapitulation of relevant particle colliders in the beginning of Chapter 4, we explain the chain of collider simulation tools needed for our phenomenological studies. Possible production mechanisms of light gravitinos are described in Chapter 5, and current experimental bounds on the gravitino mass are given. In Chapter 6, we simulate gravitino production at electron-positron colliders and we present the mono-photon+$\not{E}$ signal arising from processes involving gravitinos. Another possible signature is a single electron+$\not{E}$ in electron-photon collisions, discussed in Chapter 7. We then turn to signals from gravitinos at the LHC. We discuss a jets+$\not{E}$ signature in Chapter 8. Finally, we interpret the mono-photon+$\not{E}$ signature of the 2012 LHC data in terms of a theory with very light gravitinos in Chapter 9. We conclude with a summary of the findings of the phenomenological studies.

The work presented in this thesis is based on the following publications:

- K. Mawatari, B. Oexl and Y. Takaesu
  Associated production of light gravitinos in $e^+e^-$ and $e^-\gamma$ collisions
  *Eur. Phys. J.* **C71** (2011) 1783, [arXiv:1106.5592]

- P. de Aquino, F. Maltoni, K. Mawatari and B. Oexl
  Light gravitino production in association with gluinos at the LHC
  *JHEP* **1210** (2012) 008, [arXiv:1206.7098]

- N. D. Christensen, P. de Aquino, N. Deutschmann, C. Duhr, B. Fuks, C. Garcia-Cely, O. Mattelaer, K. Mawatari, B. Oexl and Y. Takaesu
  Simulating spin-3/2 particles at colliders
  *Eur. Phys. J.* **C73** (2013) 2580, [arXiv:1308.1668]

- K. Mawatari and B. Oexl
  Monophoton signals in light gravitino production at $e^+e^-$ colliders
  *Eur. Phys. J.* **C74** (2014) 2909, [arXiv:1402.3223]

Chapter 9 is based on on-going work:

- F. Maltoni, A. Martini, K. Mawatari and B. Oexl
  Monojet and monophoton signals in light gravitino production at the LHC

# Part I

# Theory

# CHAPTER 1

# The standard model (SM) of particle physics

The standard model (SM) of particle physics is a theory that describes the fundamental matter particles and the interactions among them. After briefly summarizing the particle content of the SM in Section 1.1, we give the example of quantum electrodynamics (QED) to illustrate how the principle of gauge invariance leads to interactions, and how the spontaneous breaking of the symmetry generates a mass term for gauge bosons, see Section 1.2. Subsequently, we present the full Lagrangian of the SM in Section 1.3. In the last part of this chapter, we present an application of the goldstone-boson equivalence theorem. This theorem allows in a certain energy regime to calculate scattering processes involving longitudinally polarized $W$-bosons by using their corresponding goldstone bosons.

## 1.1 The SM particle content

The SM particle content is summarized in Fig. 1.1. It can be categorised into fermions (spin-1/2), which comprise the matter particles, and bosons (spin-1 and spin-0), which incorporate the mediators of the fundamental forces and the Brout-Englert-Higgs scalar $H$. The fermions are divided into sub-groups called leptons and quarks according to their interactions. The electron $e^-$ is charged electrically. Together with the electrically neutral electron-neutrino $\nu_e$ it constitutes the first generation of leptons. There are two more generations, the muon $\mu$ and its associated muon-neutrino $\nu_\mu$ and the tau $\tau$ and the tau-neutrino $\nu_\tau$. Quarks are matter particles that carry both electric and color charges. There are six quarks, grouped again into three generations: the up and down quarks $(u, d)$, the charm and strange quarks $(c, s)$ and the top and bottom quarks $(t, b)$. Quarks are usually not observed as free particles but bound into hadrons. The matter particles interact with each other via three fundamental forces which are mediated by so-called gauge bosons.[1] The electromagnetic force is mediated by the massless photon $\gamma$, the weak force is communicated by the massive $Z$ and $W^\pm$ bosons and the strong force is mediated by massless gluons $G$. The $H$ boson is the only scalar particle in the SM. It was recently discovered at the Large Hadron Collider (LHC) [1–4], and is responsible for generating mass terms for the matter particles and gauge bosons.

## 1.2 Symmetry and symmetry breaking

Symmetries play an important role in the construction of a model. They are used to generate dynamics and restrict the form of possible terms in the Lagrangian; requiring the Lagrangian to be invariant under local gauge symmetries determines the form of the interactions, and forbids mass terms for gauge bosons. However, gauge bosons are allowed to be massive after the spontaneous breaking of a symmetry. In this section, we introduce these concepts by means of the abelian $U(1)_{\text{em}}$ gauge group.

[1] The fourth fundamental force, gravity, is not included in the SM.

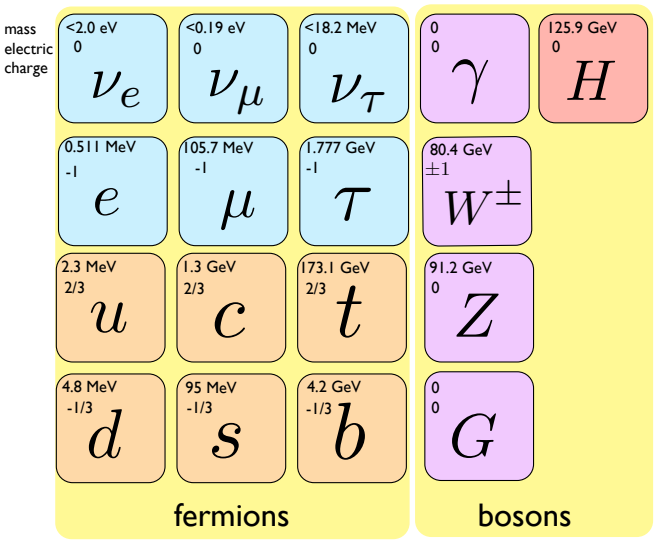


Figure 1.1: The particle content of the SM is given with the mass [7] and electric charge of the particles.

The free Lagrangian of a (massless) electron field $\psi_e$ is

$$\mathcal{L}_e = \bar{\psi}_e i \not{\partial} \psi_e, \tag{1.1}$$

where $\bar{\psi}_e = \psi_e^\dagger \gamma^0$, $\not{\partial} = \partial_\mu \gamma^\mu$ and $\gamma^\mu$ with $\mu = 0, \cdots, 3$ are the Dirac matrices. It is invariant under a *global* phase transformation $\psi_e(x) \to e^{i\alpha Q} \psi_e(x)$, where $\alpha$ is the constant transformation parameter, and $Q = -1$ is the electron charge.

However, (1.1) is not invariant under *local* phase transformations

$$\psi_e(x) \to e^{i\alpha(x) Q} \psi_e(x), \tag{1.2}$$

which allow an independent transformation at every point $x$ in space-time. By replacing the derivative $\partial^\mu$ by the covariant derivative

$$D_\mu = \partial_\mu + i g_e Q A_\mu, \tag{1.3}$$

the invariance of (1.1) can be restored if the gauge boson $A_\mu$ transforms as $A_\mu(x) \to A_\mu(x) - \frac{1}{g_e} \partial_\mu \alpha(x)$. Here, $g_e = \sqrt{4\pi\alpha_{\mathrm{EW}}}$ and $A_\mu$ is the electric field whose excitations can be identified with photons.

To allow the gauge field to be a dynamical variable, we add its kinetic term to the Lagrangian (1.1). The Lagrangian of QED is then given by

$$\mathcal{L}_{\mathrm{e}} = \bar{\psi}_e i \not{D} \psi_e - \frac{1}{4} F_{\mu\nu} F^{\mu\nu}, \tag{1.4}$$

where $F_{\mu\nu} = \partial_\mu A_\nu - \partial_\nu A_\mu$ is the electromagnetic field strength tensor. We have seen how the imposition of a local $U(1)_{\mathrm{em}}$ symmetry implies the existence of a vector particle and determines the form of the interaction between the electron and that gauge boson.

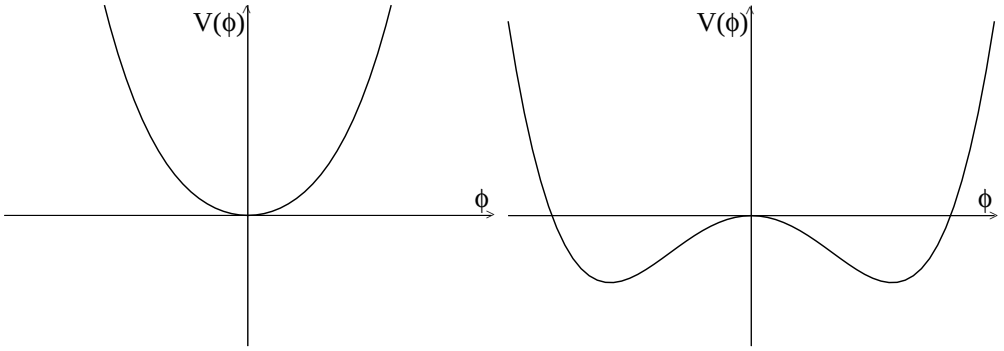


Figure 1.2: The schematic diagram of the potential $V(\phi) = -\mu^2\phi^*\phi + \lambda(\phi^*\phi)^2$ for $\mu^2 < 0$ (left) and $\mu^2 > 0$ (right).

While the electron mass term would be allowed by the local phase transformation, the mass term for the gauge boson would not. Of course this is not a problem for the photon, but we know we will need a mass term for the $W$ and $Z$ bosons to describe the weak interactions. Sticking to the example of QED, we describe how a mass term can be generated for gauge bosons by coupling them to a scalar field, which will develop a vacuum expectation value (VEV) and break the $U(1)_{\rm em}$ symmetry spontaneously. This is the famous Brout-Englert-Higgs mechanism [5,6].

Consider a complex scalar field $\phi$ with the Lagrangian given by

$$\mathcal{L}_\phi = |D_\mu\phi|^2 - V(\phi), \tag{1.5}$$

with the potential

$$V(\phi) = -\mu^2\phi^*\phi + \lambda(\phi^*\phi)^2, \tag{1.6}$$

and $\phi$ transforms under the local $U(1)_{\rm em}$ transformation as

$$\phi(x) \to e^{i\alpha(x)Q}\phi(x). \tag{1.7}$$

For $\mu^2 < 0$, the potential has its minimum at $|\phi_0| = 0$; see also the left plot in Fig. 1.2. The minimal energy state is preserved by the $U(1)_{\rm em}$ transformation. However, for $\mu^2 > 0$, a minimal energy state occurs at

$$|\phi_0| = \sqrt{\frac{\mu^2}{2\lambda}} \equiv \frac{v}{\sqrt{2}}, \tag{1.8}$$

which is not anymore invariant under (1.7); we say that the $U(1)_{\rm em}$ symmetry is spontaneously broken.

To investigate the effect of the broken symmetry in the Lagrangian given (1.5), we decompose $\phi$ into its two real components $\phi_{1,2}(x)$ and choose the VEV in the direction of $\phi_1$,

$$\phi(x) = \frac{1}{\sqrt{2}}\left(v + \phi_1(x) + i\phi_2(x)\right). \tag{1.9}$$

From the first term of (1.5), we obtain

$$|D_\mu\phi|^2 = \frac{1}{2}(\partial_\mu\phi_1)(\partial^\mu\phi_1) + \frac{1}{2}(\partial_\mu\phi_2)(\partial^\mu\phi_2) + \frac{1}{2}(g_e Q v)^2 A_\mu A^\mu + g_e Q v A_\mu \partial^\mu \phi_2 + \text{terms cubic and quartic in the fields.} \tag{1.10}$$

We see that a mass term for the gauge boson appeared, with mass $m_A = |g_e v Q|$.

The potential term turns into

$$V(\phi) = \mu^2\phi_1^2 + \text{terms cubic and quartic in the fields.} \tag{1.11}$$

We have a mass term for $\phi_1$, while the field $\phi_2$ remains massless; it is a goldstone boson, and its appearance is a general feature of the spontaneous breaking of a continuous symmetry [8,9]. It is not an independent physical particle, as can be seen when rewriting (1.9) as,

$$\phi(x) = \frac{1}{\sqrt{2}} e^{i\frac{\xi(x)}{v}}(v + h(x)), \tag{1.12}$$

where $h(x)$ and $\xi(x)$ are real fields and for small field values we can expand $\phi$ around $v$ and identify $h = \phi_1$ and $\xi = \phi_2$. By fixing the gauge parameter in (1.7) to $\alpha(x) = -\frac{\xi(x)}{v}$ we can remove the goldstone boson $\xi(x)$ from the theory. We say, the goldstone boson 'has been eaten' by the gauge boson, providing the massive boson with a physical longitudinal polarization. Although in this so-called unitary gauge the goldstone bosons have disappeared from the theory, their properties will still show up in physical observables. This will be explained in detail in section 1.4 by means of the longitudinal $WW$ scattering of the SM. Before, in the next section, we present the particle content and the Lagrangian of the SM.

## 1.3 The SM Lagrangian

As we saw in the previous section, the guiding principle to derive the interactions among the particles is the invariance of the Lagrangian under local gauge transformations. The full SM is based on the $SU(3)_c \times SU(2)_L \times U(1)_Y$ gauge group, where $SU(2)_L \times U(1)_Y$ is spontaneously broken to $U(1)_{\text{em}}$, resulting in massive $W$- and $Z$-bosons, yet keeping the photon massless.

As before, we start with the Lagrangian for the electron and the other fermions. The electron $\psi_e$ is composed of a left- and right-handed Weyl-spinor, $\psi_{e_L} = P_L\psi_e$ and $\psi_{e_R} = P_R\psi_e$. It was found experimentally that only the left handed piece couples to the $W^\pm$ bosons [10, 11], hence $\psi_{e_L}$ and $\psi_{e_R}$ are assigned to different representations of the gauge group. The left-handed electron field forms together with the (left-handed) neutrino a doublet of $SU(2)_L$, while the right-handed electron is a singlet. Similar relations hold for the quarks; see also Table 1.1, where the particles of the SM are summarized together with their quantum numbers under $SU(3)_c \times SU(2)_L \times U(1)_Y$.

| field | $SU(3)_c$ | $SU(2)_L$ | $U(1)_Y$ |
|---|---|---|---|
| $E_L = \begin{pmatrix} \psi_{\nu_e} \\ \psi_{e_L} \end{pmatrix}$ | **1** | **2** | $-\frac{1}{2}$ |
| $\psi_{e_R}$ | **1** | **1** | $-1$ |
| $Q_L = \begin{pmatrix} \psi_{u_L} \\ \psi_{d_L} \end{pmatrix}$ | **3** | **2** | $\frac{1}{6}$ |
| $\psi_{u_R}$ | **3** | **1** | $\frac{2}{3}$ |
| $\psi_{d_R}$ | **3** | **1** | $-\frac{1}{3}$ |
| $\Phi = \begin{pmatrix} \phi^+ \\ \phi^0 \end{pmatrix}$ | **1** | **2** | $\frac{1}{2}$ |
| $G^A$ | **8** | **1** | 0 |
| $W^a$ | **1** | **3** | 0 |
| $B$ | **1** | **1** | 0 |

Table 1.1: The SM fields with their quantum numbers under $SU(3)_c \times SU(2)_L \times U(1)_Y$.

The gauge invariant Lagrangian of the fermion fields is given by

$$\begin{aligned}\mathcal{L}_f =& \bar{E}_L i\not{D} E_L + \bar{\psi}_{e_R} i\not{D} \psi_{e_R} \\ &+ \bar{Q}_L i\not{D} Q_L + \bar{\psi}_{u_R} i\not{D} \psi_{u_R} + \bar{\psi}_{d_R} i\not{D} \psi_{d_R},\end{aligned} \tag{1.13}$$

where generation and color indices are suppressed for convenience. The covariant derivative is defined as

$$D_\mu = \partial_\mu + i g_s t^A G^A_\mu + i g T^a W^a_\mu + i g' Y B_\mu, \tag{1.14}$$

where $g_s$, $g$ and $g'$ are the $SU(3)_c$, $SU(2)_L$ and $U(1)_Y$ gauge coupling constants; $t^A$, $T^a$ and $Y$ are the generators of the corresponding gauge group in the representation to which the particle belongs, and $G^A_\mu$, $W^a_\mu$, and $B_\mu$ are the gauge fields. The hypercharge $Y$ is defined by $Y = Q - T^3$.

The kinetic terms of the gauge fields read

$$\mathcal{L}_V = -\frac{1}{4} G^A_{\mu\nu} G^{A,\mu\nu} - \frac{1}{4} W^a_{\mu\nu} W^{a,\mu\nu} - \frac{1}{4} B_{\mu\nu} B^{\mu\nu}, \tag{1.15}$$

with the field strength tensors

$$\begin{aligned} G^A_{\mu\nu} &= \partial_\mu G^A_\nu - \partial_\nu G^A_\mu - g_s f^{ABC} G^B_\mu G^C_\nu, \\ W^a_{\mu\nu} &= \partial_\mu W^a_\nu - \partial_\nu W^a_\mu - g \epsilon^{abc} W^b_\mu W^c_\nu, \\ B_{\mu\nu} &= \partial_\mu B_\nu - \partial_\nu B_\mu, \end{aligned} \tag{1.16}$$

where $f^{ABC}$ and $\epsilon^{abc}$ are the structure constants of $SU(3)_c$ and $SU(2)_L$. The last term of $G^A_{\mu\nu}$ and $W^a_{\mu\nu}$ gives rise to self-interactions of gauge bosons, and is necessary for gauge invariance under non-abelian gauge groups.

To generate mass terms for the weak gauge-bosons, we introduce a complex scalar

field which transforms under $SU(2)_L \times U(1)_Y$ as

$$\Phi(x) \to e^{i\alpha^a(x)T^a} e^{i\beta(x)Y} \Phi(x), \tag{1.17}$$

where $T^a = \frac{\sigma^a}{2}$ and $Y = \frac{1}{2}$. The Lagrangian is given by

$$\mathcal{L}_H = (D_\mu \Phi)^\dagger (D^\mu \Phi) - V(\Phi), \tag{1.18}$$

with the potential

$$V(\Phi) = -\mu^2 \Phi^\dagger \Phi + \lambda (\Phi^\dagger \Phi)^2. \tag{1.19}$$

As discussed in the previous section, for $\mu^2 > 0$, $\Phi$ develops a VEV that breaks $SU(2)_L \times U(1)_Y$ to $U(1)_{\text{em}}$,

$$|\Phi_0| = \sqrt{\frac{\mu^2}{2\lambda}} = \frac{v}{\sqrt{2}}. \tag{1.20}$$

With a possible parametrization

$$\Phi = \frac{1}{\sqrt{2}} \begin{pmatrix} \phi_1 + i\phi_2 \\ \phi_3 + i\phi_4 \end{pmatrix}, \tag{1.21}$$

we choose the VEV in the direction of $\phi_3$, $\langle \phi_3 \rangle = v$, $\langle \phi_i \rangle = 0$ for $i = 1, 2, 4$. In unitary gauge, $\Phi$ is given by

$$\Phi(x) = \frac{1}{\sqrt{2}} \begin{pmatrix} 0 \\ v + H(x) \end{pmatrix}. \tag{1.22}$$

The three degrees of freedom of the goldstone bosons $\phi_{1,2,4}$ are absorbed by the massive gauge fields and provide their longitudinal polarization modes. The physical scalar $H$ is the Brout-Englert-Higgs field. Inserting (1.22) in the first term of (1.18) generates mass terms for the $W^\pm, Z$ as well as interaction terms between the $H$ boson and the gauge bosons $W^\pm, Z$. The mass eigenstates of the gauge bosons are given by

$$\begin{aligned} W_\mu^\pm =& \frac{1}{\sqrt{2}} (W_\mu^1 \mp i W_\mu^2), \\ \begin{pmatrix} Z_\mu \\ A_\mu \end{pmatrix} =& \begin{pmatrix} \cos\theta_w & -\sin\theta_w \\ \sin\theta_w & \cos\theta_w \end{pmatrix} \begin{pmatrix} W_\mu^3 \\ B_\mu \end{pmatrix}, \end{aligned} \tag{1.23}$$

where the Weinberg angle $\theta_w$ is defined through

$$\cos\theta_w = \frac{g}{\sqrt{g^2 + g'^2}}, \tag{1.24}$$

and the masses are given as

$$\begin{aligned} m_W =& \frac{1}{2} g\, v, \\ m_Z =& \frac{1}{2} \sqrt{g^2 + g'^2}\, v. \end{aligned} \tag{1.25}$$

From the potential (1.19), we obtain a mass term for the $H$ boson with

$$m_H = \sqrt{2}\mu = \sqrt{2\lambda}v. \tag{1.26}$$

The Yukawa interactions of the SM fermions and the complex scalar field are given by

$$\mathcal{L}_Y = -\sum_{i,j=1}^{3} \left( \lambda^e_{ij} \bar{E}_{Li} \Phi \psi_{e_R\, j} + \lambda^u_{ij} \bar{Q}_{Li} \tilde{\Phi} \psi_{u_R\, j} + \lambda^d_{ij} \bar{Q}_{Li} \Phi \psi_{d_R\, j} \right) + h.c., \tag{1.27}$$

with $\tilde{\Phi} = i\sigma_2 \Phi^*$ and $i, j$ are the generation indices. Inserting (1.22) leads to mass terms for the fermions as well as interactions between the fermions and the $H$ boson. The mass matrices for the leptons and quarks are

$$m^e_{ij} = \frac{v}{\sqrt{2}} \lambda^e_{ij}, \;\; m^u_{ij} = \frac{v}{\sqrt{2}} \lambda^u_{ij}, \;\; m^d_{ij} = \frac{v}{\sqrt{2}} \lambda^d_{ij}. \tag{1.28}$$

## 1.4 The goldstone boson equivalence

Since we will work with goldstone particles throughout this work, we would like to demonstrate their role in scattering processes of the SM. Although we removed them from our theory by choosing a particular gauge (i.e. the unitary gauge), their properties might still show up in physical observables, according to the goldstone boson equivalence theorem [12, 13]. It states that in the high-energy limit, scattering processes involving longitudinally polarized gauge bosons can be calculated by replacing the gauge bosons by their corresponding goldstone bosons.

As explicit example, we discuss the scattering of $W$-bosons [12, 13]

$$W^+(p_1) + W^-(p_2) \to W^+(p_3) + W^-(p_4), \tag{1.29}$$

where $p_i$ denote the four momenta. In the high-energy limit, $\sqrt{s} \gg m_W$, where $\sqrt{s}$ is the center-of-mass (CM) energy of the collision, the cross section is dominated by the longitudinally polarized gauge bosons, since their wavefunctions are $\epsilon^\mu_L \propto \frac{\sqrt{s}}{m_W}$, while the transverse polarizations scale as $s^0$. The goldstone boson equivalence theorem tells us that in the high-energy limit the cross section for the scattering of longitudinally $W$-bosons is approximately the cross section for goldstone boson scattering

$$\sigma(W^+_L W^-_L \to W^+_L W^-_L) \approx \sigma(\phi^+ \phi^- \to \phi^+ \phi^-). \tag{1.30}$$

Here, $\phi^\pm$ are the goldstone bosons that would be absorbed by the $W^\pm$.

A nice feature of this example is that it shows how gauge symmetries together with the $H$ boson are responsible for preserving the unitarity of the SM. We present this in the first part of the following discussion. Subsequently, we show the equivalence of the amplitude calculated with the longitudinally polarized $W$ bosons and the amplitude

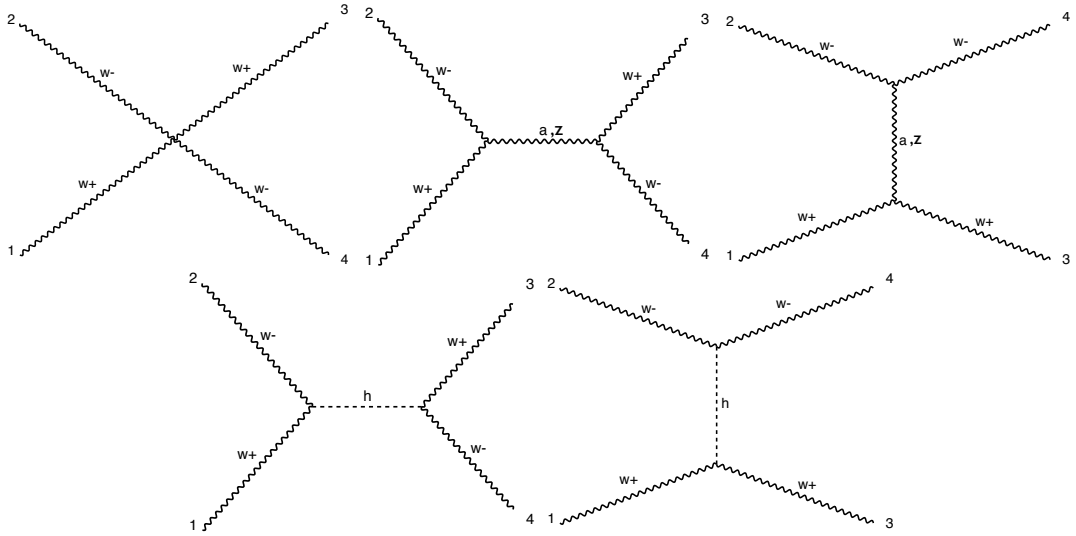


Figure 1.3: The Feynman diagrams contributing to $W_L^+W_L^- \to W_L^+W_L^-$, generated by MadGraph 5 [14]. w±, a, z,h denote a longitudinally polarized $W^\pm$ boson, a photon, a $Z$ boson, and a $H$ boson.

calculated with the corresponding goldstone bosons.

The total cross section is given by

$$\sigma(W_L^+W_L^- \to W_L^+W_L^-) = \frac{1}{32\pi s}\int d\cos\theta\,|\mathcal{M}|^2, \tag{1.31}$$

where $\cos\theta$ is the angle between the outgoing particles and the collision axis, and $\mathcal{M}$ is the sum of amplitudes of the sub-channel contributions: the four-point vertex, the $s$- and $t$-channel photon and $Z$ boson exchanges, and the $s$- and $t$-channel $H$-boson exchanges; see also Fig. 1.3,

$$\mathcal{M}(W_L^+W_L^- \to W_L^+W_L^-) = \mathcal{M}_{\text{gauge}} + \mathcal{M}_H, \tag{1.32}$$

where

$$\mathcal{M}_{\text{gauge}} = \mathcal{M}^{\text{four}} + \mathcal{M}^s_{\gamma+Z} + \mathcal{M}^t_{\gamma+Z}, \tag{1.33}$$

$$\mathcal{M}_H = \mathcal{M}^s_H + \mathcal{M}^t_H. \tag{1.34}$$

From the Lagrangian given in (1.15) and (1.18), we can derive the Feynman rules presented in Fig. 1.4.

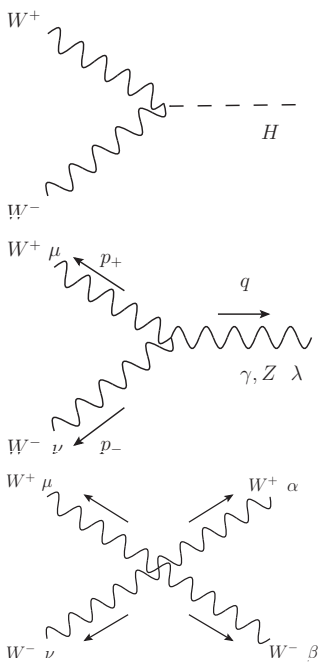


$$2i\frac{m_W^2}{v}g^{\mu\nu}$$

$$-ic\big(g^{\mu\nu}(p_- - p_+)^\lambda + g^{\nu\lambda}(q-p_-)^\mu + g^{\lambda\mu}(-q+p_+)^\nu\big)$$

$$c = \begin{cases} g_e \text{ for } \gamma \\ g\cos\theta_w \text{ for } Z \end{cases}$$

$$ig^2(2g^{\mu\alpha}g^{\nu\beta} - g^{\mu\beta}g^{\nu\alpha} - g^{\alpha\beta}g^{\mu\nu})$$

Figure 1.4: The Feynman rules for the process $W^+W^- \to W^+W^-$.

The explicit expressions for the amplitudes are given by

$$\begin{aligned}
i\mathcal{M}^{\text{four}} &= ig^2\left(2\epsilon_1\cdot\epsilon_4\,\epsilon_2\cdot\epsilon_3 - \epsilon_1\cdot\epsilon_3\,\epsilon_2\cdot\epsilon_4 - \epsilon_1\cdot\epsilon_2\,\epsilon_3\cdot\epsilon_4\right), \\
i\mathcal{M}^s_{\gamma+Z} &= ig^2\Big(\frac{\sin^2\theta_w}{s} + \frac{\cos^2\theta_w}{s-m_Z^2}\Big)\big(\epsilon_1\cdot\epsilon_2(p_2-p_1)^\mu + 2p_1\cdot\epsilon_2\epsilon_1^\mu - 2p_2\cdot\epsilon_1\epsilon_2^\mu\big) \\
&\quad\times\big(\epsilon_3\cdot\epsilon_4(p_4-p_3)_\mu - 2p_4\cdot\epsilon_3\epsilon_{4,\mu} + 2p_3\cdot\epsilon_4\epsilon_{3,\mu}\big), \\
i\mathcal{M}^t_{\gamma+Z} &= ig^2\left(\frac{\sin^2\theta_w}{t} + \frac{\cos^2\theta_w}{t-m_Z^2}\right)\big(-\epsilon_1\cdot\epsilon_3(p_1+p_3)^\mu + 2p_1\cdot\epsilon_3\epsilon_1^\mu + 2p_3\cdot\epsilon_1\epsilon_3^\mu\big) \\
&\quad\times\big(\epsilon_2\cdot\epsilon_4(p_2+p_4)_\mu - 2p_4\cdot\epsilon_2\epsilon_{4,\mu} - 2p_2\cdot\epsilon_4\epsilon_{2,\mu}\big), \\
i\mathcal{M}^s_H &= \frac{-i4m_W^4}{v^2}\frac{1}{s-m_H^2}\big(\epsilon_1\cdot\epsilon_2\,\epsilon_3\cdot\epsilon_4\big), \\
i\mathcal{M}^t_H &= \frac{-i4m_W^4}{v^2}\frac{1}{t-m_H^2}\big(\epsilon_1\cdot\epsilon_3\,\epsilon_2\cdot\epsilon_4\big),
\end{aligned} \tag{1.35}$$

where $\epsilon_i^\mu = \epsilon_L^\mu(p_i)$ and $t = (p_1-p_3)^2$, $u = (p_1-p_4)^2$ and we used the relation $g_e = g\sin\theta_w$. Since $\epsilon_L^\mu \propto \frac{\sqrt{s}}{m_W}$, we expect at least some of the amplitudes to grow with the energy as $s^2$. Naively, this leads to a cross section that rises with $s^3$, so that the probability for this process to happen would grow continuously with increasing energy and eventually hit the unitarity bound, indicating the break-down of the theory at some energy scale.[2] However, the explicit calculation shows that, due to the gauge symmetry, the leading energy dependence cancels among the amplitudes of the gauge sector. The remaining contributions from the gauge bosons grow with $s$, but those are cancelled

[2]For a review about partial wave unitarity, see Appendix A.4.

| | | $\mathcal{M}^{\text{four}}$ | $\mathcal{M}^{s}_{\gamma+Z}$ | $\mathcal{M}^{t}_{\gamma+Z}$ | |
|---|---|---|---|---|---|
| $\mathcal{O}(s^2)$ | $\frac{g^2 s^2}{16 m_W^4}[$ | $-3+6c_\theta+c_\theta^2$ | $-4c_\theta$ | $+3-2c_\theta-c_\theta^2$ | $]$ |
| $\mathcal{O}(s)$ | $\frac{g^2 s}{8 m_W^2}[$ | $4-12c_\theta$ | $-2\frac{m_Z^2}{m_W^2}c_w^2 c_\theta$ | $+(16c_\theta-\frac{m_Z^2}{m_W^2}c_w^2(3+c_\theta))$ | $]$ |

Table 1.2: The leading and next-to-leading energy dependence from the gauge sector of the helicity amplitudes for the process $W_L^+W_L^- \to W_L^+W_L^-$.

against the contributions from the $H$ boson, rendering the cross section well behaved in the high energy limit.

We now present the explicit expressions for the cancellations of the leading and next-to-leading energy dependent terms. The amplitudes in (1.35) are calculated in the limit $\sqrt{s} \gg m_W$, with the four-momenta defined in the CM-frame of the incoming $W$ bosons,

$$\begin{aligned} p_1^\mu &= \frac{\sqrt{s}}{2}(1,0,0,\beta_i)\,, \\ p_2^\mu &= \frac{\sqrt{s}}{2}(1,0,0,-\beta_i)\,, \\ p_3^\mu &= \frac{\sqrt{s}}{2}(1,\beta_f s_\theta,0,\beta_f c_\theta)\,, \\ p_4^\mu &= \frac{\sqrt{s}}{2}(1,-\beta_f s_\theta,0,-\beta_f c_\theta)\,, \end{aligned} \tag{1.36}$$

with $\beta_i = \beta_f = \sqrt{1-\frac{4m_W^2}{s}}$, $s_\theta = \sin\theta$, $c_\theta = \cos\theta$ and the corresponding longitudinal polarization vectors[3]

$$\begin{aligned} \epsilon_L^\mu(p_1) &= \frac{\sqrt{s}}{2m_W}(\beta_i,0,0,1)\,, \\ \epsilon_L^\mu(p_2) &= \frac{\sqrt{s}}{2m_W}(\beta_i,0,0,-1)\,, \\ \epsilon_L^\mu(p_3) &= \frac{\sqrt{s}}{2m_W}(\beta_f,s_\theta,0,c_\theta)\,, \\ \epsilon_L^\mu(p_4) &= \frac{\sqrt{s}}{2m_W}(\beta_f,-s_\theta,0,-c_\theta)\,. \end{aligned} \tag{1.37}$$

The terms of $\mathcal{M}_{\text{gauge}}$ that grow with energy are listed in Table 1.2, where the relations (1.25) and the abbreviations $c_w = \cos\theta_w$ and $s_w = \sin\theta_w$ are used. We observe that the $s^2$ dependent terms cancel between the four-point vertex and the $s$- and $t$-channel exchange of photon and $Z$.

In the second row of Table 1.2, the next-to-leading energy dependent terms from

[3]The two transverse and the one longitudinal polarization vectors for a massive gauge boson with momentum $p_\mu$ are defined by $\epsilon^\mu p_\mu = 0$. Throughout this work, we follow the HELAS convention [15]; see Appendix A.2.

the gauge bosons are displayed. Using the relation

$$c_w = \frac{m_W}{m_Z}, \tag{1.38}$$

they sum up to

$$i\mathcal{M}_{\text{gauge}} = i\frac{g^2 s}{8m_W^2}(1+\cos\theta) + \mathcal{O}(s^0). \tag{1.39}$$

The contributions from the $H$ boson exchange diagrams (1.34) read

$$i\mathcal{M}_H = -\frac{ig^2}{4m_W^2}\Big[\frac{s^2(1-\frac{2m_W^2}{s})^2}{s-m_H^2} + \frac{t^2(1+\frac{2m_W^2\cos\theta}{t})^2}{t-m_H^2}\Big]. \tag{1.40}$$

Since we are interested in the limit $\sqrt{s} \gg m_W$, we neglect the terms proportional to $\frac{m_W^2}{s}$ in the numerator and (1.40) can be written as

$$i\mathcal{M}_H = -\frac{ig^2 s}{8m_W^2}\Big(1+\cos\theta\Big) - \frac{ig^2 m_H^2}{4m_W^2}\Big(\frac{s}{s-m_H^2} + \frac{t}{t-m_H^2}\Big) + \mathcal{O}\Big(\frac{m_W^2}{s}\Big). \tag{1.41}$$

The first term cancels against the energy dependent term from the gauge bosons (1.39), and (1.32) gives

$$i\mathcal{M}(W_L^+W_L^- \to W_L^+W_L^-) = -\frac{ig^2 m_H^2}{4m_W^2}\Big(\frac{s}{s-m_H^2} + \frac{t}{t-m_H^2}\Big) + \mathcal{O}\Big(\frac{m_W^2}{s}, \frac{m_W}{m_H}\Big), \tag{1.42}$$

which is well behaved in the high energy limit. We note that for a light $H$ boson, the contributions from the gauge sector, i.e. the term $\sim \mathcal{O}(s^0)$ in (1.39), can be comparable to the contributions from the $H$ boson in (1.42).

We now show how (1.42) can be reproduced by calculating the scattering amplitudes using the goldstone bosons. To derive the couplings of the goldstone bosons

$$\phi^\pm = \frac{1}{\sqrt{2}}(\phi_1 \pm i\phi_2), \tag{1.43}$$

we keep the would-be goldstone bosons in the scalar doublet given in (1.21) as

$$\Phi = \begin{pmatrix} \phi^+ \\ \frac{1}{\sqrt{2}}(v+H+i\phi_3) \end{pmatrix}. \tag{1.44}$$

Inserted in the Lagrangian defined in (1.18) we obtain the Feynman rules displayed in Fig. 1.5. The involved diagrams are the scalar four-point vertex and the $s$- and $t$-channel $H$-boson exchange, see also Fig. 1.6,

$$\mathcal{M}(\phi^+\phi^- \to \phi^+\phi^-) = \mathcal{M}^{\text{four}} + \mathcal{M}_H^s + \mathcal{M}_H^t, \tag{1.45}$$

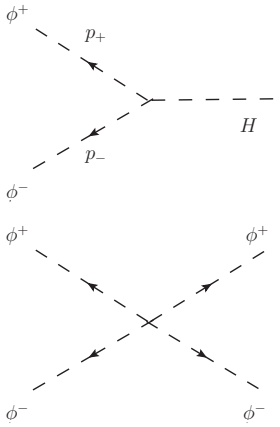


$-2iv\lambda$

$-4i\lambda$

Figure 1.5: The Feynman rules from the Higgs sector for the process $\phi^+\phi^- \to \phi^+\phi^-$.

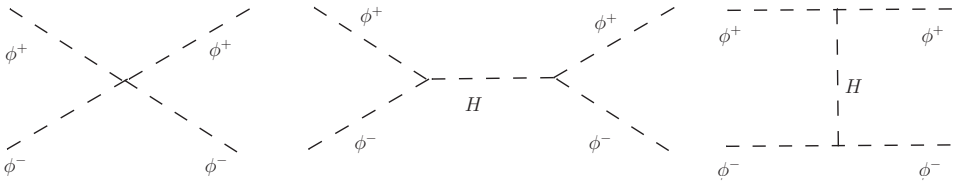


Figure 1.6: The Feynman diagrams for $\phi^+\phi^- \to \phi^+\phi^-$.

where the explicit expressions of the amplitudes are

$$\begin{aligned} i\mathcal{M}^{\text{four}} &= -4i\lambda, \\ i\mathcal{M}_H^s &= -i\frac{4\lambda^2 v^2}{s - m_H^2}, \\ i\mathcal{M}_H^t &= -i\frac{4\lambda^2 v^2}{t - m_H^2}. \end{aligned} \tag{1.46}$$

Using the relation $\lambda = \frac{m_H^2}{2v^2}$ and $v = \frac{2m_W}{g}$, this gives

$$i\mathcal{M}(\phi^+\phi^- \to \phi^+\phi^-) = -\frac{ig^2 m_H^2}{4m_W^2}\Big(\frac{s}{s - m_H^2} + \frac{t}{t - m_H^2}\Big), \tag{1.47}$$

which reproduces the leading terms in (1.42).

# CHAPTER 2

# Supersymmetry (SUSY)

Although the SM describes a lot of experimental data very successfully, we expect that there is physics beyond the SM, and the SM to be only the low-energy effective theory of a more fundamental theory. Open questions that drive the search for new physics are for example:

- How is the $H$ boson stabilized against quantum corrections?
- What explains the flavor structure of quarks and leptons?
- How can we explain neutrino masses?
- Is there a way to incorporate the gravity in the theory?
- Do the gauge couplings unify?
- What is dark matter? What is dark energy?

An attractive theory that addresses some of these open questions is supersymmetry (SUSY). In Section 2.1, we explain the first item of the above list in more detail, and show how SUSY cures the instability of the $H$ boson mass against quantum corrections.

In Section 2.2, we introduce some basics of SUSY. First, we show the relation between a Lagrangian in four-component notation as used in the previous section and the two-component notation which is usually used in SUSY theories. Next, we give a simple example of a SUSY Lagrangian, followed by introducing the so called "superspace" and "superfields" which will be very helpful in the construction of a Lagrangian invariant under SUSY transformations.

Then, we use the superspace formalism to write down the SUSY QED Lagrangian in Section 2.3 as a simple example of a fully SUSY invariant theory.

Subsequently, we give a brief description of the minimal supersymmetric model (MSSM) in Section 2.4.

## 2.1 The fine-tuning problem

In the following, we concentrate on one theoretical motivation that suggests an extension of the SM, the so-called fine-tuning or naturalness problem.

From the helicity amplitudes of the $WW$-scattering in the previous section, one can derive an upper bound on the expected $H$ boson mass from partial wave unitarity [16], which is $m_H \lesssim 1$ TeV.[1] However, when we compute the quantum corrections to the $H$ boson mass, we find that they depend quadratically on a parameter $\Lambda$, which can be interpreted as the scale at which new physics enters. That means, if $\Lambda = M_{\mathrm{Pl}} \approx 10^{19}$ GeV, the scale where quantum gravitational effects become important, the $H$ boson would naturally prefer to be very heavy. To obtain a light $H$ boson in renormalized perturbation theory, one must precisely adjust the counterterms against the radiative corrections. This is the so-called *fine-tuning* problem. We note that this adjustment

[1] The general argument of partial wave unitarity is reviewed in Appendix A.4.

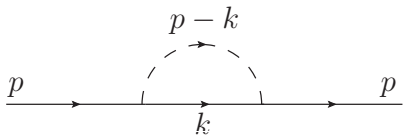


Figure 2.1: The correction to the fermion mass from the scalar $H$ boson.

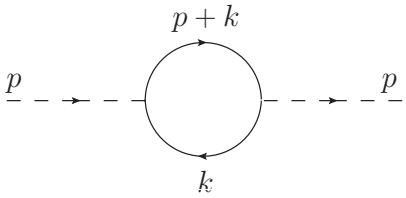


Figure 2.2: The correction to the scalar $H$ boson mass from a fermion.

can be done and hence is not a problem in itself, but it is not *natural*. To clarify what this means, we compute the radiative corrections to the mass of a fermion that couples to the $H$ boson, and compare them to the radiative corrections to the $H$ boson mass from a fermion, see e.g. [17, 18].

Assume a dirac fermion $\psi_f$ of mass $m_f$ that couples (after electroweak symmetry breaking) to the $H$ boson as

$$\mathcal{L}_f = -\frac{\lambda_f}{\sqrt{2}}\bar{\psi}_f\psi_f H, \tag{2.1}$$

where the mass and the coupling are related by $\lambda_f = \frac{\sqrt{2}m_f}{v}$.

We compute the fermion self-energy from the $H$ loop; see also Fig. 2.1,

$$-i\Sigma_f(p) = \Big(\frac{-i\lambda_f}{\sqrt{2}}\Big)^2 \int \frac{d^4k}{(2\pi)^4} \frac{i(\not{k} + m_f)}{[k^2 - m_f^2 + i\epsilon]} \frac{i}{[(p-k)^2 - m_H^2 + i\epsilon]}. \tag{2.2}$$

When evaluating the integral and using a cut-off $\Lambda$ to regularize it, we find a logarithmic dependence on the cut-off scale,

$$\delta m_f = \Sigma_f(p = m_f) \sim -m_f \ln\frac{\Lambda}{m_f} + \cdots, \tag{2.3}$$

where the dots stand for terms that are independent of $\Lambda$ or vanish when $\Lambda \to \infty$. The quantity $\Sigma_f(p = m_f)$ is interpreted as a correction to the fermion mass. We find that, when the fermion mass approaches zero, also its correction $\delta m_f$ goes to zero, a behavior that is said to be *natural*. This is because a fermionic mass term $m_f\bar{\psi}_f\psi_f$ or also a term like (2.1) breaks chiral symmetry. Hence, by setting the fermion mass to zero, and equivalently $\lambda_f \to 0$, we increase the symmetry of the Lagrangian. We say the fermion masses are protected by the chiral symmetry.

We now compute the one-loop quantum corrections from a fermion to the mass of

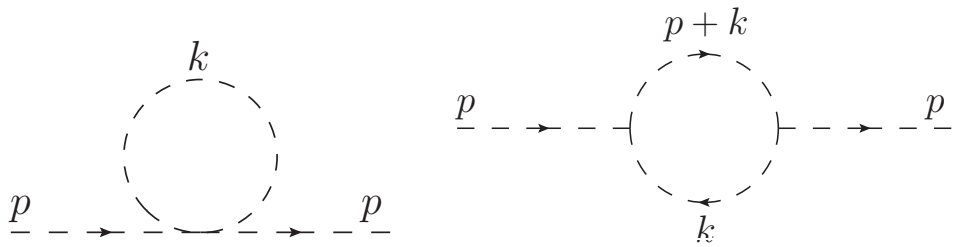


Figure 2.3: The corrections to the $H$ boson mass from scalar particles; there is a contribution from the four-point interaction (left) and a contribution from the three-point interactions (right).

the $H$ boson; see Fig. 2.2,

$$-i\Sigma_H(p^2) = (-1)\Big(\frac{-i\lambda_f}{\sqrt{2}}\Big)^2 \int \frac{d^4k}{(2\pi)^4} \frac{(i)^2 \mathrm{Tr}[(\not{p}+\not{k}+m_f)(\not{k}+m_f)]}{[(p+k)^2 - m_f^2 + i\epsilon][k^2 - m_f^2 + i\epsilon]}. \tag{2.4}$$

The minus sign arises due to fermi statistics from entangling the fermionic fields before contracting them. The explicit calculation using again the cut-off $\Lambda$ to regulate the integral gives the correction $\delta m_H^2$ to the $H$ boson mass as $\delta m_H^2 = \Sigma_H(p^2 = m_H)$

$$\delta m_H^2 = -\frac{\lambda_f^2}{8\pi^2}\Big[\Lambda^2 - 6m_f^2 \ln\frac{\Lambda}{m_f} + 2m_f\Big] + \mathcal{O}\Big(\frac{1}{\Lambda^2}\Big), \tag{2.5}$$

where for simplicity we assume the fermion to be very heavy so that we can neglect the external $H$ boson momentum squared.[2] The correction $\delta m_H^2$ is proportional to $\Lambda^2$ and does not vanish when the $H$ boson mass goes to zero. There is no symmetry that protects the $H$ boson mass, as in the case of the fermion mass.

The situation is quite different if we assume $N$ additional complex scalar particles $S_i, (i = 1, \ldots, N)$ with masses $m_S$ that couple to the $H$ boson as

$$\mathcal{L}_S = \frac{\lambda_S}{2} H^2 S_i^\dagger S_i + v\lambda_S H S_i^\dagger S_i. \tag{2.6}$$

They will also contribute corrections to the $H$ boson mass from the diagrams displayed in Fig. 2.3; the four-point interaction,

$$-i\Sigma_{H,\mathrm{four}} = iN\lambda_S \int \frac{d^4k}{(2\pi)^4} \frac{i}{k^2 - m_S^2 + i\epsilon}, \tag{2.7}$$

gives a correction $\delta m_{H,\mathrm{four}}^2 = \Sigma_{H,\mathrm{four}}(p^2 = m_H^2)$,

$$\delta m_{H,\mathrm{four}}^2 = -N\frac{\lambda_S}{16\pi^2}\Big[\Lambda^2 - 2m_S \ln\frac{\Lambda}{m_S}\Big] + \mathcal{O}\Big(\frac{1}{\Lambda^2}\Big). \tag{2.8}$$

In a similar way, the three-point interaction gives a correction $\delta m_{H,\mathrm{three}}^2 = \Sigma_{H,\mathrm{three}}(p^2 =$

[2] The qualitative result will not change; the full result can be found e.g. in [17].

$m_H^2$), with

$$-i\Sigma_{H,\text{three}} = N(iv\lambda_S)^2 \int \frac{d^4k}{(2\pi)^4} \frac{i}{[(p+k)^2 - m_S^2 + i\epsilon]} \frac{i}{[k^2 - m_S^2 + i\epsilon]}, \tag{2.9}$$

so that

$$\delta m_{H,\text{three}}^2 = -N\frac{(v\lambda_S)^2}{16\pi^2}\Big[2\ln\frac{\Lambda}{m_S} - 1\Big] + \mathcal{O}\Big(\frac{1}{\Lambda^2}\Big), \tag{2.10}$$

where we neglected again the external $H$ boson momentum squared.

Summing up all the corrections to the $H$ boson mass from (2.5) and for $N$ scalar particles (2.8) and (2.10), we find that the quadratically divergent part cancels if

$$N = 2, \tag{2.11}$$

and

$$\lambda_f^2 = -\lambda_S. \tag{2.12}$$

We are left with a correction to the $H$ boson mass that depends only logarithmically on $\Lambda$,

$$\delta m_{H,\text{tot}}^2 = \frac{\lambda_f^2}{4\pi^2}\Big[(m_f^2 - m_S^2)\ln\frac{\Lambda}{m_S} - 3m_f^2\ln\frac{m_f}{m_S}\Big] + \mathcal{O}\Big(\frac{1}{\Lambda^2}\Big), \tag{2.13}$$

hence the naturalness problem is solved.

In the next section, we will see that SUSY assigns two scalar particles to every dirac fermion as in (2.11), and relates the couplings between the scalar and fermionic interactions as in (2.12). In an exact SUSY theory, the masses of fermion and scalar boson are the same, $m_f = m_S$, so that the quantum corrections in (2.13) to the $H$ boson mass vanishes. In that case, the $H$ boson mass is protected by SUSY similar to the way the fermion mass is protected by chiral symmetry.[3]

Besides offering a solution to the fine-tuning problem, SUSY addresses also others of the questions given in the beginning of this chapter. We will see in Section 2.4 that the lightest SUSY particle is protected from decaying into SM particles, and hence provides in many SUSY models a dark matter candidate [19–21].

In the minimal supersymmetric extension of the SM (MSSM), it is possible to obtain gauge coupling unification [22]. Calculating the evolution of the SM coupling constants with the SM particle content only, one finds that the couplings come relatively close to each other at high energies, but they do not actually meet. In the MSSM, the renormalization group equations describing the energy dependence of the couplings receive extra contributions from the SUSY particles, and unification can be obtained.

[3]We note that the corrections from massive gauge boson loops, as well as the $H$ boson self-interactions also introduce quadratic divergences. In SUSY, these are cancelled by the corresponding fermionic partners of the particles.

## 2.2 Basics of SUSY

### 2.2.1 Introduction to two-component notation

To perform our phenomenological studies, we will be working most of the time with the well known four-component notation, that was used in the previous sections. However, to construct a SUSY Lagrangian, it is convenient to introduce a two-component notation. Here, we present a short description on how the two notations are related.

In four-component notation, the free Lagrangian of a massless Dirac fermion $\psi_D$ is given as in (1.1) by

$$\mathcal{L} = \bar{\psi}_D i\gamma^\mu \partial_\mu \psi_D, \tag{2.14}$$

where the $4 \times 4$ gamma matrices are given as

$$\gamma^\mu = \begin{pmatrix} 0 & \sigma^\mu \\ \bar{\sigma}^\mu & 0 \end{pmatrix}. \tag{2.15}$$

$\sigma^0$ and the Pauli matrices are shown in the Appendix A.1.[4] The four-component Dirac spinor $\psi_D$ is composed of a left- and a right-handed two-component Weyl spinor

$$\psi_D = \begin{pmatrix} \xi_\alpha \\ \bar{\chi}^{\dot{\alpha}} \end{pmatrix}, \tag{2.16}$$

where we explicitly write the spinor indices $\alpha = 1, 2$ for left-handed pieces and $\dot{\alpha} = 1, 2$ for right-handed pieces. The hermitian conjugate of a left-handed Weyl spinor is a right-handed Weyl spinor and vice-versa,

$$(\lambda_\alpha)^\dagger = \bar{\lambda}_{\dot{\alpha}}, \ (\bar{\lambda}^{\dot{\alpha}})^\dagger = \lambda^\alpha. \tag{2.17}$$

We find

$$\bar{\psi}_D = \psi_D^\dagger \gamma^0 = (\chi^\alpha \ \bar{\xi}_{\dot{\alpha}}). \tag{2.18}$$

The dot product of two Weyl spinors is defined as

$$\begin{aligned} \chi \cdot \xi &= \chi^\alpha \xi_\alpha = \varepsilon^{\alpha\beta} \chi_\beta \xi_\alpha, \\ \bar{\chi} \cdot \bar{\xi} &= \bar{\chi}_{\dot{\alpha}} \bar{\xi}^{\dot{\alpha}} = \varepsilon^{\dot{\alpha}\dot{\beta}} \bar{\chi}_{\dot{\alpha}} \bar{\xi}_{\dot{\beta}}. \end{aligned} \tag{2.19}$$

We follow the FeynRules convention, where the antisymmetric tensor is defined by $\varepsilon_{12} = \varepsilon_{\dot{1}\dot{2}} = -\varepsilon^{21} = -\varepsilon^{\dot{2}\dot{1}} = 1$ and $\varepsilon_{11} = \varepsilon_{\dot{1}\dot{1}} = \varepsilon^{22} = \varepsilon^{\dot{2}\dot{2}} = 0$. Note that $\chi \cdot \xi = \xi \cdot \chi$ and $\bar{\chi} \cdot \bar{\xi} = \bar{\xi} \cdot \bar{\chi}$. A useful summary of identities involving the epsilon tensor and $\sigma$ matrices can be found in Appendix A of [23].

[4] The spinor indices are $\sigma^\mu = \sigma^\mu_{\alpha\dot{\alpha}}, \bar{\sigma}^\mu = \bar{\sigma}^{\mu\,\dot{\alpha}\alpha}$.

In two-component notation, the Lagrangian defined in (2.14) reads

$$\begin{aligned} i\bar{\psi}_D \not{\partial} \psi_D &= i(\chi^\alpha \sigma^\mu_{\alpha\dot{\alpha}} \partial_\mu \bar{\chi}^{\dot{\alpha}} + \bar{\xi}_{\dot{\alpha}} \bar{\sigma}^{\mu\,\dot{\alpha}\alpha} \partial_\mu \xi_\alpha) \\ &= i(\bar{\chi}_{\dot{\alpha}} \bar{\sigma}^{\mu\,\dot{\alpha}\alpha} \partial_\mu \chi_\alpha + \bar{\xi}_{\dot{\alpha}} \bar{\sigma}^{\mu\,\dot{\alpha}\alpha} \partial_\mu \xi_\alpha) + \text{ total derivative}, \end{aligned} \tag{2.20}$$

where to obtain the last line we used the relation $\bar{\lambda}\bar{\sigma}^\mu \lambda' = -\lambda' \sigma^\mu \bar{\lambda}$ and integration by parts, $(\partial_\mu a)b = \partial_\mu(ab) - a\partial_\mu b$.

We note that for a Majorana fermion $\psi_M$ the left- and right handed component are related to each other,

$$\psi_M = \begin{pmatrix} \xi_\alpha \\ \bar{\xi}^{\dot{\alpha}} \end{pmatrix}. \tag{2.21}$$

### 2.2.2 A simple example of a SUSY Lagrangian

A supersymmetric transformation converts a boson into a fermion, and a fermion into a boson. To get an idea about a SUSY theory, we consider the Lagrangian describing a massless complex scalar field and a left-handed Weyl fermion,

$$\mathcal{L} = \partial_\mu \phi \partial^\mu \phi^* + i\bar{\psi}_{\dot{\alpha}} \bar{\sigma}^{\mu\,\dot{\alpha}\alpha} \partial_\mu \psi_\alpha, \tag{2.22}$$

where we explicitly write out the spinor indices. This is the so called massless Wess-Zumino model [24]. Let us show that the Lagrangian in (2.22) is invariant under the following SUSY transformations. The scalar transforms under a SUSY transformation as

$$\begin{aligned} \delta\phi &= \sqrt{2}\epsilon^\alpha \psi_\alpha, \\ \delta\phi^* &= \sqrt{2}\bar{\psi}_{\dot{\alpha}} \bar{\epsilon}^{\dot{\alpha}} \end{aligned} \tag{2.23}$$

where $\epsilon$ is an infinitesimal, anti-commuting spinorial parameter with mass dimension $[\epsilon] = -1/2$. For the moment, we consider only global SUSY theories, that is $\epsilon$ is independent of the space-time, $\partial_\mu \epsilon = 0$. The fermion transforms under SUSY transformations as

$$\begin{aligned} \delta\psi_\alpha &= -i\sqrt{2}\sigma^\mu_{\alpha\dot{\alpha}} \bar{\epsilon}^{\dot{\alpha}} \partial_\mu \phi, \\ \delta\bar{\psi}_{\dot{\alpha}} &= i\sqrt{2}\epsilon^\alpha \sigma^\mu_{\alpha\dot{\alpha}} \partial_\mu \phi^* \end{aligned} \tag{2.24}$$

Applying these SUSY transformations to the fields in the Lagrangian (2.22), $\mathcal{L}$ transforms into $\mathcal{L} \to \mathcal{L} + \delta\mathcal{L}$, and leads to a change in the action $S$

$$\begin{aligned} \delta S &= \int d^4x \; \delta\mathcal{L} \\ &= \int d^4x \left[ \partial_\mu(\delta\phi)\partial^\mu \phi^* + \partial_\mu \phi \partial^\mu(\delta\phi^*) + i(\delta\bar{\psi})_{\dot{\alpha}} \bar{\sigma}^{\mu\dot{\alpha}\alpha} \partial_\mu \psi_\alpha + i\bar{\psi}_{\dot{\alpha}} \bar{\sigma}^{\mu\dot{\alpha}\alpha} \partial_\mu(\delta\psi_\alpha) \right], \end{aligned} \tag{2.25}$$

where we kept only terms linear in $\epsilon, \bar{\epsilon}$. Inserting the explicit expressions of (2.23) and (2.24), and using partial integration for the first three terms to shift derivatives from the fermion to the scalar, gives

$$\delta S = \sqrt{2}\int d^4x \Big[ -\epsilon^\alpha \psi_\alpha \partial_\mu \partial^\mu \phi^* - \bar{\psi}_{\dot{\alpha}} \bar{\epsilon}^{\dot{\alpha}} \partial_\mu \partial^\mu \phi \\ + \epsilon^\alpha \sigma^\mu_{\alpha\dot{\alpha}} \bar{\sigma}^{\nu\,\dot{\alpha}\beta} \psi_\beta \partial_\mu \partial_\nu \phi^* + \bar{\psi}_{\dot{\alpha}} \bar{\sigma}^{\mu\,\dot{\alpha}\alpha} \sigma^\nu_{\alpha\dot{\beta}} \bar{\epsilon}^{\dot{\beta}} \partial_\mu \partial_\nu \phi^* + \partial_\mu \Lambda^\mu \Big], \tag{2.26}$$

where

$$\Lambda^\mu = \sqrt{2}\big(\epsilon^\alpha \psi_\alpha \partial^\mu \phi^* + \bar{\psi}_{\dot{\alpha}} \bar{\epsilon}^{\dot{\alpha}} \partial^\mu \phi - \epsilon^\alpha \sigma^\nu_{\alpha\dot{\alpha}} \bar{\sigma}^{\mu\,\dot{\alpha}\beta} \psi_\beta \partial \nu \phi^*\big). \tag{2.27}$$

The last term can be dropped, since it is a total derivative. By using the relation $\sigma^\mu_{\alpha\dot{\alpha}} \bar{\sigma}^{\nu\,\dot{\alpha}\beta} + \sigma^\nu_{\alpha\dot{\alpha}} \bar{\sigma}^{\mu\,\dot{\alpha}\beta} = 2\eta^{\mu\nu}\delta^\beta_\alpha$, we obtain

$$\begin{aligned} \delta S &= \sqrt{2}\int d^4x \Big[ -\epsilon^\alpha \psi_\alpha \partial_\mu \partial^\mu \phi^* - \bar{\psi}_{\dot{\alpha}} \bar{\epsilon}^{\dot{\alpha}} \partial_\mu \partial^\mu \phi \\ &\qquad + \epsilon^\alpha \psi_\alpha \partial_\mu \partial^\mu \phi^* + \bar{\psi}_{\dot{\alpha}} \bar{\epsilon}^{\dot{\alpha}} \partial_\mu \partial^\mu \phi \Big] \\ &= 0. \end{aligned} \tag{2.28}$$

We saw that the SUSY transformations do not change the Lagrangian up to total derivative, and hence leave the action invariant.

However, the particle content $\psi, \phi$ is not enough for a SUSY invariant theory, as we can see when counting the degrees of freedom. On-shell, when the equation of motions are fulfilled, the fermionic and bosonic degrees of freedom are balanced, that is we have two for the Weyl fermion and two for the complex scalar. On the other hand, off-shell, the fermion has four degrees of freedom, while we still have only two for the scalar. To get the number of degrees of freedom right, we introduce a so-called auxiliary field $F$ which has mass dimension two and is complex, so it has two degrees of freedom (off-shell). Its Lagrangian reads

$$\mathcal{L}_{\text{aux}} = F^* F, \tag{2.29}$$

and the equation of motion gives $F = 0$ and the degrees of freedom of $F$ are eliminated on-shell.[5] We will see later that this kind of auxiliary field plays an important role in the spontaneous breaking of SUSY.

In order to get an invariant action including the new term (2.29), we have to define

[5] Another reason for introducing the auxiliary field is to make the SUSY algebra close off-shell.

how $F$ transforms under SUSY transformations, and modify (2.24) as

$$\begin{aligned}
\delta F &= -i\sqrt{2}\partial_\mu \psi^\alpha \sigma^\mu_{\alpha\dot{\alpha}} \bar{\epsilon}^{\dot{\alpha}}, \\
\delta F^* &= i\sqrt{2}\epsilon^\alpha \sigma^\mu_{\alpha\dot{\alpha}} \partial_\mu \bar{\psi}^{\dot{\alpha}}, \\
\delta \psi_\alpha &= -i\sqrt{2}\sigma^\mu_{\alpha\dot{\alpha}} \bar{\epsilon}^{\dot{\alpha}} \partial_\mu \phi - \sqrt{2}\epsilon_\alpha F, \\
\delta \bar{\psi}_{\dot{\alpha}} &= \quad i\sqrt{2}\epsilon^\alpha \sigma^\mu_{\alpha\dot{\alpha}} \partial_\mu \phi^* - \sqrt{2}\bar{\epsilon}_{\dot{\alpha}} F^*.
\end{aligned} \tag{2.30}$$

We now introduce the so-called supercurrent $J^\mu_\alpha$ and the supercharges $Q_\alpha, \bar{Q}_{\dot{\alpha}}$. From Noether's theorem we know that for every continuous symmetry transformation, there is a conserved current, which for SUSY transformations is the supercurrent. For a Lagrangian that transforms into a total derivative, $\delta\mathcal{L} = \partial_\mu \Lambda^\mu$, it is defined as

$$\epsilon^\alpha J^\mu_\alpha + \bar{\epsilon}_{\dot{\alpha}} J^{\dagger\,\mu\,\dot{\alpha}} = \sum_X \frac{\partial \mathcal{L}}{\partial(\partial_\mu X)} \delta X - \Lambda^\mu, \tag{2.31}$$

where $X$ stands for all the fields involved. We note that one can always redefine the conserved current by replacing $\Lambda^\mu$ by $\Lambda^\mu + \lambda^\mu$, where $\partial_\mu \lambda^\mu = 0$.

For the example given above, the explicit expressions for the supercurrents are given by

$$\begin{aligned}
J^\mu_\alpha &= \sqrt{2}\sigma^\nu_{\alpha\dot{\alpha}} \bar{\sigma}^{\mu\,\dot{\alpha}\beta} \psi_\beta \partial_\nu \phi^*, \\
J^{\dagger\,\mu}_{\dot{\alpha}} &= \sqrt{2}\bar{\psi}_{\dot{\beta}} \bar{\sigma}^{\mu\,\dot{\beta}\beta} \sigma^\nu_{\beta\dot{\alpha}} \partial_\nu \phi.
\end{aligned} \tag{2.32}$$

Using the equation of motions for the fields, one can show that they are independently conserved,

$$\partial_\mu J^\mu_\alpha = 0, \quad \partial_\mu J^{\dagger\,\mu}_{\dot{\alpha}} = 0. \tag{2.33}$$

The supercurrent can be used to construct an invariant action. We will comment on this in Section 3.2.3.

The integration over the time component gives the generators $Q, \bar{Q}$ of SUSY transformations defined as

$$Q_\alpha = \int d^3\vec{x}\; J^0_\alpha, \quad \bar{Q}_{\dot{\alpha}} = \int d^3\vec{x}\; J^{\dagger\,0}_{\dot{\alpha}}. \tag{2.34}$$

One can show that they fulfill the SUSY algebra,

$$\{Q_\alpha, \bar{Q}_{\dot{\alpha}}\} = 2\sigma^\mu_{\alpha\dot{\alpha}} P_\mu, \quad \{Q_\alpha, Q_\beta\} = 0, \quad \{\bar{Q}_{\dot{\alpha}}, \bar{Q}_{\dot{\beta}}\} = 0, \tag{2.35}$$

where $P^\mu$ generates translations in space-time. The commutation relation with $P^\mu$ is

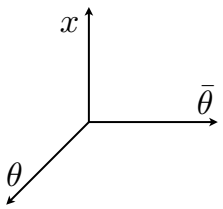


Figure 2.4: A schematic representation of the superspace.

given by

$$[P^\mu, Q_\alpha] = 0, \ [P^\mu, \bar{Q}_{\dot{\alpha}}] = 0. \tag{2.36}$$

When we have only one type of supercharge $Q_\alpha, \bar{Q}_{\dot{\alpha}}$, we call the theory $N = 1$ SUSY; only those are phenomenologically viable in four dimensional space-time.

### 2.2.3 Superspace and superfields

To construct a SUSY Lagrangian in a manifestly SUSY invariant way, it is convenient to introduce the so-called *superspace* and objects called *superfields*. The superspace is an extension of the ordinary space-time; for $N = 1$ SUSY theories, we adjoin two constant complex anti-commuting spinors $\theta_\alpha, \bar{\theta}^{\dot{\alpha}}$ (Grassmann variables) with mass dimension $[\theta] = -1/2$ to the space-time coordinate $x^\mu$; see Fig. 2.4.

A superfield $S$ is a function of these coordinates. Fields that are mapped into each other under SUSY transformations, such as $\psi, \phi$ and $F$ of the previous section, are arranged into a superfield. We can expand the superfield in a Taylor series with respect to the Grassmann variables $\theta, \bar{\theta}$, where the coefficients are functions of $x^\mu$. Due to the anticommuting property of Grassmann variables,

$$\{\theta^\alpha, \theta^\beta\} = \{\bar{\theta}_{\dot{\alpha}}, \bar{\theta}_{\dot{\beta}}\} = \{\theta^\alpha, \bar{\theta}_{\dot{\alpha}}\} = 0, \tag{2.37}$$

every term involving more than two $\theta$'s (or more than two $\bar{\theta}$'s) vanishes.

A general (scalar) superfield can be written as

$$\begin{aligned} S(x, \theta, \bar{\theta}) = {} & z(x) + \theta \cdot \xi(x) + \bar{\theta} \cdot \bar{\zeta}(x) + \theta \cdot \theta f(x) + \bar{\theta} \cdot \bar{\theta} g(x) + \theta \sigma^\mu \bar{\theta} v_\mu(x) \\ & + \bar{\theta} \cdot \bar{\theta} \theta \cdot \omega(x) + \theta \cdot \theta \bar{\theta} \cdot \bar{\rho}(x) + \theta \cdot \theta \bar{\theta} \cdot \bar{\theta} d(x). \end{aligned} \tag{2.38}$$

Here, $z, f, g, d$ are complex scalar fields, $v_\mu$ is a complex vector field and $\xi_\alpha, \bar{\zeta}^{\dot{\alpha}}, \omega_\alpha, \bar{\rho}^{\dot{\alpha}}$ are complex Weyl fermions.

A superfield transforms under a general infinitesimal SUSY transformation as

$$S \to S + \delta_\epsilon S \ \text{ with } \ \delta_\epsilon S = i(\epsilon \cdot \hat{Q} + \hat{\bar{Q}} \cdot \bar{\epsilon}) S, \tag{2.39}$$

where $\hat{Q}_\alpha, \hat{\bar{Q}}^{\dot{\alpha}}$ are the generators of SUSY transformations (differential operators) acting

on superfields. Their explicit form can be derived as [23],

$$\hat{Q}_\alpha = -i\Big(\frac{\partial}{\partial\theta^\alpha} + i\sigma^\mu_{\alpha\dot{\alpha}}\bar{\theta}^{\dot{\alpha}}\partial_\mu\Big), \quad \hat{\bar{Q}}_{\dot{\alpha}} = i\Big(\frac{\partial}{\partial\bar{\theta}^{\dot{\alpha}}} + i\theta^\alpha\sigma^\mu_{\alpha\dot{\alpha}}\partial_\mu\Big). \tag{2.40}$$

To describe the SM particle content and their SUSY partners we need two different types of superfields, *left-handed chiral* (or just chiral) superfields $\Phi$ and *vector* (or real) superfields $V$.

A left-handed chiral superfield $\Phi$ serves to describe a complex scalar field $\phi$ and the corresponding two-component fermionic field $\psi_\alpha$. It is defined by

$$\bar{D}_{\dot{\alpha}}\Phi(x,\theta,\bar{\theta}) = 0, \tag{2.41}$$

where $\bar{D}_{\dot{\alpha}}$ is the superderivative, see e.g [25],

$$\bar{D}_{\dot{\alpha}} = \frac{\partial}{\partial\bar{\theta}^{\dot{\alpha}}} - i\theta^\alpha\sigma^\mu_{\alpha\dot{\alpha}}\partial_\mu. \tag{2.42}$$

A right-handed or anti-chiral superfield $\Phi^\dagger$ is defined by requiring

$$D_\alpha\Phi^\dagger = 0, \tag{2.43}$$

where

$$D_\alpha = \frac{\partial}{\partial\theta^\alpha} - i\sigma^\mu_{\alpha\dot{\alpha}}\bar{\theta}^{\dot{\alpha}}\partial_\mu. \tag{2.44}$$

A solution to the constraint (2.41) is

$$\begin{aligned}\Phi(x,\theta,\bar{\theta}) = \phi(x) - i\theta\bar{\sigma}^\mu\bar{\theta}\partial_\mu\phi(x) - \frac{1}{4}\theta\cdot\theta\bar{\theta}\cdot\bar{\theta}\partial^\mu\partial_\mu\phi \\ + \sqrt{2}\theta\psi + \frac{i}{\sqrt{2}}\theta\cdot\theta\partial_\mu\psi\sigma^\mu\bar{\theta} - \theta\cdot\theta F.\end{aligned} \tag{2.45}$$

Besides $\phi$ and $\psi_\alpha$, we have a complex auxiliary field $F$. By introducing a variable

$$y^\mu = x^\mu - i\theta\bar{\sigma}^\mu\bar{\theta}, \tag{2.46}$$

the expression simplifies to

$$\Phi(y,\theta) = \phi(y) + \sqrt{2}\theta\cdot\psi(y) - \theta\cdot\theta F(y). \tag{2.47}$$

We note that a chiral superfield has mass dimension $[\Phi] = 1$.

The vector superfield $V$ serves to describe a massless gauge boson $A_\mu$ and a corresponding two-component fermion field $\lambda_\alpha$. It is defined by the reality condition

$$V = V^\dagger. \tag{2.48}$$

Here and in the following, we restrict ourselves to the abelian case; the extension to the

non-abelian case is straightforward and the explicit expressions can be found in [25]. From (2.48), we find that a general vector superfield contains besides $A_\mu$ and $\lambda_\alpha$ several auxiliary fields. All of these auxiliary fields except one field $D$ can be removed by choosing a specific gauge, the so-called Wess-Zumino gauge.[6] In Wess-Zumino gauge, $V$ takes the form

$$V(x,\theta,\bar\theta) = \theta\sigma^\mu\bar\theta A_\mu(x) + i\theta\cdot\theta\bar\theta\cdot\bar\lambda(x) - i\bar\theta\cdot\bar\theta\theta\cdot\lambda(x) + \frac{1}{2}\theta\cdot\theta\bar\theta\cdot\bar\theta D(x), \tag{2.49}$$

and the SUSY transformations of the fields $\lambda, A_\mu$ and $D$ are

$$\begin{aligned}
\delta\lambda_\alpha &= -i(\sigma^{\mu\nu}\epsilon)_\alpha F_{\mu\nu} + i\epsilon_\alpha D,\\
\delta\lambda_{\dot\alpha} &= \ i(\bar\epsilon\bar\sigma^{\mu\nu})_{\dot\alpha} F_{\mu\nu} - i\bar\epsilon_{\dot\alpha} D\\
\delta A_\mu &= -i\lambda\sigma_\mu\bar\epsilon + i\epsilon\sigma_\mu\bar\lambda\\
\delta D &= \ \partial_\mu[\lambda\sigma^\mu\bar\epsilon + \epsilon\sigma^\mu\bar\lambda],
\end{aligned} \tag{2.50}$$

where $F_{\mu\nu} = \partial_\mu A_\nu - \partial_\nu A_\mu$ is the field strength tensor of the vector field $A_\mu$ and $\sigma^{\mu\nu} = \frac{1}{4}[\sigma^\mu\bar\sigma^\nu - \sigma^\nu\bar\sigma^\mu]$, $\bar\sigma^{\mu\nu} = \frac{1}{4}[\bar\sigma^\mu\sigma^\nu - \bar\sigma^\nu\sigma^\mu]$. The mass dimension of a vector superfield is $[V] = 0$.

Besides the chiral superfield $\Phi$ and the vector superfield $V$, we are going to use the superfield strength tensors $W_\alpha$ and $\bar W_{\dot\alpha}$ in the construction of a SUSY invariant theory. They are chiral superfields carrying a spinor index, and defined via

$$\begin{aligned}
W_\alpha &= -\frac{1}{4}\bar D\cdot\bar D D_\alpha V,\\
\bar W_{\dot\alpha} &= -\frac{1}{4} D\cdot D\bar D_{\dot\alpha} V,
\end{aligned} \tag{2.51}$$

where we restrict the discussion again to the abelian case; for the non-abelian case, see [25]. $D_\alpha, \bar D_{\dot\alpha}$ are the superderivatives given in (2.42),(2.44). The explicit form is

$$W_\alpha(y) = -i\lambda_\alpha(y) - \frac{i}{2}(\sigma^\mu\bar\sigma^\nu\theta)_\alpha F_{\mu\nu}(y) + \theta_\alpha D(y) - \theta\cdot\theta(\sigma^\mu\partial_\mu\bar\lambda(y))_\alpha. \tag{2.52}$$

$W_\alpha$ has mass dimension $[W_\alpha] = 3/2$.

Using the superfield formalism, we can easily construct an action that is invariant under SUSY transformations. We need a Lagrangian that transforms at most into a total derivative. From the form of a chiral superfield and a vector superfield given in (2.47) and (2.49), and the transformation properties of (2.30) and (2.50), we see that possible terms for the Lagrangian are the $\theta\cdot\theta$-component of a chiral superfield, which is the so called $F$-term, and the $\theta\cdot\theta\bar\theta\cdot\bar\theta$-component of a real (vector) superfield, which is called $D$-term.[7] To project out the corresponding coefficient of a superfield, we take

[6] A gauge transformation of a vector superfield is given by $V \to V + i(\Lambda^\dagger - \Lambda)$, where $\Lambda$ is a chiral superfield gauge transformation parameter.

[7] The $D$-term of a general superfield is a SUSY invariant, but to get a real action we need a real superfield.

the integral over the corresponding Grassmann variables,

$$\int d^2\theta\, 1 = \int d^2\theta\, \theta = 0, \quad \int d^2\theta\, \theta\cdot\theta = 1,$$
$$\int d^2\bar\theta\, 1 = \int d^2\bar\theta\, \bar\theta = 0, \quad \int d^2\bar\theta\, \bar\theta\cdot\bar\theta = 1. \tag{2.53}$$

So, possible SUSY invariant actions from the $F$-term of a chiral superfield $\Phi$ and the $D$-term of a real superfield $V$ are given by

$$S_F = \int d^4x \Big( d^2\theta\ \Phi + d^2\bar\theta\ \Phi^\dagger \Big), \tag{2.54}$$
$$S_D = \int d^4x\ d^2\theta d^2\bar\theta\ V. \tag{2.55}$$

Usually, a Lagrangian is not formed out of a single superfield. The product of chiral superfields (and no anti-chiral superfields) is again a chiral superfield and called the *superpotential*, while a quantity like $\Phi^\dagger\Phi$ forms a real superfield and contributes to the *Kähler potential*.

In the next section, we give an example of a SUSY Lagrangian in the superspace formalism.

## 2.3 The SUSY Lagrangian in superspace formalism

As example, we discuss an R-parity conserving $N = 1$ global SUSY model with the $U(1)_{\rm em}$ gauge group.

Before constructing our model, let us make a comment on how Dirac fermions are implemented into chiral superfields. A Dirac fermion contains a left- and a right-handed two-component Weyl fermion, which can transform differently under gauge transformations. Each of the Weyl fermions receives its own scalar superpartner; for example, a left- handed electron $e_L$ is accompanied by a left-handed selectron $\tilde e_L$, and a right-handed electron $e_R$ by a right-handed selectron $\tilde e_R$. To describe the two pieces of a Dirac fermion by chiral superfields, we need two superfields: $e_L$ goes together with $\tilde e_L$ into one, $\Phi_L = (\tilde e_L, e_L, F_L)$, where we included also the corresponding auxiliary field $F_L$. We could put the right-handed electron in a right-handed chiral superfield; what is usually done is however something different. As explained in (2.17), the hermitian conjugate of a right-handed Weyl-fermion is a left-handed Weyl fermion and vice versa. We arrange the complex conjugate of a right-handed Weyl fermion together with the conjugate of its scalar partner into a left-handed chiral superfield, $\Phi_R = (\tilde e_R^*, e_R^c, F_R)$.

Our SUSY QED model comprises one vector superfield $V = (A^\mu, \lambda, D_V)$, describing a photon $A^\mu$ and a photino $\lambda$, and two chiral superfields $\Phi_L = (\tilde e_L, e_L, F_L)$ and $\Phi_R = (\tilde e_R^*, e_R^c, F_R)$, containing the left- and right-handed electrons $e_{L/R}$ and selectrons $\tilde e_{L/R}$.

The kinetic terms of the selectrons $\tilde e_{L/R}$ and the left- and right-handed electrons $e_{L/R}$ as well as their gauge interactions are given by the short expression[8]

[8] In Wess-Zumino gauge, we find $V^2 = \frac{1}{2}\theta\cdot\theta\bar\theta\cdot\bar\theta A^\mu A_\mu$, and $V^3 = 0$.

$$\mathcal{L}_{\text{vis chiral}} = \sum_{i=L,R} \int d^4\theta \; \Phi_i^\dagger e^{2g_e Q_i V} \Phi_i, \tag{2.56}$$

where $g_e = \sqrt{4\pi\alpha}$ and $Q_i$ is the electric charge of $\Phi_i$, i.e. $Q_{R/L} = \pm 1$. The covariant derivative is defined as

$$D_\mu = \partial_\mu + i g_e Q A_\mu. \tag{2.57}$$

For completeness, we show the Lagrangian of (2.56) in terms of the component fields by using the two-component notation,

$$\begin{aligned}\mathcal{L}_{\text{vis chiral}} = \sum_{i=L,R} \Big[ & F_i F_i^* + g_e Q_i D \tilde{e}_i \tilde{e}_i^* \\ & + \partial_\mu \tilde{e}_i \partial^\mu \tilde{e}_i^* + i e_i \sigma^\mu \partial_\mu \bar{e}_i \\ & + i g_e A^\mu \tilde{e}_i^* \overleftrightarrow{\partial} \tilde{e}_i + g_e Q_i A_\mu e_i \sigma^\mu \bar{e}_i \\ & + g_e^2 \tilde{e}_i \tilde{e}_i^* A^\mu A_\mu - i Q_i g_e \sqrt{2} \big( \tilde{e}_i \bar{\lambda} \cdot \bar{e}_i - \tilde{e}_i^* e_L \cdot \lambda \big) \Big],\end{aligned} \tag{2.58}$$

where $A \overleftrightarrow{\partial}_\mu B = A \partial_\mu B - (\partial_\mu A) B$. For the four-component notation, see Section 3.2.2.

Besides the kinetic terms and the gauge interactions, we also get the terms

$$\mathcal{L}_{\text{aux } F} = F_L^* F_L + F_R^* F_R. \tag{2.59}$$

They can be eliminated by deriving the equations of motion, which for this simple QED model read

$$F_L = 0, \quad F_R = 0. \tag{2.60}$$

The kinetic term of the photon $A^\mu$ and the photino $\lambda$ is given by

$$\mathcal{L}_{\text{vis vector}} = \frac{1}{4} \int d^2\theta \; W^\alpha W_\alpha + \text{h.c.}, \tag{2.61}$$

where $W_\alpha$ denotes the SUSY $U(1)_{\text{em}}$ field strength tensor defined in (2.51) with $D$ being the superderivative defined in (2.44).

We note that from the Lagrangian (2.56) and (2.61), we obtain terms containing the auxiliary field $D$,

$$\mathcal{L}_{\text{aux } D} = \frac{1}{2} D^2 - g_e \tilde{e}_L^* \tilde{e}_L D + g_e \tilde{e}_R^* \tilde{e}_R D. \tag{2.62}$$

Solving the equation of motion for the $D$ field gives

$$D = g_e (\tilde{e}_L^* \tilde{e}_L - \tilde{e}_R^* \tilde{e}_R). \tag{2.63}$$

The two terms (2.56) and (2.61) completely define the kinetic terms and the interactions of our simple SUSY QED model. SUSY implies that the SM particles and their SUSY partners have the same properties, including their masses. Since this is not observed experimentally, we know that SUSY must be broken. After shortly introducing the general minimal extension of the SM in the next section, we discuss the idea of spontaneous SUSY breaking, and show how mass terms can be generated for the superparticles.

## 2.4 The minimal supersymmetric SM (MSSM)

In a similar way that we constructed the Lagrangian for the SUSY QED model, one can construct the full Lagrangian of the minimal supersymmetric standard model (MSSM). The MSSM is the minimal SUSY extension of the SM, in which each of the known fundamental particles receives a SUSY partner. The spin of the SM particle and the corresponding SUSY partner differ by 1/2, but all the other properties such as quantum numbers and mass (in unbroken SUSY) are the same.

The naming scheme is as follows. The fermions, that is the leptons and quarks, receive bosonic superpartners named sleptons and squarks. These are grouped together into chiral supermutliplet. The gauge bosons receive fermionic partners called gauginos, and they are grouped together into vector supermultiplets. The $H$ bosons receive fermionic partners called higgsinos, and are arranged together into chiral superfields. We note that in the MSSM, unlike in the SM, we need two $H$ boson doublets. One reason is the cancellation of gauge anomalies. In the SM, the fermions have precisely the right quantum numbers to cancel anomalous terms.[9] Now if we add one Higgs multiplet, the contribution from the higgsino to the gauge anomaly would be uncancelled. A simple solution is to add a second Higgs doublet, so that the contributions from the two higgsinos will cancel each other.

The field content of the chiral and vector supermultiplets of the MSSM is summarized in Table 2.1 and Table 2.2, respectively, according to their transformation properties under $SU(3)_c \times SU(2)_L \times U(1)_Y$; we omit the corresponding auxiliary fields.

We note that the electrically neutral gauginos $\tilde{B}$ and $\tilde{W}^3$ mix together with the neutral higgsinos $\tilde{H}_u^0$ and $\tilde{H}_d^0$ to form the four mass eigenstates called neutralinos $\tilde{\chi}_i^0$,

$$\begin{pmatrix} \tilde{\chi}_1^0 \\ \tilde{\chi}_2^0 \\ \tilde{\chi}_3^0 \\ \tilde{\chi}_4^0 \end{pmatrix} = U \begin{pmatrix} -i\tilde{B} \\ -i\tilde{W}^3 \\ \tilde{H}_d^0 \\ \tilde{H}_u^0 \end{pmatrix}, \tag{2.64}$$

where $U$ is a $4 \times 4$ mixing matrix. For a photino-like neutralino $\tilde{\chi}_1^0$ as in the previous section, $U_{11} = \cos\theta_W$ and $U_{12} = \sin\theta_W$, $U_{13} = U_{14} = 0$. Similarly, the charged winos $\tilde{W}^{1,2}$ mix with the charged higgsinos $\tilde{H}_u^+, \tilde{H}_d^-$ to form the charginos $\tilde{\chi}_{1,2}^\pm$. We note that

[9] See e.g. Chapter 20.2 in [26].

| superfield | spin 0 | spin 1/2 | $SU(3)_c$ | $SU(2)_L$ | $U(1)_Y$ |
|---|---|---|---|---|---|
| $L_L$ | $\begin{pmatrix} \tilde{\nu}_L \\ \tilde{e}_L \end{pmatrix}$ | $\begin{pmatrix} \nu_L \\ e_L \end{pmatrix}$ | **1** | **2** | $-\frac{1}{2}$ |
| $E_R$ | $\tilde{e}_R^*$ | $e_R^c$ | **1** | **1** | 1 |
| $Q_L$ | $\begin{pmatrix} \tilde{u}_L \\ \tilde{d}_L \end{pmatrix}$ | $\begin{pmatrix} u_L \\ d_L \end{pmatrix}$ | **3** | **2** | $-\frac{1}{2}$ |
| $U_R$ | $\tilde{u}_R^*$ | $u_R^c$ | **3** | **1** | $\frac{2}{3}$ |
| $D_R$ | $\tilde{d}_R^*$ | $d_R^c$ | **3** | **1** | $-\frac{1}{3}$ |
| $H_U$ | $H_u = \begin{pmatrix} H_u^+ \\ H_u^0 \end{pmatrix}$ | $\tilde{H}_u = \begin{pmatrix} \tilde{H}_u^+ \\ \tilde{H}_u^0 \end{pmatrix}$ | **1** | **2** | $\frac{1}{2}$ |
| $H_D$ | $H_d = \begin{pmatrix} H_d^0 \\ H_d^- \end{pmatrix}$ | $\tilde{H}_d = \begin{pmatrix} \tilde{H}_d^0 \\ \tilde{H}_d^- \end{pmatrix}$ | **1** | **2** | $-\frac{1}{2}$ |

Table 2.1: The field content of the chiral supermultiplets of the MSSM, together with their quantum numbers under $SU(3)_c \times SU(2)_L \times U(1)_Y$. The fermionic fields are two-component Weyl fermions.

| superfield | spin 1/2 | spin 1 | $SU(3)_c$ | $SU(2)_L$ | $U(1)_Y$ |
|---|---|---|---|---|---|
| $V_G$ | $\tilde{g}^A$ | $g^A$ | **8** | **1** | 0 |
| $V_W$ | $\tilde{W}^a$ | $W^a$ | **1** | **3** | 0 |
| $V_B$ | $\tilde{B}$ | $B$ | **1** | **1** | 0 |

Table 2.2: The field content of the vector supermultiplets of the MSSM, together with their quantum numbers under $SU(3)_c \times SU(2)_L \times U(1)_Y$.

we follow the Les Houches accord [27] for the gaugino definitions.

With the (super)field content of the MSSM, more renormalizable and gauge invariant SUSY terms than in the previously SUSY QED model can be constructed. They are encoded in a function of chiral superfields $\Phi_i$ (and no anti-chiral superfields) that is called the superpotential $W$,

$$W = \frac{1}{2} m^{ij} \Phi_i \Phi_j + \frac{1}{6} y^{ijk} \Phi_i \Phi_j \Phi_k, \tag{2.65}$$

where $m^{ij}, y^{ijk}$ are parameters of mass dimension 1 and 0, respectively; for the explicit form of the superpotential of the MSSM, see Section 6 in [28]. From this function, one obtains e.g. Yukawa interactions, the usual fermionic mass terms of the SM and triple and quartic scalar vertices. Note that the equations of motion of the auxiliary fields $F_i$ read, after including the superpotential,

$$F_i = W_i^*, \tag{2.66}$$

where $W_i^* = \frac{\delta W^*}{\delta \phi_i^*}$.

SUSY, renormalizability and gauge invariance in the MSSM do still allow terms that violate lepton $L$ or baryon number $B$ conservation.[10] In order to forbid these terms in

[10] In the SM, lepton and baryon number $L$ and $B$, are automatically conserved by the allowed gauge

the MSSM one introduces *matter parity*, which is defined for each superfield as

$$P_M = (-1)^{3(B-L)}. \tag{2.67}$$

With this definition, the superfields containing leptons and quarks carry matter parity $P_M = -1$ and the superfields of the Higgses and gauge bosons $P_M = +1$. A Lagrangian term written in superfields is allowed if the product of all matter parities of the superfields gives $P_M = +1$.

In terms of component fields, one introduces a quantum number called *R-parity*, which is defined as

$$P_R = (-1)^{3(B-L)+2s}, \tag{2.68}$$

where $s$ is the spin of the corresponding particle. All SM particles as well as the Higgs bosons have R-parity $P_R = +1$, while their SUSY partners have $P_R = -1$. A possible term in the Lagrangian is allowed if the product of the R-parities of all component fields is $P_R = +1$.

Imposing R-parity on a SUSY theory has three important consequences. First, it forbids the decay of the lightest SUSY particle (LSP), which hence provides in many SUSY models naturally a dark matter candidate. Second, every decaying SUSY particle decays into an odd number of SUSY particles. Third, in collider experiments, R-parity conservation implies that SUSY particles can only be produced in pairs.

As mentioned at the end of previous section, we know that SUSY must be broken. In the MSSM, a mass splitting between the SM particles and their SUSY partners is obtained by introducing explicit SUSY breaking terms such as scalar mass terms to the Lagrangian. The form of these terms is restricted, since we do not want to re-introduce quadratic divergences to the scalar masses at quantum level. The allowed SUSY breaking terms are called *soft* terms.

invariant and renormalizable terms.

# CHAPTER 3

## The goldstino and the gravitino

We know that SUSY is broken because we do not observe SUSY particles with the same masses as the SM particles. How the breaking can be achieved in a phenomenologically viable way is shortly discussed in Section 3.1. We first show under which conditions SUSY is broken spontaneously in Section 3.1.1. Similar to the appearance of massless goldstone bosons in spontaneously broken gauge theories discussed in the first chapter, the spontaneous breaking of SUSY leads to a massless goldstone fermion, called the goldstino, introduced in Section 3.1.2. SUSY breaking must occur in a hidden sector, and then be transmitted to the visible sector comprising the SM particles and their superpartners by some mediation mechanism. We shortly introduce two popular mediation mechanisms in Section 3.1.3.

In Section 3.2.1, we parametrize our ignorance of how SUSY breaking is transmitted to the visible sector by effective operators that couple the fields of the goldstino supermultiplet from the hidden sector to the fields in the visible sector. The resulting effective goldstino interaction Lagrangian in terms of component fields is presented in Section 3.2.2. Subsequently, we present an alternative to derive single goldstino interactions in terms of the supercurrent in Section 3.2.3

In Section 3.3, we discuss the consequences of *local* supersymmetry. In Section 3.3.1, we see that requiring a SUSY Lagrangian to be invariant under local SUSY transformations naturally leads to a theory including gravity, so called supergravity. Besides the superfields introduced in the previous sections, we must include the supermultiplet of graviton and gravitino. In Section 3.3.2, we show how the goldstino is absorbed by the gravitino in the super-Higgs mechanism, and we derive an explicit expression for the gravitino mass. We find that the gravitino mass is directly related to the SUSY breaking scale.

In analogy to the goldstone boson equivalence theorem, it exists the gravitino-goldstino equivalence theorem, which will be presented in Section 3.4. This equivalence allows to calculate scattering processes involving light gravitinos with the much simpler formalism of goldstinos, and will be used throughout the next chapters. We then discuss as example the scattering of two photons into two gravitinos. First, in Section 3.4.1, we perform the calculations using the full spin-3/2 formalism. Similar to the example of $WW$ scattering presented in the first Chapter, we find that the high-energy behavior of the scattering amplitude is protected by symmetries. In Section 3.4.2, we then re-study the $\gamma\gamma \to \tilde{G}\tilde{G}$ process by using the effective goldstino interaction Lagrangian constructed in Section 3.2.1. As expected from the goldstino-gravitino equivalence theorem, we find a similar result as in the spin 3/2 gravitino formalism.

## 3.1 SUSY breaking

There are two possible scenarios on how SUSY can be broken. Either SUSY is broken *explicitly*, that means, one adds terms to the SUSY Lagrangian that violate SUSY explicitly. Or SUSY is broken *spontaneously*, that means the Lagrangian is still supersymmetric, but the vacuum state of the theory is not, similar to the spontaneous breaking of the local gauge symmetry in the SM discussed in Section 1.2. Since we put

a lot of effort in constructing a theory which is SUSY invariant, the second option is more appealing.

In the following, we are going to consider a theory in which SUSY is spontaneously broken. The effect of the breaking of SUSY are additional mass terms for the superpartners of the SM particles, as well as possible additional interactions; this will be demonstrated below.

### 3.1.1 Conditions for spontaneous SUSY breaking

First, we want to find an order parameter for spontaneous SUSY breaking. As we saw in Section 1.2, a symmetry is broken spontaneously if the vacuum state $|0\rangle$ is not invariant under the symmetry transformation. It follows that SUSY is broken spontaneously if

$$Q_\alpha|0\rangle \neq 0, \quad \bar{Q}_{\dot{\alpha}}|0\rangle \neq 0, \tag{3.1}$$

where $Q_\alpha, \bar{Q}_\alpha$ are the SUSY charges defined in 2.34. The energy of the theory is given by the Hamiltonian $H = P_0$, which can be written due to the SUSY algebra (2.35) as

$$H = \frac{1}{4}\big(Q_1\bar{Q}_1 + \bar{Q}_1 Q_1 + Q_2\bar{Q}_2 + \bar{Q}_2 Q_2\big). \tag{3.2}$$

If SUSY is broken, we find that the vacuum state has positive energy, $\langle 0|H|0\rangle > 0$. Assuming that the vacuum energy comes only from the scalar potential, which is given by the scalar field content of the theory (without derivative terms), this gives

$$\langle 0|V|0\rangle > 0. \tag{3.3}$$

For a general global SUSY theory

$$V = F_i^* F_i + \frac{1}{2}D^2, \tag{3.4}$$

where the auxiliary fields $F_i, D$ are understood to be replaced by their corresponding equations of motion. We find that SUSY is spontaneously broken if the auxiliary field $F_i$ of a chiral superfield, or the auxiliary field $D$ of a real superfield obtains a VEV.

### 3.1.2 The hidden sector and the goldstino

However, we can not break SUSY spontaneously (only) with the auxiliary fields appearing in the superfields describing SM particles; for details, see [28]. There is a so-called supertrace theorem, which states that the sum over the particle and SUSY particle tree

level masses, weighted by their spin, must vanish,

$$\sum_S m_S^2 - 2\sum_F m_F^2 + 3\sum_V m_V^2 = 0. \tag{3.5}$$

If SUSY is broken by some field in the visible sector, the masses of the SUSY particles should be split around the masses of the SM particles, which is of course experimentally ruled out. Therefore, one usually assumes that the SUSY breaking happens in a so-called hidden sector, and is then transferred to the visible sector by some mediation mechanism.

We do not know what particle content is in this hidden sector, and we do not know how SUSY is broken in the hidden sector. In the following, we assume one chiral superfield $X$ in the hidden sector, whose auxiliary field $F_X$ obtains a VEV and hence breaks supersymmetry. The corresponding Weyl fermion is the goldstino $\tilde{G}$, and the associated complex scalar is the sgoldstino $\phi$.[1] The superfield $X$ has matter parity $P_M = 1$, and the $R$-parity of its components is $P_R = -1$ for the goldstino, while the sgoldstino has $P_R = +1$.

The goldstino is the massless goldstone particle that always appears in the spontaneous breaking of a continuous symmetry, in complete analogy to the goldstone bosons for the case of the spontaneous breakdown of a $U(1)$ symmetry discussed in Section 1.2, or the goldstone bosons appearing from breaking $SU(2)_L \times U(1)_Y$ in the SM. Since now the generator of the broken symmetry is fermionic, also the goldstino is a fermion.

The Lagrangian of the goldstino superfield $X = (\phi, \tilde{G}, F_X)$ is given by

$$\begin{aligned}\mathcal{L}_X = &\int d^4\theta\ X^\dagger X - \left(F \int d^2\theta\ X + \text{h.c.}\right) \\ &- \frac{c_X}{4} \int d^4\theta\ (X^\dagger X)^2.\end{aligned} \tag{3.6}$$

The first term gives the kinetic term of the (s)goldstino, while the second term is a source of SUSY breaking and $F \equiv \langle F_X \rangle$ is the VEV of $F_X$.[2] The last term is non-renormalizable and provides interactions between the goldstino multiplet. This term also gives the sgoldstino mass term when replacing the auxiliary fields $F_X$ by the VEV, and hence we assign $c_X = m_\phi^2/F^2$.

### 3.1.3 Mediation of SUSY breaking

Now SUSY is broken in the hidden sector, and must be somehow transmitted to the visible sector, that means, the particles in the visible sector share some interactions with the particles of the hidden sector. There are several different models about how this can happen; we will see that they result in different SUSY breaking scales.

[1] If there are several fields obtaining a VEV, the goldstino has components in all corresponding fermionic field components, see e.g. Eq. 4.1.12 in [23].

[2] Note that we follow the FeynRules convention for chiral superfields $\Phi(y,\theta) = \phi(y) + \sqrt{2}\,\theta\cdot\psi(y) - \theta\cdot\theta\,F(y)$ [29], which fixes the sign of the Lagrangian so as to give a positive contribution to the scalar potential.

For example, in gravity mediation scenarios, it is assumed that the mediation of SUSY breaking from the hidden sector to the visible sector occurs only through gravitational interactions, hence the couplings are inversely proportional to the Planck mass $M_{\mathrm{Pl}}$. The masses of the SUSY particles in the visible sector can be derived to be, see e.g. [28]

$$m \sim \frac{F}{M_{\mathrm{Pl}}}. \tag{3.7}$$

One can guess this form also from dimensional analysis since we want the soft masses to vanish in the limit where $F \to 0$ or $M_{\mathrm{Pl}} \to \infty$.

In the discussion of the fine-tuning problem in Section 2.1, we found that the quantum corrections to the $H$-boson mass are after SUSY breaking proportional to the soft masses. In order to not re-introduce the fine-tuning problem in (2.13), we expect $m \sim \mathcal{O}(1 \text{ TeV})$, which corresponds to a SUSY breaking scale of $\sqrt{F} \sim \mathcal{O}(10^{10} \text{ TeV})$.

Another popular mediation mechanism is through the gauge interactions; for a review see [30].[3] One assumes that there are some heavy particles called messengers which are charged under the SM gauge group. These messengers have interactions with the fields of the hidden sector and the fields of the visible sector. From the interaction of the messenger fields with the goldstino superfield $X$ (in the hidden sector), which is assumed to get a VEV along its scalar and auxiliary components, $\langle X \rangle = M_{\mathrm{mess}} + \theta^2 F$, the messenger fermions receive masses proportional to the messenger scale $M_{\mathrm{mess}}$, while the messenger scalars receive masses that are split around this scale by the SUSY breaking scale $F$, $M_{\mathrm{mess}}^2 \pm F$. The fields of the visible sector do not interact directly with goldstino multiplet, but the gauge fields and gauginos do interact with the messenger fields, so that gauginos receive masses at one-loop level, and the scalars of the visible sector receive masses at two-loop level; after integrating out the messenger particles, the soft masses are roughly given by

$$m \sim \frac{g^2}{16\pi^2} \frac{F}{M_{\mathrm{mess}}}, \tag{3.8}$$

where $g$ stands for the gauge coupling. The messenger scale is $M_{\mathrm{mess}} \geq \sqrt{F}$, which gives, in order to have soft masses of $\mathcal{O}(1 \text{ TeV})$, a possible low SUSY breaking scale of $\sqrt{F} \sim \mathcal{O}(10 \text{ TeV})$.

## 3.2 Goldstino interactions

In the following, we do not specify a mediation mechanism. Instead, we parametrize the effect of mediating SUSY to the visible sector by higher dimensional operators that couple the fields in the visible sector to the goldstino multiplet in the hidden sector. As a result, we obtain interactions among the (s)goldstinos and the fields in the visible sector as well as the soft mass terms for the SUSY particles.

[3] Gravity mediation will still be present but is negligible.

### 3.2.1 The goldstino Lagrangian in the superfield formalism

For our SUSY QED model, the effective Lagrangian of the superfields from the visible sector and the goldstino superfield $X$ is given by

$$\begin{aligned}\mathcal{L}_{\text{int}} = &- \sum_{i=L,R} c_{\Phi_i} \int d^4\theta \; X^\dagger X \Phi_i^\dagger \Phi_i \\ &- \Big( \frac{c_V}{4} \int d^2\theta \; X W^\alpha W_\alpha + \text{h.c.} \Big),\end{aligned} \tag{3.9}$$

where we identify $c_{\Phi_i} = m_{\tilde{e}_i}^2/F^2$ and $c_V = 2m_\lambda/F$. The first term leads, for example, to the vertex involving a goldstino, a selectron and a electron, with coupling $m_{\tilde{e}_i}^2/F$. We also obtain a four-fermion vertex involving two electrons and two goldstinos. From the second term, we get, for example, the interaction between goldstino, photon and photino, and the interaction between the sgoldstino and two photons. We note that our Lagrangian is model independent. However, studies of non-linear SUSY revealed that additional model dependent terms for four-point effective interactions involving two goldstinos and two matter fermions are allowed [31–33]. One possible source for such terms is $D$-type SUSY breaking [34], which does not occur in our model. The relevant interactions for the rest of this work between visible sector fields and the fields of the goldstino supermultiplet are summarized in four component notation in the next section.

### 3.2.2 The goldstino Lagrangian in terms of the component fields

In the equations (2.56), (2.61), (3.6) and (3.9), we gave the Lagrangian of our model in terms of the superfields. In this Section, for completeness, we present the corresponding interaction Lagrangian in terms of the component fields. The relevant terms of the effective interaction Lagrangian among gravitinos (i.e. goldstinos) $\psi_{\tilde{G}}$ and fields in the visible sector, that is right- and left-handed selectron $\phi_{\tilde{e}_\pm}$, electron $\psi_e$, photino-like neutralino $\psi_{\tilde{\chi}}$, and photon $A^\mu$ are given in the four-component notation by

$$\begin{aligned}\mathcal{L}_{\tilde{G}} = &\mp \frac{i m_{\tilde{e}_\pm}^2}{F} (\bar{\psi}_{\tilde{G}} P_\pm \psi_e \phi_{\tilde{e}_\pm}^* - \bar{\psi}_e P_\mp \psi_{\tilde{G}} \phi_{\tilde{e}_\pm}) \\ &- \frac{m_{\tilde{\chi}}}{4\sqrt{2}F} \bar{\psi}_{\tilde{G}} [\gamma^\mu, \gamma^\nu] \psi_{\tilde{\chi}} F_{\mu\nu} \\ &- \frac{m_{\tilde{e}_\pm}^2}{F^2} \bar{\psi}_e P_\mp \psi_{\tilde{G}} \bar{\psi}_{\tilde{G}} P_\pm \psi_e,\end{aligned} \tag{3.10}$$

where $P_\pm = \frac{1}{2}(1 \pm \gamma^5)$ is the chiral projection operator and $F_{\mu\nu} = \partial_\mu A_\nu - \partial_\nu A_\mu$ the photon field strength tensor. The interactions among sgoldstino $\phi = \frac{1}{\sqrt{2}}(\phi_S + i\phi_P)$ and

gravitino or photon are given by

$$\begin{aligned}\mathcal{L}_{S,P} = &-\frac{m_\phi^2}{2\sqrt{2}F}\,\bar{\psi}_{\tilde{G}}(\phi_S + i\gamma^5\phi_P)\psi_{\tilde{G}} \\ &+ \frac{m_{\tilde{\chi}}}{2\sqrt{2}F}(\phi_S F^{\mu\nu}F_{\mu\nu} - \phi_P F^{\mu\nu}\tilde{F}_{\mu\nu}),\end{aligned} \tag{3.11}$$

where $\tilde{F}_{\mu\nu} = \frac{1}{2}\epsilon_{\mu\nu\alpha\beta}F^{\alpha\beta}$ is the dual tensor with $\epsilon_{0123} = +1$. All other relevant terms in the visible sector are

$$\begin{aligned}\mathcal{L}_{\text{vis}} = &\, g_e\bar{\psi}_e\gamma_\mu\psi_e A^\mu + ig_e(\phi^*_{\tilde{e}_\pm}\overleftrightarrow{\partial_\mu}\phi_{\tilde{e}_\pm})A^\mu \\ &\mp\sqrt{2}g_e(\bar{\psi}_{\tilde{\chi}}P_\pm\psi_e\phi^*_{\tilde{e}_\pm} + \bar{\psi}_e P_\mp\psi_{\tilde{\chi}}\phi_{\tilde{e}_\pm}),\end{aligned} \tag{3.12}$$

where $g_e = \sqrt{4\pi\alpha}$ is the QED coupling constant.

We note that we will find a relation between the SUSY breaking scale $F$ and the gravitino mass $m_{3/2}$ in Section 3.3.2,

$$F = \sqrt{3}\,\overline{M}_{\text{Pl}}m_{3/2}, \tag{3.13}$$

where $\overline{M}_{\text{Pl}}$ is the reduced Planck mass, $\overline{M}_{\text{Pl}} = M_{\text{Pl}}/\sqrt{8\pi} = 2.43 \times 10^{18}$ GeV.

We also note that we follow the convention of the SUSY Les Houches accord [27] for the covariant derivative and the gaugino and gravitino field definitions. To translate our Lagrangian into the FeynRules convention, one has to change the coupling as $g_e \to -g_e$, and redefine the fields as $\psi_{\tilde{\chi}} \to -\psi_{\tilde{\chi}}$ and $\psi_{\tilde{G}} \to -\psi_{\tilde{G}}$.

In a similar way that we constructed the goldstino interaction Lagrangian for the SUSY QED model, we can construct the Lagrangian for the full MSSM, in order to investigate the effect of a neutralino which is mixed differently than a photino, or when we want to study the jets plus missing energy signal at the LHC. In the following, we give the relevant interaction terms.

For a generally mixed neutralino, the couplings among goldstino, neutralino and photon/$Z$-boson, $\tilde{G}$-$\tilde{\chi}^0_i$-$V(=\gamma/Z)$ and among neutralino, electron and selectron $\tilde{\chi}^0_1$-$e$-$\tilde{e}_\pm$, change as

$$\begin{aligned}\mathcal{L}_{\tilde{\chi}^0_i\tilde{G}V} &= -\frac{C^{V\tilde{\chi}_i}m_{\tilde{\chi}^0_i}}{4\sqrt{2}\,F}\bar{\psi}_{\tilde{G}}[\gamma^\mu,\gamma^\nu]\psi_{\tilde{\chi}^0_i}(\partial_\mu V_\nu - \partial_\nu V_\mu) \\ \mathcal{L}_{\tilde{\chi}^0_i e\tilde{e}} &= \pm\sqrt{2}\,e\,C^{\tilde{e}\tilde{\chi}_i}_\pm\big[\bar{\psi}_{\tilde{\chi}^0_i}P_\pm\psi_e\,\phi^*_{\tilde{e}_\pm} + \bar{\psi}_e P_\mp\psi_{\tilde{\chi}^0_i}\,\phi_{\tilde{e}_\pm}\big].\end{aligned} \tag{3.14}$$

The couplings related to the neutralino mixing defined by $X_i = U_{ij}\tilde{\chi}^0_j$ in the $X =$

$(\tilde{B}, \tilde{W}^3, \tilde{H}_d^0, \tilde{H}_u^0)$ basis, where $U_{ij}$ is taken to be real, are

$$\begin{aligned} C^{\gamma\tilde{\chi}_i} &= U_{1i}\cos\theta_W + U_{2i}\sin\theta_W, \\ C^{Z\tilde{\chi}_i} &= -U_{1i}\sin\theta_W + U_{2i}\cos\theta_W, \\ C_{\pm}^{\tilde{e}\tilde{\chi}_i} &= T_{\pm}^{\tilde{e}}\frac{U_{2i}}{\sin\theta_W} + Y_{\pm}^{\tilde{e}}\frac{U_{1i}}{\cos\theta_W}, \end{aligned} \tag{3.15}$$

with the $SU(2)$ charge $T_{\pm}^{\tilde{e}}$ and the $U(1)$ charge $Y_{\pm}^{\tilde{e}}$ for $\tilde{e}_{+/-}(=\tilde{e}_{R/L})$.[4]

The effective interaction Lagrangian among goldstino, quark and squark, $\psi$-$f$-$\phi$, and among goldstino, gluino and gluon(s), $\psi$-$\lambda$-$A$(-$A$), is

$$\begin{aligned} \mathcal{L}_{\rm int} = &\pm \frac{im^2_{\phi^i_{L/R}}}{F}\left[\bar{\psi}P_{L/R}f^i(\phi^i_{L/R})^* - \bar{f}^i P_{R/L}\psi\,\phi^i_{L/R}\right] \\ &- \frac{m_\lambda}{4\sqrt{2}\,F}\bar{\psi}[\gamma^\mu,\gamma^\nu]\lambda^a F^a_{\mu\nu}, \end{aligned} \tag{3.16}$$

where $\phi_{L/R}$ denotes the left-/right-handed squark, $P_{L/R} = \frac{1}{2}(1 \mp \gamma^5)$ is the chiral projection operator, and $F^a_{\mu\nu} = \partial_\mu A^a_\nu - \partial_\nu A^a_\mu - g_s f^{abc} A^b_\mu A^c_\nu$ is the field-strength tensor of the $SU(3)_C$ gauge group ($a = 1, \cdots, 8$).

### 3.2.3 Goldstino interactions from the supercurrent

Without using the superfield formalism and introducing an explicit supermultiplet that breaks SUSY, there is a different way of constructing the goldstino interaction Lagrangian by means of the supercurrent introduced in Section 2.2.2. A similar expression for the supercurrent as derived in this example can of course be obtained from the Lagrangian in (2.56) and (2.61), or for the Lagrangian of the MSSM. We assume SUSY to be broken by a VEV of the auxiliary field of the goldstino multiplet, and want to derive the interactions of the corresponding goldstone fermion. The supercurrent of the theory combining the visible sector fields and fields of the goldstino multiplet can be written as

$$J^\mu_\alpha = i\sqrt{2}F(\sigma^\mu\bar{\tilde{G}})_\alpha + \sqrt{2}(\sigma^\nu\bar{\sigma}^\mu\tilde{G})_\alpha\partial_\nu\phi^\dagger + j^\mu_\alpha, \tag{3.17}$$

where $\tilde{G}$ denotes the goldstino and $\phi$ the sgoldstino, and $j^\mu_\alpha$ stands for all contributions from the visible sector. We are still allowed to add a quantity $\lambda^\mu$ that fulfills the relation $\partial_\mu\lambda^\mu = 0$. Supercurrent conservation holds also when SUSY is spontaneously broken. Treating $\partial_\mu J^\mu = 0$ as the equation of motion for the goldstino field, one can write down the effective goldstino Lagrangian [35,36], see also [23],

$$\begin{aligned} \mathcal{L} = &\frac{i}{2}\big(\tilde{G}\sigma^\mu\partial_\mu\bar{\tilde{G}} - \partial_\mu\sigma^\mu\bar{\tilde{G}}\big) + \frac{1}{2F}\tilde{G}\sigma^\nu\bar{\sigma}^\mu\partial_\mu(\tilde{G}\partial_\nu\phi^\dagger) + \frac{1}{2F}\bar{\tilde{G}}\bar{\sigma}^\nu\sigma^\mu\partial_\mu(\bar{\tilde{G}}\partial_\nu\phi) \\ &+ \frac{1}{2\sqrt{2}F}\big(\tilde{G}\cdot\partial_\mu j^\mu + \bar{\tilde{G}}\cdot\partial_\mu\bar{j}^\mu\big). \end{aligned} \tag{3.18}$$

[4] Massless $Z$ bosons are assumed.

After using the equations of motion, the resulting Lagrangian can be shown to reproduce the interactions involving a single goldstino in the Lagrangian derived with the superspace formalism [37]; it also reproduces the coupling of two goldstinos to the sgoldstino (the terms in the first line). However, this approach does not lead to interaction vertices of two gravitinos coupling to the visible sector particles, as for example in the four-fermion vertex derived from the first term in (3.9). These terms can be derived from non-linear realizations of SUSY, see e.g. [32]. We also note that by construction, the Lagrangian (3.18) does not contain the couplings of sgoldstinos to visible sector particles.

To summarize, the goldstino interaction Lagrangian derived from the supercurrent is well suited to study processes involving single goldstino interactions, such as e.g. goldstino production in association with another SUSY particle, or when the goldstino appears at the end of a decay chain, and processes in which the sgoldstino does not show up. However, to study processes that include vertices involving two goldstinos, such as e.g. direct goldstino pair production, the Lagrangian given in (3.18) is not sufficient, and one must include other terms. The Lagrangian given in (3.16), which is derived with the superspace formalism, does contain all relevant vertices for studies involving goldstinos and sgoldstinos in a consistent way.

## 3.3 Local SUSY and the gravitino

So far, everything stated holds for global SUSY, that is, the SUSY transformation parameter does not depend on space-time, $\partial_\mu \epsilon = 0$. We will now see what happens when allowing $\epsilon$ to vary for different points in space-time, $\epsilon = \epsilon(x)$. We saw in Section 1.2 that in order for a Lagrangian to be invariant under the *local* $U(1)$ symmetry, we have to introduce a gauge field $A_\mu$. This gauge field couples to the rest of the fields in the Lagrangian, and transforms under the local symmetry in a way that restores the invariance of the Lagrangian. When global SUSY is promoted to the local one, a very similar thing happens. The SUSY Lagrangian is no longer invariant under the local transformations. In order to cancel the non-invariant terms of the Lagrangian, one has to introduce a new "gauge" field $\Psi_\mu$. The excitations of this field are called gravitinos. However, the Lagrangian containing the gravitino interactions is not yet invariant; one has also to include the interactions with a second field $h_{\mu\nu}$, whose excitations are called gravitons. After including the two fields $\Psi_\mu$ and $h_{\mu\nu}$, the Lagrangian is invariant under local SUSY transformations. Together, the gravitino and the graviton form the basic supermultiplet of supergravity. We will now show this by a simple example; for details, see e.g. [38].

### 3.3.1 Introducing the gravitino

Let us consider the variation of the Lagrangian of the massless Wess-Zumino model describing a complex scalar $\phi$ and a Weyl fermion $\psi$,

$$\mathcal{L}_{WZ} = \partial_\mu \phi^* \partial^\mu \phi + \frac{i}{2}\big(\psi\sigma^\mu \partial_\mu \bar{\psi} - \partial_\mu \psi \sigma^\mu \bar{\psi}\big), \tag{3.19}$$

where we neglect the auxiliary fields. The SUSY variations are assumed to be, see (2.24),

$$\begin{aligned}
\delta\phi &= \sqrt{2}\epsilon(x)\psi, \\
\delta\phi^* &= \sqrt{2}\bar{\epsilon}(x)\bar{\psi}, \\
\delta\psi^\alpha &= i\sqrt{2}\big(\bar{\epsilon}(x)\bar{\sigma}^\mu\big)^\alpha \partial_\mu \phi, \\
\delta\bar{\psi}^{\dot{\alpha}} &= -i\sqrt{2}\big(\bar{\sigma}^\mu \epsilon(x)\big)^{\dot{\alpha}} \partial_\mu \phi^*,
\end{aligned} \tag{3.20}$$

Variation of the Lagrangian (3.19) gives

$$\delta\mathcal{L}_{WZ} = \frac{1}{\sqrt{2}}\partial_\mu \epsilon(x)\sigma^\nu \bar{\sigma}^\mu \psi \partial_\nu \phi^* + \frac{1}{\sqrt{2}}\bar{\psi}\bar{\sigma}^\mu \sigma^\nu \partial_\mu \bar{\epsilon}(x)\partial_\nu \phi + \text{ total derivative}, \tag{3.21}$$

hence it is not locally supersymmetric. The variations are proportional to the supercurrents, see (2.32),

$$\begin{aligned}
J^\mu_\alpha &= \sqrt{2}\sigma^\nu_{\alpha\dot{\alpha}}\bar{\sigma}^{\mu\,\dot{\alpha}\beta}\psi_\beta \partial_\nu \phi^*, \\
J^{\dagger\,\mu}_{\dot{\alpha}} &= \sqrt{2}\bar{\psi}_{\dot{\beta}}\bar{\sigma}^{\mu\,\dot{\beta}\beta}\sigma^\nu_{\beta\dot{\alpha}}\partial_\nu \phi.
\end{aligned} \tag{3.22}$$

The first two terms in (3.21) are cancelled by adding a new piece to the Lagrangian,

$$\mathcal{L}_{3/2} = -\frac{1}{2}\kappa(\Psi_\mu J^{\dagger\,\mu} + J^\mu \bar{\Psi}_\mu), \tag{3.23}$$

where $\Psi_{\mu\,\alpha}$ is a spinorial vector field that transforms under local SUSY as

$$\delta\Psi_\mu = \frac{1}{\kappa}\partial_\mu \epsilon, \quad \delta\bar{\Psi}_\mu = \frac{1}{\kappa}\partial_\mu \bar{\epsilon}. \tag{3.24}$$

Since $\Psi_\mu$ has mass dimension $[\Psi_\mu] = 3/2$, the Lagrangian (3.23) is non-renormalizable and comes with a dimensionful coupling constant which is inversely proportional to the reduced Planck mass, $\kappa = \frac{1}{\overline{M}_{\rm Pl}}$. $\Psi_\mu$ has a vector component and a spinor component and hence has spin 3/2; as mentioned before, its excitations are the gravitinos.

From the variation of (3.23), we find terms that cancel the first two terms in (3.21). In addition, we will find other terms that do not transform as a total derivative; for simplicity, we show in the following only the result for the variation of the fermionic component of (3.23),

$$\begin{aligned}
\delta\mathcal{L}_{3/2} &= -\frac{\kappa}{\sqrt{2}}\big(\Psi_\mu \sigma^\nu \bar{\sigma}^\mu \delta\psi \partial_\nu \phi^* + \delta\bar{\psi}\bar{\sigma}^\mu \sigma^\nu \bar{\Psi}_\mu \partial_\nu \phi\big) \\
&= -i\kappa\big(\epsilon(x)\sigma_\mu \bar{\Psi}_\nu - \Psi_\nu \sigma_\mu \bar{\epsilon}(x)\big)T^{\mu\nu},
\end{aligned} \tag{3.25}$$

where $T^{\mu\nu}$ is the energy momentum tensor of the scalar field,

$$T^{\mu\nu} = -\eta^{\mu\nu}\partial^{\rho}\phi\partial_{\rho}\phi^{*} + \partial^{\mu}\phi\partial^{\nu}\phi^{*} + \partial^{\nu}\phi\partial^{\mu}\phi^{*}. \tag{3.26}$$

In a similar way, the variation of (3.23) of the scalar fields $\delta\phi$ gives a a term that couples the gravitino to the energy momentum tensor of the fermions. To cancel (3.25), we have to consider the interactions of the scalar field with the spin-two graviton field $h_{\mu\nu}$. We add to our Lagrangian the term[5]

$$\mathcal{L}_{h} = -\kappa\, h_{\mu\nu}T^{\mu\nu}. \tag{3.27}$$

This term cancels (3.25) if $h_{\mu\nu}$ transforms under local SUSY transformations as

$$\delta h_{\mu\nu} = -\frac{i}{2}\big(\epsilon(x)\sigma_{\mu}\bar{\Psi}_{\nu} - \Psi_{\nu}\sigma_{\mu}\bar{\epsilon}(x) + (\mu \leftrightarrow \nu)\big). \tag{3.28}$$

The interactions introduced above are part of the Lagrangian of linearized supergravity (linearized because we consider only interactions with one graviton field $h_{\mu\nu}$.)

In general, that is for theories more complex than the simple Wess-Zumino model considered here, single gravitino interactions can be constructed by coupling the gravitino to the supercurrent $J^{\mu}$ of the theory as in (3.23), in a similar way to deriving the goldstino couplings presented in Section 3.2.3. We do not present the full Lagrangian here because of its lengthy and complicated expression; a full set of interactions can be found e.g in [39], and the relevant interaction terms for this work are given in Section 3.4.1.

For completeness, let us give the kinetic terms of graviton and gravitino,

$$\frac{1}{\sqrt{-g}}\mathcal{L} = -\frac{1}{2\kappa^{2}}R - \frac{1}{2}\epsilon^{\mu\nu\rho\sigma}\bar{\Psi}_{\mu}\gamma^{5}\gamma_{\nu}\partial_{\rho}\Psi_{\sigma}, \tag{3.29}$$

where $R$ is the Ricci scalar and $g = det\, g^{\mu\nu}$.

In the next section, we show how the gravitino becomes massive when the local SUSY is broken spontaneously.

### 3.3.2 The super-Higgs mechanism

When local SUSY is preserved, both the gravitino $\Psi_{\mu}$ and the graviton $h_{\mu\nu}$ are massless. When the local SUSY is broken spontaneously, the gravitino becomes massive.

For illustration, let us refer again to the spontaneous breaking of a local symmetry discussed in Section 1.2. Before breaking the local $U(1)$ symmetry spontaneously, we

[5] This term can obtained by generalising the Lagrangian (3.19) of flat space-time to a Lagrangian in curved space-time; the graviton is defined as a small perturbation of the metric $g_{\mu\nu}$ from the flat space-time. We get the interactions of the graviton field by expanding $g_{\mu\nu}(x) = \eta_{\mu\nu} + 2\kappa h_{\mu\nu}(x) + \mathcal{O}(\kappa^{2}), g^{\mu\nu}(x) = \eta^{\mu\nu} + 2\kappa\bar{h}^{\mu\nu}(x) + \mathcal{O}(\kappa^{2})$, and $\bar{h}^{\mu\nu}(x) = -\eta^{\mu\rho}\eta^{\nu\sigma}h_{\rho\sigma}$. The first term of (3.19) turns for curved space-time into $\mathcal{L}^{c} = \sqrt{-g}g^{\mu\nu}\partial_{\mu}\phi\partial\nu\phi^{*}$, where $g = det\, g_{\mu\nu}$ and we already used the fact that the covariant derivative acting on scalars reduces to the partial derivative, $\nabla_{\mu}\phi = \delta_{\mu}\phi$. Using the metric expansion given above and $\sqrt{-g} = 1 + \kappa\eta^{\mu\nu}h_{\mu\nu} + \mathcal{O}(\kappa^{2})$, one can show that $\mathcal{L}^{c}$ can be written as $\mathcal{L}^{c} = \partial_{\mu}\phi\partial^{\mu}\phi^{*} - \kappa h_{\mu\nu}T^{\mu\nu}$, where we omit higher orders in $\kappa$.

have a massless gauge boson $A_\mu$. After breaking, we have a massive gauge boson and a massless goldstone boson $\xi$ in our theory. The goldstone boson mixes with the gauge field $A_\mu$, see (1.10). By choosing unitary gauge and shifting the gauge field by $A_\mu \to A_\mu - \frac{1}{g_e}\partial_\mu \xi$, the goldstone boson is removed from the theory and provides the physical longitudinal polarisation state for the massive gauge boson.

In unbroken local supergravity, we start with a massless gravitino, which has physical polarization states $\pm\frac{3}{2}$. After breaking the local SUSY, one obtains a massive gravitino as well as a massless goldstino $\tilde{G}$. The goldstino was already introduced in Section 3.1. By a redefinition of the gravitino field, the goldstino is removed from the theory, and we are left with a massive gravitino possessing spin $\pm 3/2$ and spin $\pm 1/2$ polarization states. In the following, we present a simplified version of this so-called super-Higgs mechanism [40–42]; for a more detailed discussion, see [39, 43].

A general global SUSY theory is described by the superpotential $W$, the Kähler potential $K$ and the gauge kinetic function $f_{ab}$. The superpotential for a renormalizable theory was already introduced in (2.65), and may contain higher order terms for a non-renormalizable theory such as the one we are discussing. The Kähler potential is a function of real superfields, and the gauge kinetic function is a function of chiral superfields; for details, see equation 4.10.1 and 7.6.2 in [28].

In supergravity theories, the superpotential and the Kähler potential are combined into one function called the Kähler function $G$,

$$G = \frac{K}{\overline{M}_{\rm Pl}^2} + \log\left(\frac{W}{\overline{M}_{\rm Pl}^3}\right) + \log\left(\frac{W^*}{\overline{M}_{\rm Pl}^3}\right), \tag{3.30}$$

where the superfields in $W, K$ are replaced by their scalar components. From now on, to simplify the expressions, we will not write the factors of $\overline{M}_{\rm Pl}$ anymore. We will put them back in the end by dimensional analysis.

The scalar potential of supergravity reads (compare to (3.4) for global SUSY) [42,44]

$$V = e^G\big(G^i (G^{-1})^j_i G_j - 3\big), \tag{3.31}$$

where $G^i = \frac{\partial G}{\partial \phi_i}$, $G_i = \frac{\partial G}{\partial \phi_i^*}$, $G_i^j = \frac{\partial^2 G}{\partial \phi_i^* \partial \phi_j}$; here and in the following, we restrict the discussion to $F$-terms and neglect possible contributions from $D$-terms.[6] We assume canonically normalized terms so that $G_i^j = \delta_i^j$.

As in global SUSY, the local SUSY is broken when one or more of the auxiliary fields $F_i$ obtains a VEV, $\langle F_i \rangle \neq 0$. The equations of motion for the auxiliary fields $F_i$ read (compare to (2.66) for a general global SUSY theory)

$$F_i = e^{G/2} (G^{-1})^i_j G_j, \tag{3.32}$$

where we neglect contributions from fermions. Since $e^{G/2}$ is different from 0, the relevant

[6] The expressions containing $D$-terms can be found e.g. in [43].

quantity for SUSY breaking is

$$\langle G_i \rangle \neq 0, \tag{3.33}$$

and the SUSY breaking scale is

$$\langle F_i \rangle = e^{G_0/2} (G_0^{-1})_i^j G_{0j} \tag{3.34}$$

where $G_0 = \langle G \rangle$ and $G_{0j}^i = \delta_j^i$ as mentioned before.

The relevant terms of the Lagrangian describing gravitino and goldstino fields after SUSY breaking are given by

$$\frac{1}{\sqrt{-g}} \mathcal{L} = i e^{G/2} \bar{\Psi}_\mu \gamma^{\mu\nu} \Psi_\nu + \frac{1}{\sqrt{2}} e^{G/2} G_i \bar{\Psi}_\mu \gamma^\mu \psi^i, \tag{3.35}$$

where $\gamma^{\mu\nu} = \frac{i}{4}[\gamma^\mu, \gamma^\nu]$ and the goldstino is defined as $\tilde{G} = G_i \psi^i$. The second term mixes the gravitino and the goldstino. It can be removed by redefining the gravitino field,

$$\Psi'_\mu = \Psi_\mu - \frac{i}{3\sqrt{2}} \gamma_\mu \tilde{G} - \frac{\sqrt{2}}{3} e^{-G/2} \partial_\mu \tilde{G}. \tag{3.36}$$

The gravitino "absorbs" the goldstino and gains helicity $\pm 1/2$ states.

We now show how the gravitino mass is related to the SUSY breaking scale. The gravitino mass can be read off the first term in (3.35); re-introducing the factor $\overline{M}_{\rm Pl}$, it is given by

$$m_{3/2} = e^{G_0/2} \overline{M}_{\rm Pl}, \tag{3.37}$$

To find a simple expression for the gravitino mass in terms of the SUSY breaking scale, we assume that only one auxiliary field obtains a VEV, and that the potential (3.31) vanishes at the minimum, $V_0 = 0$; this implies $G_{0j} = \sqrt{3}$. From (3.37) and (3.34), we find the relation [41, 42]

$$m_{3/2} = \frac{F}{\sqrt{3}\, \overline{M}_{\rm Pl}}. \tag{3.38}$$

## 3.4 The gravitino-goldstino equivalence

Similar to the goldstone boson equivalence theorem discussed in Section 1.4, there is a gravitino-goldstino equivalence theorem [35, 45]. It represents an enormous simplification for calculations of scattering amplitudes involving gravitinos. The goldstino-gravitino equivalence theorem states that "$S$-matrix elements for longitudinally polarized gravitinos [...] are asymptotically equal up to corrections of the order $\frac{m_{3/2}}{\sqrt{s}}$ to corresponding $S$-matrix elements where each longitudinally polarized gravitino is replaced by the corresponding goldstino" [45]. To obtain the goldstino interaction Lagrangian

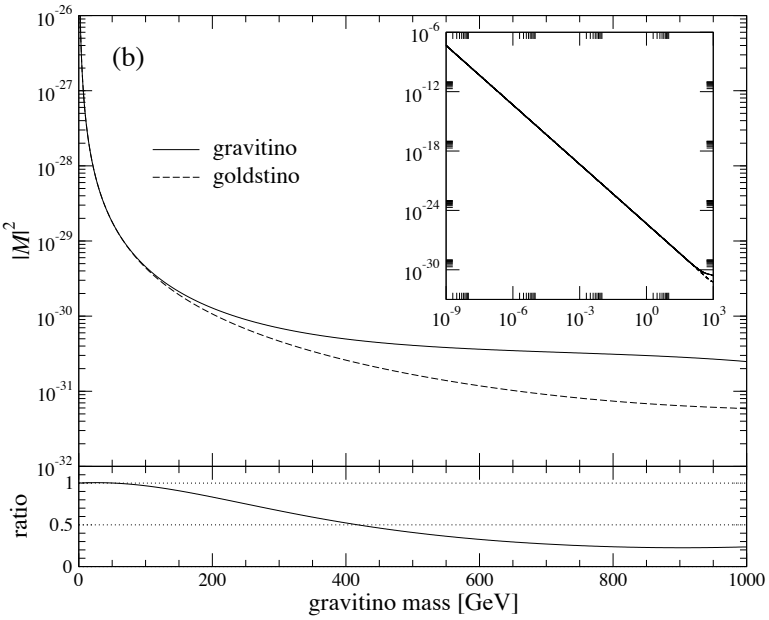


Figure 3.1: Squared matrix elements of gravitino (solid) and goldstino (dashed) productions associated with a gluino for the $gg$ initial state, $gg \to \tilde{g}\tilde{G}$ , at $\sqrt{s} = 2$ TeV and $\cos\theta = 0.5$ as a function of the gravitino mass. The squark and gluino masses are fixed at 1 TeV. The ratios of the squared matrix elements are also shown. The figure is taken from [48].

from the gravitino interaction Lagrangian, we make the replacement

$$\Psi_\mu \sim \sqrt{\frac{2}{3}} \frac{1}{m_{3/2}} \partial_\mu \psi \tag{3.39}$$

in the Lagrangian describing the interactions of the gravitino. Here, $\psi$ denotes the goldstino field. As result, we obtain the corresponding effective goldstino interaction Lagrangian in *derivative* form, see e.g. [46, 47]. Using the equations of motions to replace the derivatives with the corresponding masses, we obtain the effective goldstino interaction Lagrangian in *non-derivative* form [37, 46, 47]. This Lagrangian turns out to be exactly the same as the one we derived in global SUSY in Section 3.1. The only difference is that the goldstino now is effectively the gravitino with a mass $m_{3/2}$. When our parameter choices fulfill the requirement for the goldstino-gravitino equivalence theorem, $m_{3/2} \ll \sqrt{s}$, we can perform calculations involving gravitinos by using the much easier formalism of the spin 1/2 goldstino.

To quantify the parameter region in which the goldstino Lagrangian is a valid approximation to the gravitino Lagrangian, we refer to Fig. 3.1, which was extracted from [48]. It compares the squared matrix elements of gravitino (solid) and goldstino (dashed) productions associated with a gluino at a center of mass energy of 2 TeV for different gravitino masses. We see that for small gravitino masses, $\sqrt{\hat{s}} \gg m_{3/2}$, the amplitudes for goldstino and gravitino agree well with each other.

Throughout this work, we will always consider gravitino masses and center-of-mass

energies that fulfill $\sqrt{s} \gg m_{3/2}$, hence we can safely work within the goldstino equivalence limit.

To give an example, we calculate the process $\gamma\gamma \to \tilde{G}\tilde{G}$ in both formalisms. First, we use the spin-3/2 gravitino interaction Lagrangian. Due to the complexity of the calculations, we restrict ourselves to one specific helicity amplitude which dominates the cross section at high energies. Second, we calculate the same process using the effective goldstino Lagrangian derived in Section 3.2.1. As expected from the goldstino-gravitino equivalence theorem, we find agreement up to corrections of $\mathcal{O}\big(m_{3/2}/\sqrt{s}\big)$.

### 3.4.1 $\gamma\gamma \to \tilde{G}\tilde{G}$ using the spin 3/2 formalism

In the following, we study the scattering process of two photons into two gravitinos, $\gamma\gamma \to \tilde{G}\tilde{G}$. The process has been studied in the context of tree unitarity violation by Bhattacharya and Roy [49].[7] We want to show two features of this process, in analogy to the scattering of longitudinal $W$ bosons in Section 1.4. In the process $W_L W_L \to W_L W_L$, we found that the leading energy dependence of the helicity amplitudes is cancelled among the helicity amplitudes of the gauge bosons, while the next-to-leading energy dependence was cancelled between gauge bosons and the $H$ boson. Subsequently, we reproduced the resulting amplitude by using the goldstone boson equivalence theorem. In the process $\gamma\gamma \to \tilde{G}\tilde{G}$, we show that the leading energy dependence of the scattering amplitude cancels between amplitudes involving the gravitino and the graviton. We then comment on the cancellation of the next-to-leading energy dependent term but we do not show any calculations because of the complexity of the calculations. Subsequently, in the next section, we demonstrate that we can reproduce the (remaining) leading energy dependence by performing the calculations with goldstinos, thanks to the gravitino-goldstino equivalence theorem. After this section, we will use the simplification of this equivalence throughout the rest of this work.

The relevant interaction Lagrangian is given by

$$\mathcal{L} = -\frac{1}{2\overline{M}_{\rm Pl}}\overline{\Psi}_\mu \gamma^{\nu\rho}\gamma^\mu \lambda F_{\nu\rho} - \frac{1}{\overline{M}_{\rm Pl}}(T_\gamma^{\mu\nu} + T_{\tilde{G}}^{\mu\nu})h_{\mu\nu}, \tag{3.40}$$

where $\Psi_\mu$ is the spin-$\frac{3}{2}$ gravitino field, $\lambda$ the photino field, $F_{\mu\nu}$ the field strength tensor for a photon $A_\mu$ and $\gamma^{\mu\nu} = \frac{i}{4}[\gamma^\mu, \gamma^\nu]$. The second term describes the interactions of a spin-2 graviton $h_{\mu\nu}$ with photons [51] and gravitinos through their energy-momentum tensor, $T_\gamma^{\mu\nu}$ and $T_{\tilde{G}}^{\mu\nu}$ for the photon and gravitino, respectively. Those two last quantities

[7] Initially, we re-studied this process to validate the implementation of general spin $\frac{3}{2}$ particles into the FeynRules and Aloha packages, see [50].

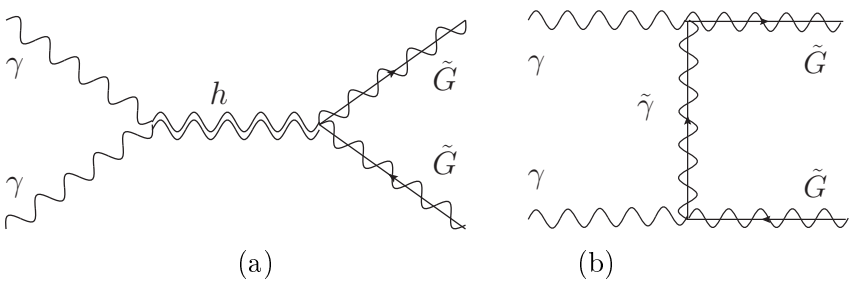


Figure 3.2: The relevant diagrams contributing to the fastest energy growth in the $\gamma\gamma \to \tilde{G}\tilde{G}$ process. They consist of an $s$-channel graviton exchange diagram (a) and $t,u$-channel photino exchange diagrams (b).

are given by

$$\begin{aligned}
T^{\mu\nu}_{\gamma} &= \frac{1}{4}\eta^{\mu\nu}F^{\rho\sigma}F_{\rho\sigma} - F^{\mu}_{\rho}F^{\nu\rho} \\
&\quad - \frac{1}{\xi}\eta^{\mu\nu}\left\{A_\rho\,\partial^\rho\partial^\sigma A_\sigma + \frac{1}{2}(\partial^\rho A_\rho)(\partial^\sigma A_\sigma)\right\} \\
&\quad + \frac{1}{\xi}\left(A^\mu\partial^\nu\partial^\rho A_\rho + A^\nu\partial^\mu\partial^\rho A_\rho\right), \\
T^{\mu\nu}_{\tilde{G}} &= \frac{1}{8}\epsilon^{\lambda\rho\sigma\mu}\overline{\Psi}_\lambda\gamma^5\gamma^\nu\overleftrightarrow{\partial_\sigma}\Psi_\rho + (\mu\leftrightarrow\nu) \\
&\quad - \frac{i}{8}\epsilon^{\lambda\rho\sigma\mu}\partial_\tau(\overline{\Psi}_\lambda\gamma^5\{\gamma_\sigma,\gamma^{\nu\tau}\}\Psi_\rho) + (\mu\leftrightarrow\nu) \\
&\quad - im_{3/2}\overline{\Psi}_\lambda(\eta^{\mu\nu}\gamma^{\lambda\rho} - \eta^{\rho\nu}\gamma^{\lambda\mu} - \eta^{\rho\mu}\gamma^{\lambda\nu})\Psi_\rho\,,
\end{aligned} \tag{3.41}$$

where the dependence on the gauge fixing parameter $\xi$ in the photon energy-momentum tensor has been kept explicit although we adopt Feynman gauge, *i.e.*, $\xi = 1$, in the rest of this section.[8] The gravitino energy momentum tensor is derived from the free gravitino Lagrangian,

$$\mathcal{L} = \frac{1}{2}\epsilon^{\mu\nu\rho\sigma}\Psi_\mu\gamma^5\gamma_\nu\partial_\rho\Psi_\sigma + im_{3/2}\bar{\Psi}_\mu\gamma^{\mu\nu}\Psi_\nu, \tag{3.42}$$

where we already fixed a free parameter in order to obtain this form of the Lagrangian.[9] Moreover, the operator $\overleftrightarrow{\partial_\sigma}$ stands for

$$\overline{\Psi}_\lambda\cdots\overleftrightarrow{\partial}_\sigma\Psi_\rho = \overline{\Psi}_\lambda\cdots\partial_\sigma\Psi_\rho - \left(\partial_\sigma\overline{\Psi}_\lambda\right)\cdots\Psi_\rho\,. \tag{3.43}$$

We compute explicitly the helicity amplitudes $\mathcal{M}_{\lambda_1\lambda_2,\lambda_3\lambda_4}$ associated with the process

$$\gamma(p_1,\lambda_1) + \gamma(p_2,\lambda_2) \to \tilde{G}(p_3,\lambda_3) + \tilde{G}(p_4,\lambda_4). \tag{3.44}$$

There are three diagrams which contribute to the fastest energy growth in this

[8] This gauge is chosen in order to be in agreement with the HELAS [15] convention, which uses Feynman gauge for massless gauge boson propagators (and unitary gauge for massive).

[9] For other possible forms of the Lagrangian, see e.g. [52].

process, an $s$-channel graviton exchange diagram and $t,u$-channel photino exchange diagrams, as shown in Figure 3.2.

The helicity amplitudes can be expressed as a sum of $s$-, $t$- and $u$-channel contributions,

$$\mathcal{M}_{\lambda_1\lambda_2,\lambda_3\lambda_4} = \mathcal{M}^s + \mathcal{M}^t + \mathcal{M}^u, \tag{3.45}$$

with the helicity dependence of the right-hand side of the equation being suppressed for clarity. We derive, starting from the Feynman rules extracted from the Lagrangian of Eq. (3.40),

$$\begin{aligned}
i\mathcal{M}^s &= -\frac{1}{\overline{M}_{\rm Pl}^2}\frac{1}{s}\,\epsilon_\mu(p_1)\epsilon_\nu(p_2)\,\Gamma_\gamma^{\mu\nu,\alpha\beta}B_{\alpha\beta,\gamma\delta}\,\bar{u}_\rho(p_3)\Gamma_{\tilde{G}}^{\gamma\delta,\rho\sigma}v_\sigma(p_4),\\
i\mathcal{M}^t &= \frac{i}{16\overline{M}_{\rm Pl}^2}\frac{1}{t_{\tilde{\gamma}}}\,\epsilon_\mu(p_1)\epsilon_\nu(p_2)\\
&\quad\times\bar{u}_\rho(p_3)[\not{p}_1,\gamma^\mu]\gamma^\rho(\not{p}_3-\not{p}_1+m_{\tilde{\gamma}})\gamma^\sigma[\gamma^\nu,\not{p}_2]v_\sigma(p_4),\\
i\mathcal{M}^u &= \frac{i}{16\overline{M}_{\rm Pl}^2}\frac{1}{u_{\tilde{\gamma}}}\,\epsilon_\mu(p_1)\epsilon_\nu(p_2)\\
&\quad\times\bar{u}_\rho(p_3)[\not{p}_2,\gamma^\nu]\gamma^\rho(\not{p}_1-\not{p}_4+m_{\tilde{\gamma}})\gamma^\sigma[\gamma^\mu,\not{p}_1]v_\sigma(p_4),
\end{aligned} \tag{3.46}$$

where the Mandelstam variables are defined by $s=(p_1+p_2)^2$, $t_{\tilde{\gamma}}=(p_1-p_3)^2-m_{\tilde{\gamma}}^2$ and $u_{\tilde{\gamma}}=(p_1-p_4)^2-m_{\tilde{\gamma}}^2$, $m_{\tilde{\gamma}}$ being the photino mass. The Lorentz structure of each amplitude has been embedded into the functions

$$\begin{aligned}
B^{\alpha\beta,\gamma\delta} &= \frac{1}{2}(\eta^{\alpha\gamma}\eta^{\beta\delta}+\eta^{\alpha\delta}\eta^{\beta\gamma}-\eta^{\alpha\beta}\eta^{\gamma\delta}),\\
\Gamma_\gamma^{\mu\nu,\alpha\beta} &= (p_1\cdot p_2)\,C_{\alpha\beta,\mu\nu}+D_{\alpha\beta,\mu\nu}+E_{\alpha\beta,\mu\nu}\,,\\
\Gamma_{\tilde{G}}^{\gamma\delta,\rho\sigma} &= \frac{1}{4}\epsilon^{\rho\sigma\lambda\gamma}\gamma^5\gamma^\delta(p_3-p_4)_\lambda+(\gamma\leftrightarrow\delta)\\
&\quad+\frac{i}{8}\epsilon^{\rho\sigma\lambda\gamma}\gamma^5\{\gamma_\lambda,\sigma^{\delta\tau}\}(p_3+p_4)_\tau+(\gamma\leftrightarrow\delta)\\
&\quad-im_{3/2}(\eta^{\rho\gamma}\eta^{\delta\sigma}+\eta^{\sigma\gamma}\eta^{\delta\rho}-\eta^{\gamma\delta}\eta^{\rho\sigma}),
\end{aligned} \tag{3.47}$$

with

$$\begin{aligned}
C^{\alpha\beta,\mu\nu} &= \eta^{\alpha\mu}\eta^{\beta\nu}+\eta^{\alpha\nu}\eta^{\beta\mu}-\eta^{\alpha\beta}\eta^{\mu\nu},\\
D^{\alpha\beta,\mu\nu} &= p_1^\nu p_2^\mu\eta^{\alpha\beta}\\
&\quad+(p_1^\alpha p_2^\beta\eta^{\mu\nu}-p_1^\nu p_2^\beta\eta^{\alpha\mu}-p_1^\beta p_2^\mu\eta^{\alpha\nu}+(\alpha\leftrightarrow\beta)),\\
E^{\alpha\beta,\mu\nu} &= \eta^{\alpha\beta}(p_1^\mu p_1^\nu+p_2^\mu p_2^\nu+p_1^\mu p_2^\nu)\\
&\quad-(p_1^\mu p_1^\beta\eta^{\nu\alpha}+p_2^\nu p_2^\beta\eta^{\mu\alpha}+(\alpha\leftrightarrow\beta)).
\end{aligned} \tag{3.48}$$

The explicit expression for the gravitino wavefunction can be found in the Appendix A.2.

We now select a particular helicity combination and choose to investigate the properties of the $\mathcal{M}_{1,-1,\frac{1}{2},-\frac{1}{2}}$ amplitude, as it gives rise to the leading energy growth with the partonic center-of-mass (CM) energy $\sqrt{s}$. Expanding the $s$-, $t$- and $u$-channel con-

tributions to the considered amplitudes in terms of the gravitino mass, one gets

$$\begin{aligned}
\mathcal{M}^s &= -\frac{s}{12\overline{M}_{\rm Pl}^2}(1+c_\theta)s_\theta\Big[\frac{s}{m_{3/2}^2}+4\Big]+\mathcal{O}(m_{3/2}^2/s),\\
\mathcal{M}^t &= \frac{s}{6\overline{M}_{\rm Pl}^2 x_t}s_\theta^3+\mathcal{O}(m_{3/2}^2/s),\\
\mathcal{M}^u &= \frac{s}{24\overline{M}_{\rm Pl}^2 x_u}(1+c_\theta)^2 s_\theta\Big[\frac{s}{m_{3/2}^2}+1+\frac{1}{x_u}(1+c_\theta)\Big]+\mathcal{O}(m_{3/2}^2/s),
\end{aligned} \tag{3.49}$$

where $s_\theta$ and $c_\theta$ stand for the sine and cosine of the scattering angle $\theta$ defined as the angle between the $\vec{p}_1$ and $\vec{p}_3$ directions in the partonic center-of-mass frame. We also introduce the reduced variables $x_{t,u}=\frac{m_{\tilde\gamma}^2}{s}+\frac{1}{2}(1\mp c_\theta)$.

In the limit of large center-of-mass energies, or equivalently when $m_{\tilde\gamma}/\sqrt{s}\to 0$, we can expand the terms $\propto\frac{1}{x_{t,u}}$, and we find that the $s^2$ energy growth behavior of the $s$- and $u$-channel diagrams cancels,

$$\mathcal{M}_{1,-1,\frac{1}{2},-\frac{1}{2}}\to-\frac{s}{6\overline{M}_{\rm Pl}^2}s_\theta\Big[\frac{m_{\tilde\gamma}^2}{m_{3/2}^2}-\frac{3}{2}(1+c_\theta)\Big]+\mathcal{O}(m_{3/2}^2/s), \tag{3.50}$$

in complete analogy to the cancellation of the highest energy dependence in the $WW$ scattering discussed in Section 1.4. We note that a linear $s$-dependence still remains [49]. The gravitino mass enters in the first term in the nominator. For a very light gravitino, the first term will dominate over the last term; we will find that it is exactly this first term which is reproduced by performing the calculations in the gravitino-goldstino equivalence limit in the next section.

Figure 3.3 illustrates the energy dependence of the projected partial wave amplitude,[10]

$$J^2_{1,-1,\frac{1}{2},-\frac{1}{2}}=\frac{1}{32\pi}\int_{-1}^{1}\mathrm{d}\cos\theta\, d^2_{21}(\theta)\,\mathcal{M}_{1,-1,\frac{1}{2},-\frac{1}{2}}, \tag{3.51}$$

for different photino masses. In this expression, we introduce the $J=2$ Wigner $d$-function $d^2_{21}(\theta)=-\frac{1+\cos\theta}{2}\sin\theta$. The analytic result of Eq. (3.50) (dashed line) is derived in the $\sqrt{s}\gg m_{3/2},m_{\tilde\gamma}$ limit [49] and agrees with our numerical predictions calculated by MadGraph 5 in the high-energy region where this approximation is valid. In contrast, in the low-energy regime, the sub-leading term to Eq. (3.50) in the $m_{\tilde\gamma}^2/s$ expansion becomes relevant, and one observes the deviation of the approximate analytical result from our numerical predictions.

Finally, partial wave unitarity requires

$$\big|J^2_{1,-1,\frac{1}{2},-\frac{1}{2}}\big|<\frac{1}{2}, \tag{3.52}$$

which is shown by a gray line on the figure.

To complete our analogy with the example of $WW$ scattering, we comment on the cancellation of the next-to-leading energy dependence. The next-to-fastest en-

[10] For the derivation, see Appendix A.4.

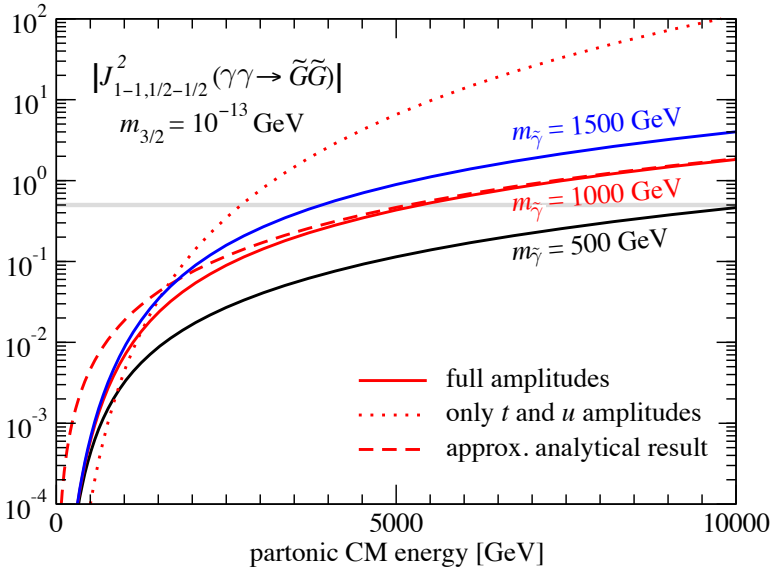


Figure 3.3: Energy dependence of the projected partial wave amplitude $\left|J^2_{1-1,\frac{1}{2}-\frac{1}{2}}\right|$ defined in Eq. (3.51) for the $\gamma\gamma \to \tilde{G}\tilde{G}$ process and for different choices of the photino mass. The solid lines are calculated by MadGraph 5 and use the full amplitude. For the $m_{\tilde{\gamma}} = 1000$ GeV case, we also show the analytical results in the $\sqrt{s} \gg m_{3/2}, m_{\tilde{\gamma}}$ limit of Ref. [49] (dashed) as well as the $s^2$ dependence resulting from the $t$- and $u$-channel diagram contributions only (dotted).

ergy growth appears in $s$-channel sgoldstino exchange diagrams, see Fig. 3.4. One can show [49] that the leading energy dependence for each single amplitude is $\propto s^{3/2}$, and again a cancellation happens between the photino exchange diagrams and the sgoldstino diagrams; for details, see [49].

In the next section, we discuss the full process $\gamma\gamma \to \tilde{G}\tilde{G}$ again in detail using the gravitino-goldstino equivalence.

### 3.4.2 $\gamma\gamma \to \tilde{G}\tilde{G}$ using the goldstino formalism

In this section, we restudy the process $\gamma\gamma \to \tilde{G}\tilde{G}$ using the gravitino-goldstino equivalence theorem. We show analytically that we reproduce the leading energy dependent term in (3.50), and verify numerically that the goldstino equivalence reproduces the results of the previous section for the whole parameter space presented in Figure 3.3. Since the expressions for the helicity amplitudes are much simpler for the spin-1/2 goldstino, we present them in detail and discuss their parameter dependence at the end of this section.

We use the effective goldstino interaction Lagrangian derived in Section 3.2.1 for a SUSY QED model with a photino-like neutralino, and which is presented in terms of the component fields in Section 3.2.2.

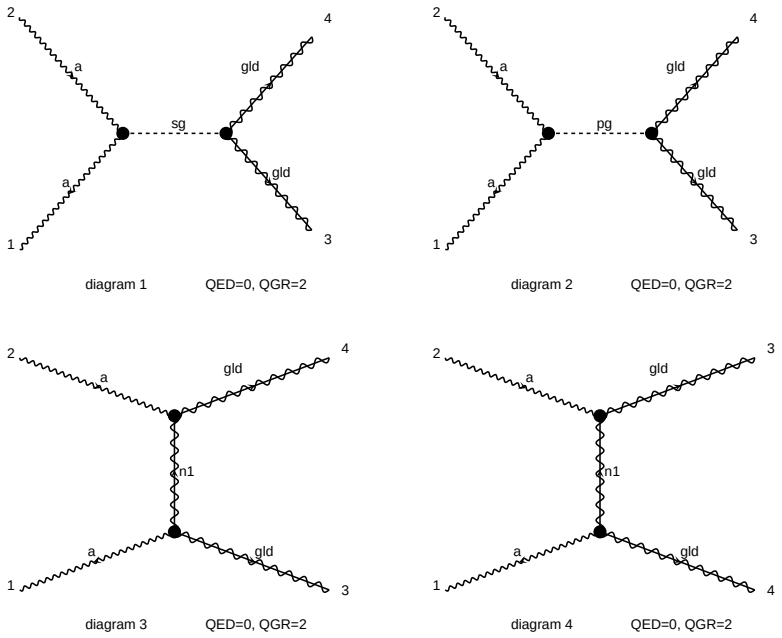


Figure 3.4: Feynman diagrams for gravitino pair production in $\gamma\gamma$ collisions, generated by MadGraph 5 [14]. `gld`, `sg`, `pg`, and `n1` denote a gravitino, a scalar sgoldstino, a pseudoscalar sgoldstino, and a neutralino, respectively.

We present the helicity amplitudes explicitly for the process

$$\gamma\left(p_1,\lambda_1\right)+\gamma\left(p_2,\lambda_2\right)\to\tilde{G}\Big(p_3,\frac{\lambda_3}{2}\Big)+\tilde{G}\Big(p_4,\frac{\lambda_4}{2}\Big), \tag{3.53}$$

where the four momenta ($p_i$) and helicities ($\lambda_i=\pm1$) are defined in the center-of-mass (CM) frame of the $\gamma\gamma$ collision. As seen in Fig. 3.4, the helicity amplitudes are given by the sum of the $s$-channel scalar ($S$) and pseudoscalar ($P$) sgoldstino amplitudes and the $t,u$-channel photino exchange amplitudes:

$$\begin{aligned}\mathcal{M}_{\lambda_1\lambda_2,\lambda_3\lambda_4}&=\epsilon_\mu(p_1,\lambda_1)\epsilon_\nu(p_2,\lambda_2)\\&\quad\times\left(\mathcal{M}^{S,\mu\nu}_{\lambda_3\lambda_4}+\mathcal{M}^{P,\mu\nu}_{\lambda_3\lambda_4}+\mathcal{M}^{t,\mu\nu}_{\lambda_3\lambda_4}+\mathcal{M}^{u,\mu\nu}_{\lambda_3\lambda_4}\right),\end{aligned} \tag{3.54}$$

where the photon wavefunctions are factorized. Using the straightforward Feynman rules for Majorana fermions [53], the above amplitudes are written, based on the effective

| $\lambda_1\lambda_2\,\lambda_3\lambda_4$ | $\hat{\mathcal{M}}^S$ | $\hat{\mathcal{M}}^P$ | $\hat{\mathcal{M}}^t$ | $\hat{\mathcal{M}}^u$ |
|---|---|---|---|---|
| $\pm\pm\,\pm\pm$ | $\mp\frac{m_\phi^2}{s-m_\phi^2}$ | $-\frac{m_\phi^2}{s-m_\phi^2}$ | | |
| $\pm\pm\,\mp\mp$ | $\pm\frac{m_\phi^2}{s-m_\phi^2}$ | $+\frac{m_\phi^2}{s-m_\phi^2}$ | $-\frac{m_{\tilde\gamma}^2}{t-m_{\tilde\gamma}^2}(1-\cos\theta)$ | $-\frac{m_{\tilde\gamma}^2}{u-m_{\tilde\gamma}^2}(1+\cos\theta)$ |
| $\pm\mp\,\pm\mp$ | | | | $\frac{m_{\tilde\gamma}\sqrt{s}}{(u-m_{\tilde\gamma}^2)}\frac{1}{2}(1+\cos\theta)\sin\theta$ |
| $\pm\mp\,\mp\pm$ | | | $-\frac{m_{\tilde\gamma}\sqrt{s}}{(t-m_{\tilde\gamma}^2)}\frac{1}{2}(1-\cos\theta)\sin\theta$ | |

Table 3.1: The reduced helicity amplitudes $\hat{\mathcal{M}}_{\lambda_1\lambda_2,\lambda_3\lambda_4}$ defined in (3.59) for $\gamma_{\lambda_1}\gamma_{\lambda_2}\to\tilde{G}_{\lambda_3}\tilde{G}_{\lambda_4}$.

Lagrangian in Section 3.2.2, as

$$i\mathcal{M}^{S,\mu\nu}_{\lambda_3\lambda_4}=-\frac{im_{\tilde\gamma}m_\phi^2}{F^2}\frac{1}{s-m_\phi^2}\,(p_1\cdot p_2\,g^{\mu\nu}-p_2^\mu p_1^\nu)\,\bar{u}(p_3,\lambda_3)v(p_4,\lambda_4), \tag{3.55}$$

$$i\mathcal{M}^{P,\mu\nu}_{\lambda_3\lambda_4}=-\frac{im_{\tilde\gamma}m_\phi^2}{F^2}\frac{1}{s-m_\phi^2}\,\epsilon^{\mu\nu\alpha\beta}\,p_{2\alpha}p_{1\beta}\,\bar{u}(p_3,\lambda_3)i\gamma^5v(p_4,\lambda_4), \tag{3.56}$$

$$i\mathcal{M}^{t,\mu\nu}_{\lambda_3\lambda_4}=-\frac{im_{\tilde\gamma}^2}{8F^2}\frac{1}{t-m_{\tilde\gamma}^2}\,\bar{u}(p_3,\lambda_3)[\gamma^\mu,\not{p}_1](\not{p}_1-\not{p}_3-m_{\tilde\gamma})[\not{p}_2,\gamma^\nu]v(p_4,\lambda_4), \tag{3.57}$$

$$i\mathcal{M}^{u,\mu\nu}_{\lambda_3\lambda_4}=\frac{im_{\tilde\gamma}^2}{8F^2}\frac{1}{u-m_{\tilde\gamma}^2}\,\bar{u}(p_3,\lambda_3)[\gamma^\mu,\not{p}_2](\not{p}_1-\not{p}_4+m_{\tilde\gamma})[\not{p}_1,\gamma^\nu]v(p_4,\lambda_4), \tag{3.58}$$

where a common sgoldstino mass is taken as $m_{S,P}=m_\phi$ and $F=\sqrt{3}\,\overline{M}_{\rm Pl}m_{3/2}$ is the SUSY breaking scale. The reduced helicity amplitudes $\hat{\mathcal{M}}$ are defined as

$$\mathcal{M}_{\lambda_1\lambda_2,\lambda_3\lambda_4}=\frac{m_{\tilde\gamma}s^{3/2}}{2(\sqrt{3}\,\overline{M}_{\rm Pl}m_{3/2})^2}\,\hat{\mathcal{M}}_{\lambda_1\lambda_2,\lambda_3\lambda_4}, \tag{3.59}$$

and presented in Table 3.1. The analytic expression for the total cross section can be found in [54], and our numerical results agree well with it.

It turns out that only the $u$-channel $\tilde\gamma$-exchange amplitude contributes to the helicity amplitude responsible for the leading energy growth discussed in the previous section,

$$\mathcal{M}^{\rm gold}_{1,-1,\frac{1}{2},-\frac{1}{2}}=\frac{m_{\tilde\gamma}^2s^2}{4(\sqrt{3}\,\overline{M}_{\rm Pl}m_{3/2})^2}\frac{1}{(u-m_{\tilde\gamma}^2)}(1+\cos\theta)\sin\theta, \tag{3.60}$$

where $u=-\frac{s}{2}(1+\cos\theta)$. To show agreement with (3.50), we take the limit $\sqrt{s}\gg m_{\tilde\gamma}$,

$$\mathcal{M}^{\rm gold}_{1,-1,\frac{1}{2},-\frac{1}{2}}\to-\frac{s}{6\overline{M}_{\rm Pl}^2}\sin\theta\frac{m_{\tilde\gamma}^2}{m_{3/2}^2}. \tag{3.61}$$

As expected, we reproduce only the term proportional to $\frac{1}{m_{3/2}^2}$. Since the second term in (3.50) is suppressed by $1/\overline{M}_{\rm Pl}^2$, the error is negligible for very light gravitino masses. Of course, the goldstino equivalence is independent of the limit $\sqrt{s}\gg m_{\tilde\gamma}$. In the limit

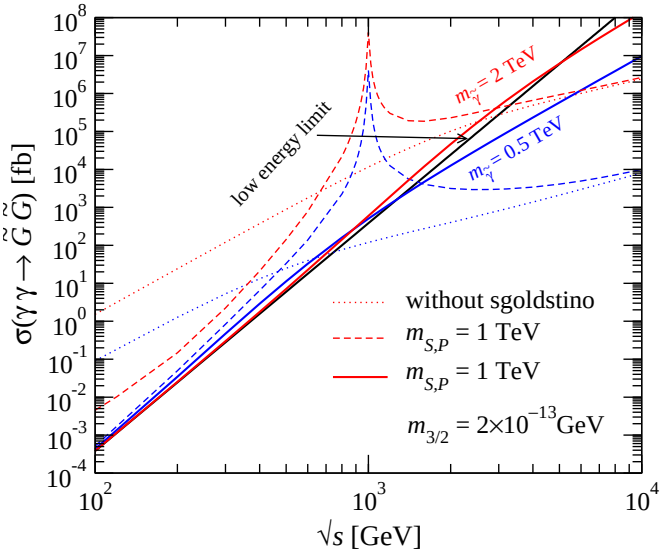


Figure 3.5: Total cross sections of $\gamma\gamma \to \tilde{G}\tilde{G}$ as a function of the collision energy for $m_{3/2} = 2 \times 10^{-13}$ GeV. The sgoldstino masses are taken to be 1 TeV (dashed) and 100 TeV (solid), while the photino mass is fixed at 0.5 TeV (blue) and 2 TeV (red). We also show the cross section in the low energy limit (black solid) as well as the contributions without the sgoldstino interactions (dotted).

$m_{\tilde{\gamma}} \gg \sqrt{s}$, the terms $\sim 1/m_{3/2}^2$ of the analytic result of (3.49) agree with the analytic result for $\mathcal{M}_{1,-1,\frac{1}{2},-\frac{1}{2}}$ in (3.59), as can be seen by expanding both amplitudes around $\sqrt{s}/m_{\tilde{\gamma}} \approx 0$. We have verified numerically that we obtain results similar to those of Figure 3.3 for the whole parameter space.

Finally, we want to present the dependence of the cross section of $\gamma\gamma \to \tilde{G}\tilde{G}$ on the center-of-mass energy and parameters of the theory; we especially focus on the role of the sgoldstino. Figure 3.5 shows the total cross sections as a function of the CM energy $\sqrt{s}$ for $m_{\tilde{\gamma}} = 0.5$ TeV (blue) and $m_{\tilde{\gamma}} = 2$ TeV (red) with $m_{3/2} = 2 \times 10^{-13}$ GeV. First, let us consider the heavy sgoldstino case, $m_\phi = 100$ TeV. In the low-energy limit, $\sqrt{s} \ll m_{\phi,\tilde{\gamma}}$, the total cross section is given by [54]

$$\sigma = \frac{s^3}{640\pi(\sqrt{3}\,\overline{M}_{\rm Pl} m_{3/2})^4}, \tag{3.62}$$

shown by a black-solid line in Fig 3.5. Due to a cancellation between the sgoldstino and photino amplitudes for $\lambda_1 = \lambda_2 = -\lambda_3 = -\lambda_4$ as can be seen in Table 3.1, the dominant contribution is given by the amplitudes for $\lambda_1 = -\lambda_2$, which are proportional to $s^2$ in the low-energy limit. To emphasize the importance of the interference, the contribution without the sgoldstino amplitudes is also shown by a dotted line in Fig. 3.5. On the other hand, in the case where the photino mass is smaller than the CM energy, $m_{\tilde{\gamma}} \ll \sqrt{s} \ll m_\phi$, the cross section is dominated by the sgoldstino contributions and deviates from the one in the low-energy limit.

We now turn to the case where the sgoldstinos are relatively light, $m_\phi = 1$ TeV. In our SUSY QED model, the partial decay width of the sgoldstinos are given by [55]

$$\Gamma(S, P \to \tilde{G}\tilde{G}) = \frac{m_\phi^5}{32\pi(\sqrt{3}\,\overline{M}_{\rm Pl} m_{3/2})^2}, \tag{3.63}$$

$$\Gamma(S, P \to \gamma\gamma) = \frac{m_{\tilde{\gamma}}^2 m_\phi^3}{32\pi(\sqrt{3}\,\overline{M}_{\rm Pl} m_{3/2})^2}. \tag{3.64}$$

For $m_\phi = 1$ TeV and $m_{3/2} = 2 \times 10^{-13}$ GeV (i.e. $\sqrt{F} \approx 918$ GeV), the width for a gravitino pair is 14.0 GeV and for a photon pair is 3.5 (55.9) GeV for $m_{\tilde{\gamma}} = 0.5$ (2) TeV. For the $m_{\tilde{\gamma}} = 2$ TeV case, the finite width effect can be seen as a deviation from the cross section (3.62) in the low-energy region in Fig. 3.5. For $\sqrt{s} \approx m_\phi$, one can clearly see the resonant peak. In the high-energy limit, $\sqrt{s} \gg m_{\phi,\tilde{\gamma}}$, the cross section approaches the value obtained by neglecting the sgoldstino amplitudes, since the $\lambda_1 = -\lambda_2$ amplitudes become dominant; see Table 3.1.

Finally, we note that collider signatures of sgoldstinos have been studied in [55–66], and our model can be also applied for such sgoldstino phenomenology.

# Part II

# Collider phenomenology

# CHAPTER 4

# Introduction to collider phenomenology

Collider phenomenology plays a crucial role in building a bridge between theoretical predictions and experimental observations. Our intention is to predict observable collider signatures of theoretical models describing the gravitino interactions, to interpret experimental data in terms of the model parameter space, and to guide experimental searches on where to look for signatures arising from light gravitinos.

We start this chapter by reviewing the relevant lepton and hadron colliders for this work. After introducing two main parameters describing the "performance" of a collider in Section 4.1.1, we discuss the benefits of lepton collisions in Section 4.1.2. We review the option of performing electron-photon collisions at $e^+e^-$ colliders, and introduce the photon luminosity function. We briefly outline the Large Electron Positron collider (LEP) that had operated at the CERN laboratory from 1989 until 2000 and present the planned International Linear Collider (ILC). Subsequently, in Section 4.1.3 some important differences of hadronic collisions with respect to leptonic collisions are pointed out before commenting on the proton-antiproton collider Tevatron, which had been running at the Fermi National Accelerator Laboratory in the United States from 1983 until 2012 as well as the Large Hadron Collider (LHC), which is the collider of our era. It is located at CERN and started operating in 2010. The relevant kinematical variables used in our collider studies are introduced in Section 4.1.4.

We would like to predict collider signatures expected from our theory. Starting from a Lagrangian, there is a full chain of simulation tools, that allows us to make predictions of the expected cross sections as well as kinematical distributions. We review the chain of simulation tools for collider phenomenology used throughout this work in Section 4.2.1. In hadronic collisions with a high center-of-mass energy, one has multiple parton final states, which are well described by a parton shower, introduced in Section 4.2.2. The result from the parton shower must be consistently combined with the result from the matrix element, in a procedure called "matrix element/parton shower merging", presented in Section 4.2.3.

## 4.1 Lepton and hadron colliders

### 4.1.1 Collider parameters

One of the parameters to characterize high-energy particle collisions is the center-of-mass (CM) energy $\sqrt{s}$, which is defined by

$$s = (p_1 + p_2)^2, \tag{4.1}$$

where $p_{1,2}$ denote the four-momenta of the two colliding particles. Another important parameter is the instantaneous luminosity $L$, which is a function of beam parameters, given by, see e.g. [7],

$$L = f \frac{n_1 n_2}{4\pi \sigma_x \sigma_y}, \tag{4.2}$$

where $n_{1,2}$ is the number of particles in a bunch, $f$ is the frequency of the collisions and $\sigma_{x,y}$ characterizes the beam size in the horizontal and vertical direction perpendicular to the beam pipe. The expected number of events $N$ and the total cross section $\sigma$ are related by[1]

$$N = \mathcal{L} \times \sigma(s), \tag{4.3}$$

where $\mathcal{L}$ is the integrated luminosity, $\mathcal{L} = \int dt\, L$.

### 4.1.2 Electron-positron colliders

Since electrons interact only through the electroweak force, one expects less backgrounds than in hadron collisions and no uncertainties related to the strong force, so that electron colliders are appropriate to perform precision measurements. Yet, because electron-positron colliders usually have a lower CM energy than proton colliders, they are less suited for discoveries.

At lepton colliders, the precise CM energy $\sqrt{s}$ is known, and one can tune the $\sqrt{s}$, which allows e.g. the scanning of threshold production.

Using polarized lepton beams can be helpful to increase or decrease the cross section for processes that have different couplings to left- and right handed particles. We will exploit this fact to reduce the SM background in our search for a new physics signal.

The largest $e^+e^-$ collider ever built was the Large Electron Positron collider (LEP) [67] at the European Organization for Nuclear research (CERN) near Geneva. LEP was a circular collider with a circumference of about 27 km, and it had been running from 1989 until 2000 with CM energies between $\sqrt{s} = 91$ and 209 GeV, and with a luminosity between $L \approx 10^{30}$ and $10^{32}$ cm$^{-2}s^{-1}$. The four LEP experiments were ALEPH, DELPHI, L3 and OPAL. Amongst others, LEP provided precision measurements of the $W$ and $Z$ masses and widths [68, 69], and measured the running of the strong coupling $\alpha_s$ [70].

The International Linear Collider (ILC) [71] is a linear $e^+e^-$ collider, foreseen to be built in Japan in the near future. It has a length of about 31 km, see Fig. 4.1 and is designed to start with a CM energy of $\sqrt{s} = 250$ GeV, which can be increased to $\sqrt{s} = 500$ GeV and, after an upgrade, up to $\sqrt{s} = 1$ TeV. The designed luminosity is $L \approx 10^{34}$ cm$^{-2}s^{-1}$. The main purpose of the ILC is to perform precision measurements in order to probe the identity of the $H$ boson, and continue the search for new physics.

At the ILC, there exists an option to perform $e^-\gamma$ or $\gamma\gamma$ collisions. A high-energy photon beam is provided by the backward Compton scattering of laser photons on a high-energy electron beam [73, 74]; see Fig. 4.2. The probability to find a photon with a specific energy fraction $x = E_\gamma/E_e$ of the incident electron beam is given by the

[1] In practice, we have to take into account also the detector acceptance and the efficiency of event selection in the derivation of expected number of events.

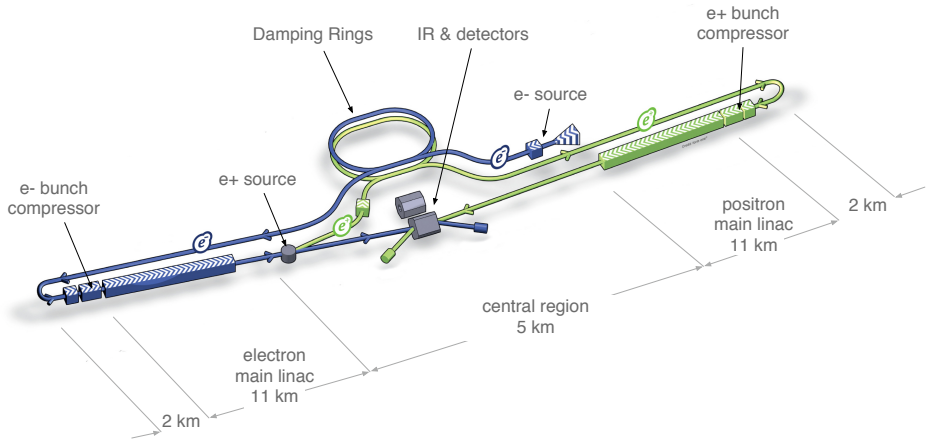


Figure 4.1: The schematic layout of the ILC, taken from [72].

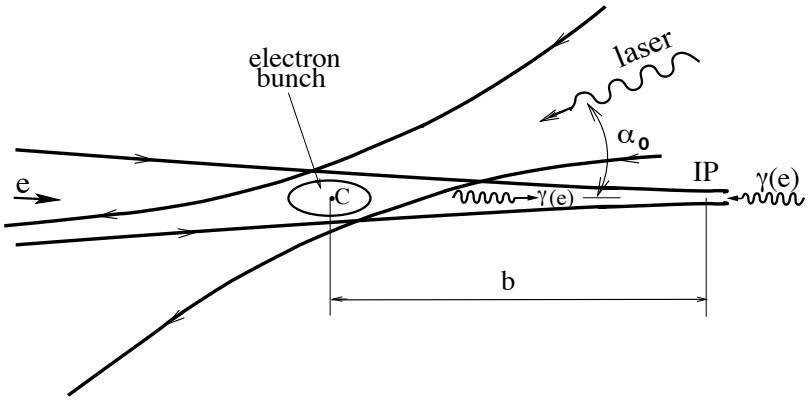


Figure 4.2: A schematic representation of producing a photon by backward compton scattering; figure taken from [72].

photon luminosity function [72, 73]

$$f_\gamma(x,y) = \frac{1}{N(y)}\Big[\frac{1}{1-x} + 1 - x - 4r(1-r) + P_e P_l\, ry(1-2r)(2-x)\Big], \tag{4.4}$$

where $y$ is a parameter controlled by the laser energy,[2] $r = x/(1-x)y$, and $P_e$ ($P_l$) is the incident electron beam (laser photon) polarization. The integral $\int f_\gamma(x,y)\,dx$ is normalized to unity by

$$N(y) = \Big(1 - \frac{4}{y} - \frac{8}{y^2}\Big)\ln(1+y) + \frac{1}{2} + \frac{8}{y} - \frac{1}{2(1+y)^2} + P_e P_l\Big[\Big(1+\frac{2}{y}\Big)\ln(1+y) - \frac{5}{2} + \frac{1}{1+y} - \frac{1}{2(1+y)^2}\Big]. \tag{4.5}$$

[2] $y = 4E_e E_l/m_e^2$ in the zero angle limit of the Compton scattering.

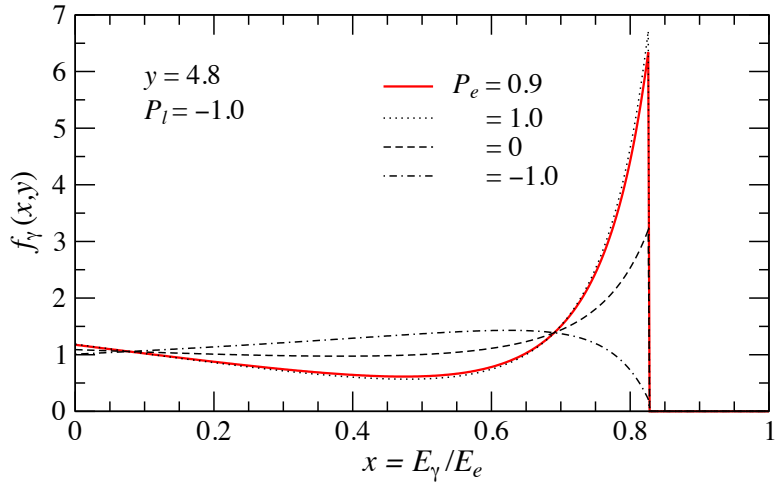


Figure 4.3: The distribution functions of Compton back-scattered photons in (4.4) for different electron beam polarizations.

Figure 4.3 shows the luminosity function for different electron beam polarizations, with $y = 4.8$ and $P_l = -1.0$ as an optimal parameter choice [72]. The maximal energy fraction is fixed by $x_{\max} = y/(1+y)$, e.g. $x_{\max} \sim 0.83$ for $y = 4.8$. The distribution with highly polarized electron and laser beams ($P_e P_l \sim -1$) has a strong peak at the high-energy endpoint. We make use of this formulae in Chapter 4.

### 4.1.3 Hadron colliders

A main difference in hadron collisions compared to lepton collisions lies in the composite nature of the hadrons. The hard scattering does not occur among two hadrons, but among their constituent quarks or gluons. We now present the "master formula" for proton - proton ($p$-$p$) collisions, which relates the partonic cross section to the $pp$ cross section. Assume two protons to collide and produce a final state $X$. The two partons $i, j$ involved in the hard scattering process carry a momentum fraction $x_1, x_2$ of the incident proton momenta. Thanks to the QCD factorization theorem, the cross section of a hard proton-proton collision can approximately be written as, see e.g. [75]

$$\sigma_{pp\to X} = \sum_{i,j} \int dx_1 dx_2 \, f_{1,i}(x_1, \mu_F) f_{2,j}(x_2, \mu_F) \, \sigma_{i,j\to X}(x_1, x_2, \mu_F), \tag{4.6}$$

where the sum runs over all possible partons that can produce the final state. The factorization scale $\mu_F$ is indicating the separation between perturbative and non-perturbative dynamics, and usually set by the typical energy scale of the process. The partonic cross section $\sigma_{i,j\to X}$ can be calculated perturbatively, while the parton distribution functions (PDFs) $f_{1,i}, f_{2,j}$ parametrize the non-perturbative aspects of the collision. They give the probability for a parton to have momentum fraction $x$, and they are process-independent and measured in experiment. As example, we present the CTEQ6M PDFs

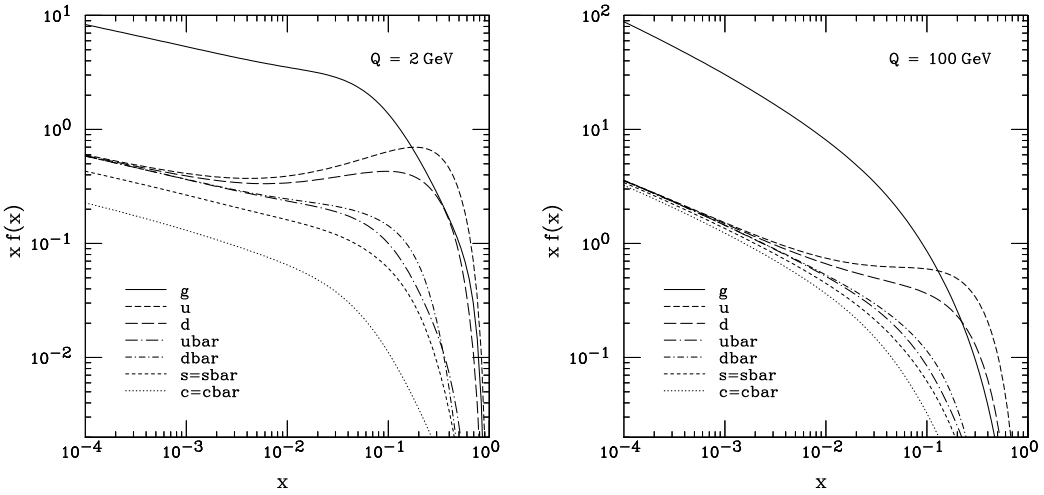


Figure 4.4: The CTEQ6M PDFs for two energy scales, $Q = 2$ and 100 GeV, extracted from [76].

for two different energy scales $\mu_F = Q = 2$ and 10 GeV in Fig. 4.4.

Due to less synchrotron radiation, hadrons can be accelerated to high energies more easily than leptons. Therefore, hadron colliders are well-suited to perform discoveries. Unfortunately, we have to deal with high QCD backgrounds in hadron collisions due to the compositness of the protons and because partons are strongly interacting particles. In strong interactions, the radiative corrections can be considerable, and higher order corrections must be taken into account in order to obtain precise theoretical predictions for cross sections as well as kinematic distributions.

The Tevatron [77] was a circular proton-antiproton collider with a circumference of about 6 km at the Fermi National Accelerator Laboratory (Fermilab) in Batavia in the United States. It had been running from 1988 until 1996 with a CM energy of $\sqrt{s} = 1.8$ TeV and a maximal luminosity of $L \approx 10^{31}$ cm$^{-2}s^{-1}$, and after an upgrade, from 2001 until 2011 with CM energy $\sqrt{s} = 1.96$ TeV and a maximal luminosity $L \approx 10^{32}$ cm$^{-2}s^{-1}$. The two general purpose detectors were CDF and D0. At Tevatron, the top quark was discovered in 1995 [78, 79]. Due to low statistics, the discovery of the $H$ boson could not be established; in the combined results of CDF and D0 an excess of about $3\sigma$ was observed over the expected background [80].

The Large Hadron Collider (LHC) [81] is a proton-proton collider hosted at CERN in the former LEP tunnel.[3] The LHC started its run in 2010 with a CM energy $\sqrt{s} = 7$ TeV and a maximal luminosity of $L = 3.7 \times 10^{33}$ cm$^{-2}s^{-1}$. In 2012, it ran with CM energy $\sqrt{s} = 8$ TeV and a maximal luminosity of $L = 7.7 \times 10^{33}$ cm$^{-2}s^{-1}$ [82]. The LHC is currently shut down and being upgraded to a CM energy of $\sqrt{s} = 13$ TeV and will start again in 2015.

[3] A part of the run-time, it collides lead nuclei.

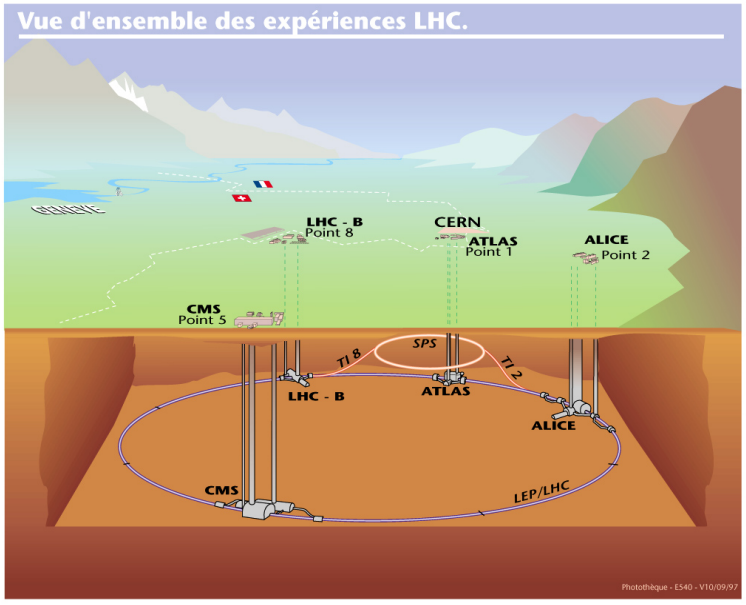


Figure 4.5: A schematic presentation of the LHC beam pipe and the main experiments; the picture belongs to CERN [85].

There are four main experiments at the LHC, the two general purpose experiments ATLAS [83] and CMS [84], and two specialized experiments LHCb and ALICE designed to study physics related to $b$ quarks and to study quark-gluon plasma, respectively. The LHC beams and the location of the experiments are schematically presented in Fig. 4.5. The most important result of the LHC was the discovery of a new boson [1,2] with a mass around $m = 126$ GeV, which behaves so far very much like the SM $H$ boson [3,4].

### 4.1.4 Kinematical variables

We briefly introduce the kinematical variables that will be used throughout the next chapters. The transverse momentum is defined as

$$p_T = \sqrt{p_x^2 + p_y^2} = |\vec{p}| \sin\theta, \tag{4.7}$$

where $\theta$ is the angle between the beam axis and the particle in the final state. The rapidity $y$ is given by

$$y = \frac{1}{2} \ln \frac{E + p_z}{E - p_z}, \tag{4.8}$$

which becomes for massless particles or in the limit $E \gg m$ equal to the pseudorapidity *eta*,

$$\eta = \frac{1}{2} \ln \frac{1 + \cos\theta}{1 - \cos\theta} = -\ln \tan \frac{\theta}{2}. \tag{4.9}$$

The missing energy is the absolute value of the vectorial sum over the transverse momenta of all invisible particles,

$$\not{E}_T = \left| \sum \vec{p}_{T,miss} \right|. \tag{4.10}$$

Since the sum over final state (transverse) momenta is zero, the sum over the $p_T$ of all invisible final state particles is defined as the sum over the $p_T$ over all visible final state particles with a negative sign,

$$\sum \vec{p}_{T,miss} = -\sum \vec{p}_{T,vis}. \tag{4.11}$$

Another quantity that we use is $H_T$, which is the scalar sum over all visible transverse momenta,

$$H_T = \sum |\vec{p}_{T,vis}|. \tag{4.12}$$

## 4.2 Simulations of collision events

The goal of this work is to perform phenomenological studies of a beyond SM (BSM) physics theory, in particular a SUSY theory including the gravitino. We would like to understand a possible collider signature of a given process in terms of the parameters of the theory and investigate the possibility to distinguish our signal from the SM background.

### 4.2.1 Simulation tools for collider phenomenology

To compare an expected signal of our BSM theory with data, it takes several steps:

1. Write down the Lagrangian describing a theory and derive the Feynman rules.
2. Draw the Feynman diagrams for a given process.

   Write down the corresponding amplitudes.

   Calculate the cross section and generate events at parton level.
3. If strongly interacting particles are involved, to obtain the event at hadron level simulate parton shower and hadronization effects.
4. Simulate the detector response to have the reconstructed event.
5. Analyse the event by looking at distributions, applying cuts etc.

We have a complete chain of tools facilitating this procedure, schematically presented in Fig. 4.6 and which is summarized in the following. For details, we refer to the manuals of the specific programs.

We start by providing the Lagrangian as well as a model file containing the particle content and parameters to the FeynRules package [29,86]. FeynRules is a Mathematica based program that automatically extracts the Feynman rules associated with

Lagrangian $\mathcal{L} = \bar{\psi} i \not{D} \psi$

**FeynRules**

Feynman rules $-ig\gamma^\mu$

UFO model: vertices.py, parameters.py, ...

Process $pp \to j\nu\bar{\nu}$

**MadGraph**

Feynman diagrams

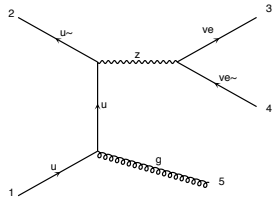


Helicity amplitudes $i\mathcal{M} \sim \bar{v}(p_2, \lambda_2)\gamma^\nu(\not{p}_1 - \not{p}_5)\gamma^\mu u(p_1, \lambda_1) \cdots$

Events at the parton level

```
 2  -1   0   0  502   0   0.00000000000E+00  0.00000000000E+00
-2  -1   0   0   0  501   0.00000000000E+00  0.00000000000E+00
23   2   1   2   0   0  -0.10517156134E+03 -0.10962553294E+02 ...
14   1   3   3   0   0  -0.12058574507E+03 -0.12149486638E+02
-14  1   3   3   0   0   0.15414183729E+02  0.11869333442E+01
21   1   1   2 502 501  0.10517156134E+03  0.10962553294E+02
```

Parton-level event file: unweighted_events.lhe

**Pythia**

Parton shower, hadronization

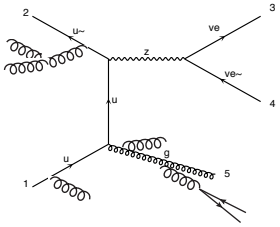


Hadron-level event file: pythia_events.hep

**Delphes**

Detector response, jet clustering

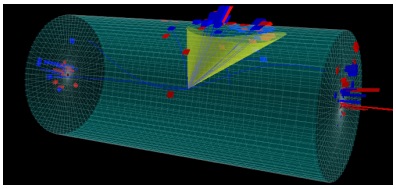

Reconstructed-level event file: delphes_events.lhco

**MadAnalysis**

Selection cuts, analysis

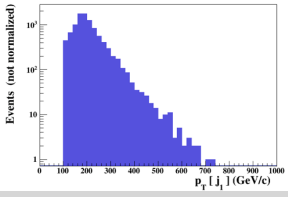


Figure 4.6: Schematic representation of the procedure followed in a phenomenological study. The simulation tools we employ are also shown on the left, and the output/input files are displayed in blue. For details, see text.

the Lagrangian, and stores them together with the other model information in a UNIVERSAL FEYNRULES OUTPUT (UFO) [87] model file. The UFO model is passed to MADGRAPH 5 [14,88–92] or other matrix-element generators such as CALCHEP [93–96], SHERPA [97,98] or WHIZARD [99,100]. We restrict the description to MADGRAPH since this is the event generator we use. All of the following programs are interfaced to MADGRAPH and can be run within the MADGRAPH environment.

Inside MADGRAPH, we specify our process of interest in terms of the initial and final state particles. MADGRAPH generates the Feynman diagrams and the corresponding helicity amplitudes for this process and provides the code needed to evaluate the matrix elements at a specific phase space point. This code is used by the Monte Carlo event generator MADEVENT [89] to calculate the cross section and to produce unweighted events, that means, events as distributed in nature.[4] The information of the events, that is the masses and momenta as well as the spin, color connection and flavor of the final state particles is stored in an "event file" in the Les Houches format [102]. Another option in MADGRAPH is to output a *standalone* version of the matrix element evaluation. In the standalone version, we can evaluate the helicity amplitudes on a specific phase-space point. This option is especially useful for the validation of a model.

When we generate hard scattering events, we must correctly take into account extra initial and final state radiations for a QCD process. Those radiations have soft and collinear singularities and are well described by a parton shower such as PYTHIA [103, 104], SHERPA [97, 98], or HERWIG [105, 106], which simulate successive splittings between the (hard) scale of the scattering until the hadronization scale, which is the scale that separates the perturbative from the non-perturbative regime. For a brief description of a parton shower, see the next section. In the final state, we do not observe partons but hadrons. The transition from partons to hadrons is described by non-perturbative models such as the string model [107,108] implemented in PYTHIA or the cluster model [109]. We use PYTHIA for hadronization of the final state partons.

After hadronization, we perform a simulation of the detector response of the final state particles by using DELPHES [110,111].[5] Inside DELPHES, the hadrons are clustered into jets; DELPHES uses FASTJET [113] for the jet clustering.[6]

The final event file can then be further analyzed with MADANALYSIS [115, 116], for example to apply selection cuts and to investigate kinematical distributions.

### 4.2.2 Parton shower

In a hard QCD scattering process with a high energy scale, the probability for extra emissions is high, leading to a final state with many partons. However, the computa-

[4] The evaluation of the matrix elements is carried out by successive calls to the Helicity Amplitude Subroutines (HELAS) library [15]. In MADGRAPH 5, this library is automatically written by ALOHA (Automatic Libraries of Helicity amplitudes) [101] after having specified our process of interest. ALOHA produces a helicity wavefunction for each external leg in a Feynman diagram, and subsequently combines the wavefunctions into vertices, and the vertices into Feynman diagrams. By calling the HELAS subroutine, the value of the matrix element (amplitude squared) is returned.

[5] Another detector simulation tool implemented into MADGRAPH is PGS [112].

[6] For a very nice review about different jet clustering algorithms, see [114].

tional effort for a matrix element with numerous final states is very expensive, which makes the matrix element less suited to describe a high-multiplicity final state. Further on, the matrix element diverges for soft (low-energetic) and collinear (parallel) emissions of extra partons, as we will see now. These multiple soft and collinear emissions are described with a parton shower.

Assume a hard scattering process with $n$ final state particles, and the final state parton $a$ to split into two partons $b$ and $c$.[7] In the collinear limit, when the angle between the final state partons goes to zero, $\theta \to 0$, the matrix element factorizes as [117]

$$|\mathcal{M}_{n+1}|^2 d\Phi_{n+1} \simeq |\mathcal{M}_n|^2 d\Phi_n dp(t), \tag{4.13}$$

where the differential probability for emission between the energy scale $t$ and $t + dt$ is given by

$$dp(t) = \frac{\alpha_s}{2\pi}\frac{dt}{t} dz P_{a\to bc}(z). \tag{4.14}$$

Here, $t$ is usually the virtuality of the splitting parton, $t = (p_b + p_c)^2 \sim z(1-z)E^2\theta^2$; it tends to zero in the collinear limit. $z$ is the energy fraction of parton $b$ from parton $a$, and $P_{a\to bc}(z)$ is the Altarelli-Parisi splitting function [118] describing the radiation of an extra parton or splitting into two partons in the collinear limit.

When integrating over the full phase space, $dp(t)$ will diverge. However, the probability for an extra emission should be finite. This can be understood as follows. If the extra emission is below a certain scale, we can not resolve the two final state partons (after splitting or radiation) from one single final state parton. It is in this phase space region where the probability diverges, such that the probability for having no resolvable emission tends to infinity. However, we have to take into account also contributions from virtual corrections to our process, which are also divergent. The KLN theorem [119, 120] states that the divergent piece from the unresolvable emission of final state collinear splittings and soft emissions cancels against the divergence from the virtual correction. Together, the sum of the unresolvable emission and the virtual correction are finite.

The so-called *Sudakov form factor* sums the virtual corrections and real emissions to all orders. It gives the probability that a particle evolves between two scales $Q^2$ and $t$ without any resolvable emission,

$$\Delta(Q^2, t) = \exp\left[ -\int_t^{Q^2} dp(t') \right], \tag{4.15}$$

where $dp(t)$ is given by (4.14). This Sudakov form factor is used by a parton shower to generate successive branchings of final state partons. The parton shower program determines the scale $t_1$ of the first branching by throwing a random number $0 < r < 1$,

[7] We restrict the discussion to final state radiation; a similar procedure is applied for extra emissions from initial state particles.

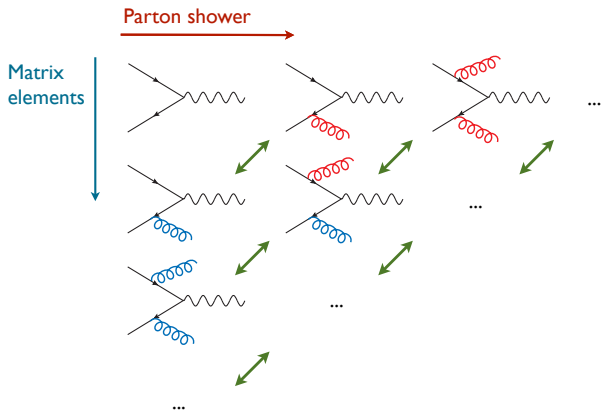


Figure 4.7: Extra emissions generated by matrix element and by parton shower. The arrows indicate possible double counting.

and solving the equation $r = \Delta(Q^2, t_1)$ for $t_1$. If $t_1$ is bigger than the hadronization scale $Q_0^2$ , a branching is generated, and a new random number is thrown; if $t_1 < Q_0^2$, the parton shower stops.

### 4.2.3 Parton shower/matrix element merging

We found that the matrix element (ME) is well suited to describe hard and well-separated emissions, while the parton shower (PS) is used to describe soft and collinear emissions. To get a correct description of a final state involving multiple jets one must combine the ME approach and the PS. This is done in a consistent way in a procedure called *parton shower/matrix element merging*. Consistent means that we must avoid the double counting of certain events, schematically presented in Fig. 4.7. Starting e.g. from the process $q\bar{q} \to Z$, we generate additional $1, 2, ..$ emissions with the ME. We then pass the event file to the PS generator, which generates additional emissions. The arrows indicate possible double counting. The double counting can be avoided by restricting the ME and the PS to different regions in phase space, characterizing the hardness of the extra emission. Further on, we must ensure smooth transitions for observables when changing from one approach to the other. This can be checked by means of the stability of the total cross section and distributions.

Several multi-jet merging algorithms have been proposed: the CKKW-based method [121, 122], the MLM scheme [123, 124], the pseudo-shower algorithm [125], and the shower-$k_T$ scheme [126].

In our analysis we make use of the shower-$k_T$ scheme, which is based on event rejection, as implemented in MadGraph for fixed-order ME generation and interfaced to Pythia6.4 for PS and hadronization. In this scheme, ME multi-parton events are generated with a minimum separation, $Q_{\rm cut}$ and $p_{T_{\rm min}}$, between final-state partons $(ij)$ and between final- and initial-state partons $(iB)$ characterized by the $k_T$ jet measure:

$$d_{ij}^2 = \min(p_{T_i}^2, p_{T_j}^2)\, \Delta R_{ij}^2 > Q_{\rm cut}^2, \quad d_{iB}^2 = p_{T_i}^2 > p_{T_{\rm min}}^2, \tag{4.16}$$

with $\Delta R_{ij}^2 = 2[\cosh(\eta_i - \eta_j) - \cos(\phi_i - \phi_j)]$, where $p_{T_i}$, $\eta_i$ and $\phi_i$ are the transverse momentum, pseudorapidity and azimuth of particle $i$ [127]. The renormalization scale for $\alpha_s$ for each QCD emission vertex is set to the $k_T$ value, while the factorization scale for the parton densities and the renormalization scale for the hard 2→2 process is given by the transverse mass of the particles produced in the central process. The ME-level events are then passed to PYTHIA and showered using the $p_T$-ordered shower, and PYTHIA reports the scale $Q^{\mathrm{PS}}_{\mathrm{hardest}}$ of the hardest emission in the shower. For lower parton-multiplicity samples an event is rejected if $Q^{\mathrm{PS}}_{\mathrm{hardest}} > Q_{\mathrm{cut}}$, while for the highest multiplicity sample an event is rejected if $Q^{\mathrm{PS}}_{\mathrm{hardest}} > Q^{\mathrm{ME}}_{\mathrm{softest}}$, the scale of the softest ME parton in the event. See more details in [126].

# CHAPTER 5

# Light gravitinos at colliders

This chapter gives an overview of light gravitino production at colliders. Section 5.1 shows that there are three different production mechanisms for gravitinos at colliders, and two of them are sensitive to the gravitino mass. We find that direct gravitino production at colliders becomes relevant for very light gravitinos. We comment on previous studies of gravitino production mechanism and briefly summarize the studies we will present in the next chapters.

Experimental bounds on the gravitino mass are summarized in Section 5.2. While we pay special attention to the results from searches for gravitinos at colliders, we also briefly review bounds on light gravitino dark matter from cosmology, and comment on bounds from stellar evolution.

In Section 5.3, we introduce two possible theoretical models that suggest a gravitino light enough for direct production to become relevant at colliders.

Finally, we shortly describe tools specialised to simulate gravitino production at colliders in Section 5.4.

## 5.1 Production mechanisms for light gravitinos

In the following, we consider $R$-parity conserving scenarios, and assume that the gravitino is the lightest SUSY particle (LSP); it is stable and escapes detectors. There are three production mechanisms at colliders for light gravitinos:

1. *Pair production:* A pair of gravitinos can be produced directly, such as $e^+e^- \to \tilde{G}\tilde{G}$ and $pp \to \tilde{G}\tilde{G}$. The cross section for gravitino pair production is extremely sensitive to the gravitino mass since it scales inversely proportional to the gravitino mass to the fourth,

$$\sigma_{\text{pair}} \propto \frac{1}{m_{3/2}^4}. \tag{5.1}$$

   The derivation and explicit formulae for specific processes will be presented in the next chapters.

2. *Associated production:* A gravitino can be directly produced in association with another SUSY particle, e.g. $e^+e^- \to \tilde{\chi}_1^0\tilde{G}$, $e\gamma \to \tilde{e}\tilde{G}$ and $pp \to \tilde{g}\tilde{G}, \tilde{q}\tilde{G}$. The cross section is inversely proportional to the square of the gravitino mass

$$\sigma_{\text{associated}} \propto \frac{1}{m_{3/2}^2}, \tag{5.2}$$

   which is less sensitive to the gravitino mass than gravitino pair production. Again, we will derive and present the explicit formulae in the next chapters.

3. *Indirect production*: A gravitino can appear at the end of a decay chain, i.e. through decays of the next-to-lightest SUSY particle (NLSP). In this case, the production rate of gravitinos is independent of the gravitino mass.[1]

[1] For a very light gravitino, $t/u$-channel exchanged gravitinos can enhance usual SUSY particle pair

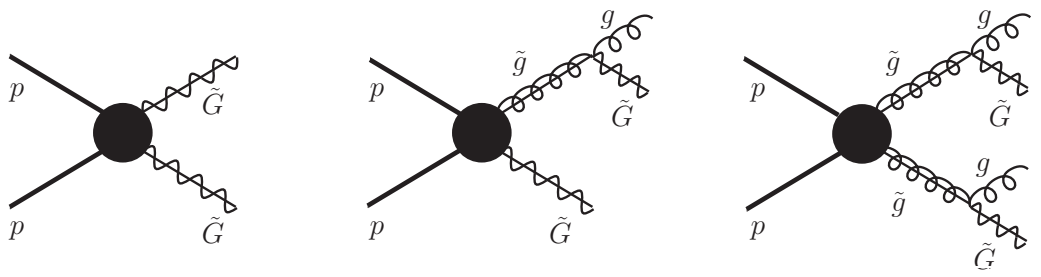


Figure 5.1: Examples of three possible mechanisms for LSP gravitino production at the LHC, for a gluino NLSP which promptly decays into a gravitino and a gluon; pair production (left), associated production with a gluino (middle) and indirect production (right).

The signature arising from processes with LSP gravitinos is missing energy ($\not{E}$) plus $X$, where the $\not{E}$ is carried away by two gravitinos and $X$ depends on the production mechanism. For illustration, in Fig. 5.1 we show three production mechanisms and resulting signatures at $pp$ colliders for a gluino NLSP, which is assumed to promptly decay into a gluon and a gravitino.

Since the gravitinos escape detection, gravitino pair production becomes observable with some extra radiations, e.g. a photon and a gluon or quark, leading to a mono-photon+$\not{E}$ and mono-jet+$\not{E}$ signal, respectively.

Associated production gives rise to a signal through the decay of the associated SUSY particle. For instance, $e^+e^- \to \tilde{\chi}_1^0\tilde{G} \to \tilde{G}\tilde{G}\gamma$, $e\gamma \to \tilde{e}\tilde{G} \to \tilde{G}\tilde{G}e$ and $pp \to \tilde{g}(\tilde{q})\tilde{G} \to \tilde{G}\tilde{G}g(q)$ give rise to a mono-photon+$\not{E}$, mono-electron+$\not{E}$ or mono-jet+$\not{E}$ signal, respectively.

Indirect production with the subsequent decay gives rise to the signal again through the decay of the SUSY particle, e.g. $pp \to \tilde{g}\tilde{g} \to \tilde{G}\tilde{G}gg$ results in a di-jet+$\not{E}$ signal.

To summarize, there are two production mechanisms for very light gravitinos at colliders that are sensitive to the gravitino mass, pair production and associated production, where the former is observable at colliders with additional radiations. Both processes become significant at colliders when the mass of the gravitino is very light as

$$m_{3/2} \sim \mathcal{O}(10^{-14} - 10^{-12}\ \text{GeV}), \tag{5.3}$$

since the interactions are always suppressed by the Planck scale.

We note that the cross sections of the two production mechanisms that are sensitive to the gravitino mass behave differently with respect to the mass of other SUSY particles. We will find that the cross section for the gravitino pair production increases with increasing mass of the $t$-channel exchanged SUSY particle until some limit. On the other hand, the cross section for associated gravitino production with a SUSY particle decreases with increasing mass of the associated particle, due to the phase space closure.

production, e.g. gluino pair production; see more details in Section 8.1.2.

Before turning to the experimental bounds on the gravitino mass, we briefly summarize the previous theoretical studies on gravitino production relevant for the rest of this work, and comment on the contributions to light gravitino phenomenology which have been performed throughout this work.

The $\tilde{G}\tilde{G}(+\gamma)$ and $\tilde{G}\tilde{G}(+\text{jet})$ production has been investigated only in models where all SUSY particles except for the gravitino are assumed to be very heavy [128–130].

Several studies on the associated gravitino productions have been performed so far. For instance, $\tilde{\chi}_1^0$-$\tilde{G}$ productions at $e^+e^-$ colliders [131–135] and hadron colliders [134], $\tilde{e}$-$\tilde{G}$ productions in $e\gamma$ collisions [136], and $\tilde{g}$-$\tilde{G}$ [137–141] and $\tilde{q}$-$\tilde{G}$ [140,141] productions at hadron colliders.

The impact of light gravitinos on the signature expected in $\tilde{g}\tilde{g}$ production has been studied in [137–140]. We note that for QCD processes with a large CM energy, the probability for extra QCD emission becomes large. For a realistic study of e.g. $pp \to \tilde{g}\tilde{G}$ associated production, the extra radiation has to be taken into account. This has not been done in the above studies. Further on, if the extra emission happens to be hard, the $\tilde{g}\tilde{G}$ production process might give the same final state as the $\tilde{g}\tilde{g}$ production process.

In this work, we revisit the mono-photon+$\not{E}$ signal arising from gravitino production at $e^+e^-$ colliders. We simultaneously study the two contributing sub-processes, $\tilde{G}\tilde{G}$ production and $\tilde{\chi}_1^0\tilde{G}$ associated production. We explicitly give the helicity amplitudes for both two-to-two production processes and present cross sections with different mass spectra and different energies especially for a future linear collider. We examine selection efficiencies by kinematical cuts and beam polarizations for the signal and SM background processes, and investigate the energy and angular distributions of the photon. We show how to extract information on SUSY particle masses.

We also consider gravitino production in association with a selectron which subsequently decays into an electron and a gravitino in $e^-\gamma$ collisions. We present the explicit helicity amplitudes for the production process, and discuss the mono-electron plus missing-energy signal, including the Compton back-scattered photon energy spectrum for incident photons. While the heavy-mass limit for all SUSY particles except gravitino and selectron are assumed in Ref. [136], we take into account the $t$-channel intermediate neutralinos and show a possibility to determine their mass in the signal distributions.

For the LHC, we study the jets+$\not{E}$ signature for the case where the gluino is assumed to be the NLSP. We consider both the associated gravitino production with a gluino and gluino pair production. By merging matrix elements with parton showers, we generate inclusive signal and background samples and show how information on the gluino and gravitino mass can be obtained by simple final state observables.

Finally, we investigate the mono-photon+$\not{E}$ signal at the LHC arising from gravitino pair production. We re-interpret an existing search, and derive a lower bound on the gravitino mass.

## 5.2 Experimental bounds on the gravitino mass

We present a short review about the experimental bounds on the gravitino mass. Special attention is paid to the bounds from collider searches. The current interpretations of mono-photon+$\not{E}$ or mono-jet+$\not{E}$ signatures in terms of gravitino production rely either on gravitino-pair production, or on associated gravitino production. In the last part of this section, we briefly review the bounds from cosmology on light gravitino dark matter and the bounds obtained from stellar evolution. We note that the gravitino mass bound is commonly translated to a bound on the SUSY breaking scale by the relation derived in Section 3.3.2, $F = \sqrt{3}\,\overline{M}_{\rm Pl} m_{3/2}$.

### 5.2.1 Bounds from direct gravitino pair production

Both the mono-photon+$\not{E}$ and mono-jet+$\not{E}$ signals have been interpreted in terms of direct gravitino pair production, where all other SUSY particles are assumed to be very heavy [130].

In the search for mono-photon+$\not{E}$, the four collaborations at the LEP, OPAL, ALEPH, L3 and DELPHI, independently put lower bounds on the gravitino mass [142–145], and those are summarized in [146] as

$$m_{3/2} \geq 1.37 \times 10^{-14}\ \text{GeV}. \tag{5.4}$$

The CDF collaboration at the Tevatron put a similar bound of [147]

$$m_{3/2} \geq 1.17 \times 10^{-14}\ \text{GeV}. \tag{5.5}$$

For the jet+$\not{E}$ channel, CDF gives the lower bound of [148]

$$m_{3/2} \geq 1.1 \times 10^{-14}\ \text{GeV}. \tag{5.6}$$

We emphasize that allowing the other SUSY masses to be light would modify the bound on the gravitino mass in these searches.

### 5.2.2 Bounds from associated gravitino production

The mono-photon+$\not{E}$ and mono-jet+$\not{E}$ signal have also been interpreted in terms of $\tilde{\chi}_1^0$-$\tilde{G}$ associated production and $\tilde{g}$-$\tilde{G}$ or $\tilde{q}$-$\tilde{G}$ associated production, respectively. The LEP experiment provides the bound on the gravitino mass as a function of the neutralino and selectron masses [145], see Fig. 5.2. We find e.g.

$$m_{3/2} \geq 10^{-14}\ \text{GeV} \tag{5.7}$$

for $m_{\tilde{\chi}_1^0} = 140$ GeV and $m_{\tilde{e}} = 150$ GeV. As described above, for a heavy neutralino, the cross section of this production process decreases, which explains why the bounds on the gravitino mass become weaker and finally vanish around 200 GeV, which is the maximum CM energy of the LEP.

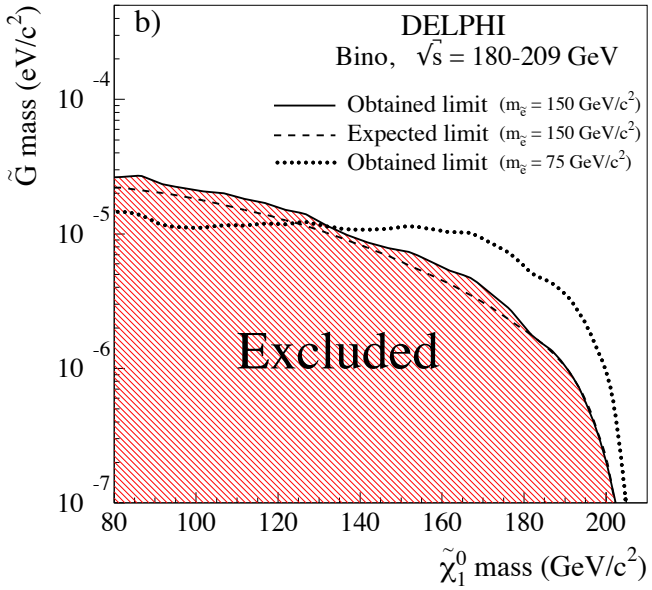


Figure 5.2: The exclusion plot in the $m_{\tilde{\chi}_1^0}-m_{\tilde{G}}$ plane, obtained from the interpretation of the mono-photon plus missing energy signal in terms of neutralino-gravitino associated production by the DELPHI collaboration. The plot is extracted from [145].

The mono-jet+$\not{E}$ signal at the LHC is interpreted by ATLAS in terms of $\tilde{g}\tilde{G}$ and $\tilde{q}\tilde{G}$ associated production, using data from the 2012 run at a CM energy $\sqrt{s} = 8$ TeV which corresponds to an integrated luminosity of $\mathcal{L} = 10.5$ fb$^{-1}$ [149]. They translated the agreement between the observed number of events and the expected number of events from the SM into a 95 % confidence level (CL) upper limit on the visible cross section which is defined by production cross section times acceptance times efficiency, ($\sigma \times A \times \varepsilon$). A new physics contribution with a cross section above $\sigma \times A \times \varepsilon = 0.05$ pb is excluded at 95 % CL for the selection cuts specified in [149]. Figure 5.3 shows the interpretation of this upper bound on the cross section in terms of gravitino production in association with a gluino or squark, as a function of the gluino/squark masses. Degenerate squark and gluino masses are assumed. The blue lines are the theoretical predictions for the cross section of gravitino associated production for different gravitino masses. A lower bound of

$$m_{3/2} \geq 2 \times 10^{-13} \text{ GeV} \tag{5.8}$$

is found for gluino or a squark masses around 500 GeV. This result provides the currently strongest bounds on the gravitino mass from collider searches, and corresponds to a lower bound on the SUSY breaking scale of about $\sqrt{F} \approx 918$ GeV. In the high gluino/squark mass region, the limits on the gravitino mass become very weak due to phase space closure.

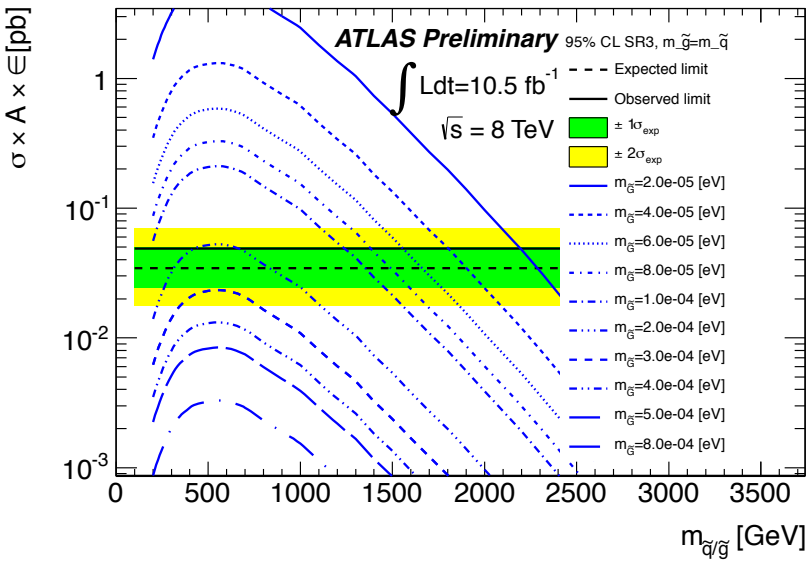


Figure 5.3: The interpretation of the mono-jet plus missing energy signal in terms of gravitino production in association with a squark or gluino by ATLAS [149]. It is shown the 95 % CL upper limit on the visible cross section as a function of the squark/gluino mass, which are assumed to be degenerate. The blue lines are the theoretical predictions for cross section for different gravitino masses.

### 5.2.3 Bounds from cosmology and stellar evolution

If gravitinos are dark matter, their primordial origin depends on the mass [21]; if the gravitino is lighter than about 1 keV, its interactions are strong enough to allow it to be in thermal equilibrium with the plasma after the reheating period. After the freeze-out, it will be relativistic and hence constitute hot dark matter.

Since relativistic particles "damp" the formation of small scale structures in the universe, see e.g. [150], hot dark matter can only constitute a fraction of the observed total dark matter in the universe. Feng et al. give an upper bound on the gravitino mass of [151]

$$m_{3/2} < 15 - 30 \times 10^{-9} \text{ GeV}, \tag{5.9}$$

consistent with the observed small scale structure and assuming another particle to constitute cold dark matter.

A very light gravitino behaves effectively like a massless neutrino at the time of big bang nucleosynthesis (BBN), and might affect the primordial abundance of helium-4 [152].[2] The number of neutrino-like particles $N_{eff}$ is constrained to be $N_{eff} < 3.3$ [152,153]. Therefore, the gravitino is required not to significantly contribute to the

[2] At the time of the BBN, the universe is radiation dominated. The expansion rate $H$ depends on the amount of photons, electron-positron pairs and neutrinos. If the number of neutrino-like particles increases, $H$ increases, so the universe expands faster. An increase in $H$ has the effect that the interconversion of neutrons and protons freezes out earlier, leading to a higher abundance of neutrons, which finally gives a higher abundance of primordial $^4$He.

number of neutrino-like particles, and one can estimate a lower bound on the gravitino mass. Moroi et al. derive [154]

$$m_{3/2} \geq 10^{-13}\ \text{GeV}\Big(\frac{m_{\tilde{l}}}{100\ \text{GeV}}\Big), \tag{5.10}$$

where $m_{\tilde{l}}$ denotes the slepton mass and the bound is valid only if the freeze-out temperature is much bigger than the slepton mass [155]. Assuming a freeze-out temperature much lower than the soft masses, Ghergetta sets the weaker bound [155]

$$m_{3/2} \geq 10^{-15}\ \text{GeV}, \tag{5.11}$$

for the photino mass of $m_{\tilde{\gamma}} \approx \mathcal{O}(100\ \text{GeV})$ and $N_{eff} < 3.6$.

Finally, we comment on the bounds on the gravitino mass from stellar evolution. Gravitinos can be produced in a supernova core. If the gravitino escapes the supernova, it carries energy away and hence contributes to the cooling of the supernova [156, 157]. From the observed neutrino luminosity of the supernova SN1987A, Dicus et al. put the lower bound [157][3]

$$m_{3/2} \geq 0.6 - 6 \times 10^{-15}\ \text{GeV}. \tag{5.12}$$

Finally, from the energy loss of a red giant star also a bound can be derived [160],

$$m_{3/2} \geq 6 \times 10^{-16}\ \text{GeV}. \tag{5.13}$$

## 5.3 Theoretical models suggesting a very light gravitino

Direct gravitino production becomes relevant at colliders if the gravitino is very light, see (5.3), $m_{3/2} \sim \mathcal{O}(10^{-14} - 10^{-12}\ \text{GeV})$. As derived in Section 3.3.2, the gravitino mass is directly proportional to the SUSY breaking scale, $m_{3/2} = F/(\sqrt{3}\,\overline{M}_{\text{Pl}})$, so that the lower bounds on the gravitino mass translate into lower bounds on the SUSY breaking scale.

In Section 3.1, we saw that different SUSY mediation mechanisms correspond to very different SUSY breaking scales. A very light gravitino as in (5.3) is suggested by the context of no-scale supergravity [161–163] and some extra-dimensional models [164, 165], while typical gauge-mediated SUSY breaking (GMSB) scenarios expect a mass of 1 eV-10 keV [30].

In no-scale supergravity, the idea is that the function $G^i(G^{-1})^j_i G_j$ showing up in the classical potential given in (3.31) is $G^i(G^{-1})^j_i G_j = 3$ for all field values, such that the classical potential is identical to 0 (not only at the vacuum). In their model, Ellis et al. [162] choose a specific gauge kinetic function that leads to a relation between the

[3] We note that these bounds are extremely strengthened if the sgoldstino is assumed to be as light as the gravitino [158]. However, such a light sgoldstino is theoretically not well motivated since it does not obey a naturalness criterion [159].

gravitino and the gaugino mass. The gaugino mass $m_{\tilde{g}}$ is determined dynamically by radiative corrections. For a specific choice for the Kähler potential $G$, they find

$$m_{3/2} = \mathcal{O}\left(\frac{m_{\tilde{g}}^p}{M_{\rm Pl}^{p-1}}\right), \tag{5.14}$$

where $m_{\tilde{g}}$ is of the order of the electroweak scale, and $1 < p < 2$. For $p \approx 2$, this allows for a gravitino as light as in (5.3).

The extra dimensional models that can predict such a light gravitino are Randall-Sundrum-type. The five-dimensional space-time is bounded by two four-dimensional branes, the UV (or Planck) brane and the IR (or TeV) brane. The extra dimension is of length $L = \pi R$ and "warped". The warp factor $e^{-\pi kR}$ is 0 at the UV brane and maximal at the IR brane ($k$ is the space-time curvature). In their model [164], Ghergetta and Pomarol choose $kR \sim 12$. As a result, if the effective scale is $M_{\rm Pl}$ at the UV brane, it can be of the order of TeV at the IR brane. SUSY is broken at the IR brane, so the effective scale of SUSY breaking is also $\mathcal{O}$(TeV). It is assumed that the fermions and their superpartners live on the UV brane, and gauge as well as gravity fields in the bulk. The SUSY breaking is then mediated via gauge interactions; gauginos receive tree-level masses, while the scalars get massive only at loop level,

$$m^2 \sim \frac{g^2}{16\pi^2}(\text{TeV})^2. \tag{5.15}$$

The gravitino couples with gravitational strength to the IR brane, hence its mass is derived to be of order

$$m_{3/2} = \mathcal{O}\left(\frac{\text{TeV}^2}{M_{\rm Pl}}\right). \tag{5.16}$$

This may lead to a gravitino as light as in (5.3).

## 5.4 Simulation tools for gravitino phenomenology

For the last few years simulation tools in the FeynRules and MadGraph frameworks for processes involving gravitinos/goldstinos have been intensively developed [48, 50, 166], making phenomenological studies easier. The main part of the thesis is based on the further development, the validation and the phenomenological applications of these tools.

We can study gravitino interactions using the spin 3/2 formalism, as presented in the study of the $\gamma\gamma \to \tilde{G}\tilde{G}$ production process in Section 3.4.1. To this end, we implemented the interactions of gravitino and graviton (3.40) into FeynRules and constructed a model file which allows us to study the strongest energy dependent amplitude. We note that this study was used to validate the implementation of general spin-3/2 particles in FeynRules and Aloha [50].

As discussed in Section 3.4, when the CM energy is much bigger than the gravitino

mass, $\sqrt{s} \gg m_{3/2}$, gravitino interactions can be studied using the effective goldstino interaction Lagrangian, thanks to the gravitino-goldstino equivalence theorem. This is always the case for studies of light gravitino production at colliders, and we use this approach throughout the rest of this work. We note that we call the goldstino the gravitino in the following.

Most of the recent studies on gravitino production at colliders [47, 167–171] rely on the effective gravitino Lagrangian derived by supercurrent conservation, see Section 3.2.3, and hence contain only interactions with a single gravitino. This approach only allows to study production processes where one gravitino is directly produced, such as associated production with another SUSY particle, or when the gravitino appears at the end of a decay chain.

To study interaction processes where a pair of gravitinos is directly produced, we need to take into account effective vertices involving two gravitinos as well as sgoldstinos. The recent development of FeynRules [25] makes it easier to construct a consistent model by using the superfield formalism. We implemented a SUSY Lagrangian in the superfield formalism [172], including all the relevant interactions for light gravitino production at colliders. We note that the $\tilde{G}\tilde{G}$ production process contains a four-fermion interaction involving two Majorana particles. The current MadGraph 5 (v2.0.2) does not support four-fermion vertices involving more than one Majorana particle, and hence does not accept our UFO model file generated by FeynRules. Therefore, first, we modified MadGraph 5 to allow us to import the model. Second, after generating the process, the corresponding four-point contact amplitudes should be modified by hand to have correct fermion flows.

# CHAPTER 6

## Mono-photon signals in gravitino production in $e^+e^-$ collisions

We revisit gravitino production leading to the monophoton plus missing energy signature at future $e^+e^-$ colliders,

$$e^+e^- \to \gamma\tilde{G}\tilde{G} \to \gamma + \not{E}. \tag{6.1}$$

We consider a SUSY model where the gravitino is the LSP, and the neutralino the NLSP which promptly decays into a photon and a gravitino. In such scenarios there are two possible processes providing the signal: *gravitino pair production* ($\tilde{G}\tilde{G}$) and *neutralino-gravitino associated production* ($\tilde{\chi}\tilde{G}$). The former leads to the monophoton final state via an additional photon radiation, while the latter via the subsequent neutralino decay into a photon and an LSP gravitino. Their relative importance varies with the gravitino and neutralino masses, with neutralino mixing and with kinematical cuts.

In Section 6.1, we investigate the $e^+e^- \to \tilde{G}\tilde{G}$ production process in detail. We explicitly give the helicity amplitudes for the two-to-two production processes, and present the cross sections with different collision energies and mass spectra.

Subsequently, we repeat the study for the $e^+e^- \to \tilde{\chi}_1^0\tilde{G}$ production process in Section 6.2. We give the helicity amplitudes and show how the total cross section varies for different neutralino mixings and SUSY masses. We derive the expression for the decay width of the neutralino, and discuss the angular dependence of the differential cross section as a function of the selectron mass.

In Section 6.3, we discuss the relative importance of the both processes for different parameter choices, and fix the parameters for the following study. We shortly comment on the validation of our model.

In Section 6.4, we present the signal and background distributions. After specifying the final selection cuts, we show how polarized beams may enhance the signal over background ratio. We show that the signal cross section and the photon spectra provide information on the masses of the SUSY particles as well as the SUSY breaking scale.

## 6.1 Gravitino pair production

Gravitino pair production gives rise to the monophoton plus missing energy signature when an additional photon is emitted [128, 129],

$$e^+e^- \to \tilde{G}\tilde{G} + \gamma. \tag{6.2}$$

In this section, we investigate in detail the two-to-two production process.

### 6.1.1 Helicity amplitudes

We present the helicity amplitudes explicitly for the two-to-two process

$$e^-\Big(p_1, \frac{\lambda_1}{2}\Big) + e^+\Big(p_2, \frac{\lambda_2}{2}\Big) \to \tilde{G}\Big(p_3, \frac{\lambda_3}{2}\Big) + \tilde{G}\Big(p_4, \frac{\lambda_4}{2}\Big), \tag{6.3}$$

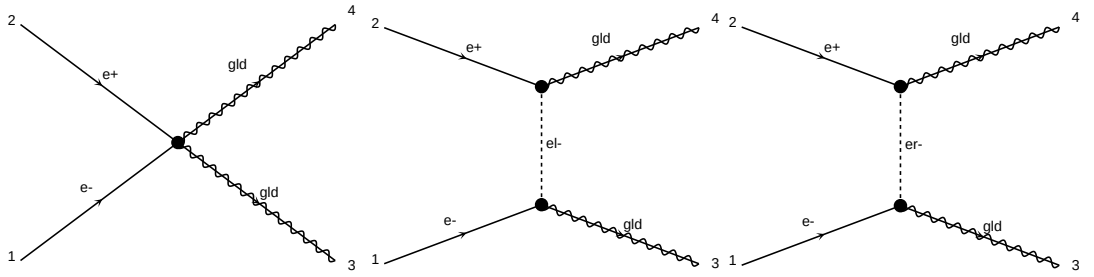


Figure 6.1: Samples of Feynman diagrams for gravitino pair production in $e^+e^-$ collisions, generated by (modified) MadGraph 5 [14]. `gld`, `el`, and `er` denote a gravitino, a left-handed selectron, and a right-handed selectron, respectively.

where the four momenta ($p_i$) and helicities ($\lambda_i = \pm 1$) are defined in the center-of-mass (CM) frame of the $e^+e^-$ collision.

In the massless limit of $e^\pm$, one can find that all amplitudes are zero when both the electron and the positron have the same helicity, and hence we fix $\lambda_2 = -\lambda_1$. The same helicity relation holds for the massless gravitinos in the final state, leading to $\lambda_4 = -\lambda_3$. Since we will assume gravitinos with mass $m_{3/2} \sim \mathcal{O}(10^{-13}\ \text{GeV})$, we neglect the gravitino mass in the phase space but keep it in the couplings. In addition, for the $\lambda_1 = +1$ ($\lambda_1 = -1$), only right-handed (left-handed) selectrons can contribute to the total amplitudes. Therefore, the helicity amplitudes for the above process can be expressed as the sum of the four-point contact amplitude and the $t, u$-channel selectron exchange amplitudes (see also Fig. 6.1):

$$\mathcal{M}_{\lambda_1,\lambda_3} = \mathcal{M}^c_{\lambda_1,\lambda_3} + \mathcal{M}^t_{\lambda_1,\lambda_3} + \mathcal{M}^u_{\lambda_1,\lambda_3}. \tag{6.4}$$

Using the straightforward Feynman rules for Majorana fermions given in [53], the above amplitudes are written, based on the effective gravitino Lagrangian in Section 3.2.2, as

$$i\mathcal{M}^c_{\lambda_1,\lambda_3} = -\frac{im^2_{\tilde{e}_{\lambda_1}}}{F^2}\big(\hat{\mathcal{M}}^t_{\lambda_1,\lambda_3} - \hat{\mathcal{M}}^u_{\lambda_1,\lambda_3}\big), \tag{6.5}$$

$$i\mathcal{M}^t_{\lambda_1,\lambda_3} = -\frac{im^4_{\tilde{e}_{\lambda_1}}}{F^2(t - m^2_{\tilde{e}_{\lambda_1}})}\,\hat{\mathcal{M}}^t_{\lambda_1,\lambda_3}, \tag{6.6}$$

$$i\mathcal{M}^u_{\lambda_1,\lambda_3} = \frac{im^4_{\tilde{e}_{\lambda_1}}}{F^2(u - m^2_{\tilde{e}_{\lambda_1}})}\,\hat{\mathcal{M}}^u_{\lambda_1,\lambda_3}, \tag{6.7}$$

where $m_{\tilde{e}_\pm}$ denotes the right/left-handed selectron mass for notational convenience and $F = \sqrt{3}\,\overline{M}_{\rm Pl} m_{3/2}$ is the SUSY breaking scale, see (3.38). The reduced helicity amplitudes are

$$\begin{aligned}
\hat{\mathcal{M}}^t_{\lambda_1,\lambda_3} &= \bar{u}(p_3,\lambda_3)P_{\lambda_1}u(p_1,\lambda_1)\,\bar{v}(p_2,-\lambda_1)P_{-\lambda_1}v(p_4,-\lambda_3),\\
\hat{\mathcal{M}}^u_{\lambda_1,\lambda_3} &= \bar{u}(p_4,-\lambda_3)P_{\lambda_1}u(p_1,\lambda_1)\,\bar{v}(p_2,-\lambda_1)P_{-\lambda_1}v(p_3,\lambda_3),
\end{aligned} \tag{6.8}$$

where $P_\pm = \frac{1}{2}(1 \pm \gamma^5)$ is the chiral projection operator.

| $\lambda_1\lambda_3$ | | $\mathcal{M}^c$ | $\mathcal{M}^t$ | $\mathcal{M}^u$ | |
|---|---|---|---|---|---|
| $\pm\mp$ | $-\dfrac{s\,m^2_{\tilde{e}_{\lambda_1}}}{2(\sqrt{3}\,\overline{M}_{\rm Pl} m_{3/2})^2}\,(1-\cos\theta)$ | $\Big[$ 1 | $+\dfrac{m^2_{\tilde{e}_{\lambda_1}}}{t-m^2_{\tilde{e}_{\lambda_1}}}$ | | $\Big]$ |
| $\pm\pm$ | $-\dfrac{s\,m^2_{\tilde{e}_{\lambda_1}}}{2(\sqrt{3}\,\overline{M}_{\rm Pl} m_{3/2})^2}\,(1+\cos\theta)$ | $\Big[$ 1 | | $+\dfrac{m^2_{\tilde{e}_{\lambda_1}}}{u-m^2_{\tilde{e}_{\lambda_1}}}$ | $\Big]$ |

Table 6.1: The helicity amplitudes $\mathcal{M}_{\lambda_1,\lambda_3}$ defined in (6.4) for $e^-_{\lambda_1}e^+_{-\lambda_1} \to \tilde{G}_{\lambda_3}\tilde{G}_{-\lambda_3}$.

With the four momenta defined as

$$\begin{aligned} p_1^\mu &= \frac{\sqrt{s}}{2}(1,0,0,1), \\ p_2^\mu &= \frac{\sqrt{s}}{2}(1,0,0,-1), \\ p_3^\mu &= \frac{\sqrt{s}}{2}(1,\sin\theta,0,\cos\theta), \\ p_4^\mu &= \frac{\sqrt{s}}{2}(1,-\sin\theta,0,-\cos\theta), \end{aligned} \tag{6.9}$$

we present the helicity amplitudes in Table 6.1.

### 6.1.2 Total cross section

From the helicity amplitudes presented in the previous section, we derive the total cross section

$$\begin{aligned} \sigma = \frac{1}{192\pi(\sqrt{3}\,\overline{M}_{\rm Pl} m_{3/2})^4} \sum_{\lambda=\pm} \frac{m^4_{\tilde{e}_\lambda}}{s^2} \Big[ & s^3 - 3m^2_{\tilde{e}_\lambda} s^2 + 9m^4_{\tilde{e}_\lambda} s \\ & + 3m^6_{\tilde{e}_\lambda}\Big(1 - \frac{m^2_{\tilde{e}_\lambda}}{s+m^2_{\tilde{e}_\lambda}} + 4\log\frac{m^2_{\tilde{e}_\lambda}}{s+m^2_{\tilde{e}_\lambda}}\Big)\Big]. \end{aligned} \tag{6.10}$$

Figure 6.2 shows the total cross sections as a function of the CM energy $\sqrt{s}$ for three different selectron masses $m_{\tilde{e}_\pm} = 0.5$, 1 and 2 TeV. The gravitino mass is fixed at $m_{3/2} = 2\times10^{-13}$ GeV, which corresponds to the SUSY breaking scale $\sqrt{F} \approx 918$ GeV. We stress that the cross section is extremely sensitive to the gravitino mass since it scales inversely proportional to the gravitino mass to the fourth,

$$\sigma(\tilde{G}\tilde{G}) \propto 1/m^4_{3/2}. \tag{6.11}$$

We also note that the cross section tends to be larger for the heavier selectrons since the couplings are proportional to $m^2_{\tilde{e}}$.

In the low-energy limit, $\sqrt{s} \ll m_{\tilde{e}_\pm}$, as one can easily see from the explicit amplitudes in Table 6.1, a strong cancellation happens between $\mathcal{M}^c$ and $\mathcal{M}^{t,u}$, leading to a cross

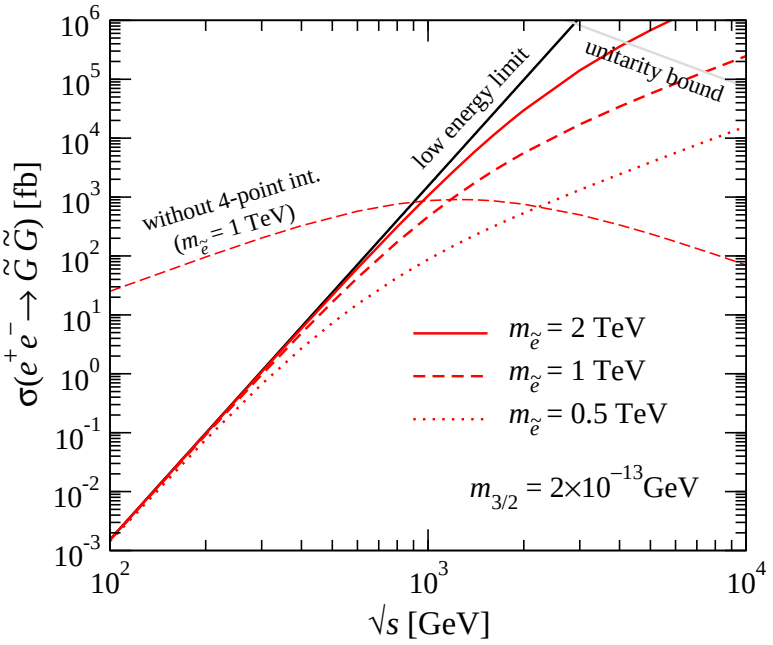


Figure 6.2: Total cross sections of $e^+e^- \to \tilde{G}\tilde{G}$ as a function of the collision energy for different selectron masses $m_{\tilde{e}_\pm} = 0.5, 1, 2$ TeV with $m_{3/2} = 2 \times 10^{-13}$ GeV. The cross section in the low energy limit is presented by a black solid line. The contribution without the four-point interaction for $m_{\tilde{e}_\pm} = 1$ TeV is also shown as a reference.

section scaling as [32, 129]

$$\sigma = \frac{s^3}{160\pi(\sqrt{3}\,\overline{M}_{\rm Pl} m_{3/2})^4}, \tag{6.12}$$

presented by a black line in Fig. 6.2. The contribution without the four-point amplitude is also shown as a reference, where one can see the effect of the huge cancellation. It should be noted here that the low-energy limit, which is always assumed in the previous studies [128, 129, 173, 174], may not be a good approximation for future colliders since the selectron masses should be less or of the order of the SUSY breaking scale and might be within the reach of the CM energies. Therefore, one should consider the full expression of the cross section. Figure 6.2 indeed shows that, as $\sqrt{s}$ is increasing, the effect of the selectron mass becomes significant. When the CM energy is bigger than the selectron mass, $\sqrt{s} > m_{\tilde{e}}$, the contribution from $\mathcal{M}^c$ becomes more important than that from $\mathcal{M}^{t,u}$. We note that the current gravitino mass bound by the $\tilde{G}\tilde{G}(+\gamma)$ production presented in Section 5.2.1 could weaken if the selectrons are light enough.

Finally, we briefly discuss the unitarity bound. The projected partial wave amplitude is given by

$$\mathcal{J}^J_{\lambda_1,\lambda_3} = \frac{1}{32\pi}\int_{-1}^{1} d\cos\theta\, d^J_{\lambda_1\lambda_3}(\theta)\,\mathcal{M}_{\lambda_1,\lambda_3} \tag{6.13}$$

with the Wigner $d$-function. Unitarity requires the lowest non-vanishing partial wave

to be $|\mathcal{J}^{J=1}_{\lambda_1,\lambda_3}| < 1/2$, leading to the upper bound of the cross section, which is shown by a gray line in Fig. 6.2. One can see that the lighter selectrons remedy the bad unitarity behavior. It should also be noted that, since we consider the effective model which is valid up to $m_{SUSY}/F$, a higher energy requires a higher SUSY breaking scale (i.e. a heavier gravitino) or lighter SUSY particles for reliable predictions.

## 6.2 Neutralino-gravitino associated production

Gravitino production in association with a neutralino and the subsequent neutralino decay,

$$e^+e^- \to \tilde{\chi}\tilde{G} \to \gamma\tilde{G}\tilde{G}, \tag{6.14}$$

leads to the $\gamma + \not{E}$ signal already at the leading order [131–135, 167]. Throughout this section, we allow the neutralino to be a mixture of bino and wino and investigate the effect on the total cross section. The effective goldstino interaction Lagrangian including the effect of neutralino mixing different from a photino is given in (3.14).

### 6.2.1 Helicity amplitudes

We present the helicity amplitudes explicitly for the production process

$$e^-\Big(p_1, \frac{\lambda_1}{2}\Big) + e^+\Big(p_2, \frac{\lambda_2}{2}\Big) \to \tilde{\chi}^0_1\Big(p_3, \frac{\lambda_3}{2}\Big) + \tilde{G}\Big(p_4, \frac{\lambda_4}{2}\Big), \tag{6.15}$$

where again the four-momentum ($p_i$) and helicity ($\lambda_i = \pm 1$) of each particle are defined in the center-of-mass (CM) frame of the $e^+e^-$ collisions.

Similar to the case of $\tilde{G}\tilde{G}$ production, in the massless limit of $e^\pm$, one can find that all the amplitudes are zero when both the electron and the positron have the same helicity, or $\lambda_1 = \lambda_2$. In addition, for the $\lambda_1 = +1$ ($\lambda_1 = -1$) case, only the right-handed (left-handed) selectron can contribute to the total amplitudes. Therefore, the helicity amplitudes for the above process can be expressed as the sum of $s$-, $t$-, and $u$-channel amplitudes:

$$\mathcal{M}_{\lambda,\lambda_3\lambda_4} = \mathcal{M}^s_{\lambda,\lambda_3\lambda_4} + \mathcal{M}^t_{\lambda,\lambda_3\lambda_4} + \mathcal{M}^u_{\lambda,\lambda_3\lambda_4} \tag{6.16}$$

with $\lambda \equiv \lambda_1 = -\lambda_2$, where each amplitude with $\lambda = +1$ ($\lambda = -1$) corresponds to the Feynman graph 3+4, 2 (1), and 6 (5), respectively, in Fig. 6.3.

We present the amplitudes based on the effective goldstino interaction Lagrangian,

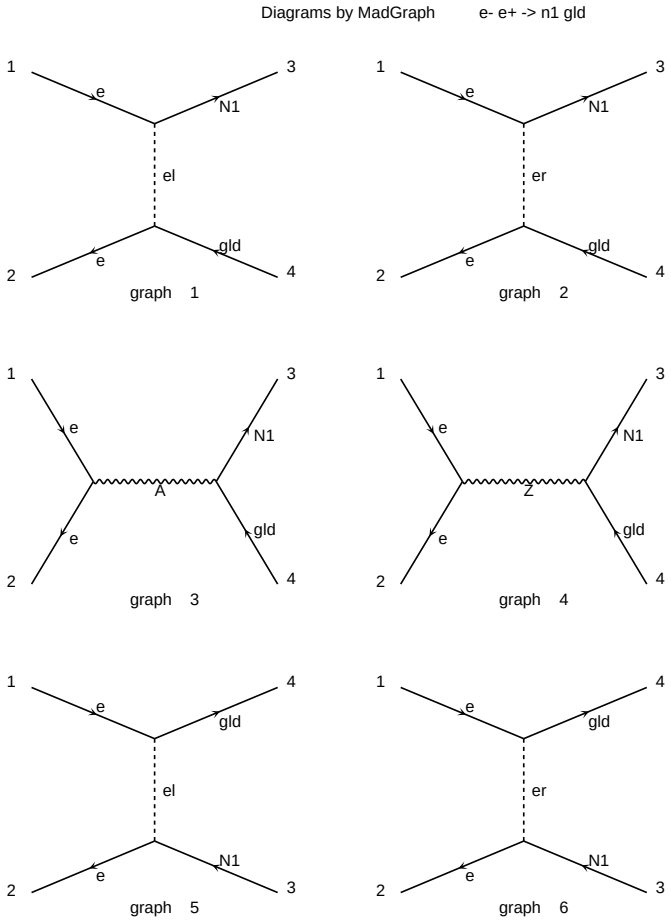


Figure 6.3: Feynman diagrams for the $\tilde{\chi}_1^0$-$\tilde{G}$ production in $e^+e^-$ collisions, generated by `MadGraph` [48]. `N1`, `gld`, `el`, and `er` denote a lightest neutralino, a gravitino, a left-handed selectron, and a right-handed selectron, respectively.

given in (3.14), in the usual four-spinor basis:

$$i\mathcal{M}^s_{\lambda,\lambda_3\lambda_4} = \frac{e\,C^s_\lambda\, m_{\tilde{\chi}_1^0}}{2\sqrt{6}\,\overline{M}_{\rm Pl} m_{3/2}} \frac{1}{s}\,\bar{v}(p_2,-\lambda)\gamma^\mu u(p_1,\lambda) \times \bar{u}(p_3,\lambda_3)[\not{p}_3 + \not{p}_4, \gamma_\mu] v(p_4,\lambda_4), \tag{6.17a}$$

$$i\mathcal{M}^t_{\lambda,\lambda_3\lambda_4} = \frac{-\sqrt{2}\,e\,C^{\tilde{e}\tilde{\chi}_1}_\lambda m^2_{\tilde{e}_\lambda}}{\sqrt{3}\,\overline{M}_{\rm Pl} m_{3/2}} \frac{1}{t - m^2_{\tilde{e}_\lambda}} \times \bar{u}(p_3,\lambda_3) u(p_1,\lambda)\,\bar{v}(p_2,-\lambda) v(p_4,\lambda_4), \tag{6.17b}$$

$$i\mathcal{M}^u_{\lambda,\lambda_3\lambda_4} = \frac{-\sqrt{2}\,e\,C^{\tilde{e}\tilde{\chi}_1}_\lambda m^2_{\tilde{e}_\lambda}}{\sqrt{3}\,\overline{M}_{\rm Pl} m_{3/2}} \frac{1}{u - m^2_{\tilde{e}_\lambda}} \times \bar{u}(p_4,\lambda_4) u(p_1,\lambda)\,\bar{v}(p_2,-\lambda) v(p_3,\lambda_3), \tag{6.17c}$$

where $m_{\tilde{e}_\pm}$ denotes the right-/left-handed selectron mass for notational convenience,

and

$$C_\lambda^s = C^{\gamma\tilde{\chi}_1} - \frac{s}{s - m_Z^2 + i m_Z \Gamma_Z} g_\lambda C^{Z\tilde{\chi}_1} \tag{6.18}$$

with $Z$-boson couplings to right- and left-handed charged leptons,

$$g_+ = \frac{\sin\theta_W}{\cos\theta_W} \quad \text{and} \quad g_- = \frac{-1 + 2\sin^2\theta_W}{2\sin\theta_W\cos\theta_W}, \tag{6.19}$$

respectively.[1] The couplings $C^{\gamma\tilde{\chi}_i}, C^{Z\tilde{\chi}_i}, C^{\tilde{e}\tilde{\chi}_i}$ related to the neutralino mixing defined by $X_i = U_{ij}\tilde{\chi}_j^0$ in the $X = (\tilde{B}, \tilde{W}^3, \tilde{H}_d^0, \tilde{H}_u^0)$ basis, where $U_{ij}$ is taken to be real, are

$$\begin{aligned} C^{\gamma\tilde{\chi}_i} &= U_{1i}\cos\theta_W + U_{2i}\sin\theta_W, \\ C^{Z\tilde{\chi}_i} &= -U_{1i}\sin\theta_W + U_{2i}\cos\theta_W, \\ C_\pm^{\tilde{e}\tilde{\chi}_i} &= T_\pm^{\tilde{e}}\frac{U_{2i}}{\sin\theta_W} + Y_\pm^{\tilde{e}}\frac{U_{1i}}{\cos\theta_W}, \end{aligned} \tag{6.20}$$

with the $SU(2)$ charge $T_\pm^{\tilde{e}}$ and the $U(1)$ charge $Y_\pm^{\tilde{e}}$ for $\tilde{e}_{+/-}(= \tilde{e}_{R/L})$, that is $T_-^{\tilde{e}} = Y_-^{\tilde{e}} = -1/2$ and $T_+^{\tilde{e}} = 0$, $Y_+^{\tilde{e}} = -1$. Here, for simplicity, we assume the lightest neutralino as a pure gaugino, which makes the $\tilde{G}$-$\tilde{H}_{d,u}^0$-$Z$ couplings irrelevant to our study. It should be noted that $C_\lambda^s$ and $C_\lambda^{\tilde{e}\tilde{\chi}_1}$ are related with each other as

$$C_\lambda^s \sim -C_\lambda^{\tilde{e}\tilde{\chi}_1} + \mathcal{O}\Big(\frac{m_Z^2}{s}\Big) \tag{6.21}$$

for $\sqrt{s} \gg m_Z$; this is always the case in the following discussions.

To present the explicit helicity amplitudes, let us now define the kinematical variables of the process (6.15) in the $e^+e^-$ laboratory frame as

$$\begin{aligned} p_1^\mu &= \tfrac{\sqrt{s}}{2}(1,0,0,1), \\ p_2^\mu &= \tfrac{\sqrt{s}}{2}(1,0,0,-1), \\ p_3^\mu &= \tfrac{\sqrt{s}}{2}\big(1 + \tfrac{m_{\tilde{\chi}}^2}{s}, \beta\sin\theta, 0, \beta\cos\theta\big), \\ p_4^\mu &= \tfrac{\sqrt{s}}{2}\big(1 - \tfrac{m_{\tilde{\chi}}^2}{s}, -\beta\sin\theta, 0, -\beta\cos\theta\big), \end{aligned} \tag{6.22}$$

with $\beta = 1 - m_{\tilde{\chi}_1^0}^2/s$. Throughout our study we neglect the gravitino mass, except in the gravitino couplings.

For notational convenience we define the reduced helicity amplitudes, $\hat{\mathcal{M}}$, as

$$i\mathcal{M}_{\lambda,\lambda_3\lambda_4} = \frac{-e}{\sqrt{6}\,\overline{M}_{\rm Pl} m_{3/2}} \sqrt{\beta}\, s\, \hat{\mathcal{M}}_{\lambda,\lambda_3\lambda_4}, \tag{6.23}$$

and these are presented in Table 6.2. The following features of the amplitudes are worth noting:

[1] Strictly speaking, the $Z$-exchange amplitude in (6.17a) is valid only for $\sqrt{s} \gg m_Z$ since massless gauge bosons are assumed in the effective Lagrangian (3.14).

| $\lambda$ | $\lambda_3\lambda_4$ | | $\hat{\mathcal{M}}^s$ | $\hat{\mathcal{M}}^t$ | $\hat{\mathcal{M}}^u$ |
|---|---|---|---|---|---|
| $\pm$ | $\pm\mp$ | $(1+\cos\theta)$ | $\left[ \frac{m_{\tilde{\chi}}^2}{s} C_\pm^s \right.$ | | $\left. -\frac{m_{\tilde{e}_\pm}^2}{u-m_{\tilde{e}_\pm}^2} C_\pm^{\tilde{e}\tilde{\chi}_1} \right]$ |
| $\pm$ | $\mp\pm$ | $-(1-\cos\theta)$ | $\left[ \frac{m_{\tilde{\chi}}^2}{s} C_\pm^s \right.$ | $-\frac{m_{\tilde{e}_\pm}^2}{t-m_{\tilde{e}_\pm}^2} C_\pm^{\tilde{e}\tilde{\chi}_1}$ | $\left. \right]$ |
| $\pm$ | $\pm\pm$ | $\pm\frac{m_{\tilde{\chi}}}{\sqrt{s}}\sin\theta$ | $\left[ C_\pm^s \right.$ | $-\frac{m_{\tilde{e}_\pm}^2}{t-m_{\tilde{e}_\pm}^2} C_\pm^{\tilde{e}\tilde{\chi}_1}$ | $\left. \right]$ |
| $\pm$ | $\mp\mp$ | $\mp\frac{m_{\tilde{\chi}}}{\sqrt{s}}\sin\theta$ | $\left[ C_\pm^s \right.$ | | $\left. -\frac{m_{\tilde{e}_\pm}^2}{u-m_{\tilde{e}_\pm}^2} C_\pm^{\tilde{e}\tilde{\chi}_1} \right]$ |

Table 6.2: The reduced helicity amplitudes $\hat{\mathcal{M}}_{\lambda,\lambda_3\lambda_4}$ for $e^-_\lambda e^+_{-\lambda} \to \tilde{\chi}^0_{1\lambda_3}\tilde{G}_{\lambda_4}$.

1. As mentioned before, for the $\lambda = +1$ ($\lambda = -1$) case only $\tilde{e}_+$ ($\tilde{e}_-$) can be exchanged in the $t$- and $u$-channel amplitudes, and all the amplitudes are zero for $\lambda_1 = \lambda_2$.

2. The overall angular dependence is dictated by $J = 1$ $d$ functions as

$$\mathcal{M}_{\lambda,\lambda_3\lambda_4} \propto d^1_{\lambda,(\lambda_3-\lambda_4)/2}(\theta). \tag{6.24}$$

3. $\mathcal{M}^s$ and $\mathcal{M}^{t,u}$ interfere subtractively with each other; especially for the $\lambda_3 = \lambda_4$ case they almost cancel in the wide range of the parameter space, and hence the amplitudes with $\lambda_3 = -\lambda_4$ are dominant for the most of the cases except for the $m_{\tilde{\chi}^0_1} \sim m_{\tilde{e}_\pm}$ region. We note that in the very high-energy region the amplitudes with $\lambda_3 = \lambda_4$ become important since $\mathcal{M}^s$ becomes dominant, making those amplitudes be proportional to $\sqrt{s}$ while the amplitudes with $\lambda_3 = -\lambda_4$ are independent of $\sqrt{s}$; in that region the cross section does not depend on the selectron masses but on the produced neutralino mass.

4. For the $\lambda_3 = -\lambda_4$ case, in the threshold region, where $t, u = -s\beta(1\mp\cos\theta)/2 \to 0$, an additional $\beta$ can be extracted from the reduced amplitudes due to $C^s_\pm \sim -C^{\tilde{e}\tilde{\chi}_1}_\pm$ in (6.21). Together with $\beta^{1/2}$ in (6.23), the amplitudes are proportional to $\beta^{3/2}$. Therefore, including the phase space factor $\beta$, the threshold excitation of the total cross section is given by [131, 133, 134][2]

$$\sigma \propto \beta^4. \tag{6.25}$$

5. $\mathcal{M}^t$ and $\mathcal{M}^u$ depend on the selectron mass and become larger as the selectron mass increases, while $\mathcal{M}^s$ is independent of $m_{\tilde{e}}$.

We note that our helicity-summed amplitude squared agrees with Eq. (28) in [134] for the photino case, and also with Eq. (3) of [141] for the gluino associated process

[2]Note that $\beta$ is defined as $(1 - m^2_{\tilde{\chi}^0_1}/s)^{1/2}$ in Refs. [133, 134].

$q\bar{q} \to \tilde{g}\tilde{G}$ after substitutions for the masses and the couplings as

$$\begin{aligned} & m_{\tilde{\chi}_1^0} \to m_{\tilde{g}}, \quad m_{\tilde{e}_{R/L}} \to m_{\tilde{q}_{R/L}}, \\ & e \to -g_s T^a, \quad C_\lambda^s \to 1, \quad C_\lambda^{\tilde{e}\tilde{\chi}_1} \to -1. \end{aligned} \tag{6.26}$$

### 6.2.2 Total cross section

Let us now present the total cross sections and the kinematical distributions for the production process (6.15). The initial-helicity ($\lambda$) dependent cross section is given by

$$d\sigma_\lambda = \frac{1}{2s}\frac{1}{2}\sum_{\lambda_{3,4}} |\mathcal{M}_{\lambda,\lambda_3\lambda_4}|^2 d\Phi_2 \tag{6.27}$$

with the two-body phase space factor $d\Phi_2 = \int \frac{d\cos\theta}{2}\frac{d\varphi}{2\pi}\frac{1}{8\pi}\beta$. $\sigma_{\rm unpol} = (\sigma_+ + \sigma_-)/2$ is the usual spin-summed and averaged cross section.

We point out that unlike the gravitino pair production (6.11), the total cross section is inversely proportional to the square of the gravitino mass

$$\sigma(\tilde{\chi}\tilde{G}) \propto 1/m_{3/2}^2, \tag{6.28}$$

and hence the sensitivity to the gravitino mass is weaker than in the $\tilde{G}\tilde{G}$ production.

Figure 6.4 shows total cross sections of the gravitino productions associated with a bino-, wino and photino-like neutralino in $e^+e^-$ collisions as a function of the CM energy $\sqrt{s}$, where the neutralino and selectron masses are fixed as $m_{\tilde{\chi}_1^0} = 300$ GeV and $m_{\tilde{e}_+} = m_{\tilde{e}_-} = 800$ GeV. We take the gravitino mass $m_{3/2} = 10^{-13}$ GeV in this plot. In the figure the threshold region for the unpolarized bino-like neutralino cross section is enlarged, and one can see that the production cross section is strongly suppressed as shown in (6.25), in contrast to the threshold excitation for the standard fermion ($\propto \beta$) and the scalar ($\propto \beta^3$) pair productions [175]. This is one of the particular signatures for the associated gravitino productions.

For the case of the bino-like neutralino, or $|U_{11}| \sim 1$ and $|U_{21}| \sim 0$ in (6.20), the cross section with right-handed electrons ($\sigma_+$) dominates the one with left-handed ($\sigma_-$). For the heavy selectron case the $t$- and $u$-channel contributions are dominant, and therefore the ratio of the $\lambda$-dependent cross sections is roughly given in terms of the $\tilde{\chi}_1^0$-$e$-$\tilde{e}_\pm$ couplings as

$$\frac{\sigma_\pm}{2\sigma_{\rm unpol}} \sim \frac{|C_\pm^{\tilde{e}\tilde{\chi}_1}|^2}{|C_+^{\tilde{e}\tilde{\chi}_1}|^2 + |C_-^{\tilde{e}\tilde{\chi}_1}|^2}. \tag{6.29}$$

The bino case gives $\sigma_+/2\sigma_{\rm unpol} \sim 0.8$, which one can observe in Fig. 6.4. For the case of the wino-like neutralino, or $|U_{11}| \sim 0$ and $|U_{21}| \sim 1$, the right-handed cross section vanishes, i.e. $\sigma_{\rm unpol} = \sigma_-/2$. For a photino-like neutralino, or $|U_{11}| \sim \cos\theta_W$ and $|U_{21}| \sim \sin\theta_W$, the left- and right-handed cross sections are the same, such that $\sigma_{\rm unpol} = \sigma_+ = \sigma_-$. One can conclude that the $\tilde{\chi}_1^0$-$\tilde{G}$ production process with polarized electron

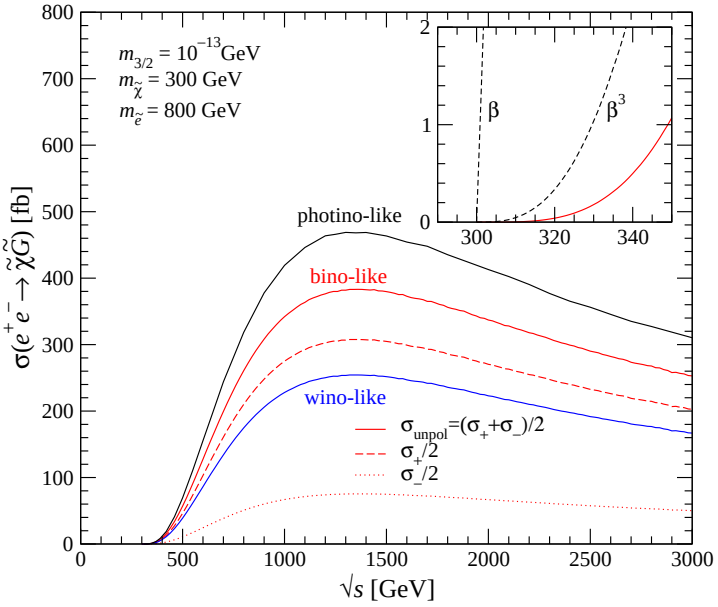


Figure 6.4: Total cross sections of associated gravitino productions with a photino/bino-/wino-like neutralino in $e^+e^-$ collisions, $e^+e^- \to \tilde{\chi}_1^0\tilde{G}$, for $m_{3/2} = 10^{-13}$ GeV as a function of the collision energy. The neutralino and selectron masses are fixed at 300 GeV and 800 GeV, respectively. The initial-helicity dependent cross sections $\sigma_\lambda$ are shown by a dashed line for $\lambda = +1$ and a dotted line for $\lambda = -1$. The threshold region is enlarged and the hypothetical dependence $\sigma \propto \beta$ and $\beta^3$ with the same coefficient is also shown.

beam can explore the neutralino mixing. The detailed study for various neutralino mixing has been done in Refs. [133, 134], while we assume a photino-like neutralino in the following analyses for simplicity.

In Fig. 6.5, the neutralino-mass dependence of the cross sections is shown for $\sqrt{s} =$ 500 GeV and 1 TeV. Due to the threshold behavior in (6.25), the cross sections are strongly suppressed as the neutralino mass is approaching the collider energy.[3] It should be emphasized here that the cross section is quite sensitive to the mass of the $t, u$-channel intermediate selectrons, even if the collider energy cannot reach them [133, 134]. The heavier selectron exchange increases the cross section since the $t, u$-channel amplitudes are proportional to the selectron mass squared as one can see in Table 6.2. We also note that, however, the goldstino couplings become too strong at some point for heavy selectrons to perform the reliable perturbative calculations.

### 6.2.3 Angular distribution of the neutralino

Before taking the neutralino decay into account, we discuss the angular distribution of the produced neutralino. As we will see, the $\tilde{\chi}_1^0 \to \gamma\tilde{G}$ decay is isotropic, and hence the photon distribution is given by purely kinematical effects of the decaying neutralino.

[3] For the case of $m_{\tilde{e}_\pm} = 500$ GeV at $\sqrt{s} = 1$ TeV, the cross section is not so strongly suppressed as $\beta^4$. This is because in this parameter region the contributions from the amplitudes with $\lambda_3 = \lambda_4$ are significant and these amplitudes do not provide an additional suppression factor $\beta$.

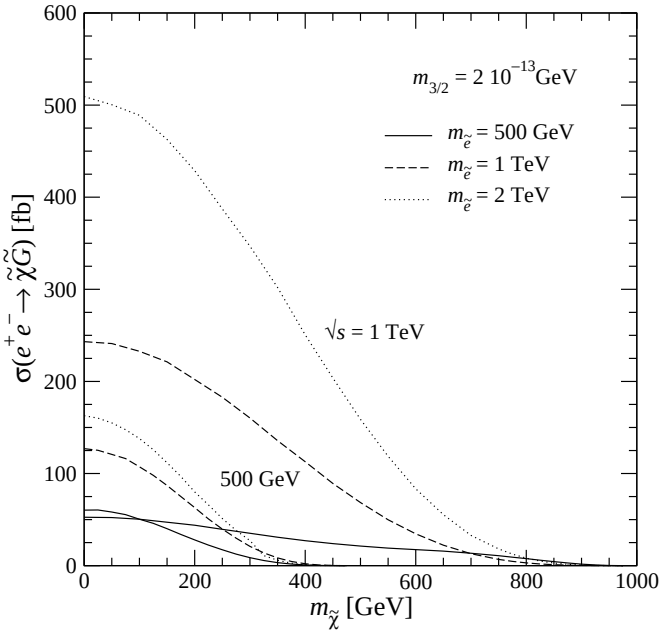


Figure 6.5: Total cross sections of $e^+e^- \to \tilde{\chi}_1^0\tilde{G}$ at $\sqrt{s} = 500$ GeV and 1 TeV for $m_{3/2} = 2 \times 10^{-13}$ GeV as a function of the neutralino mass. The selectron masses are fixed at 500 (solid), 1000 (dashed) and 2000 (dotted) GeV, respectively.

We show the helicity amplitudes for the neutralino decay into a photon and a gravitino,

$$\tilde{\chi}_1^0\Big(p_1, \frac{\lambda_1}{2}\Big) \to \gamma(p_2, \lambda_2) + \tilde{G}\Big(p_3, \frac{\lambda_3}{2}\Big). \tag{6.30}$$

The partial decay rate in the neutralino rest frame is given by

$$\Gamma = \frac{1}{2m_{\tilde{\chi}_1^0}} \frac{1}{2} \int \sum_{\lambda_{1,2,3}} |\mathcal{M}_{\lambda_1,\lambda_2\lambda_3}|^2 d\Phi_2, \tag{6.31}$$

and the helicity amplitudes are calculated as

$$\begin{aligned} \mathcal{M}_{+,++} = -\mathcal{M}_{-,--} &= \frac{-C^{\gamma\tilde{\chi}_1} m_{\tilde{\chi}_1^0}^3}{\sqrt{3}\,\overline{M}_{\rm Pl} m_{3/2}} \cos\frac{\theta^*}{2}, \\ \mathcal{M}_{+,--} = \mathcal{M}_{-,++} &= \frac{-C^{\gamma\tilde{\chi}_1} m_{\tilde{\chi}_1^0}^3}{\sqrt{3}\,\overline{M}_{\rm Pl} m_{3/2}} \sin\frac{\theta^*}{2}, \end{aligned} \tag{6.32}$$

with $C^{\gamma\tilde{\chi}_1}$ in (6.20) and the decay angle $\theta^*$ defined from the quantization axis of the neutralino spin. The angular dependence is dictated by $J = 1/2$ $d$ functions as

$$\mathcal{M}_{\lambda_1,\lambda_2\lambda_3} \propto d^{1/2}_{\lambda_1/2,\,\lambda_2-\lambda_3/2}(\theta^*). \tag{6.33}$$

Summing over the initial or final helicities for the amplitudes squared gives the isotropic

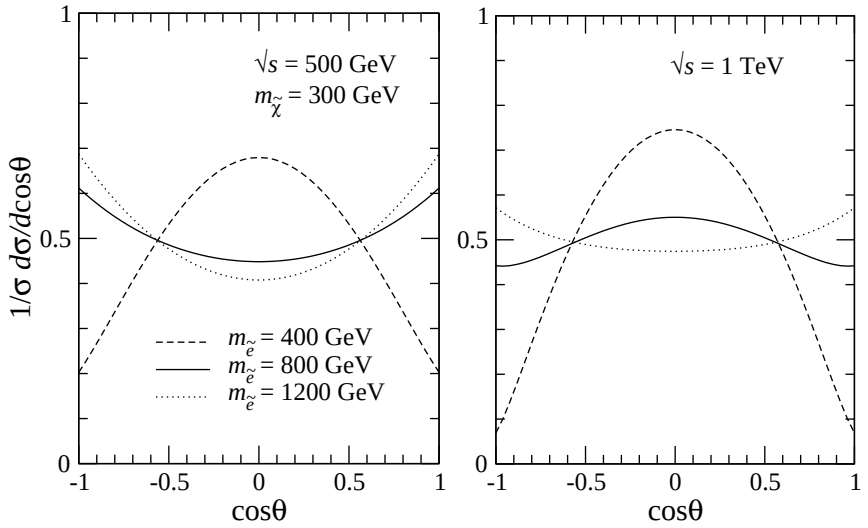


Figure 6.6: Normalized angular distributions of the neutralino in $e^+e^- \to \tilde{\chi}_1^0\tilde{G}$ at $\sqrt{s} = 500$ GeV (left) and 1 TeV (right) for $m_{\tilde{\chi}_1^0} = 300$ GeV, where the selectron masses are taken to be 400, 800 and 1200 GeV.

decay distribution in the rest frame, and one can find the well-known decay rate,

$$\Gamma(\tilde{\chi}_1^0 \to \gamma\tilde{G}) = \frac{|C^{\gamma\tilde{\chi}_1}|^2\, m_{\tilde{\chi}_1^0}^5}{48\pi \overline{M}_{\rm Pl}^2 m_{3/2}^2}. \tag{6.34}$$

For a photino like neutralino for $m_{\tilde{\chi}} = 750$ GeV and $m_{3/2} = 2 \times 10^{-13}$ GeV, the width is 6.6 GeV. With the neutralino being the NLSP, the branching ratio is unity, $B(\tilde{\chi} \to \gamma\tilde{G}) = 1$.

In Fig. 6.6, the normalized $\cos\theta$ distributions of the neutralino in $e^+e^- \to \tilde{\chi}_1^0\tilde{G}$ at $\sqrt{s} = 500$ GeV (left) and 1 TeV (right) are shown for $m_{\tilde{\chi}_1^0} = 300$ GeV. One can find that not only the total cross section as shown in Fig. 6.5 but also the angular distribution is quite sensitive to the mass of the $t, u$-channel intermediate selectrons [134]. When the selectron mass is close to the neutralino mass, the cross section is suppressed around $|\cos\theta| = 1$ since a cancellation occurs between $\mathcal{M}^s$ and $\mathcal{M}^{t,u}$ for the $\lambda_3 = -\lambda_4$ case due to $(t - m_{\tilde{e}}^2) = -s$ for $\cos\theta = -1$ and $(u - m_{\tilde{e}}^2) = -s$ for $\cos\theta = 1$; see also Table 6.2. For the heavy selectron case, on the other hand, the neutralino tends to be produced to the forward and backward regions since the selectron exchange diagrams are dominant and give the $(1 + \cos\theta)^2$ or $(1 - \cos\theta)^2$ angular dependence. We note that the contributions from the $\lambda_3 = \lambda_4$ case, which could give $\sin^2\theta$ dependence, are negligible for heavy selectron masses as mentioned before.

## 6.3 Physics parameters and validation

To examine a viable SUSY parameter space for the $\gamma + \not{E}$ signal at future $e^+e^-$ colliders, we present in Fig. 6.7 the total cross sections of $e^+e^- \to \gamma\tilde{G}\tilde{G}$ at $\sqrt{s} = 1$ TeV as a

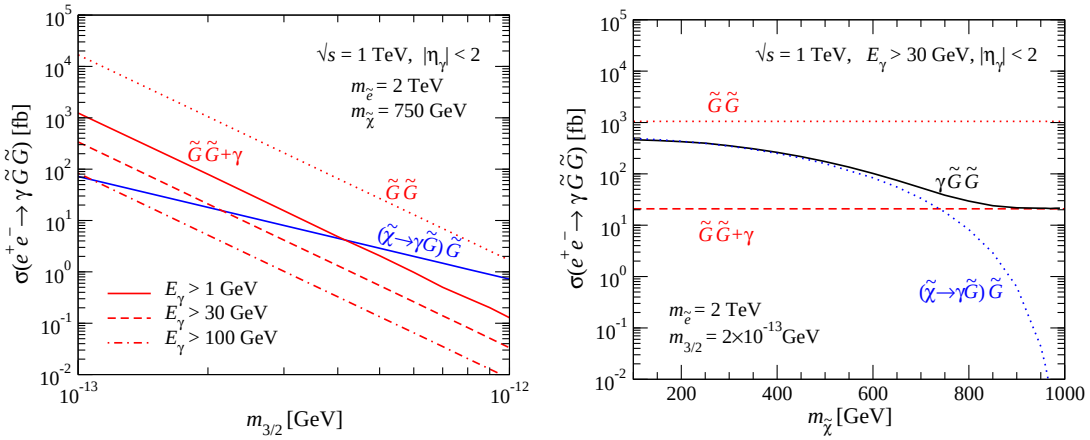


Figure 6.7: Total cross sections of $e^+e^- \to \gamma\tilde{G}\tilde{G}$ as a function of the gravitino mass (left) and the neutralino mass (right) for $m_{\tilde{e}_\pm} = 2$ TeV at $\sqrt{s} = 1$ TeV. The contributions of the gravitino pair production and the neutralino-gravitino associated production are separately shown by red and blue lines, respectively. The cross section of $e^+e^- \to \tilde{G}\tilde{G}$ is also shown by a red dotted line as a reference. On the left plot the contributions of the $\tilde{G}\tilde{G}$ production are shown with different photon energy cuts $E_\gamma > 1$, 30 and 100 GeV, while the $E_\gamma$ cut is fixed at 30 GeV on the right.

function of the gravitino mass (left) and the neutralino mass (right), where we fix the left- and right-handed selectron masses at 2 TeV. The representative Feynman diagrams for the process are depicted in Fig. 6.8. The contributions of the $\tilde{G}\tilde{G}$ and $\tilde{\chi}\tilde{G}$ productions are separately shown by red and blue lines, respectively.

As discussed in (6.11) and (6.28) and shown in the left plot in Fig. 6.7, the cross sections of the both subprocesses strongly depend on the gravitino mass.

The monophoton signal from the gravitino pair ($\tilde{G}\tilde{G} + \gamma$) is suppressed by the QED coupling $\alpha$ with respect to the two-to-two process and strongly depends on the kinematical cuts due to the soft and collinear singularity of the initial state radiation. The cut dependence on the photon energy is presented in the left plot in Fig. 6.7. On the other hand, since the energy of the photons coming from the neutralino decay is restricted as

$$\frac{m_{\tilde{\chi}}^2}{2\sqrt{s}} < E_\gamma < \frac{\sqrt{s}}{2}, \tag{6.35}$$

the signal of $\tilde{\chi}\tilde{G}$ is not affected by the lower cuts on the photon energy unless the neutralino is light.

In the following, we impose the minimal cuts for the detection of photons as

$$E_\gamma > 0.03\sqrt{s}, \quad |\eta_\gamma| < 2, \tag{6.36}$$

and fix the gravitino mass at $2 \times 10^{-13}$ GeV, which lies above the current exclusion limit by the jet+$\not{E}$ search at the LHC for the gravitino production in association with a gluino or a squark with masses around 500 GeV [149], see also Section 5.2.1.

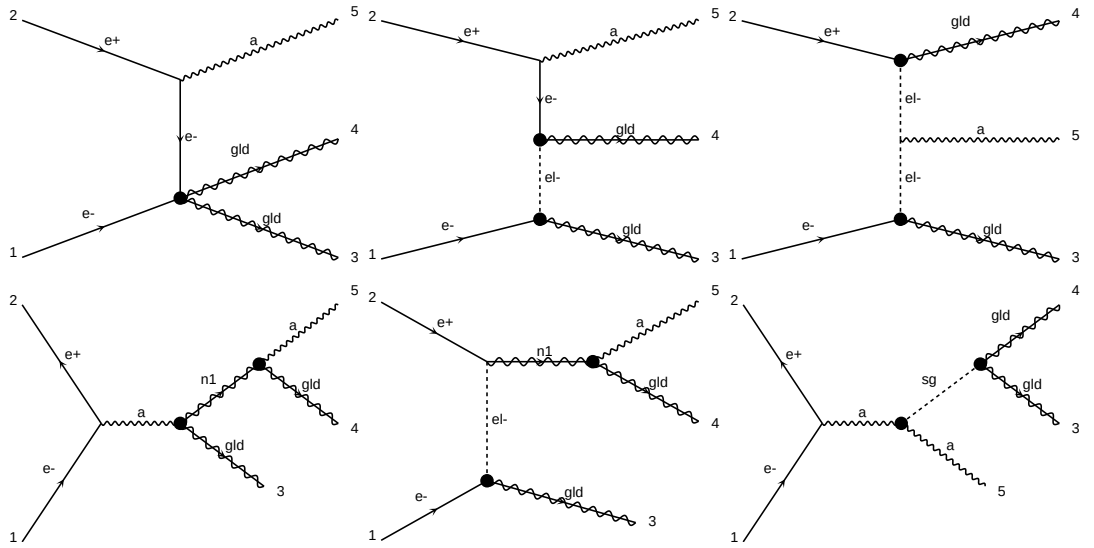


Figure 6.8: Representative Feynman diagrams for $e^+e^- \to \tilde{G}\tilde{G}\gamma$, generated by (modified) MadGraph 5 [14]. `n1` and `sg` denote a neutralino and a sgoldstino, respectively.

The right plot of Fig. 6.7 shows the neutralino mass dependence of the full signal cross section with the minimal cuts (6.36). While the $\tilde{G}\tilde{G}$ contribution is independent of the neutralino mass, the contribution from the $\tilde{\chi}\tilde{G}$ production is strongly suppressed when the neutralino mass approaches the CM energy due to the phase space closure. Therefore, the dominant subprocess can be different for different neutralino masses, giving rise to distinctive photon spectra. It should be noted that the interference between the two subprocesses is very small unless the neutralino width is too large. We verified this numerically by computing the two subprocess separately and checking that the sum of those reproduces the full $e^+e^- \to \gamma\tilde{G}\tilde{G}$ cross section, as in the figure. We suppress a possible contribution from the sgoldstinos by taking their masses to be too heavy to be produced on-shell.[4] We note that, if those are lighter than the $e^+e^-$ collision energy, the sgoldstino production in association with a photon and the subsequent decay contributes to the $\gamma\tilde{G}\tilde{G}$ final state. In Section 3.4.2, we briefly discussed the effect of sgoldstinos in the $\gamma\gamma \to \tilde{G}\tilde{G}$ process.

In the following, we focus on three different neutralino masses which exemplify different distributions. First, we fix the neutralino mass at 750 GeV so that $\sigma(\tilde{\chi}\tilde{G}) \sim \sigma(\tilde{G}\tilde{G} + \gamma)$. We subsequently take a lighter (heavier) neutralino at 650 (850) GeV so that the $\tilde{\chi}\tilde{G}$ ($\tilde{G}\tilde{G}$) production is dominant.

Before moving to the simulation, let us comment on our model implementation and the validation. We have implemented the SUSY QED Lagrangian given in Section 3.2.2 by using the superspace module into FeynRules 2 [29], which provides the Feynman rules in terms of the physical component fields and the UFO model file [87, 101] for matrix-element generators such as MadGraph 5 [14]. As mentioned in Section 5.4 the current MadGraph 5 (v2.0.2) [14] does not support four-fermion vertices involving

[4] We note that sgoldstinos with masses much smaller than the selectron mass do not obey a naturalness criterion [159].

more than one Majorana particle, so we have to modify MadGraph 5 and the helicity amplitudes as described in Section 5.4. We note that this model implementation allows us to generate different contributing processes, i.e. $\tilde{G}\tilde{G}$ and $\tilde{\chi}\tilde{G}$, within one event simulation (for a photino-like neutralino). To perform the simulations with a neutralino that is differently mixed than a photino, we implemented also the effective goldstino interaction Lagrangian given in (3.14).

We have explicitly checked our numerical results of the total cross sections by comparing with the analytic results for the two-to-two processes in Sections 6.1.2 and 6.2.2. For the $\tilde{G}\tilde{G}$ process, we compared our numerical results for the differential cross section of the two-to-three process in the low-energy limit, $\sqrt{s} \ll m_{\tilde{e},\tilde{\chi},S,P}$, with the analytic expression given in [129].

Moreover, our analytic amplitudes are checked numerically for each helicity combination by using the model implementations as described above.

## 6.4 Mono-photon plus missing energy signals

We now perform the simulation of monophoton events with missing energy for a future $e^+e^-$ collider. An irreducible SM background comes from $e^+e^- \to \gamma\nu\bar{\nu}$. To remove contributions from $e^+e^- \to \gamma Z \to \gamma\nu\bar{\nu}$, we impose the $Z$-peak cut

$$E_\gamma < \frac{s - m_Z^2}{2\sqrt{s}} - 5\Gamma_Z, \tag{6.37}$$

in addition to the minimal cuts (6.36). The background from the $t$-channel $W$-exchange process, which is the most significant one, can be efficiently reduced by using a positively polarized $e^-$ beam and a negatively polarized $e^+$ beam.

In Table 6.3, the signal cross sections of each subprocess, $\tilde{\chi}\tilde{G}$ and $\tilde{G}\tilde{G}$, as well as the SM background at $\sqrt{s} = 1$ TeV are presented without and with polarized $e^\pm$ beams. The dependence of the total cross section on the beam polarization is,

$$\sigma(P_{e^-}, P_{e^+}) = 2\sum_\lambda \Big(\frac{1 + P_{e^-}\lambda}{2}\Big)\Big(\frac{1 - P_{e^+}\lambda}{2}\Big)\,\sigma_\lambda, \tag{6.38}$$

where the beam polarizations $P_{e^\pm}$ ($|P_{e^\pm}| \leq 1$) are defined as the fraction of polarized electrons and positrons, respectively. Since for a photino-like neutralino the cross section is independent of the polarization, we can easily calculate the effect of polarized beams. In the following, we use the beam polarization $P_{e^\pm}$ as[5]

$$(P_{e^-}, P_{e^+}) = (0.9, -0.6), \tag{6.39}$$

leading to signal cross sections that are enhanced by a factor of 1.54. Further on, we apply the kinematical cuts of (6.36) and (6.37). For the SUSY signal, we take the three benchmark neutralino masses with the gravitino and selectron masses fixed at

[5] $|P_{e^-}| > 0.8$ and $|P_{e^+}| > 0.5$ are designed at the International Linear Collider (ILC) [176].

| $(P_{e^-}, P_{e^+})$ | $m_{\tilde{\chi}}$ [GeV] | $(m_{\tilde{e}} = 1$ TeV) $\tilde{\chi}\tilde{G}$ | $\tilde{G}\tilde{G}$ | $(m_{\tilde{e}} = 2$ TeV) $\tilde{\chi}\tilde{G}$ | $\tilde{G}\tilde{G}$ | [fb] SM bkg |
|---|---|---|---|---|---|---|
| $(0, 0)$ | 650 | 19.7 | | 49.2 | | |
| | 750 | 6.0 | 10.4 | 15.8 | 21.1 | 1452 |
| | 850 | 1.0 | | 2.5 | | |
| $(0.9, -0.6)$ | 650 | 30.4 | | 75.8 | | |
| | 750 | 9.2 | 16.1 | 24.3 | 32.7 | 64.9 |
| | 850 | 1.5 | | 3.4 | | |

Table 6.3: Cross sections in fb unit of each subprocess for the signal $e^+e^- \to \gamma\tilde{G}\tilde{G}$ and of the SM background $e^+e^- \to \gamma\nu\bar{\nu}$ at $\sqrt{s} = 1$ TeV, without and with beam polarizations. The kinematical cuts of (6.36) and (6.37) are applied. For the signal three (two) different neutralino (selectron) masses are taken with the gravitino mass fixed at $2 \times 10^{-13}$ GeV.

$2 \times 10^{-13}$ GeV and 2 TeV. We observe that the signal cross sections are enhanced by the polarized $e^{\pm}$ beams, while the SM background is significantly reduced.

Figure 6.9 presents the photon energy $E_\gamma$ (left) and rapidity $\eta_\gamma$ (right) distributions for the three signal benchmarks and for the SM background. The signal energy spectra show two distinct features. First, there is a peak in the low-energy region which arises from the $\tilde{G}\tilde{G}$ production process since the initial state radiation is dominant as in the SM background. We also note that the low-energy spectra are independent of the neutralino mass. Second, there is a flat contribution in the high-energy region coming from $\tilde{\chi}\tilde{G}$ production, reflecting the isotropic neutralino decay.[6] The contribution becomes smaller for the heavier neutralino (see also Table 6.3), and the lower edge allows us to extract the neutralino mass from (6.35).

The rapidity distributions are distinctive between the signal and the SM background. The photon coming from $\tilde{G}\tilde{G}$ production gives a flat $\eta_\gamma$ distribution while the photon coming from the neutralino decay results in the central region. In contrast, the photons of the SM background are emitted in the forward region.

To conclude, we discuss the selectron mass dependence. We do this independently for the low-energy peak, which arises purely from $\tilde{G}\tilde{G}$ production, and for the flat contribution arising from $\tilde{\chi}\tilde{G}$ associated production in the higher energy region.

As discussed in Sect. 6.1, the total rate of the $e^+e^- \to \tilde{G}\tilde{G}$ process depends on the selectron masses. In addition, the photon spectrum becomes harder for lighter selectrons; see Fig. 6.10, where we show the normalized photon energy distributions for $m_{\tilde{e}_\pm} = 0.5$, 2, 10 TeV and for the $\sqrt{s}/m_{\tilde{e}} = 0$ limit [129]. The distribution for $m_{\tilde{e}_\pm} =$ 10 TeV is in good agreement with the one in the high-mass limit. We note that in this limit the $e^+e^- \to \gamma\tilde{G}\tilde{G}$ differential cross section can be described by the $e^+e^- \to \tilde{G}\tilde{G}$ cross section times the standard photon splitting function in a good approximation [129]. Finally, we discuss the selectron mass dependence of the flat contribution arising from $\tilde{\chi}\tilde{G}$ production. Again, as discussed in Section 6.2.1, the cross section depends on

[6] We point out that the photonic energy distributions of Fig. 9 in Ref. [134] should be flat and not depend on the selectron mass.

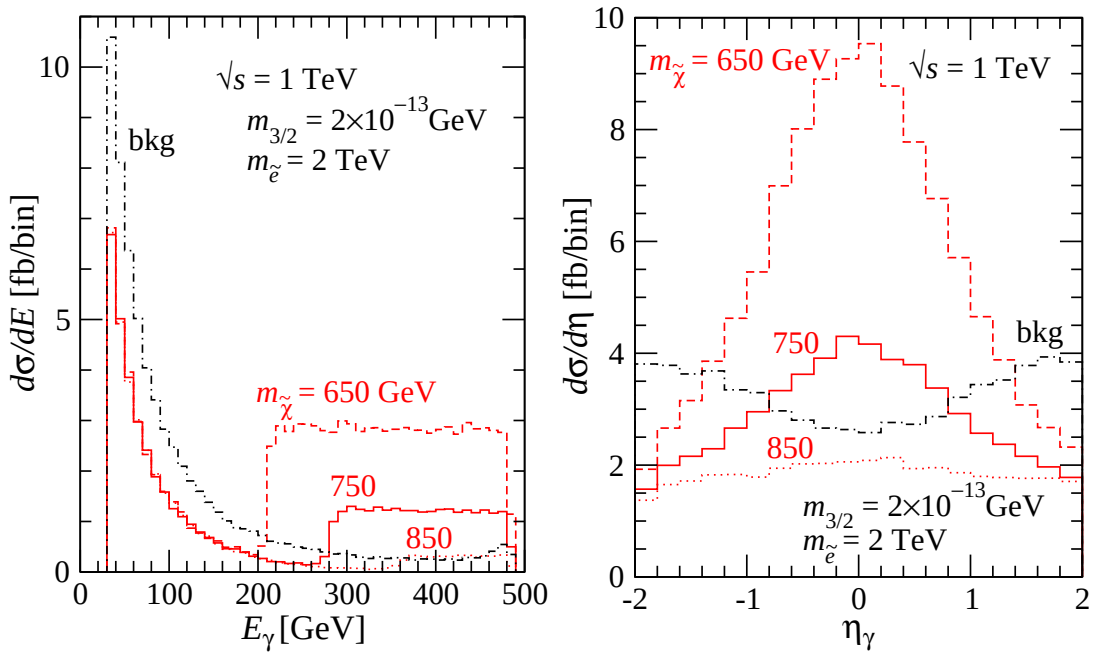


Figure 6.9: Photon energy (left) and rapidity (right) distributions for $e^+e^- \to \gamma\tilde{G}\tilde{G}$ at $\sqrt{s} = 1$ TeV for different neutralino masses with $m_{3/2} = 2 \times 10^{-13}$ GeV and $m_{\tilde{e}_\pm} = 2$ TeV. The kinematical cuts in (6.36) and (6.37) as well as the beam polarizations in (6.39) are applied. The SM background is also shown.

the selectron mass. In Fig. 6.11, we present the normalized angular dependence of the photon for the signal and the SM background in the laboratory frame, at $\sqrt{s} = 500$ GeV (left) and 1 TeV (right), where the selectron mass of 400, 800 and 1200 GeV with the 300 GeV neutralino mass are considered. The original angular distributions of the neutralino in Fig. 6.6 are flattened for the case of a 500 GeV collider since the neutralino decays isotropically in its rest frame and the boost effect is small. On the other hand, the angular distributions still survive for the case of a 1 TeV collider. This indicates a possibility to examine the mass of the $t, u$-channel selectrons when the decaying neutralino has a large momentum. We note that a kinematical cut on the forward and backward regions would also help to reduce the background.

## 6.5 Summary

In this chapter, we revisited gravitino pair production and neutralino-gravitino associated production, and studied the $\gamma + \not{E}$ signal for future $e^+e^-$ colliders.

We explicitely presented the helicity amplitudes for the both production processes, which gave us a deep understanding of the SUSY mass dependence of the production cross sections and the angular distributions.

We discussed the parameter dependence of the signal cross sections in detail, and showed that the relative importance between the two signal processes varies with the gravitino and neutralino masses and neutralino mixing, as well as with kinematical cuts.

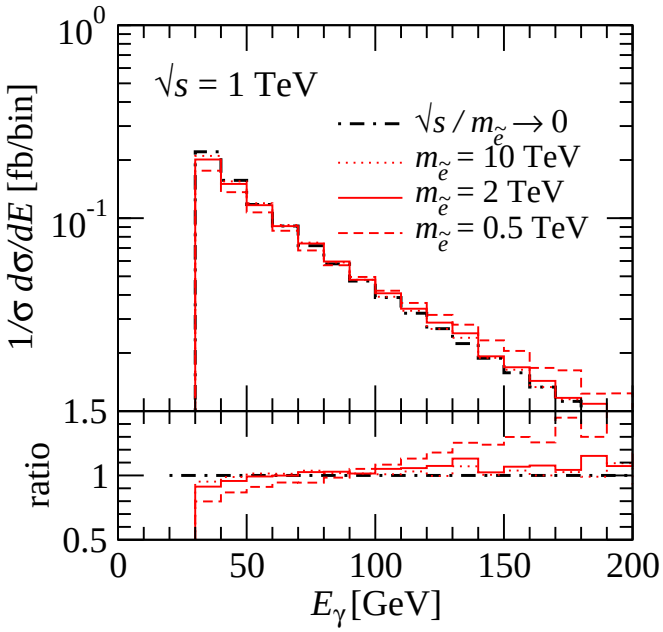


Figure 6.10: Normalized photon energy distributions for $e^+e^- \to \gamma\tilde{G}\tilde{G}$ at $\sqrt{s} = 1$ TeV for $m_{\tilde{e}_\pm} = 0.5$, 2, 10 TeV and for the high-mass limit, where the kinematical cuts (6.36) are applied. The ratios to the case in the high-mass limit are also shown.

We performed the event simulation for the SUSY signal as well as the SM background, taking into account the signal selection cut and the beam polarizations, and showed that the photon spectra from the two subprocesses are very distinctive. This is because the photon coming from the $\tilde{G}\tilde{G}$ production is mostly initial state radiation, while the the $\tilde{\chi}\tilde{G}$ associated production process leads to an energetic photon from the neutralino decay. We expect that future $e^+e^-$ colliders could explore the parameter space around our benchmark points and hence provide information on the masses of the relevant SUSY particles as well as the SUSY breaking scale.

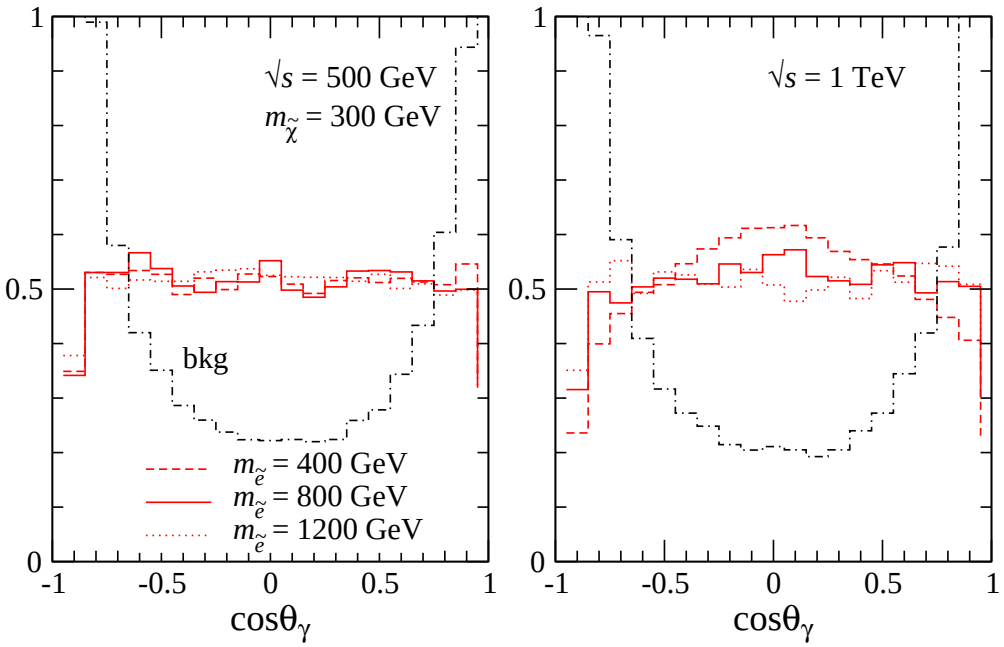


Figure 6.11: Normalized angular distributions of the photon in the laboratory frame for $e^+e^- \to \tilde{\chi}_1^0\tilde{G} \to \gamma\tilde{G}\tilde{G}$ at $\sqrt{s} = 500$ GeV (left) and 1 TeV (right), where $m_{\tilde{e}_\pm} = 400$ (solid), 800 (dashed) and 1200 (dotted) GeV with $m_{\tilde{\chi}_1^0} = 300$ GeV are considered. The kinematical cuts in (6.36) and (6.37) and the beam polarizations $(P_{e^-}, P_{e^+}) = (0.9, -0.6)$ are taken into account. The normalized angular distributions of the SM background are also shown by dot-dashed lines.

# CHAPTER 7

## Mono-electron signals in gravitino production in $e^-\gamma$ collisions

We consider gravitino productions in association with a selectron which subsequently decays into an electron and a gravitino at an $e\gamma$ collider, which is an option at a future linear collider [176],

$$e^-\gamma \to \tilde{e}^-\tilde{G} \to e^-\tilde{G}\tilde{G},$$

in an $R$-parity conserving scenario where the gravitino is the LSP and the selectron the NLSP.

We start by discussing the selectron-gravitino production process in detail in Section 7.1. We present the explicit helicity amplitudes. Subsequently, we investigate the dependence of the total cross section on the selectron mass, and discuss the angular dependence of the produced selectron for various neutralino masses and CM energies.

In Section 7.2, we present the selection cuts and discuss the mono-electron plus missing-energy signal.

## 7.1 Selectron-gravitino associated production

In this section, we repeat a study as for the neutralino-gravitino associated production for a scenario of a selectron NLSP with a gravitino LSP. We consider associated gravitino productions with a selectron, especially a right-handed selectron, in $e^-\gamma$ collisions with the prompt selectron decay into an electron and a gravitino,

$$e^-\gamma \to \tilde{e}_R^-\tilde{G} \to e^-\tilde{G}\tilde{G}, \tag{7.1}$$

leading to a mono-electron plus missing-energy signal.

While the heavy-mass limit for all SUSY particles except gravitino and selectron are assumed in Ref. [136], we take into account the $t$-channel intermediate neutralinos and show a possibility to determine their mass in the signal distributions.

### 7.1.1 Helicity amplitudes

We present the helicity amplitudes explicitly for the production process:

$$e^-\Big(p_1, \frac{\lambda_1}{2}\Big) + \gamma(p_2, \lambda_2) \to \tilde{e}_R^-(p_3) + \tilde{G}\Big(p_4, \frac{\lambda_4}{2}\Big). \tag{7.2}$$

The helicity amplitudes for the process are expressed as sums of $s$-, $t$-, and $u$-channel amplitudes

$$\mathcal{M}_{\lambda_1\lambda_2,\lambda_4} = \mathcal{M}^s + \sum_{i=1}^{4}\mathcal{M}^{t_i} + \mathcal{M}^u, \tag{7.3}$$

corresponding to the Feynman graph 6, (2+3+4+5), and 1, respectively, in Fig. 7.1. Based on the effective goldstino interaction Lagrangian given in Section 3.2.2, they are

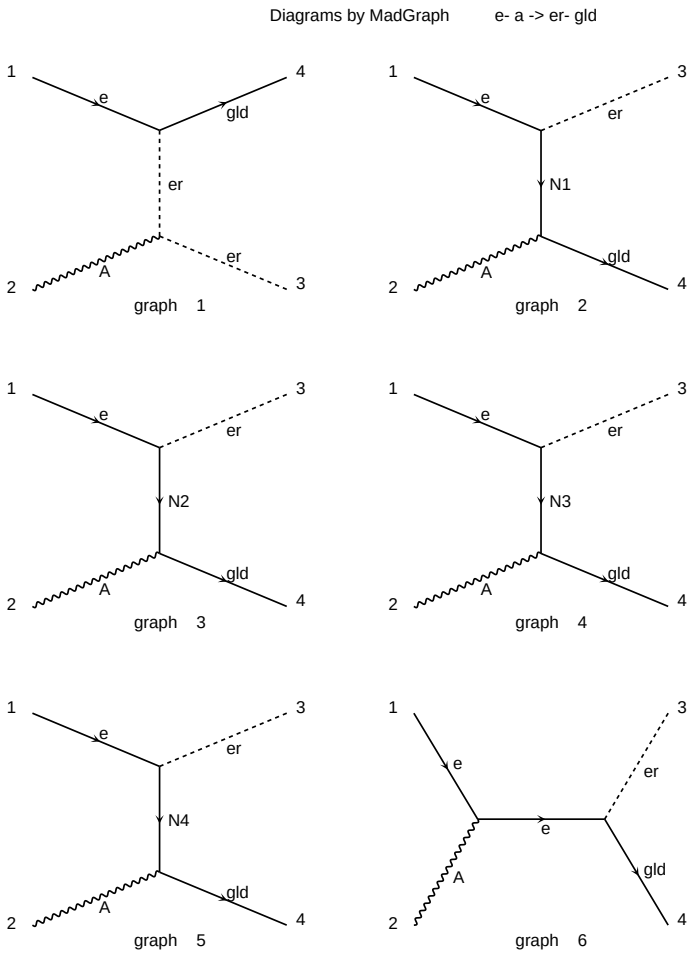


Figure 7.1: Feynman diagrams for the $\tilde{e}_R^-$-$\tilde{G}$ production in $e^-\gamma$ collisions, generated by `MadGraph` [48].

given in the four-spinor basis by

$$i\mathcal{M}^{s}_{\lambda_1\lambda_2,\lambda_4} = \frac{-e\, m^2_{\tilde{e}_{\lambda_1}}}{\sqrt{3}\,\overline{M}_{\rm Pl} m_{3/2}} \frac{1}{s}\, \epsilon_\mu(p_2,\lambda_2) \times \bar{u}(p_4,\lambda_4)(\not{p}_1 + \not{p}_2)\gamma^\mu u(p_1,\lambda_1), \tag{7.4a}$$

$$i\mathcal{M}^{t_i}_{\lambda_1\lambda_2,\lambda_4} = \frac{e\, m_{\tilde{\chi}_i^0} C^{\gamma\tilde{\chi}_i} C^{\tilde{e}\tilde{\chi}_i}_{\lambda_1}}{2\sqrt{3}\,\overline{M}_{\rm Pl} m_{3/2}} \frac{1}{t - m^2_{\tilde{\chi}_i^0}}\, \epsilon_\mu(p_2,\lambda_2) \times \bar{u}(p_4,\lambda_4)[\not{p}_2, \gamma^\mu](\not{p}_1 - \not{p}_3 + m_{\tilde{\chi}_i^0})u(p_1,\lambda_1), \tag{7.4b}$$

$$i\mathcal{M}^{u}_{\lambda_1\lambda_2,\lambda_4} = \frac{-e\, m^2_{\tilde{e}_{\lambda_1}}}{\sqrt{3}\,\overline{M}_{\rm Pl} m_{3/2}} \frac{1}{u - m^2_{\tilde{e}_{\lambda_1}}}\, \epsilon_\mu(p_2,\lambda_2) \times \bar{u}(p_4,\lambda_4)u(p_1,\lambda_1)\,(p_3 + p_1 - p_4)^\mu, \tag{7.4c}$$

with the couplings $C^{\gamma\tilde{\chi}_i}$ and $C^{\tilde{e}\tilde{\chi}_i}_{\pm}$ defined in (6.20). Only the $\lambda_1 = +1$ case contributes to the $\tilde{e}_R$ (or $\tilde{e}_+$ in our notation) production in the final state, which is relevant in our

| $\lambda_1\lambda_2$ | $\lambda_4$ | | $\hat{\mathcal{M}}^s$ | $\hat{\mathcal{M}}^t$ | $\hat{\mathcal{M}}^u$ | |
|---|---|---|---|---|---|---|
| $++$ | $-$ | $2\sin\frac{\theta}{2}$ [ | $\frac{m_{\tilde{e}}^2}{s}$ | $-\sum_i C^{\gamma\tilde{\chi}_i}C_+^{\tilde{e}\tilde{\chi}_i}\frac{m_{\tilde{\chi}_i}^2}{t-m_{\tilde{\chi}_i}^2}$ | $+\frac{m_{\tilde{e}}^2}{u-m_{\tilde{e}}^2}\beta\frac{1+\cos\theta}{2}$ | ] |
| $+-$ | $+$ | $(1-\cos\theta)\cos\frac{\theta}{2}$ [ | | $-\sum_i C^{\gamma\tilde{\chi}_i}C_+^{\tilde{e}\tilde{\chi}_i}\frac{\sqrt{s}m_{\tilde{\chi}_i}}{t-m_{\tilde{\chi}_i}^2}\beta$ | | ] |
| $+-$ | $-$ | $-(1+\cos\theta)\sin\frac{\theta}{2}$ [ | | | $\frac{m_{\tilde{e}}^2}{u-m_{\tilde{e}}^2}\beta$ | ] |

Table 7.1: The reduced helicity amplitudes $\hat{\mathcal{M}}_{\lambda_1\lambda_2,\lambda_4}$ for $e^-_{\lambda_1}\gamma_{\lambda_2}\to\tilde{e}^-_R\tilde{G}_{\lambda_4}$.

following analyses. On the other hand, the $\lambda_1=-1$ case gives nonzero amplitudes only for the $\tilde{e}_L$ production.

We define the reduced helicity amplitudes, $\hat{\mathcal{M}}$, as

$$i\mathcal{M}_{\lambda_1\lambda_2,\lambda_4}=\frac{-e}{\sqrt{6}\,\overline{M}_{\rm Pl}m_{3/2}}\sqrt{\beta}\,s\,\hat{\mathcal{M}}_{\lambda_1\lambda_2,\lambda_4}, \tag{7.5}$$

and these are shown in Table 7.1. Similar to (6.22), the four-momenta and helicities of the external particles are defined in the $e\gamma$ CM frame with $\beta=1-m_{\tilde{e}_R}^2/s$. The following features of the amplitudes are worth noting:

1. The amplitude $\mathcal{M}_{++,+}$ is zero since the coupling structures do not allow this helicity combination for a massless gravitino.

2. The overall angular dependence is dictated by $J=1/2$ or $J=1$ $d$ functions as

$$\mathcal{M}_{\lambda_1\lambda_2,\lambda_4}\propto d^{|\lambda_1/2-\lambda_2|}_{\lambda_1/2-\lambda_2,-\lambda_4/2}(\theta). \tag{7.6}$$

3. The amplitude $\mathcal{M}^t$ depends on the mass of the propagating neutralinos; as the neutralino mass increases, $\mathcal{M}^t_{++,-}$ becomes larger, while $\mathcal{M}^t_{+-,+}$ becomes smaller. On the other hand, the $\mathcal{M}^s$ and $\mathcal{M}^u$ do not depend on their mass but on the selectron mass.

4. The right-handed selectron can couple only to the bino component of neutralinos $\tilde{\chi}_i^0$, i.e. $U_{1i}$ in the $\tilde{\chi}_i^0$-$e$-$\tilde{e}_R$ coupling in (6.20). Therefore, e.g. for the bino-like lightest neutralino case, only the $\tilde{\chi}_1^0$-exchange amplitude is nonzero among the four neutralino amplitudes.

5. In the threshold region, similar to the $e^+e^-\to\tilde{\chi}_1^0\tilde{G}$ process discussed in Section 6.2.1, the amplitudes are proportional to $\beta^{3/2}$, which gives rise to a strong suppression on the production cross section.

6. In the high-energy limit, the amplitude $\mathcal{M}_{+-,+}$ becomes dominant, and hence the cross section depends on the neutralino mass but not on the produced selectron mass.

We note that our helicity amplitudes in Table 7.1 agree with Eqs. (4) and (5) in [136],[1] where the heavy neutralino mass limit is assumed. The helicity-summed amplitude squared also agrees with Eq. (7) of [141] for the squark associated process $qg \to \tilde{q}\tilde{G}$ after substitutions for the masses and the couplings as in (6.26) and the exchange of $t \leftrightarrow u$. Moreover, we checked our amplitudes for each helicity combination numerically by the gravitino/goldstino code in `MG/MEv4` [48, 166].

In practice, a high-energy photon beam is provided by the backward Compton scattering of laser photons on a high-energy electron beam [73, 74], as an option of a future linear collider [176], as discussed in Section 4.1.2.[2]

### 7.1.2 Total cross section

The full cross section at an $e\gamma$ collider is calculated by convoluting the $e\gamma$ cross section ($\sigma^{e\gamma}$) with the photon distribution function of Eq. (4.4) as

$$\sigma(s_{ee}) = \int_{x_{\min}}^{x_{\max}} f_\gamma(x,y)\, \sigma^{e\gamma}(s)\, dx \tag{7.7}$$

with $x_{\min} = m_{\tilde{e}}^2/s_{ee}$ and $s = x s_{ee}$, where $\sqrt{s_{ee}}$ is the original $e^-e^-$ CM energy. The spin-summed and averaged $e\gamma$ cross section is obtained by $\sigma^{e\gamma} = (\sigma_+^{e\gamma} + \sigma_-^{e\gamma})/2$ with the photon-helicity ($\lambda_2$) dependent cross section

$$d\sigma_{\lambda_2}^{e\gamma} = \frac{1}{2s}\frac{1}{2}\sum_{\lambda_{1,4}} |\mathcal{M}_{\lambda_1\lambda_2,\lambda_4}|^2 d\Phi_2. \tag{7.8}$$

Figure 7.2 shows total cross sections of the associated gravitino productions with a right-handed selectron in $e^-\gamma$ collisions as a function of the selectron mass, where the CM energy, $\sqrt{s_{ee}}$, of the $e^-e^-$ system is fixed at 500 GeV and 1 TeV. The parameters for the photon luminosity function in (4.4) are taken to be $y = 4.8$ and $P_e P_l = -0.9$. For simplicity, we assume a bino-like lightest neutralino so that only the $\tilde{\chi}_1^0$-exchange amplitude is taken into account for the $t$-channel amplitude; see comment 4 in Sect. 7.1.1. We note that $\sigma \propto 1/m_{3/2}^2$ and we take $m_{3/2} = 10^{-13}$ GeV in our study. When the selectron mass is close to the collider energy, the cross sections are strongly suppressed due to $\sigma^{e\gamma} \propto \beta^4$ as mentioned in comment 5 in Sect. 7.1.1, similar to the $e^+e^- \to \tilde{\chi}_1^0\tilde{G}$ process in Fig. 6.5. In addition, the production cross section is nonzero only when $m_{\tilde{e}_R} < \sqrt{x_{\max} s_{ee}}$. It should be stressed here that the cross section is quite sensitive to the mass of the $t$-channel intermediate neutralinos, even if the collider energy cannot reach their mass.

[1] Except the sign in the parentheses of the first term in Eq. (4) in [136].

[2] Although the scattered photons are polarized when $P_e \neq 0$ or $P_l \neq 0$ [72, 74], we average the two opposite polarized modes, $(P_e > 0, P_l < 0)$ and $(P_e < 0, P_l > 0)$, so that we consider $f_\gamma(x,y)$ as the unpolarized distribution function in the following analyses.

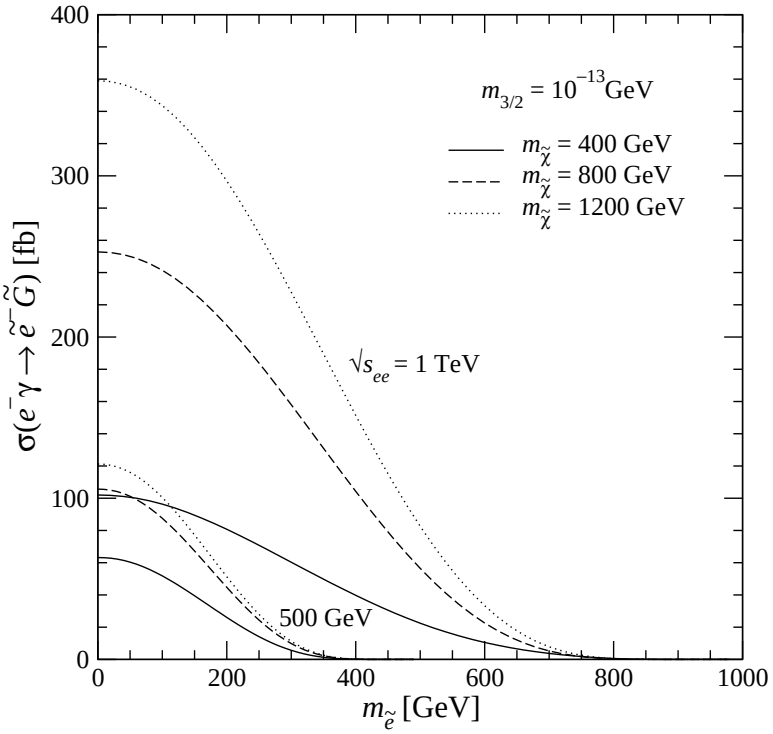


Figure 7.2: Total cross sections of associated gravitino productions with a right-handed selectron in $e^-\gamma$ collisions, $e^-\gamma \to \tilde{e}_R^-\tilde{G}$, at $\sqrt{s_{ee}} = 500$ GeV and 1 TeV for $m_{3/2} = 10^{-13}$ GeV as a function of the selectron mass. The neutralino mass is fixed at 400 (solid), 800 (dashed) and 1200 (dotted) GeV, respectively.

### 7.1.3 Angular distribution of the selectron

Before we consider the selectron decay, let us look in detail at the angular distribution of the produced selectron in the $e\gamma$ system since the scalar decay $\tilde{e}_R \to e\tilde{G}$ is isotropic and hence the electron distribution is given by purely kinematical effects of the decaying selectron and the boost from the $e^-\gamma$ CM frame to the $e^-e^-$ laboratory frame. In Fig. 7.3, the $\cos\theta$ distributions of the selectron in $e^-\gamma \to \tilde{e}_R^-\tilde{G}$ for $m_{3/2} = 10^{-13}$ GeV and $m_{\tilde{e}_R} = 300$ GeV are shown, where the scattering angle $\theta$ is defined from the momentum direction of the incident electron in the $e\gamma$ CM frame. We fix the $e\gamma$ CM energy as $\sqrt{s} = \sqrt{x_{\max} s_{ee}}$, where the photon luminosity sharply peaks for $P_e P_l \sim -1$ (see Fig. 4.3), i.e. 455 GeV for a 500 GeV collider (left) and 910 GeV for a 1 TeV collider (right). One can find that not only the total cross section as shown in Fig. 7.2 but also the angular distribution is quite sensitive to the mass of the $t$-channel intermediate neutralinos. As the neutralino mass is increasing, the cross section with $\lambda_2 = +1$ becomes larger and the peak is shifted to the backward since the $t$-channel amplitude becomes more important and its intrinsic $\sin\frac{\theta}{2}$ angular dependence is revealed as $1/(t - m_{\tilde{\chi}}^2)$ goes to $1/m_{\tilde{\chi}}^2$. On the other hand, the cross section with $\lambda_2 = -1$ becomes smaller. As easily seen in Table 7.1, the productions to the forward region ($\cos\theta = 1$) are forbidden for all helicity combinations because of the angular momentum conservation, while the productions to the backward region ($\cos\theta = -1$) are allowed only for the $\lambda_2 = +1$ case.

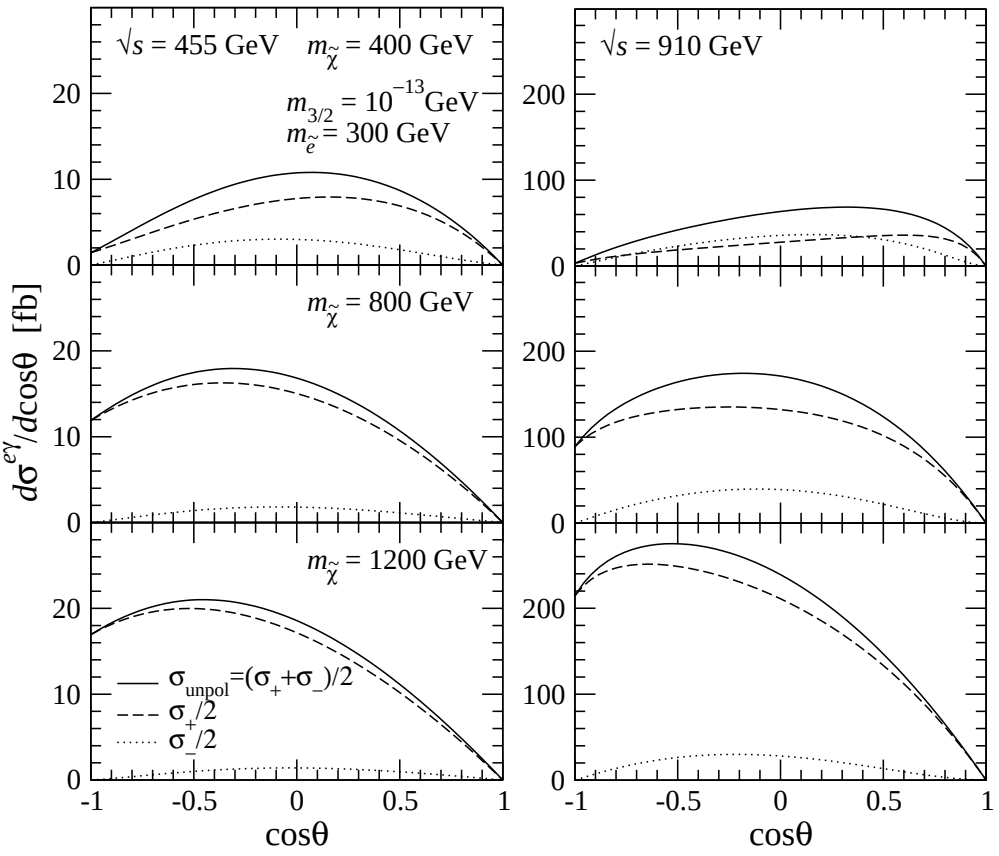


Figure 7.3: Angular distributions of the selectron in $e^-\gamma \to \tilde{e}_R^-\tilde{G}$ at $\sqrt{s} = 455$ (left) and 910 (right) GeV in the $e\gamma$ CM frame, with $m_{3/2} = 10^{-13}$ GeV and $m_{\tilde{e}_R} = 300$ GeV. The neutralino mass is taken to be 400 (top), 800 (middle) and 1200 (bottom) GeV, respectively. The photon-helicity dependent cross sections $d\sigma^{e\gamma}_{\lambda_2}$ are also shown by dashed lines ($\lambda_2 = +1$) and dotted lines ($\lambda_2 = -1$).

The decay of the selectron into an electron and a gravitino is isotropic. The partial decay rate of the selectron into an electron and a gravitino is given by

$$\Gamma(\tilde{e}_R \to e\tilde{G}) = \frac{m^5_{\tilde{e}_R}}{48\pi \overline{M}^2_{\rm Pl} m^2_{3/2}}, \tag{7.9}$$

and $\Gamma(\tilde{e}_R \to e\tilde{G}) = 0.27$ GeV with $m_{\tilde{e}_R} = 300$ GeV and $m_{3/2} = 10^{-13}$ GeV.

## 7.2 Mono-electron plus missing energy signals

Let us now turn to the simulations for the signal of single-electron plus missing energy in the $e^-e^-$ laboratory frame. An irreducible SM background for the event of mono-electron plus missing energy comes from $e^-\gamma \to e^-\nu\bar{\nu}$. In addition to the minimal cuts

| $\sigma$ [fb] | | $P_{e^-} =$ | 0 | 0.9 |
|---|---|---|---|---|
| $\sqrt{s_{ee}} = 500$ GeV | $m_{\tilde{\chi}} = 400$ GeV | | 5 | 9 |
| | 800 GeV | | 9 | 16 |
| | 1200 GeV | | 10 | 18 |
| | SM background | | 2594 | 284 |
| $\sqrt{s_{ee}} = 1$ TeV | $m_{\tilde{\chi}} = 400$ GeV | | 58 | 110 |
| | 800 GeV | | 152 | 289 |
| | 1200 GeV | | 220 | 416 |
| | SM background | | 2796 | 290 |

Table 7.2: Cross sections in fb unit for the signal, $e^-\gamma \to \tilde{e}_R^-\tilde{G} \to e^-\tilde{G}\tilde{G}$, and the SM background, $e^-\gamma \to e^-\nu\bar{\nu}$, at $\sqrt{s_{ee}} = 500$ GeV and 1 TeV without and with the electron beam polarization $P_{e^-} = 0.9$. We take $m_{3/2} = 10^{-13}$ GeV, $m_{\tilde{e}_R} = 300$ GeV, and $B(\tilde{e}_R \to e\tilde{G}) = 1$. The minimal cuts in (7.10) and the $Z$-peak cut in (7.11) are taken into account.

for the detection of electrons

$$E_e > 0.03\sqrt{s}, \quad |\eta_e| < 2, \tag{7.10}$$

we impose the $Z$-peak cut

$$M_{\rm miss} > 100 \text{ GeV}, \tag{7.11}$$

which can remove the contributions from $e^-\gamma \to e^-Z \to e^-\nu\bar{\nu}$. The main background contribution coming from the $W$-exchange can be reduced by using a polarized electron beam.

In Table 7.2, the selection efficiencies for the signal and background processes without and with the electron beam polarization are presented, where the above two kinematical cuts, (7.10) and (7.11), are taken into account and it is assumed that the branching ratio of the selectron decay to an electron and a gravitino is unity, $B(\tilde{e}_R \to e\tilde{G}) = 1$. The cross sections both for the signal and background are calculated by `MG/MEv4` [90] with gravitino interactions [48, 166], where we also implemented the photon luminosity function of (4.4). By using a positively polarized electron beam of $P_{e^-} = 0.9$, the signal is enhanced by a factor of 1.9 because the cross section with $\lambda_1 = -1$ is zero, while the background can be reduced by a factor of 10. It must be noted again that the signal cross section is inversely proportional to the gravitino mass squared.

Figure 7.4 presents normalized energy distributions of the electron for the signal and the SM background, corresponding to 20,000 events each, at $\sqrt{s_{ee}} = 500$ GeV (left) and 1 TeV (right), where the lightest neutralino mass of 400, 800 and 1200 GeV with the 300 GeV selectron mass are considered. The kinematical cuts in (7.10) and (7.11) and the electron beam polarization $P_{e^-} = 0.9$ are taken into account. We notice again that the electron distribution is given by two boost effects, along the momentum of the decaying selectron and along the beam axis. The momentum of the incident electron is chosen to the $+z$ direction, and hence the produced electrons in the $e\gamma$ CM frame

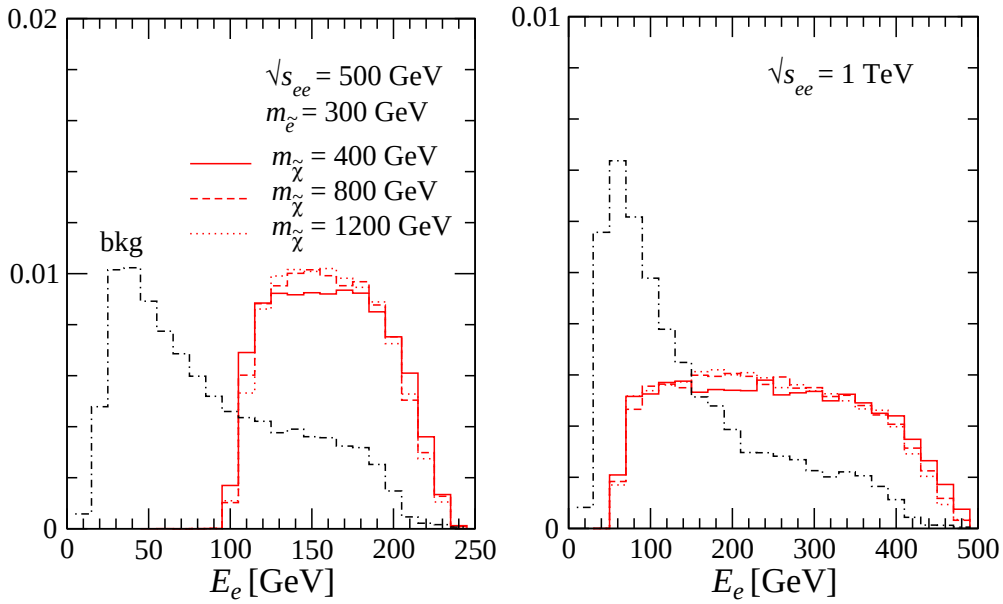


Figure 7.4: Normalized energy distributions of the electron for $e^-\gamma \to \tilde{e}_R^-\tilde{G} \to e^-\tilde{G}\tilde{G}$ at $\sqrt{s_{ee}} = 500$ GeV (left) and 1 TeV (right), where $m_{\tilde{\chi}} = 400$ (solid), 800 (dashed) and 1200 (dotted) GeV with $m_{\tilde{e}_R} = 300$ GeV are considered. The kinematical cuts in (7.10) and (7.11) and the electron beam polarization $P_{e^-} = 0.9$ are taken into account. Those of the SM background are also shown by dot-dashed lines.

are boosted to the forward direction. Although the signal distributions no longer have either a flat shape or a sharp edge due to the boost along the beam direction, the energy is restricted as

$$\frac{m_{\tilde{e}_R}^2}{2\sqrt{s_{ee}}} < E_e < \frac{\sqrt{s_{ee}}}{2}, \tag{7.12}$$

where the lower edge can determine the selectron mass. The energetic electrons tend to be suppressed since the original selectron productions in the forward region are not allowed. Moreover, the $z$-axis boost effect makes the distributions slightly different for the different neutralino mass, which can be dictated by the peak shift in Fig. 7.3. Since the background is located mostly in the low-energy region, an appropriate cut on the energy can help to enhance the signal over the background.

Finally, the angular distributions of the electron are shown in Fig. 7.5, where the angle $\theta_e$ is measured from the direction of the electron beam, or the $+z$ direction, in the $e^-e^-$ laboratory frame. The electrons tend to be produced more in the forward region ($\cos\theta_e > 0$) due to the system boost. For the $\sqrt{s_{ee}} = 500$ GeV case the original $m_{\tilde{\chi}}$ dependence in the angular distributions of the selectron shown in Fig. 7.3 is no longer observed, while the dependence can be seen at $\sqrt{s_{ee}} = 1$ TeV. This indicates that we would be able to determine the mass of the $t$-channel neutralinos when the collider energy is relatively higher than the selectron mass. We note that the background can be reduced further by a kinematical cut on the backward region.

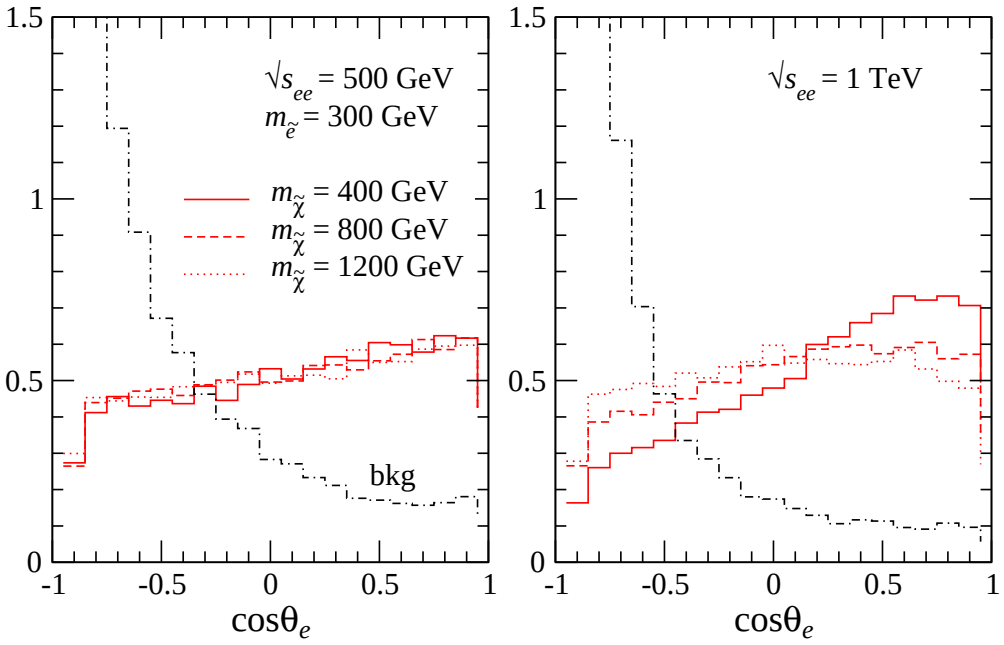


Figure 7.5: Normalized angular distributions of the electron in the $e^-e^-$ laboratory frame for $e^-\gamma \to \tilde{e}_R^-\tilde{G} \to e^-\tilde{G}\tilde{G}$. The detail is the same as Fig. 7.4.

Before closing this section, we point out that selectron-neutralino associated productions in neutralino LSP scenarios lead to the same signal, $e + \not{E}$, and have been studied intensively [177–180]. Since the LSP mass is quite different between the two models, $\mathcal{O}(10^{-13}$ GeV) for the $\tilde{G}$ LSP and $\mathcal{O}(100$ GeV) for the $\tilde{\chi}_1^0$ LSP, the distributions of the final electron are distinctive and could provide a hint of SUSY breaking mechanism.

## 7.3 Summary

We considered gravitino productions associated with a selectron which subsequently decays into an electron and a gravitino at an $e\gamma$ collider, $e^-\gamma \to \tilde{e}^-\tilde{G} \to e^-\tilde{G}\tilde{G}$.

We presented the explicit helicity amplitudes for the production process, and discussed the mono-electron plus missing-energy signal, including the energy spectrum of the backward-Compton scattered photons for incident photons.

Similar to the $e^+e^- \to \tilde{\chi}_1^0\tilde{G}$ process, we found that the production cross section and the kinematical distributions of the electron in the final state are quite sensitive to the mass of the $t$-channel intermediate neutralinos as well as the mass of the decaying selectron.

In the next chapters, we discuss possible signatures arising from gravitino production at the LHC.

# CHAPTER 8

## Jets plus missing energy signals in gravitino production at the LHC

We study the jets plus missing energy signature at the LHC,

$$pp \to \text{jets} + \not{E}_T, \tag{8.1}$$

in an $R$-parity conserving scenario where the gravitino is the LSP and very light. We consider gluinos to be the NLSP and to promptly decay into a gluon and a gravitino. All other SUSY particles are assumed to be too heavy to be produced on-shell. The missing energy will be carried by two gravitinos due to the $R$-parity conservation, and two processes, *gluino-gravitino associated production* and *gluino pair production* contribute to the signal, to be described in detail in Section 8.1. We note that contributions from direct gravitino pair production are neglected in this study.

To be able to identify new physics in such a multi-jet signature at the LHC, a reliable and precise simulation of the signal as well as of the QCD background is crucial. This can be provided by merging matrix elements (ME) with parton showers (PS). Thanks to the availability of new simulation tools is now possible to apply the ME+PS merging procedure to avoid double counting for such a signal which contains two different types of subprocesses. In section 8.2, we briefly describe the ME/PS merging technique employed in this work and the validation of our signal and background event generation.

In Section 8.3 we examine basic selection cuts to curb the SM background, and discuss how distributions of the jets and missing transverse energy can be used to determine the SUSY particle masses.

## 8.1 Light gravitino production at the LHC

Two main production mechanisms, gluino-gravitino associated production ($pp \to \tilde{g}\tilde{G}$), and gluino pair production ($pp \to \tilde{g}\tilde{g}$) , whose importance varies with the gravitino and gluino masses, can contribute to the final state

$$pp \to \text{partons} + \tilde{G}\tilde{G}, \tag{8.2}$$

which gives the jets+$\not{E}_T$ signature. Before considering the two processes in detail, we remark that gravitino pair production ($pp \to \tilde{G}\tilde{G}$), where the scalar superpartners of the goldstinos (the so-called sgoldstinos) $s$-channel exchange diagrams and the $t, u$-channel gluino as well as squark exchange diagrams are involved, might give rise to the jets+$\not{E}_T$ signal when extra QCD radiation is significant, see Sections 3.4.2 and 6.1. However, these signal events can be expected only in the low $p_T$ region. Therefore, we expect them to be negligible in our signal region and we do not include them in this work.

### 8.1.1 Gluino-gravitino associated production

Gravitino production associated with a gluino and the subsequent gluino decay,

$$pp \to \tilde{g}\tilde{G} \to g\tilde{G}\tilde{G}, \tag{8.3}$$

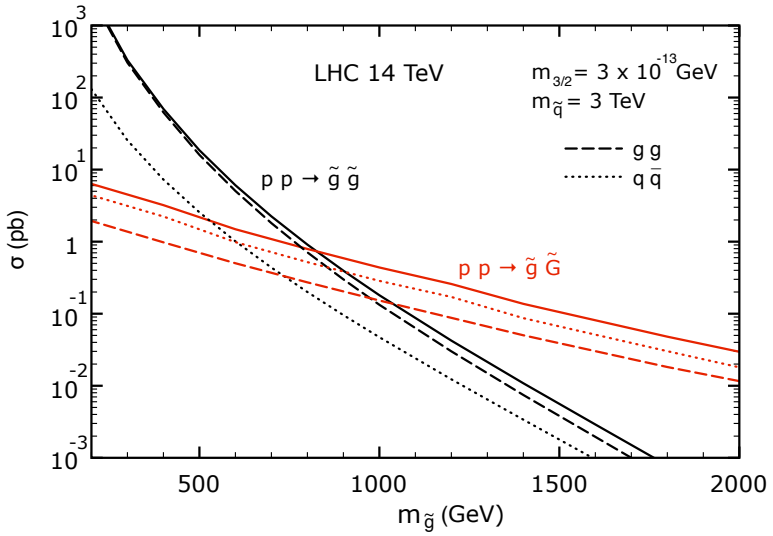


Figure 8.1: Total cross sections of the gluino-gravitino associated production for the gravitino mass $m_{3/2} = 3 \times 10^{-13}$ GeV, $pp \to \tilde{g}\tilde{G}$ (red), and the gluino pair production, $pp \to \tilde{g}\tilde{g}$ (black), at the LHC with $\sqrt{s} = 14$ TeV as a function of the gluino mass. The dashed and dotted lines represent the contributions of the $gg$ and $q\bar{q}$ initial states, respectively. The squark masses are fixed at 3 TeV.

arises from the $gg$ and $q\bar{q}$ initial states, and leads to a mono-jet plus missing energy signal at the leading order (LO). The partonic cross section can be computed by using the effective goldstino interaction Lagrangian, given in Section 3.2.2, and the analytic expression can be found, e.g., in [141]. The analytic helicity amplitudes for $q\bar{q} \to \tilde{g}\tilde{G}$ are equivalent to those presented in Section 6.2.1 for the $e^+e^- \to \tilde{\chi}_1^0\tilde{G}$ process after substitutions for the masses and the couplings as shown in Eq. (6.26).

The cross section for the process is inversely proportional to the square of the Planck scale times the gravitino mass

$$\sigma(pp \to \tilde{g}\tilde{G}) \propto 1/(M_{\rm Pl}\, m_{3/2})^2, \tag{8.4}$$

and therefore it becomes significant at colliders only when the gravitino is very light, $m_{3/2} \sim \mathcal{O}(10^{-12}$ GeV) or less. As expected, gravitino production associated with other SUSY particles also follows the scaling of eq. (8.4).

Fig. 8.1 presents the total cross section of the gluino-gravitino associated production (8.3) for $m_{3/2} = 3 \times 10^{-13}$ GeV at the LHC with $\sqrt{s} = 14$ TeV as a function of the gluino mass. The CTEQ6L1 parton distribution functions [76] are employed, and the renormalization and factorization scales are fixed at the average mass of the final state particles, i.e. $\mu_R = \mu_F = (m_{\tilde{g}} + m_{3/2})/2 \sim m_{\tilde{g}}/2$. As the cross section scales as $m_{3/2}^{-2}$, we fix the gravitino mass here so that the production cross section becomes comparable to the gluino pair production process (shown by black lines). We also show contributions of each subprocess, the $gg$ and $q\bar{q}$ initial state, with a dashed and dotted line, respectively. The $gg$ subprocess depends only on the gluino mass once the

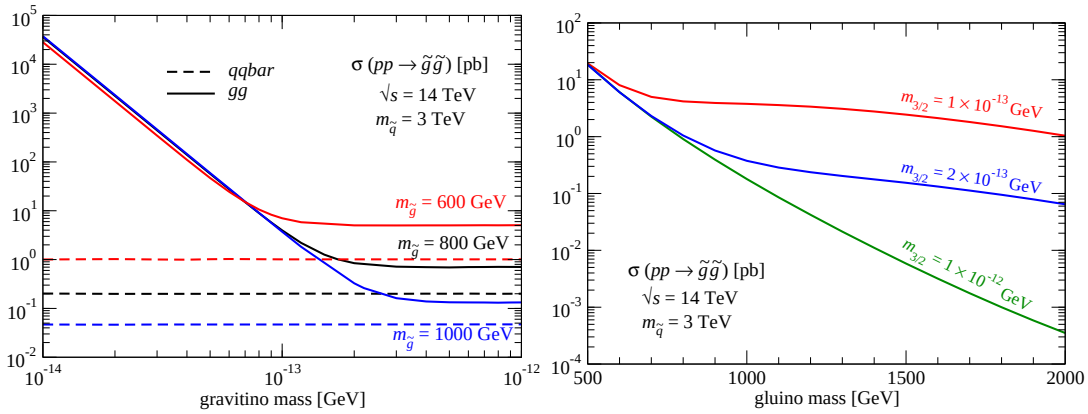


Figure 8.2: Total cross sections for gluino pair-production at the LHC, running at a center-of-mass energy of 14 TeV, presented as a function of the gravitino mass (left) and of the gluino mass (right). Squark masses are fixed to 3 TeV.

gravitino mass is fixed, while the $q\bar{q}$ initiated cross section also depends on the $t$- and $u$-channel-exchanged squark masses. Here, the masses of the left-handed and right-handed squarks are fixed at 3 TeV. It should be noted that those contributions are not decoupled in the large squark mass, and the heavier squark exchange increases the cross section since the gravitino-quark-squark couplings are proportional to the squark mass squared. Therefore, as one can see in Fig. 8.1, the cross section of the $q\bar{q}$ channel can be larger than that of the $gg$ channel even at the LHC.

### 8.1.2 Gluino pair production

In the scenario where the gravitino is the LSP and the gluino the NLSP, gluino pair production gives rise to a di-jet plus missing energy signature at the lowest order:

$$pp \to \tilde{g}\tilde{g} \to gg\tilde{G}\tilde{G}. \tag{8.5}$$

The LO cross section is shown in Fig. 8.1 as a function of the gluino mass.Unlike the $\tilde{g}\tilde{G}$ associated production, the $\tilde{g}\tilde{g}$ production needs the partonic energy to be at least twice the gluino mass, and hence the cross section falls rapidly with the increase of the gluino mass. For light gluinos the contribution from the $gg$ initial state is dominant, while for heavy gluinos the production via the $q\bar{q}$ initial state becomes considerable.

We comment on the gravitino mass dependence of the $\tilde{g}\tilde{g}$ production process. In addition to the SUSY QCD interaction diagrams, there is the $t$- and $u$-channel gravitino exchange contribution when the final state arises from gluon scattering [50,137–140].

In Figure 8.2, we present the different contributions to the total cross section for gluino pair-production $pp \to \tilde{g}\tilde{g}$ at the LHC, running at a center-of-mass energy of 14 TeV. In the left panel of the figure, we fix the squark masses to 3 TeV and investigate the dependence of the cross section on the gravitino mass, for several choices of the gluino mass. The solid lines refer to the contribution from gluon scattering while the dashed lines are related to the quark-antiquark one. The gravitino diagrams contribute

significantly only when the gravitino is very light with respect to the gluino mass. In other words, when $m_{3/2} \lesssim 1,2$ and $3 \cdot 10^{-13}$ GeV for a gluino of 600, 800 and 1000 GeV, respectively.

In the right panel of Figure 8.2, we analyze the dependence of the total cross section on the gluino mass for squark masses of 3 TeV and various values of the gravitino mass. This illustrates the scaling of the cross section in $1/m_{3/2}^4$ in the parameter space regions where gravitino diagrams dominate the cross section.

For our study, we are going to fix our parameters according to a benchmark point where the $t$- and $u$-channel gravitino exchange contribution is negligible, and hence consider the $\tilde{g}\tilde{g}$ production to be independent of the gravitino mass.

As one can see in Fig. 8.1, because of the $m_{3/2}^{-2}$ scaling behavior of $\sigma(pp \to \tilde{g}\tilde{G})$, the different gravitino and gluino masses alter the $n$-jet topology in the final state. In other words, the kinematic distributions and the number of jets in the final state might be able to give us some information on the gluino mass and/or the gravitino mass. However, as discussed in Section 4.2.3, the detailed analysis of the multi-jet events requires the ME+PS merging prescription. In the next section, therefore, we will promote the previous LO studies [137–141] to a full-fledged simulation via a state-of-the-art event generator.

Before turning to the ME+PS merging procedure, we briefly mention the decay width of the NLSP gluino. The partial width of a gluino decay into a gluon and a gravitino is given by

$$\Gamma(\tilde{g} \to g\tilde{G}) = \frac{m_{\tilde{g}}^5}{48\pi \overline{M}_{\mathrm{Pl}}^2 m_{3/2}^2}, \tag{8.6}$$

where $\overline{M}_{\mathrm{Pl}}$ is the reduced Planck mass and the gravitino mass in the phase space is neglected. For instance, for $m_{\tilde{g}} = 800$ GeV and $m_{3/2} = 3 \times 10^{-13}$ GeV, the width is 4.1 GeV. In our simplified SUSY mass spectrum the branching ratio is unity, $B(\tilde{g} \to g\tilde{G}) = 1$, while one in the usual SPS7 and SPS8 GMSB benchmarks is discussed in [141]. We remind the reader that the $\tilde{g} \to g\tilde{G}$ decay is isotropic, and hence the gluon jet distribution is given by purely kinematical effects of the decaying gluino.

## 8.2 Merging matrix elements with parton showers

In this section, we discuss the procedure used in this work to merge matrix elements (ME) and parton showers (PS) for the process (8.2) as well as for the SM background, and show the validation of our simulations.

At the LO, $\tilde{g}\tilde{G}$ and $\tilde{g}\tilde{g}$ production are expected to lead to missing energy in association with mono-jet and di-jet, respectively. However, for production processes with large partonic center-of-mass energy such as for heavy gluino production, initial and final state QCD radiation becomes important, resulting in multi-jet final states, and might modify or alter the LO predictions for the relevant observables.[1] In the present

[1] The probability for no emission is given by the Sudakov form factor, see (4.15). After integration,

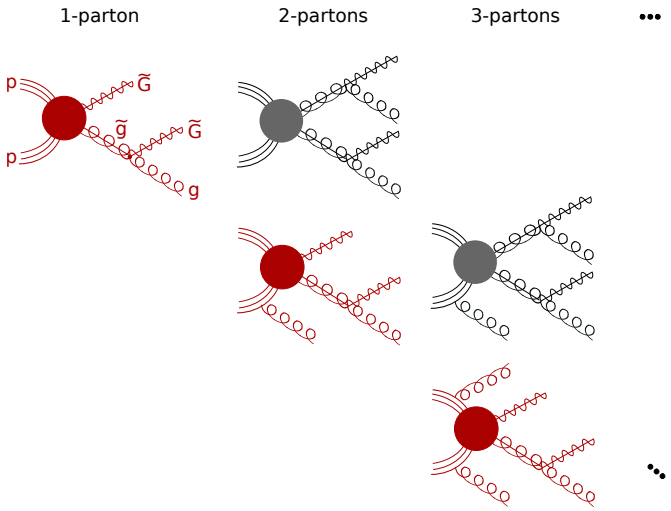


Figure 8.3: Schematic diagrams for $pp \to \text{partons} + \tilde{G}\tilde{G}$. In the first row the leading gluino-gravitino (red) and gluino-pair (black) diagrams are sorted. The diagrams are ordered with the number of additional QCD partons in rows, while with the total parton multiplicity in columns.

study, therefore, we consider the processes beyond the LO ones, schematically presented in Fig. 8.3.

The signal may contain not only hard jets from the decay of the gluinos as well as well-separated QCD radiation, but also soft and/or collinear jets, which, if not properly treated, lead to large logarithms, see Section 4.2.2. In event simulations, the hard partons are described well by a fixed-order ME approach, while the soft and collinear partons can be correctly described by a PS approach. To combine the two approaches avoiding double counting, one needs an appropriate merging procedure, see Section 4.2.3. In the last decade several techniques to consistently merge multi-parton final states have been developed [124]. They are now implemented in various event generators, and tested against experimental data (see [181] for a review). Moreover, the importance of the ME+PS merging for new physics has been pointed out in different contexts [126, 182–186].

In our analysis we make use of the shower-$k_T$ scheme, which is based on event rejection, and discussed in detail in Section 4.2.3.

### 8.2.1 Physics parameters and observables

Throughout this chapter, we consider a gluino with mass $m_{\tilde{g}} = 800$ GeV, which lies above the exclusion limit for certain simplified SUSY models or general gauge mediation models with the 7-TeV LHC data [187, 188][2], and conduct analyses for the LHC at

the exponent contains logarithms $\sim exp(-\alpha_s/(2\pi)\log(Q^2/t))$. Starting from a hard scale $Q$, the probability for no emission up to the hadronization scale $t = Q_0^2 \approx 1$ GeV$^2$ is very small.

[2]Both ATLAS and CMS set a more stringent bound on the gluino mass using 20 fb$^{-1}$ of the 2012 data set at $\sqrt{s} = 8$ TeV [189, 190]. We note, hoewver, that their interpretation relies on simplified models that give rise to four jets at leading order.

$\sqrt{s} = 14$ TeV.

All the left- and right-handed squarks are fixed at 3 TeV. The corresponding LO gluino-pair production cross section $\sigma(\tilde{g}\tilde{g})$ is about 1 pb at the 14-TeV LHC; see Fig. 8.1. As discussed in detail in Section 8.1.1, the gluino-gravitino associated production cross section $\sigma(\tilde{g}\tilde{G})$ strongly depends on the gravitino mass. In the following we focus on three different gravitino masses which exemplify the different final states. First, we fix the gravitino mass at $3 \times 10^{-13}$ GeV so that $\sigma(\tilde{g}\tilde{G}) \sim \sigma(\tilde{g}\tilde{g})$. We subsequently take a lighter and a heavier gravitino as

$$\text{A}\,(m_{3/2} = 1 \times 10^{-13}\,\text{GeV}): \qquad \sigma^{\text{A}}(\tilde{g}\tilde{G}) \sim 9 \times \sigma(\tilde{g}\tilde{g}), \tag{8.7a}$$

$$\text{B}\,(m_{3/2} = 3 \times 10^{-13}\,\text{GeV}): \qquad \sigma^{\text{B}}(\tilde{g}\tilde{G}) \sim \sigma(\tilde{g}\tilde{g}), \tag{8.7b}$$

$$\text{C}\,(m_{3/2} = 9 \times 10^{-13}\,\text{GeV}): \qquad \sigma^{\text{C}}(\tilde{g}\tilde{G}) \sim \frac{1}{9} \times \sigma(\tilde{g}\tilde{g}). \tag{8.7c}$$

Hence, $\tilde{g}\tilde{G}$ associated production is dominant for case A, while $\tilde{g}\tilde{g}$ production is the main channel of the gravitino production for case B. The two production processes are comparable in case B.

We have fixed the above benchmarks based on the LO predictions for the cross sections. It is well known, however, that higher order QCD corrections can enhance the expected rates. For instance, the next-to-leading order (NLO) cross section for the gluino pair is 1.96 times larger than the LO cross section for $m_{\tilde{g}} = 800$ GeV with $m_{\tilde{q}} = 3$ TeV at the 14-TeV LHC [191], while NLO corrections to $pp \to \tilde{g}\tilde{G}$ have not yet appeared in the literature. We note that our analyses can be easily redone with a different overall normalization and yet the main features will not change. In any case our approach is complementary to a fixed-order NLO calculation which reliably predicts cross sections and observables involving at most one jet, while ME+PS merged computations provide a reliable prediction for multi-jet based observables and more exclusive quantities that can be directly used in experimental simulations.

Within the present study, the relevant observables are related either to jets or missing energy. Here, we will focus on the following variables:

- transverse momentum of the leading and second jets, $p_T = |\vec{p}_T|$;
- missing transverse energy, $\not{E}_T$;
- sum of all the jet $p_T$'s, $H_T \equiv \sum_j p_T^j$;
- jet multiplicity.

### 8.2.2 Technical setup for simulations

To simulate the signal process (8.2), we have implemented the effective gravitino interaction Lagrangian (3.16) into FeynRules [25,86], which provides the UFO model file [87,101] for ME generators. We use MadGraph5 (MG5) [14] to generate the ME multi-parton events both for the gravitino signal and the SM background, and employ Pythia6.4 [103] for PS and hadronization. The shower-$k_T$ scheme is applied for the

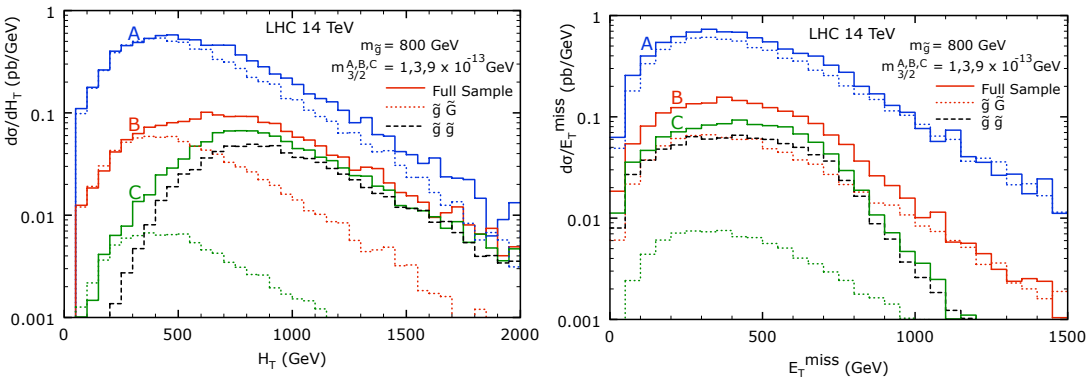


Figure 8.4: Shower $k_T$ merging results for inclusive signal samples of $pp \to \text{jets} + \not{E}_T$ at $\sqrt{s} = 14$ TeV, where the gravitino mass is taken to be $m_{3/2}^{\text{A,B,C}} = 1, 3, 9 \times 10^{-13}$ GeV and the gluino mass is fixed at 800 GeV. The contributions of the gluino-gravitino associated production and the gluino-pair production are also separately shown by dotted and solid lines, respectively.

ME+PS merging as described in Section 4.2.3. We have checked that all the ME-level results as well as the merged results agreed with those by MG/MEv4 with the gravitino code [166] and also the goldstino code [48].

In the following analyses, we generate signal events with parton multiplicity from one to three, $pp \to \tilde{G}\tilde{G} + 1, 2, 3$ partons, and merging separation parameters $Q_{\text{cut}} = 100$ GeV and $p_{T_{\text{min}}} = 50$ GeV. The choice of the merging parameters will be discussed in Section 8.2.3. Note that the employment of the ME+PS merging scheme allows us to treat different contributing processes (e.g. the $\tilde{g}\tilde{G}$ and $\tilde{g}\tilde{g}$ production processes in our case) within one event simulation and without double counting.

We also consider the irreducible $Z$+jets SM background, $pp \to Z(\to \nu\bar{\nu}) + 1, 2, 3$ partons, with merging separation parameters $Q_{\text{cut}} = p_{T_{\text{min}}} = 30$ GeV. Simulation of the other main background, e.g. $W$+jets and top pair, which requires more dedicated analysis, is beyond the scope of the present study, and we refer to, e.g., [184] for details and to [187, 192] for the experimental analysis.

For the jet clustering, we employ FastJet [113]. Jets are defined by the anti-$k_T$ algorithm [193] with a distance parameter of 0.5, and are required to satisfy $|\eta_j| < 4.5$ and $p_{T_j} > 50$ GeV. We order the clustered jets by their transverse momentum.

### 8.2.3 Validation

Although the above merging parameters have been chosen in accordance with the guidelines in [126], we have explicitly checked the stability of the cross section with respect to the variation of the arbitrary scale $Q_{\text{cut}}$.

The smoothness of distributions across the transition between ME and PS regimes was also examined for various $Q_{\text{cut}}$ values and kinematical distributions. Solid lines in Fig. 8.4 show the inclusive signal samples of $pp \to \text{jets} + \not{E}_T$ in the $H_T$ (left) and $\not{E}_T$ (right) distributions. One can see the smooth distributions for all the three benchmark

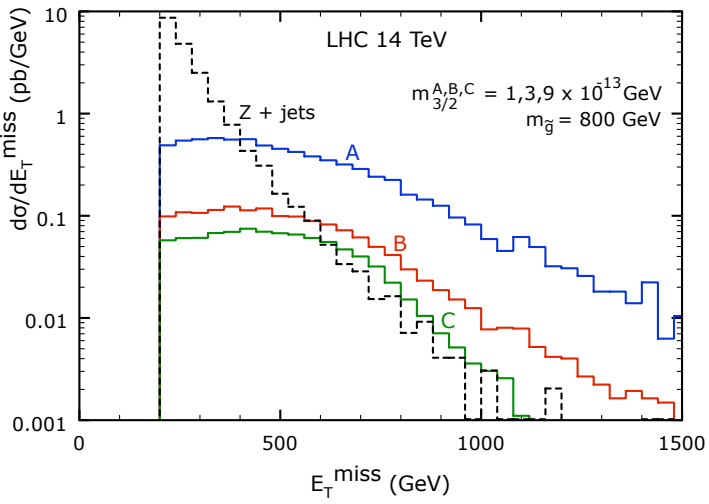


Figure 8.5: The same as the lower plot in Fig. 8.4 with the irreducible $Z(\to \nu\bar{\nu})$+jets background (dashed), where the $\not{E}_T > 200$ GeV cut is imposed.

points A, B, and C in (8.7) for $m_{3/2} = 1, 3,$ and $9 \times 10^{-13}$ GeV, respectively.

In addition, as a nontrivial validation check, we have generated the gravitino production subprocesses separately: $pp \to \tilde{g}(\to g\tilde{G})\tilde{G} + 0, 1$ partons and $pp \to \tilde{g}(\to g\tilde{G})\tilde{g}(\to g\tilde{G}) + 0, 1$ partons, employing the same merging procedure that we used before on the full signal sample, and verified that the sum of those samples reproduces the full inclusive results. In Fig. 8.4, we present contributions of each subprocess, the $\tilde{g}\tilde{G}$ production (dotted) and the $\tilde{g}\tilde{g}$ production (dashed). The sum of the two samples agrees with the full samples (solid). We note that the cross section for the $\tilde{g}\tilde{G}$ production follow the $m_{3/2}^{-2}$ scaling, while the $\tilde{g}\tilde{g}$ production is independent of the gravitino mass.

For case B, as requested in (8.7b), the full signal cross section consists of two equally relevant contributions coming from the $\tilde{g}\tilde{G}$ and $\tilde{g}\tilde{g}$ production processes. In contrast, the signal of the lighter gravitino (case A) is dominated by the $\tilde{g}\tilde{G}$ associated production process, and the signal for the heavier gravitino (case C) consists mainly of the $\tilde{g}\tilde{g}$ production process.

The $H_T$ distributions for the $\tilde{g}\tilde{G}$ production have a peak around half of the gluino mass since there is a gluon coming from the gluino decay, whose energy is $m_{\tilde{g}}/2$ in the gluino rest frame. On the other hand, the $\tilde{g}\tilde{g}$ production exhibits a peak around $m_{\tilde{g}}$ due to the two gluino decays.

The missing transverse energy $\not{E}_T$ is defined as the absolute value of the vectorial sum of the transverse momenta of the two gravitinos. The gluino-gravitino associated production leads to higher $\not{E}_T$ events than the gluino-pair production, which is explained in detail in the next section.

Finally, we show the $\not{E}_T$ distribution for the irreducible $Z(\to \nu\bar{\nu})$+jets background in Fig. 8.5, where $\not{E}_T = p_{T_Z}$. Since the background overwhelms the signal and dominates

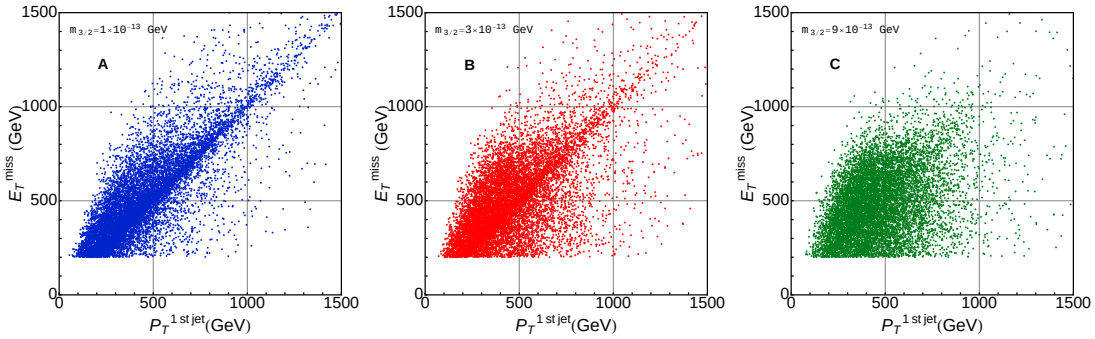


Figure 8.6: Scatter plots of the $pp \to \text{jets} + \not{E}_T$ signal at $\sqrt{s} = 14$ TeV in the $(p_T^{\text{1st jet}}, \not{E}_T)$ plane for $m_{3/2}^{\text{A,B,C}} = 1, 3, 9 \times 10^{-13}$ GeV from left to right, where the gluino mass is 800 GeV.

in the low $\not{E}_T$ region, we impose the minimal missing transverse energy cut

$$\not{E}_T > 200 \text{ GeV} \tag{8.8}$$

in the following analyses.

## 8.3 Jets plus missing energy signals

We now investigate the kinematical distributions further, focusing on the correlation between the $p_T$ of the leading jet and the missing transverse energy, in order to differentiate our three benchmark signals as well as to identify basic selection cuts to curb the irreducible background.

Fig. 8.6 presents scatter plots in the $(p_T^{\text{1st jet}}, \not{E}_T)$ plane for the three cases defined in eqs. (8.7), where the minimal $\not{E}_T > 200$ GeV cut is applied. For case A, where gluino-gravitino associated production is dominant, we find a strong correlation between the two observables as $\not{E}_T \sim p_T^{\text{1st jet}}$, especially for the high $p_T$ region, and this can be explained as follows. One of two gravitinos in the final state is produced in association with a gluino, and hence $\vec{p}_{T_{\tilde{G}}} = -\vec{p}_{T_{\tilde{g}}}$ at LO. The produced gluino decays into a gluon and a (almost) massless gravitino, and those are boosted along the gluino momentum direction and can share the momentum like $\vec{p}_{T_g} \sim \vec{p}_{T_{\tilde{G}}} \sim \vec{p}_{T_{\tilde{g}}}/2$. This leads to a balance between the $p_T$ of the gluon jet and the missing transverse energy, which is the vectorial sum of the two gravitino momenta. QCD radiation will alter this naive expectation and most of the events which scatter apart from the $\not{E}_T = p_T^{\text{1st jet}}$ line come from samples with extra partons. For case C, in contrast, where gluino-pair production is the main subprocess and both gluino decays are a source of the leading jet, there is no such a strong correlation between $p_T^{\text{1st jet}}$ and $\not{E}_T$. In the high $p_T$ region, i.e. for the highly-boosted gluino-pair production, a similar argument could be applied yet a cancellation between the back-to-back gravitinos occurs, hence events with large $\not{E}_T$ are suppressed. This can be already observed in Fig. 8.4. Case B lies in between cases A and C, where both production subprocesses contribute.

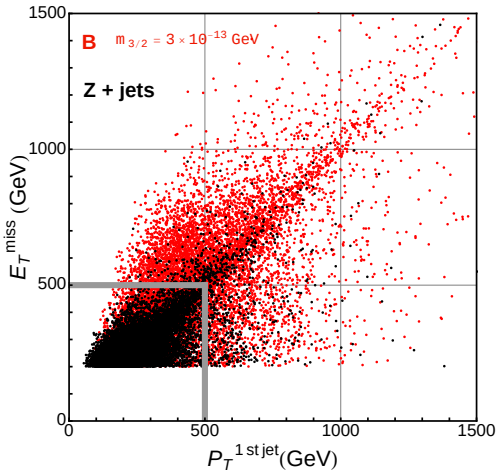


Figure 8.7: The same as the middle plot in Fig. 8.6 with the $Z$+jets background (black dots).

| $\sigma$ (pb) | A | B | C | bkg |
|---|---|---|---|---|
| $\not{E}_T > 200$ GeV | 7.50 | 1.53 | 0.90 | 19.4 |
| + $p_T^{1\text{st jet}} > 500$ GeV or $\not{E}_T > 500$ GeV | 3.81 | 0.85 | 0.55 | 0.81 |

Table 8.1: Cross sections for the signals and the background at the 14-TeV LHC, with the minimal $\not{E}_T$ cut (8.8) and with the additional selection cuts (8.9).

In Fig. 8.7 the SM $Z$+jets background is added on the scatter plot for case B with black dots. Also here, we find (a weaker) $\not{E}_T \sim p_T^{1\text{st jet}}$ correlation resulting from the $Z + j$ sample. The background events are concentrated in the low $p_T$ and $\not{E}_T$ region, typically less than 500 GeV, while the gravitino signal events are mainly scattered to the higher energy region up to about 800 GeV, i.e. the gluino mass, as well as to the $\not{E}_T \sim p_T^{1\text{st jet}}$ region for cases A and B. Therefore, besides the minimal $\not{E}_T$ cut in (8.8), we impose the selection cuts

$$p_T^{1\text{st jet}} > 500 \text{ GeV} \quad \text{or} \quad \not{E}_T > 500 \text{ GeV}, \tag{8.9}$$

shown by thick grey lines in Fig. 8.7.

We present cross sections for the gravitino signals and the $Z$+jets background in Table 8.1, where the minimal $\not{E}_T$ cut (8.8) and the additional selection cuts (8.9) are taken into account. After the selection cuts, the background is reduced quite effectively, while about half of the signal events pass those cuts.

Distributions of the relevant observables given in Section 8.2.1 are collected in Fig. 8.8 for the gravitino signals as well as the $Z$+jets background. Compared to Fig. 8.4, events in the low $H_T$ and $\not{E}_T$ regions are removed by the kinematical cuts (8.8) and (8.9). In the missing energy distribution, as discussed above, the lighter gravitino results in higher $\not{E}_T$ events.

The shapes of the $p_T$ of the leading jet are similar for the three cases since the hard jets mainly come from the gluino decays, but the $p_T$ distribution of the lighter gravitino

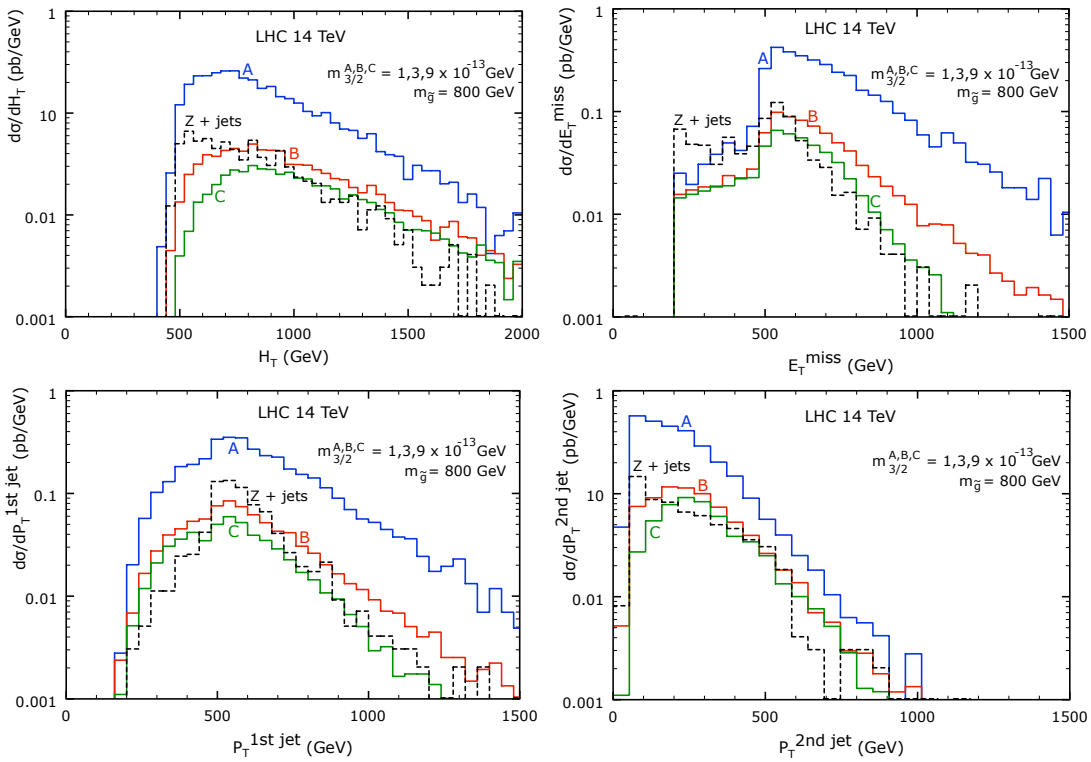


Figure 8.8: Distributions of the jets+$\not{E}_T$ events at the 14-TeV LHC for the gravitino signal with $m_{3/2}^{\rm A,B,C} = 1, 3, 9 \times 10^{-13}$ GeV and $m_{\tilde{g}} = 800$ GeV as well as for the $Z$+jets background. Besides the minimal missing transverse energy cut $\not{E}_T > 200$ GeV, the selection cuts, $p_T^{\rm 1st\,jet} > 500$ GeV or $\not{E}_T > 500$ GeV, are imposed.

case is slightly harder than that of the heavier gravitino due to the higher boost effect from the $\tilde{g}\tilde{G}$ associated production. We also note that the signal events for all the three cases dominate the background in the $p_T^{\rm 1st\,jet} < 500$ GeV region. The distributions of the $p_T$ of the second jet are more distinctive, especially in the low $p_T$ region. Two gluino decays in the gluino-pair production lead to two hard gluon jets. On the other hand, the second jet resulting from the $\tilde{g}\tilde{G}$ production as well as the $Z$+jets background comes from QCD radiation, and tends to be soft.

Finally, we present jet multiplicities for an integrated luminosity of $\mathcal{L} = 10$ fb$^{-1}$ in Fig. 8.9. The jet multiplicity depends on the requirement of the minimal $p_T$ of jets, and we take the different $p_{T_j}$ cuts of 50 GeV (left) and 150 GeV (right). Case A as well as the SM background have a peak at a lower multiplicity than cases B and C, as expected. When we count only jets whose $p_T$ is larger than 150 GeV, i.e. only very hard jets, distributions of the jet multiplicity recover the LO expectations: the $\tilde{g}\tilde{G}$ associated production tends to produce mono-jet events, while the $\tilde{g}\tilde{g}$ production is likely to give di-jet events.

As seen in Fig. 8.8 and 8.9, the distributions are significantly different among the three benchmarks as well as between the signal and the background. In other words, they are sensitive to the gravitino mass when it is light enough so that the $\tilde{g}\tilde{G}$ associated

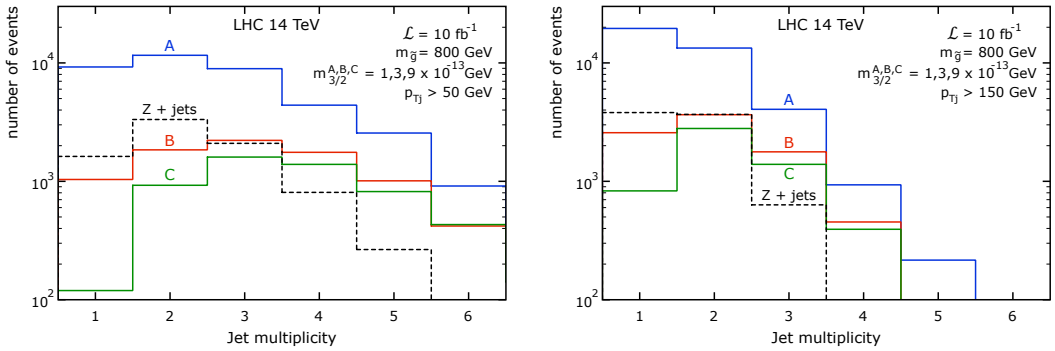


Figure 8.9: Jet multiplicities for an integrated luminosity of 10 fb$^{-1}$, with $p_{T_j} > 50$ GeV (left) and $p_{T_j} > 150$ GeV (right). The detail is the same as Fig. 8.8.

production process can contribute to the signal. We note that, although we fixed the gluino mass at 800 GeV in the present study, a different gluino mass also alters the distributions, which could allow us to explore both the gravitino and gluino masses at the LHC.

## 8.4 Summary

We have studied a jets plus missing energy signature at the LHC in a scenario where the gravitino is the LSP and the gluino is the NLSP which promptly decays into a gluon and a gravitino. We considered a very light gravitino of $m_{3/2} \sim \mathcal{O}(10^{-13}$ GeV), where two production subprocesses can yield jets+$\not{E}_T$: gluino-gravitino associated production and gluino-pair production. By using the shower-$k_T$ ME+PS merging scheme implemented in MadGraph, we have simulated the inclusive signal samples as well as the SM $Z$+jets irreducible background.

Special attention has been devoted to the ME+PS merging procedure to avoid double counting for such a signal which contains two different types of subprocesses. In addition to checking the $Q_{\rm cut}$ independence of the cross sections and the smoothness of the distributions, we have generated the merged $\tilde{g}\tilde{G}$ and $\tilde{g}\tilde{g}$ signal samples separately and confirmed that the sum of them reproduced the full inclusive results.

To show how distributions of the jets+$\not{E}_T$ signature can provide information on the gravitino and gluino masses, we have investigated three benchmark scenarios which exemplify the different final states. Due to the fact that the distributions are quite different between the $\tilde{g}\tilde{G}$ and $\tilde{g}\tilde{g}$ production processes and due to the $m_{3/2}^{-2}$ scaling of the $\tilde{g}\tilde{G}$ production cross section, the kinematical distributions and the jet multiplicity exhibit distinctive features among the three cases as well as between the signal and the background. The LHC may be able to explore the parameter space around our benchmark points and hence to provide information on the gluino mass as well as the gravitino mass, yielding information on the SUSY breaking scale.

# CHAPTER 9

## Mono-photon signals in gravitino production at the LHC

Both the ATLAS and CMS collaborations analysed the mono-photon+$\not{E}_T$ signal in the data from the 7-TeV LHC run [194,195]. From the agreement between the observed number of events and the predictions of the SM background they set upper limits on the expected cross section from new physics processes. We interpret the results in terms of light gravitino production in order to derive a bound on the gravitino mass, which translates into a bound on the SUSY breaking scale.

Similar to the study of the mono-photon+$\not{E}_T$ signal presented in Chapter 6 for $e^+e^-$ colliders, there are two production mechanisms for a gravitino LSP that can provide the $\gamma+\not{E}_T$ signal at the LHC: gravitino-pair production with an extra photon emission and gravitino production in association with a neutralino, with the subsequent neutralino decay into a photon and a gravitino. In this study, for simplicity, we consider the heavy neutralino limit, such that only gravitino pair production contributes, and we assume degenerate squark masses. We note that only the $q\bar{q}$ initial state gives rise to the $\gamma+\not{E}$ signal at the LHC. Based on the existing $\gamma+\not{E}_T$ 7-TeV LHC analysis [194], where non-SUSY BSM models were studied, we set a bound on the gravitino mass.

For the SUSY signal simulation, we extended the SUSY QED model presented in Section 3.2.1 to the quark sector, implement it into FeynRules2 [29] and pass it by means of the UFO library [87,101] to MadGraph5_aMC@NLO [92] for event generation. We employ Pythia6.4 [103] for parton shower and hadronization, Delphes3 [111] for fast detector simulation with the ATLAS setup, and MadAnalysis5 [115] for the event sample analysis. We note again that special implementations are needed to treat the Majorana four-point interactions in MadGraph5; see more details in 5.4.

For the event selection, we follow the $\gamma+\not{E}_T$ analysis by ATLAS at $\sqrt{s}=7$ TeV [194]. A photon is required with $p_T>150$ GeV and $|\eta|<2.37$ (except $1.37<|\eta|<1.52$ due to the transition region between the barrel and end-cap calorimeters). The missing transverse energy $\not{E}_T>150$ GeV is also required. Possible jets produced by ISR are defined by the anti-$k_T$ algorithm [113] with the distance parameter of 0.4 and in the region $|\eta|<4.5$. While events with one jet are kept for the signal with ISR, events with more than one jet with $p_T>30$ GeV are rejected. The photon, the missing energy vector and jets are required to be well separated as $\Delta\phi(\gamma,\not{E}_T)>0.4$, $\Delta R(\gamma,j)>0.4$, and $\Delta\phi(\not{E}_T,j)>0.4$, where $\Delta R=\sqrt{(\Delta\eta)^2+(\Delta\phi)^2}$.

Figure 9.1 shows the $p_T$ distributions of the photon for $pp\to\gamma\tilde{G}\tilde{G}$ at $\sqrt{s}=7$ TeV, where all the above selection cuts are applied except the $p_T^\gamma$ and $\not{E}_T$ cuts. The gravitino mass is fixed at $10^{-13}$ GeV, while the masses of squarks are taken at 1, 2, and 20 TeV. As discussed in the mono-photon signal at $e^+e^-$ colliders in Section 6.1.2, the cross section for the gravitino pair production becomes larger as the $t$-channel squark masses increase. The SUSY signal is harder than the SM background. This is partly due to the $2\to3$ kinematics of the signal, whereas the background essentially has the $2\to2$ kinematics, and partly because of the non-renomalizable nature of the operators involved in the process. We note again that the signal rate strongly depends on the gravitino mass as $1/m_{3/2}^4$ and also on the kinematical cuts.

The ATLAS $\gamma+\not{E}_T$ study with 4.6 fb$^{-1}$ of collisions at $\sqrt{s}=7$ TeV reported

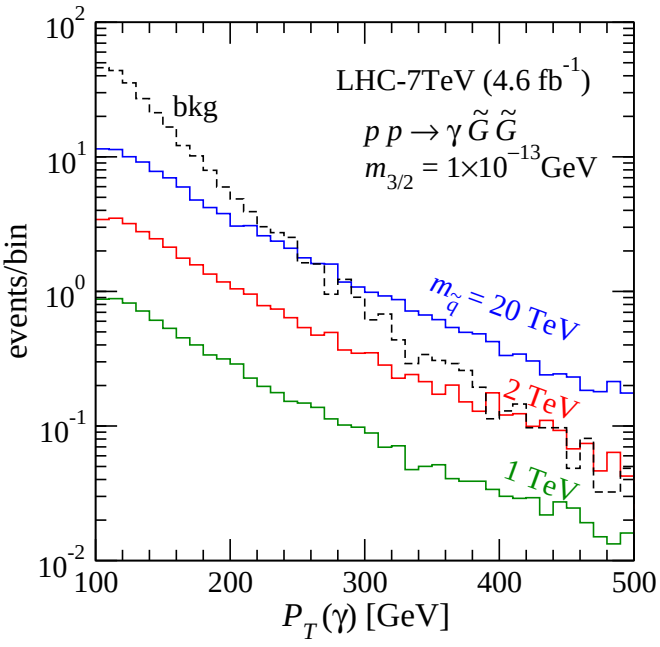


Figure 9.1: Transverse momentum distributions of the photon for $pp \to \gamma\tilde{G}\tilde{G}$ at $\sqrt{s} =$ 7 TeV with $m_{3/2} = 10^{-13}$ GeV for three squark masses. All selection cuts described in the text are applied except the $p_T^\gamma$ and $\not{E}_T$ cuts. The $Z(\to \nu\bar{\nu}) + \gamma$ background is also shown as a reference.

model-independent 90% and 95% confidence level (CL) upper limits on the visible cross section, defined as the production cross section times kinematical acceptance times detection efficiency ($\sigma \times A \times \varepsilon$). The values are 5.6 fb and 6.8 fb, respectively [194]. Figure 9.2 presents the visible cross sections for $pp \to \gamma\tilde{G}\tilde{G}$ at $\sqrt{s} = 7$ and 13 TeV as a function of the gravitino mass for three different squark masses. The horizontal lines show the ATLAS 90% and 95% CL limits. The signal $A \times \varepsilon$ in our simulation is about 25% at $\sqrt{s} = 7$ TeV for all three cases, which is compatible with the one in the ATLAS analysis for other BSM models.[1] $A \times \varepsilon$ slightly increases to 28% for $\sqrt{s} = 13$ TeV, where the same selection criteria are applied.

Gravitino masses below about $1 \times 10^{-13}$ GeV are excluded at 95% CL for the heavy SUSY mass limit, which is translated to the lower bound on the SUSY breaking scale of about 650 GeV. For light squark masses the limits are lower, for example, $m_{3/2} \sim 6 \times 10^{-14}$ GeV, i.e. $\sqrt{F} \sim 500$ GeV for 1-TeV squarks. These results significantly improve previous ones at LEP and the Tevatron, and are comparable with the recent ATLAS 8-TeV monojet analysis [149].[2] The coming LHC Run-II with $\sqrt{s} = 13$ TeV is expected to explore heavier gravitinos up to $\mathcal{O}(10^{-12}$ GeV), i.e. a few TeV of the SUSY breaking scale.

We note that we assumed the heavy neutralino limit in this section. However, if the neutralino is light enough and promptly decays, production of the on-shell neutralino

[1] Similar to the ATLAS study, we generated events at the parton level with a minimum photon $p_T$ of 80 GeV.

[2] In the ATLAS study, only associated gravitino production with a gluino or a squark was considered.

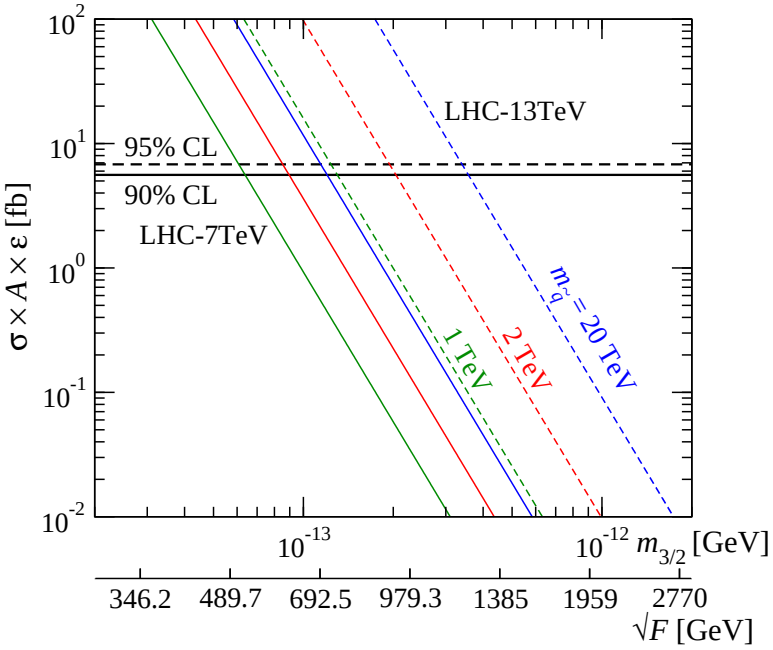


Figure 9.2: Visible cross sections for $pp \to \gamma\tilde{G}\tilde{G}$ at $\sqrt{s} = 7$ TeV (solid) and 13 TeV (dashed) as a function of the gravitino mass for different squark masses, 1 (green), 2 (red), and 20 (blue) TeV. The gravitino mass is also translated to the SUSY breaking scale by $F = \sqrt{3}\,\overline{M}_{\rm Pl} m_{3/2}$. The predictions are compared with model-independent 90% and 95% confidence level (CL) upper limits by the ATLAS-7TeV analysis [194].

can give rise to characteristic harder photons. This leads to a different production rate as well as $A \times \varepsilon$, and hence the limits can be modified.

We also note that, in the heavy squark limit and for very light gravitinos, the validity of the theory is questionable. In order to allow a perturbative expansion, the squark masses should not be much bigger than the SUSY breaking scale. In addition, for the effective approach to be valid, the energy scale of the process should be less than the scale $\Lambda \sim F/m_{\rm SUSY}$. Also theoretical considerations about the mediation of SUSY breaking suggest the SUSY particle masses to be less or similar to the SUSY breaking scale. Lighter SUSY masses or heavier gravitinos remedy these issues.

To summarize, we interpreted the upper limit on the visible cross section of the mono-photon plus missing energy signal arising from a new physics process reported by ATLAS in terms of light gravitino production. We assumed the heavy neutralino limit, such that only gravitino pair production contributes to the signal. We found that for the heavy SUSY mass limit, gravitino masses below about $1 \times 10^{-13}$ GeV are excluded at 95% CL. For light squark masses the limits are lower. The coming LHC Run-II with $\sqrt{s} = 13$ TeV is expected to explore heavier gravitinos up to $\mathcal{O}(10^{-12}$ GeV).

# CHAPTER 10

# Summary

The SM predicts the outcome of many experiments with a high precision. Yet, there exist both theoretical motivations and experimental observations calling for new physics. With the LHC, we have a powerful machine at hand to search for BSM physics, and future colliders are planned. In order to interpret the data delivered by experiments, phenomenological studies are needed.

In this work, we performed phenomenological studies for a SUSY theory with a gravitino LSP. The gravitino is a spin 3/2 particle that arises in SUSY theories when the SUSY transformation parameter is space-time dependent, similar to the way gauge fields appear by gauging the symmetries of the SM. It becomes massive after the spontaneous breaking of SUSY by absorbing the goldstino via the super-Higgs mechanism. As a result, the mass of the gravitino is directly related to the SUSY breaking scale $F$. Moreover, the spin 1/2 components of the gravitino inherit the interaction strength of the goldstino, which scales with $1/F$. Therefore, for low scale SUSY breaking scenarios, gravitino interactions might become strong enough to lead to observable signatures in collider experiments. Thanks to the gravitino-goldstino equivalence theorem, the gravitino interactions in scattering processes at colliders can be well described by the goldstino interactions, which represents an enormous calculational simplification. To illustrate the equivalence of the full spin 3/2 gravitino formalism and the spin 1/2 goldstino formalism, we discussed the leading energy dependence of gravitino pair production in photon-photon collisions in the two approaches. We note that this study was a part of the validation of the implementation of general spin 3/2 particles into the collider simulation tools FeynRules and Aloha.

There are three possible ways gravitinos can show up in scattering processes in $R$-parity conserving scenarios, which we considered throughout this work. First, a pair of gravitinos can be produced directly. Since the gravitinos escape the detection, this process leads to an observable signature after extra radiation. Second, one gravitino can be produced in association with another SUSY particle. Third, gravitinos can show up at the end of a decay chain. The first two processes are sensitive to the gravitino mass and scale with $1/m_{3/2}^4$ and $1/m_{3/2}^2$, respectively. They give rise to an observable signal in collider experiments only for very light gravitinos with a mass of $m_{3/2} \sim \mathcal{O}(10^{-14} - 10^{-12}$ GeV) since the interactions are suppressed by the Planck scale.

To study gravitino pair production, we need a consistent model containing interaction vertices involving two gravitinos as well as sgoldstinos, the scalar superpartners of goldstinos. By using the superspace formalism, we constructed a SUSY model that allows us to study the whole parameter space for all contributing processes, and implemented the model in the FeynRules and MadGraph 5 frameworks. We note that special implementations in MadGraph 5 are needed to treat the Majorana four-fermion interaction arising in gravitino pair production.

We studied the signatures of the gravitino LSP for future $e^+e^-$ colliders as well as for the LHC in a mass range where all the three production processes may lead to a signal that can be detected. The signal is $X$ plus missing energy ($\not{E}$), where $X$ depends on the production mechanism and the missing energy is carried away by two gravitinos. In the following, we summarize our studies for the different final state signatures

expected at $e^+e^-$ colliders and the LHC.

1. Mono-photon+$\not{E}$ signal in $e^+e^-$ collisions: We analysed the mono-photon+$\not{E}$ signal for future $e^+e^-$ colliders arising from direct gravitino production in a scenario where the gravitino is the LSP, and the neutralino is the NLSP. Two processes contribute: gravitino pair production ($\tilde{G}\tilde{G}$) and neutralino-gravitino associated production ($\tilde{\chi}_1^0\tilde{G}$). They give rise to the signal via an additional photon radiation and via the neutralino decay, respectively.

We explicitly presented the helicity amplitudes for both production processes, which give us a deep understanding for the SUSY-mass dependence of the production cross sections and the angular distributions. We discussed the parameter dependence of the two signal cross sections in detail, and showed that the relative importance of the two processes varies with the gravitino and neutralino masses as well as with kinematical cuts.

We performed the event simulation for the SUSY signal as well as the SM background, taking into account signal selection cuts and beam polarizations, and showed that the photon spectra from the two subprocesses are very distinctive. This is because the photon coming from the $\tilde{G}\tilde{G}$ production is mostly initial state radiation, while the $\tilde{\chi}_1^0\tilde{G}$ associated production process leads to an energetic photon from the neutralino decay. We showed that the energy and angular distributions of the photon in the final state can explore the mass of the neutralino as well as the mass of the $t$-channel exchange selectrons.

2. Mono-electron+$\not{E}_T$ signal in $e^-\gamma$ collisions: We also considered gravitino LSP production associated with a selectron NLSP which subsequently decays into an electron and a gravitino in $e\gamma$ collisions, $e^-\gamma \to \tilde{e}^-\tilde{G} \to e^-\tilde{G}\tilde{G}$, leading to a mono-electron+$\not{E}_T$ signal. We repeated a similar analysis as for the neutralino-gravitino production process. We presented the explicit helicity amplitudes for the production process, and discussed the mono-electron+$\not{E}_T$ signal, including the energy spectrum of the backward-Compton scattered photons for incident photons. We found that the production cross section and the kinematical distributions of the electron in the final state are quite sensitive to the mass of the $t$-channel intermediate neutralinos as well as the mass of the decaying selectron.

3. Jets+$\not{E}_T$ signal in $pp$ collisions: After having gained a detailed understanding of the parameter dependencies of gravitino production in $e^+e^-$ and $e^-\gamma$ collisions, we investigated gravitino production at the LHC. We have studied a jets+$\not{E}_T$ signature in a scenario where the gravitino is the LSP and the gluino is the NLSP which promptly decays into a gluon and a gravitino. We considered two production processes that yield the jets+$\not{E}_T$ signal: gluino-gravitino associated production ($\tilde{g}\tilde{G}$) and gluino-pair production ($\tilde{g}\tilde{g}$). At leading order, the first process gives rise to a mono-jet+$\not{E}_T$ signal, while the latter gives a di-jet+$\not{E}_T$ signal. We took into account the effects of possible extra emissions. By using the shower-$k_T$ matrix-element and parton shower (ME+PS)

merging scheme implemented in MadGraph, we have simulated the inclusive signal samples as well as the SM ($Z \to \nu\bar{\nu}$)+jets irreducible background.

Special attention has been devoted to the ME+PS merging procedure to avoid double counting for such a signal which contains two different types of subprocesses. In addition to checking independence of the cross sections on the matching parameter $Q_{\rm cut}$ and the smoothness of the distributions, we have generated the merged $\tilde{g}\tilde{G}$ and $\tilde{g}\tilde{g}$ signal samples separately and confirmed that the sum of them reproduced the full inclusive results.

To show how distributions of the jets+$\not{E}_T$ signature can provide information on the gravitino and gluino masses, we have investigated three benchmark scenarios which illustrate the different final states. Due to the fact that the distributions are quite different between the $\tilde{g}\tilde{G}$ and $\tilde{g}\tilde{g}$ production processes and due to the $m_{3/2}^{-2}$ scaling behaviour of the $\tilde{g}\tilde{G}$ production cross section, the kinematical distributions and the jet multiplicity exhibit distinctive features among the three cases as well as between the signal and the background.

4. Mono-photon+$\not{E}_T$ signal in $pp$ collisions: Finally, we applied our studies to an existing search for new physics at the LHC. Based on the mono-photon+$\not{E}$ analysis of the data delivered by the 7 TeV run of the LHC, we set a lower bound on the gravitino LSP mass. We considered the heavy neutralino limit such that only $\tilde{G}\tilde{G}$ production contributes, and investigated the effect of different squark masses. We exclude gravitino masses below about $1 \times 10^{-13}$ GeV at 95% CL for the heavy SUSY mass limit. This bound translates into a lower bound on the SUSY breaking scale of about 650 GeV. For light squark masses the limits are lower, for example, $m_{3/2} \sim 6 \times 10^{-14}$ GeV, i.e. $\sqrt{F} \sim 500$ GeV for 1-TeV squarks.

To conclude, we expect that the LHC as well as future $e^+e^-$ colliders can explore light gravitino production for a gravitino with mass $m_{3/2} \sim \mathcal{O}(10^{-14} - 10^{-9}$ GeV). The properties of the signatures strongly depend not only on $m_{3/2}$ but also on the other SUSY particle masses. By interpreting the mono-photon+$\not{E}$ search from the 7 TeV LHC run in terms of our theory, we put a stronger bound on the gravitino mass, i.e. the SUSY breaking scale, than found in similar searches performed by the LEP and Tevatron collaborations. We also predicted the prospects of the upgraded 13 TeV LHC as well as the future ILC to explore the parameter space of theories with light gravitinos.

Finally, we emphasize that through these studies, we contributed to the development and validation of the collider simulation tools relevant to connect theories with gravitinos to experimental data. With these tools as well as with the information provided by our studies, we look forward to future phenomenological studies by theorists as well as data analysis in terms of gravitino production by experimentalists.

# APPENDIX A

## Appendix

## A.1 Conventions

The metric is given by

$$g_{\mu\nu} = \mathrm{diag}(1, -1, -1, -1), \tag{A.1}$$

and the fully antisymmetric tensor of rank four is defined by $\epsilon_{0123} = 1$. The four-vectors built upon the Pauli matrices are given by

$$\sigma^\mu = \big(1, \sigma^i\big) \quad \text{and} \quad \bar{\sigma}^\mu = \big(1, -\sigma^i\big), \tag{A.2}$$

where the Pauli matrices $\sigma^i$ with $i = 1, 2, 3$ read

$$\sigma^1 = \begin{pmatrix} 0 & 1 \\ 1 & 0 \end{pmatrix}, \quad \sigma^2 = \begin{pmatrix} 0 & -i \\ i & 0 \end{pmatrix}, \quad \sigma^3 = \begin{pmatrix} 1 & 0 \\ 0 & -1 \end{pmatrix}. \tag{A.3}$$

This allows to write the generators of the Lorentz algebra in the (two-component) left-handed and right-handed spinorial representations as

$$\sigma^{\mu\nu} = \frac{i}{4}\Big(\sigma^\mu\bar{\sigma}^\nu - \sigma^\nu\bar{\sigma}^\mu\Big) \quad \text{and} \quad \bar{\sigma}^{\mu\nu} = \frac{i}{4}\Big(\bar{\sigma}^\mu\sigma^\nu - \bar{\sigma}^\nu\sigma^\mu\Big), \tag{A.4}$$

respectively.

Moving to four-component spinors, Dirac matrices are defined in the Weyl representation by

$$\gamma^\mu = \begin{pmatrix} 0 & \sigma^\mu \\ \bar{\sigma}^\mu & 0 \end{pmatrix}, \tag{A.5}$$

and span the Clifford algebra

$$\Big\{\gamma^\mu, \gamma^\nu\Big\} = 2g^{\mu\nu}. \tag{A.6}$$

Additionally, the fifth Dirac matrix $\gamma_5$ is given by

$$\gamma_5 = i\gamma^0\gamma^1\gamma^2\gamma^3 = \begin{pmatrix} -1 & 0 \\ 0 & 1 \end{pmatrix}. \tag{A.7}$$

The $\gamma$-matrices allow to build the generators of the Lorentz algebra in the four-component spinorial representation,

$$\gamma^{\mu\nu} = \frac{i}{4}\Big(\gamma^\mu\gamma^\nu - \gamma^\nu\gamma^\mu\Big). \tag{A.8}$$

## A.2 Wavefunctions

We present the wavefunctions for spin-$\frac{1}{2}, 1, \frac{3}{2}$ and 2 fields for a vector

$$p^\mu = (E, |\vec{p}|\sin\theta\cos\phi, |\vec{p}|\sin\theta\sin\phi, |\vec{p}|\cos\theta). \tag{A.9}$$

We follow the HELAS conventions [15].

### Spin-$\frac{1}{2}$ fields

The spin-$\frac{1}{2}$ wavefunctions for a particle with helicity $\pm 1/2$ are given by

$$\begin{aligned} u_{+1/2}(p) &= \begin{pmatrix} \sqrt{E-|\vec{p}|}\begin{pmatrix} \cos\frac{\theta}{2} \\ \sin\frac{\theta}{2}e^{i\phi} \end{pmatrix} \\ \sqrt{E+|\vec{p}|}\begin{pmatrix} \cos\frac{\theta}{2} \\ \sin\frac{\theta}{2}e^{i\phi} \end{pmatrix} \end{pmatrix}, \\ u_{-1/2}(p) &= \begin{pmatrix} \sqrt{E+|\vec{p}|}\begin{pmatrix} -\sin\frac{\theta}{2}e^{-i\phi} \\ \cos\frac{\theta}{2} \end{pmatrix} \\ \sqrt{E-|\vec{p}|}\begin{pmatrix} -\sin\frac{\theta}{2}e^{-i\phi} \\ \cos\frac{\theta}{2} \end{pmatrix} \end{pmatrix}, \end{aligned} \tag{A.10}$$

and for an antiparticle by

$$\begin{aligned} v_{+1/2}(p) &= \begin{pmatrix} -\sqrt{E+|\vec{p}|}\begin{pmatrix} -\sin\frac{\theta}{2}e^{-i\phi} \\ \cos\frac{\theta}{2} \end{pmatrix} \\ \sqrt{E-|\vec{p}|}\begin{pmatrix} -\sin\frac{\theta}{2}e^{-i\phi} \\ \cos\frac{\theta}{2} \end{pmatrix} \end{pmatrix}, \\ v_{-1/2}(p) &= \begin{pmatrix} \sqrt{E-|\vec{p}|}\begin{pmatrix} \cos\frac{\theta}{2} \\ \sin\frac{\theta}{2}e^{i\phi} \end{pmatrix} \\ -\sqrt{E+|\vec{p}|}\begin{pmatrix} \cos\frac{\theta}{2} \\ \sin\frac{\theta}{2}e^{i\phi} \end{pmatrix} \end{pmatrix}. \end{aligned} \tag{A.11}$$

### Spin-1 fields

The polarization vectors associated with a spin-1 particle with mass $M$ are given by

$$\begin{aligned} \epsilon_+^\mu(p) &= \frac{1}{\sqrt{2}}\begin{pmatrix} 0 \\ -\cos\theta\cos\phi + i\sin\phi \\ -\cos\theta\sin\phi - i\cos\phi \\ \sin\theta \end{pmatrix}, \\ \epsilon_0^\mu(p) &= \frac{1}{M}\begin{pmatrix} |\vec{p}| \\ E\sin\theta\cos\phi \\ E\sin\theta\sin\phi \\ E\cos\theta \end{pmatrix}, \\ \epsilon_-^\mu(p) &= \frac{1}{\sqrt{2}}\begin{pmatrix} 0 \\ \cos\theta\cos\phi + i\sin\phi \\ \cos\theta\sin\phi - i\cos\phi \\ -\sin\theta \end{pmatrix}, \end{aligned} \tag{A.12}$$

whereas those associated with a spin-1 antiparticle read

$$\begin{aligned}\bar{\epsilon}_+^\mu(p) &= \epsilon_+^{\mu*}(p),\\ \bar{\epsilon}_0^\mu(p) &= \epsilon_0^{\mu*}(p),\\ \bar{\epsilon}_-^\mu(p) &= \epsilon_-^{\mu*}(p).\end{aligned} \tag{A.13}$$

### Spin-$\frac{3}{2}$ fields

The gravitino wavefunctions are given by the product of a spin-$\frac{1}{2}$ and a spin-1 polarization vector; for a derivation, see [50]. For each helicity, they are given for a particle by

$$\begin{aligned}u^\mu_{3/2,3/2}(p) &= \epsilon_+^\mu(p)u_{+1/2}(p),\\ u^\mu_{3/2,1/2}(p) &= \sqrt{\frac{2}{3}}\epsilon_0^\mu(p)u_{+1/2}(p) + \frac{1}{\sqrt{3}}e^{i\phi}\epsilon_+^\mu(p)u_{-1/2}(p),\\ u^\mu_{3/2,-1/2}(p) &= \sqrt{\frac{2}{3}}e^{i\phi}\epsilon_0^\mu(p)u_{-1/2}(p) + \frac{1}{\sqrt{3}}\epsilon_-^\mu(p)u_{+1/2}(p),\\ u^\mu_{3/2,-3/2}(p) &= e^{i\phi}\epsilon_-^\mu(p)u_{-1/2}(p),\end{aligned} \tag{A.14}$$

and the corresponding antiparticle

$$\begin{aligned}v^\mu_{3/2,3/2}(p) &= \epsilon_+^{\mu*}(p)v_{+1/2}(p)\\ v^\mu_{3/2,1/2}(p) &= \sqrt{\frac{2}{3}}\epsilon_0^{\mu*}(p)v_{+1/2}(p) + \frac{1}{\sqrt{3}}e^{-i\phi}\epsilon_+^{\mu*}(p)v_{-1/2}(p),\\ v^\mu_{3/2,-1/2}(p) &= \sqrt{\frac{2}{3}}e^{-i\phi}\epsilon_0^{\mu*}(p)v_{-1/2}(p) + \frac{1}{\sqrt{3}}\epsilon_-^{\mu*}(p)v_{+1/2}(p)\\ v^\mu_{3/2,-3/2}(p) &= e^{-i\phi}\epsilon_-^{\mu*}(p)v_{-1/2}(p).\end{aligned} \tag{A.15}$$

### Spin-2 fields

Just as in the case of the spin-$\frac{3}{2}$ fields, the spin-2 wavefunctions can be formed as the direct product of two spin-1 polarization vectors. They are given by

$$\begin{aligned}\epsilon^{\mu\nu}_{2,2}(p) =& \epsilon_+^\mu(p)\epsilon_+^\nu(p),\\ \epsilon^{\mu\nu}_{2,1}(p) =& \frac{1}{\sqrt{2}}\left(\epsilon_0^\mu(p)\epsilon_+^\nu(p) + \epsilon_+^\mu(p)\epsilon_0^\nu(p)\right),\\ \epsilon^{\mu\nu}_{2,0}(p) =& \frac{1}{\sqrt{6}}\left(\epsilon_-^\mu(p)\epsilon_+^\nu(p) + 2\epsilon_0^\mu(p)\epsilon_0^\nu(p) + \epsilon_+^\mu(p)\epsilon_-^\nu(p)\right)\\ \epsilon^{\mu\nu}_{2,-1}(p) =& \frac{1}{\sqrt{2}}\left(\epsilon_-^\mu(p)\epsilon_0^\nu(p) + \epsilon_0^\mu(p)\epsilon_-^\nu(p)\right),\\ \epsilon^{\mu\nu}_{2,-2}(p) =& \epsilon_-^\mu(p)\epsilon_-^\nu(p).\end{aligned} \tag{A.16}$$

The antiparticle polarization vectors are given by

$$\bar{\epsilon}^{\mu\nu}_{2,\sigma}(p) = \epsilon^{\mu\nu *}_{2,\sigma}(p). \tag{A.17}$$

## A.3 Propagators

On-shell, a propagator is fully determined by the spin of the particle. In particular, the numerator of the propagator is given by the sum over the polarization vectors in the following way

$$\lim_{p^2 \to M^2} (p^2 - M^2 + i\epsilon)\Delta^j(p) = \sum_\sigma u_{j,\sigma}(p) u^*_{j,\sigma}(p), \tag{A.18}$$

where $\Delta^j(p)$ is the full propagator for a spin-$j$ particle. Off-shell, the propagator can be different as long as the difference vanishes when evaluated on-shell. This difference is due to the presence of lower spin components in the propagator which are removed on-shell by the classical equations of motion for the field. These extra components are determined by the associated terms in the quadratic part of the Lagrangian, which is model-dependent; for details, see [50]. In this section, we show that the on-shell relation above holds in the spin-$\frac{1}{2}$, spin-1, spin-$\frac{3}{2}$ and spin-2 cases.

### Spin-$\frac{1}{2}$ fields

Using the polarization vectors given in Section A.2, we find

$$\sum_{\sigma=-1/2}^{1/2} u_\sigma(p)\bar{u}_\sigma(p) = \tag{A.19}$$

$$\begin{pmatrix} M & 0 & E - |\vec{p}|\cos\theta & -e^{-i\phi}|\vec{p}|\sin\theta \\ 0 & M & -e^{i\phi}|\vec{p}|\sin\theta & E + |\vec{p}|\cos\theta \\ E + |\vec{p}|\cos\theta & e^{-i\phi}|\vec{p}|\sin\theta & M & 0 \\ e^{i\phi}|\vec{p}|\sin\theta & E - |\vec{p}|\cos\theta & 0 & M \end{pmatrix}.$$

This is to be compared with the spin-$\frac{1}{2}$ propagator, which is exactly the same both on-shell and off-shell since there is no possible spin lower by an integer that can contribute,

$$\not{p} + M = \sum_{\sigma=-1/2}^{1/2} u_\sigma(p)\bar{u}_\sigma(p). \tag{A.20}$$

So, the spin-$\frac{1}{2}$ propagator is fixed entirely by its spin.

We have also checked that antiparticle polarization vectors satisfy a similar relation,

$$\not{p} - M = \sum_{\sigma=-1/2}^{1/2} v_\sigma(p)\bar{v}_\sigma(p). \tag{A.21}$$

**Spin-1 fields**

Again, using the particle polarization vectors given in Section A.2, we find

$$\sum_{\sigma=-1}^{1} \epsilon_\sigma^\mu \epsilon_\sigma^{\nu *} = \frac{1}{M^2} \begin{pmatrix} |\vec{p}|^2 & \cdots \\ E|\vec{p}| \sin\theta \cos\phi & \cdots \\ E|\vec{p}| \sin\theta \sin\phi & \cdots \\ E|\vec{p}| \cos\theta & \cdots \end{pmatrix} . \tag{A.22}$$

The propagator numerator is given by

$$\Pi_1^{\mu\nu} = -g^{\mu\nu} + \frac{p^\mu p^\nu}{M^2} = \frac{1}{M^2} \begin{pmatrix} E^2 - M^2 & \cdots \\ E|\vec{p}| \sin\theta \cos\phi & \cdots \\ E|\vec{p}| \sin\theta \sin\phi & \cdots \\ E|\vec{p}| \cos\theta & \cdots \end{pmatrix} . \tag{A.23}$$

In these last two equations, we have omitted the matrix elements of the second, third and fourth column for brevity. We have however checked that they all agree with each other on-shell, so that

$$\lim_{p^2 \to M^2} \left( -g^{\mu\nu} + \frac{p^\mu p^\nu}{M^2} \right) = \sum_{\sigma=-1}^{1} \epsilon_\sigma^\mu \epsilon_\sigma^{\nu *} . \tag{A.24}$$

Similar results can be obtained starting from antiparticle polarization vectors.

In the off-shell case, we find that the propagator numerator differs from the sum over the polarization vectors due to the presence of spin-0 components controlled by the quadratic part of the Lagrangian, see [50].

**Spin-$\frac{3}{2}$ fields**

In this case, there are four sets of indices so that we omit to display the entire results for brevity. However, we have checked every element and find that

$$\lim_{p^2 \to M^2} \Pi_{RS}^{\mu\nu} = \sum_{i=-3/2}^{3/2} u_{3/2,i}^\mu \bar{u}_{3/2,i}^\nu , \tag{A.25}$$

where the numerator of the propagator reads

$$\begin{aligned} \Pi_{RS}^{\mu\nu} &= \Big[ -g^{\mu\nu} + \frac{p^\mu p^\nu}{M^2} \Big] \Big[ \not{p} + M \Big] - \frac{1}{3} \Big[ \gamma^\mu + \frac{p^\mu}{M} \Big] \Big[ \not{p} - M \Big] \Big[ \gamma^\nu + \frac{p^\nu}{M} \Big] \\ &= -\Big[ \not{p} + M \Big] \Big[ g^{\mu\nu} - \frac{2}{3} \frac{p^\mu p^\nu}{M^2} - \frac{1}{3} \gamma^\mu \gamma^\nu - \frac{1}{3M} \big( p^\nu \gamma^\mu - p^\mu \gamma^\nu \big) \Big] . \end{aligned} \tag{A.26}$$

This is the propagator used by MadGraph 5. We have also checked that the related antiparticle relation

$$\lim_{p^2 \to M^2} \Pi_{RSanti}^{\mu\nu} = \sum_{i=-3/2}^{3/2} v_{3/2,i}^\mu \bar{v}_{3/2,i}^\nu , \tag{A.27}$$

holds, where

$$\begin{aligned}\Pi^{\mu\nu}_{RSanti} &= \Big[-g^{\mu\nu}+\frac{p^\mu p^\nu}{M^2}\Big]\Big[\not{p}-M\Big]-\frac{1}{3}\Big[\gamma^\mu-\frac{p^\mu}{M}\Big]\Big[\not{p}+M\Big]\Big[\gamma^\nu-\frac{p^\nu}{M}\Big]\\ &= -\Big[\not{p}-M\Big]\Big[g^{\mu\nu}-\frac{2}{3}\frac{p^\mu p^\nu}{M^2}-\frac{1}{3}\gamma^\mu\gamma^\nu+\frac{1}{3M}\big(p^\nu\gamma^\mu-p^\mu\gamma^\nu\big)\Big].\end{aligned} \tag{A.28}$$

Many terms are different in the off-shell case due to the presence of spin-$\frac{1}{2}$ components. These are model-dependent, as is the exact form of the propagator. For example, another spin-$\frac{3}{2}$ propagator that has been used in the literature [166] has its numerator given by

$$\tilde{\Pi}^{\mu\nu}=\Big(\not{p}+M\Big)\Big[\Big(-g^{\mu\nu}+\frac{p^\mu p^\nu}{M^2}\Big)+\frac{1}{3}\Big(g^{\mu\alpha}-\frac{p^\mu p^\alpha}{M^2}\Big)\Big(g^{\nu\beta}-\frac{p^\nu p^\beta}{M^2}\Big)\gamma_\alpha\gamma_\beta\Big]. \tag{A.29}$$

The difference between the numerators of the propagators of Eq. (A.26) and Eq. (A.29) is

$$\Pi^{\mu\nu}_{RS}-\tilde{\Pi}^{\mu\nu}=\frac{(p^2-M^2)}{3M^2}\Big[\frac{p^\mu p^\nu}{M^2}(\not{p}+M)-(p^\mu\gamma^\nu-p^\nu\gamma^\mu)\Big], \tag{A.30}$$

which vanishes on-shell.

**Spin-2 fields**

For spin-2, one form of the propagator numerator is given by

$$\Pi^{\mu\nu\alpha\beta}_2=\frac{1}{2}\Pi^{\mu\alpha}_1\Pi^{\nu\beta}_1+\frac{1}{2}\Pi^{\mu\beta}_1\Pi^{\nu\alpha}_1-\frac{1}{3}\Pi^{\mu\nu}_1\Pi^{\alpha\beta}_1, \tag{A.31}$$

which is the propagator used by MadGraph 5. Other forms differ in their off-shell effects. The resulting tensor is much too long for every term to be included. We have however checked every term and find exact agreement with the sum of the polarization vectors as in

$$\lim_{p^2\to M^2}\Pi^{\mu\nu\alpha\beta}_2=\sum_{\sigma=-2}^{2}\epsilon^{\mu\nu}_{2,\sigma}\epsilon^{\alpha\beta *}_{2,\sigma}. \tag{A.32}$$

## A.4 Partial wave unitarity

We want to derive the requirement of partial wave unitarity for a process $i\to f$. In the following, we assume a two particle inital and final state characterized by the initial state helicities $\lambda_i=\lambda_a,\lambda_b$ and final state helicities $\lambda_f=\lambda_c,\lambda_d$. The helicity amplitude $\mathcal{M}_{\lambda_a\lambda_b\lambda_c\lambda_d}(s,\theta)$ can be expanded in partial waves,

$$\mathcal{M}_{\lambda_a\lambda_b\lambda_c\lambda_d}(s,\theta)=16\pi\sum_J(2J+1))\mathcal{M}^J_{\lambda_a\lambda_b\lambda_c\lambda_d}(s)d^J_{\lambda_a-\lambda_b,\lambda_c-\lambda_d}(\theta), \tag{A.33}$$

where $d^J_{\lambda_a-\lambda_b,\lambda_c-\lambda_d}(\theta)$ are the Wigner $d$-functions. If the angular momentum of the initial state is described by $|Jm\rangle$, where $J$ is the total angular momentum and $m$ is the angular momentum along the initial direction, and the final state is described by

$\langle J, m', \theta|$, where $m'$ is the projection of the angular momentum on the final direction, then the wavefunction overlap is given by $d^J_{m,m'} = \langle J, m', \theta | J, m\rangle$. For a $2 \to 2$ scattering process in the center of mass frame, one can derive $m$ to be the difference in the initial state helicities, $m = \lambda_a - \lambda_b$ and $m'$ the difference in the final state helicities $m' = \lambda_c - \lambda_d$ (for details, see e.g. [50] and for the explicit expression of the $d$-functions, see the PDG [7]).

We rewrite the last expression using the orthogonality relation of the Wigner $d$-function

$$\int d\cos\theta d^J_{a,b}(\theta) d^{J'}_{a,b}(\theta) = \delta_{JJ'} \frac{2}{2J+1}, \tag{A.34}$$

so that

$$\mathcal{M}^J_{\lambda_a\lambda_b\lambda_c\lambda_d}(s) = \frac{1}{32\pi} \int d\cos\theta \mathcal{M}_{\lambda_a\lambda_b\lambda_c\lambda_d}(s,\theta) d^J_{\lambda_a-\lambda_b,\lambda_c-\lambda_d}(\theta). \tag{A.35}$$

Now we make use of the optical theorem, which states that the imaginary part of the amplitude for elastic scattering in forward direction is related to the sum over all possible accessible final states $n$ at the scattering CM energy $\sqrt{s}$,

$$\mathrm{Im}\mathcal{M}_{ii}(A \to A) = s\beta \sum_n \sigma_{tot}(A \to n) = \frac{1}{64\pi^2} \sum_n \int d\Omega |\mathcal{M}(A \to n)|^2, \tag{A.36}$$

where $\beta$ is a kinematical factor showing up for massive particles and $d\Omega = d\cos\theta d\varphi$. By use of (A.33) and (A.34), we can derive from (A.36)

$$\mathrm{Im}\mathcal{M}^J_{ii} = \sum_n |\mathcal{M}^J_{in}|^2. \tag{A.37}$$

It follows

$$\mathrm{Im}\mathcal{M}^J_{ii} = |\mathcal{M}^J_{ii}|^2 + \sum_{n\neq i} |\mathcal{M}^J_{in}|^2 \geq |\mathcal{M}^J_{ii}|^2, \tag{A.38}$$

that $|\mathcal{M}^J_{ii}| \leq 1$. For a final state $f \neq i$, we find

$$|\mathcal{M}^J_{if}|^2 \leq \sum_{n\neq i} |\mathcal{M}^J_{in}|^2 = \mathrm{Im}|\mathcal{M}^J_{ii}| - |\mathcal{M}^J_{ii}|^2 \leq |\mathcal{M}^J_{ii}| - |\mathcal{M}^J_{ii}|^2 = |\mathcal{M}^J_{ii}|(1 - |\mathcal{M}^J_{ii}|), \tag{A.39}$$

leading to $|\mathcal{M}^J_{if}| \leq 1/2$ for $f \neq i$.

# Bibliography


[1] **ATLAS** Collaboration, G. Aad et al., *Observation of a new particle in the search for the Standard Model Higgs boson with the ATLAS detector at the LHC*, *Phys.Lett.* **B716** (2012) 1–29, [arXiv:1207.7214].

[2] **CMS** Collaboration, S. Chatrchyan et al., *Observation of a new boson at a mass of 125 GeV with the CMS experiment at the LHC*, *Phys.Lett.* **B716** (2012) 30–61, [arXiv:1207.7235].

[3] **ATLAS** Collaboration, *Combined coupling measurements of the Higgs-like boson with the ATLAS detector using up to 25 $fb^{-1}$ of proton-proton collision data*, *ATLAS-CONF-2013-034*, *ATLAS-COM-CONF-2013-035* (2013).

[4] **CMS** Collaboration, *Combination of standard model Higgs boson searches and measurements of the properties of the new boson with a mass near 125 GeV*, *CMS-PAS-HIG-13-005* (2013).

[5] F. Englert and R. Brout, *Broken Symmetry and the Mass of Gauge Vector Mesons*, *Phys.Rev.Lett.* **13** (1964) 321–323.

[6] P. W. Higgs, *Broken Symmetries and the Masses of Gauge Bosons*, *Phys.Rev.Lett.* **13** (1964) 508–509.

[7] **Particle Data Group** Collaboration, J. Beringer et al., *Review of Particle Physics (RPP)*, *Phys.Rev.* **D86** (2012) 010001.

[8] J. Goldstone, A. Salam, and S. Weinberg, *Broken Symmetries*, *Phys.Rev.* **127** (1962) 965–970.

[9] J. Goldstone, *Field Theories with Superconductor Solutions*, *Nuovo Cim.* **19** (1961) 154–164.

[10] T. Lee and C.-N. Yang, *Question of Parity Conservation in Weak Interactions*, *Phys.Rev.* **104** (1956) 254–258.

[11] C. Wu, E. Ambler, R. Hayward, D. Hoppes, and R. Hudson, *Experimental Test of Parity Conservation in Beta Decay*, *Phys.Rev.* **105** (1957) 1413–1414.

[12] J. M. Cornwall, D. N. Levin, and G. Tiktopoulos, *Derivation of Gauge Invariance from High-Energy Unitarity Bounds on the s Matrix*, *Phys.Rev.* **D10** (1974) 1145.

[13] B. W. Lee, C. Quigg, and H. Thacker, *Weak Interactions at Very High-Energies: The Role of the Higgs Boson Mass*, *Phys.Rev.* **D16** (1977) 1519.

[14] J. Alwall, M. Herquet, F. Maltoni, O. Mattelaer, and T. Stelzer, *MadGraph 5 : Going Beyond*, *JHEP* **1106** (2011) 128, [arXiv:1106.0522].

[15] H. Murayama, I. Watanabe, and K. Hagiwara, *HELAS: HELicity Amplitude Subroutines for Feynman diagram evaluations*, *KEK-91-11* (1992).

[16] D. Dicus and V. Mathur, *Upper bounds on the values of masses in unified gauge theories*, *Phys.Rev.* **D7** (1973) 3111–3114.

[17] S. Dawson, *The MSSM and why it works*, *BNL-HET-SD-97-4* (1997) 261–339, [hep-ph/9712464].

[18] A. Djouadi, *The Anatomy of electro-weak symmetry breaking. II. The Higgs bosons in the minimal supersymmetric model*, *Phys.Rept.* **459** (2008) 1–241, [hep-ph/0503173].

[19] G. Jungman, M. Kamionkowski, and K. Griest, *Supersymmetric dark matter*, *Phys.Rept.* **267** (1996) 195–373, [hep-ph/9506380].

[20] K. Griest and M. Kamionkowski, *Supersymmetric dark matter*, *Phys.Rept.* **333** (2000) 167–182.

[21] F. D. Steffen, *Dark Matter Candidates - Axions, Neutralinos, Gravitinos, and Axinos*, *Eur.Phys.J.* **C59** (2009) 557–588, [arXiv:0811.3347].

[22] N. Polonsky, *Supersymmetry: Structure and phenomena. Extensions of the standard model*, *Lect.Notes Phys.* **M68** (2001) 1–169, [hep-ph/0108236].

[23] B. Fuks, *Supersymmetry - When Theory Inspires Experimental Searches*, arXiv:1401.6277.

[24] J. Wess and B. Zumino, *Supergauge Transformations in Four-Dimensions*, *Nucl.Phys.* **B70** (1974) 39–50.

[25] C. Duhr and B. Fuks, *A superspace module for the FeynRules package*, *Comput.Phys.Commun.* **182** (2011) 2404–2426, [arXiv:1102.4191].

[26] M. E. Peskin and D. V. Schroeder, *An Introduction to quantum field theory*, *ISBN-9780201503975* (1995).

[27] P. Z. Skands, B. Allanach, H. Baer, C. Balazs, G. Belanger, et al., *SUSY Les Houches accord: Interfacing SUSY spectrum calculators, decay packages, and event generators*, *JHEP* **0407** (2004) 036, [hep-ph/0311123].

[28] S. P. Martin, *A Supersymmetry primer*, hep-ph/9709356.

[29] A. Alloul, N. D. Christensen, C. Degrande, C. Duhr, and B. Fuks, *FeynRules 2.0 - A complete toolbox for tree-level phenomenology*, arXiv:1310.1921.

[30] G. Giudice and R. Rattazzi, *Theories with gauge mediated supersymmetry breaking*, *Phys.Rept.* **322** (1999) 419–499, [hep-ph/9801271].

[31] M. A. Luty and E. Ponton, *Effective Lagrangians and light gravitino phenomenology*, *Phys.Rev.* **D57** (1998) 4167–4173, [hep-ph/9706268].

[32] A. Brignole, F. Feruglio, and F. Zwirner, *On the effective interactions of a light gravitino with matter fermions*, *JHEP* **9711** (1997) 001, [hep-th/9709111].

[33] T. Clark, T. Lee, S. Love, and G.-H. Wu, *On the interactions of light gravitinos*, *Phys.Rev.* **D57** (1998) 5912–5915, [hep-ph/9712353].

[34] A. Brignole, J. Casas, J. Espinosa, and I. Navarro, *Low scale supersymmetry breaking: Effective description, electroweak breaking and phenomenology*, *Nucl.Phys.* **B666** (2003) 105–143, [hep-ph/0301121].

[35] P. Fayet, *Mixing Between Gravitational and Weak Interactions Through the Massive Gravitino*, *Phys.Lett.* **B70** (1977) 461.

[36] P. Fayet, *Scattering Cross-Sections of the Photino and the Goldstino (Gravitino) on Matter*, *Phys.Lett.* **B86** (1979) 272.

[37] T. Lee and G.-H. Wu, *Interactions of a single goldstino*, *Phys.Lett.* **B447** (1999) 83–88, [hep-ph/9805512].

[38] B. Fuks and M. Rausch de Traubenberg, *Supersymétrie, exercices avec solutions*. Ellipses, ellipses editions ed., 2011. ISBN: 978-2-729-86318-0.

[39] H. P. Nilles, *Supersymmetry, Supergravity and Particle Physics*, *Phys.Rept.* **110** (1984) 1–162.

[40] D. Volkov and V. Soroka, *Higgs Effect for Goldstone Particles with Spin 1/2*, *JETP Lett.* **18** (1973) 312–314.

[41] S. Deser and B. Zumino, *Broken Supersymmetry and Supergravity*, *Phys.Rev.Lett.* **38** (1977) 1433.

[42] E. Cremmer, B. Julia, J. Scherk, S. Ferrara, L. Girardello, et al., *Spontaneous Symmetry Breaking and Higgs Effect in Supergravity Without Cosmological Constant*, *Nucl.Phys.* **B147** (1979) 105.

[43] D. Cerdeno and C. Munoz, *An introduction to supergravity*, *PoS* **CORFU98** (1998) 011.

[44] E. Cremmer, S. Ferrara, L. Girardello, and A. Van Proeyen, *Yang-Mills Theories with Local Supersymmetry: Lagrangian, Transformation Laws and SuperHiggs Effect*, *Nucl.Phys.* **B212** (1983) 413.

[45] R. Casalbuoni, S. De Curtis, D. Dominici, F. Feruglio, and R. Gatto, *A gravitino - goldstino high-energy equivalence theorem*, *Phys.Lett.* **B215** (1988) 313.

[46] T. Moroi, *Effects of the gravitino on the inflationary universe*, `hep-ph/9503210`.

[47] K. Mawatari, *Associated production of light gravitinos at future linear colliders*, `arXiv:1202.0507`.

[48] K. Mawatari and Y. Takaesu, *HELAS and MadGraph with goldstinos*, *Eur.Phys.J.* **C71** (2011) 1640, [`arXiv:1101.1289`].

[49] T. Bhattacharya and P. Roy, *Tree unitarity in broken supergravity. 2. Double gravitino amplitude*, *Nucl.Phys.* **B328** (1989) 481.

[50] N. D. Christensen, P. de Aquino, N. Deutschmann, C. Duhr, B. Fuks, et al., *Simulating spin-$\frac{3}{2}$ particles at colliders*, *Eur.Phys.J.* **C73** (2013) 2580, [`arXiv:1308.1668`].

[51] K. Hagiwara, J. Kanzaki, Q. Li, and K. Mawatari, *HELAS and MadGraph/MadEvent with spin-2 particles*, *Eur.Phys.J.* **C56** (2008) 435–447, [`arXiv:0805.2554`].

[52] M. Benmerrouche, R. Davidson, and N. Mukhopadhyay, *Problems of Describing Spin 3/2 Baryon Resonances in the Effective Lagrangian Theory*, *Phys.Rev.* **C39** (1989) 2339–2348.

[53] A. Denner, H. Eck, O. Hahn, and J. Kublbeck, *Feynman rules for fermion number violating interactions*, *Nucl.Phys.* **B387** (1992) 467–484.

[54] A. Brignole, F. Feruglio, and F. Zwirner, *Aspects of spontaneously broken N=1 global supersymmetry in the presence of gauge interactions*, *Nucl.Phys.* **B501** (1997) 332–374, [`hep-ph/9703286`].

[55] E. Perazzi, G. Ridolfi, and F. Zwirner, *Signatures of massive sgoldstinos at $e^+e^-$ colliders*, *Nucl.Phys.* **B574** (2000) 3–22, [`hep-ph/0001025`].

[56] D. A. Dicus and P. Roy, *Restrictions on Gravitino Mass From Chiral Scalar and Pseudoscalar Production*, *Phys.Rev.* **D42** (1990) 938–940.

[57] E. Perazzi, G. Ridolfi, and F. Zwirner, *Signatures of massive sgoldstinos at hadron colliders*, *Nucl.Phys.* **B590** (2000) 287–305, [`hep-ph/0005076`].

[58] D. Gorbunov, *Light sgoldstino: Precision measurements versus collider searches*, *Nucl.Phys.* **B602** (2001) 213–237, [hep-ph/0007325].

[59] D. Gorbunov, V. Ilyin, and B. Mele, *Sgoldstino events in top decays at LHC*, *Phys.Lett.* **B502** (2001) 181–188, [hep-ph/0012150].

[60] **DELPHI** Collaboration, P. Abreu et al., *Search for the sgoldstino at $\sqrt{s}$ from 189 GeV to 202 GeV*, *Phys.Lett.* **B494** (2000) 203–214, [hep-ex/0102044].

[61] P. Checchia and E. Piotto, *Sensitivity to sgoldstino states at the future linear $e^+e^-$ and photon colliders*, hep-ph/0102208.

[62] D. S. Gorbunov and A. V. Semenov, *CompHEP package with light gravitino and sgoldstinos*, hep-ph/0111291.

[63] D. Gorbunov and N. Krasnikov, *Prospects for sgoldstino search at the LHC*, *JHEP* **0207** (2002) 043, [hep-ph/0203078].

[64] S. Demidov and D. Gorbunov, *LHC prospects in searches for neutral scalars in $pp \to \gamma\gamma$ + jet: SM Higgs boson, radion, sgoldstino*, *Phys.Atom.Nucl.* **69** (2006) 712–720, [hep-ph/0405213].

[65] C. Petersson and A. Romagnoni, *The MSSM Higgs Sector with a Dynamical Goldstino Supermultiplet*, *JHEP* **1202** (2012) 142, [arXiv:1111.3368].

[66] B. Bellazzini, C. Petersson, and R. Torre, *Photophilic Higgs from sgoldstino mixing*, *Phys.Rev.* **D86** (2012) 033016, [arXiv:1207.0803].

[67] R. Assmann, M. Lamont, and S. Myers, *A brief history of the LEP collider*, *Nucl.Phys.Proc.Suppl.* **109B** (2002) 17–31.

[68] **L3** Collaboration, M. Acciarri et al., *Measurements of mass, width and gauge couplings of the W boson at LEP*, *Phys.Lett.* **B413** (1997) 176–190.

[69] **OPAL** Collaboration, M. Akrawy et al., *Measurement of the $Z^0$ Mass and Width with the OPAL Detector at LEP*, *Phys.Lett.* **B231** (1989) 530.

[70] S. Bethke, *Determination of the QCD coupling $\alpha_s$*, *J.Phys.* **G26** (2000) R27, [hep-ex/0004021].

[71] T. Behnke, J. E. Brau, B. Foster, J. Fuster, M. Harrison, et al., *The International Linear Collider Technical Design Report - Volume 1: Executive Summary*, arXiv:1306.6327.

[72] **ECFA/DESY Photon Collider Working Group** Collaboration, B. Badelek et al., *TESLA: The Superconducting electron positron linear collider with an integrated X-ray laser laboratory. Technical design report. Part 6. Appendices. Chapter 1. Photon collider at TESLA*, *Int.J.Mod.Phys.* **A19** (2004) 5097–5186, [hep-ex/0108012].

[73] I. Ginzburg, G. Kotkin, V. Serbo, and V. I. Telnov, *Production of High-Energy Colliding gamma gamma and gamma e Beams with a High Luminosity at Vlepp Accelerators*, *JETP Lett.* **34** (1981) 491–495.

[74] I. Ginzburg, G. Kotkin, S. Panfil, V. Serbo, and V. I. Telnov, *Colliding gamma e and gamma gamma Beams Based on the Single Pass e+ e- Accelerators. 2. Polarization Effects. Monochromatization Improvement*, *Nucl.Instrum.Meth.* **A219** (1984) 5–24.

[75] J. C. Collins, D. E. Soper, and G. F. Sterman, *Factorization of Hard Processes in QCD*, *Adv.Ser.Direct.High Energy Phys.* **5** (1988) 1–91, [hep-ph/0409313].

[76] J. Pumplin, D. Stump, J. Huston, H. Lai, P. M. Nadolsky, et al., *New generation of parton distributions with uncertainties from global QCD analysis*, *JHEP* **0207** (2002) 012, [hep-ph/0201195].

[77] P. D. Grannis and M. J. Shochet, *The Tevatron Collider Physics Legacy*, *Ann.Rev.Nucl.Part.Sci.* **63** (2013) 467–502.

[78] **CDF** Collaboration, F. Abe et al., *Observation of top quark production in $\bar{p}p$ collisions*, *Phys.Rev.Lett.* **74** (1995) 2626–2631, [hep-ex/9503002].

[79] **D0** Collaboration, S. Abachi et al., *Observation of the top quark*, *Phys.Rev.Lett.* **74** (1995) 2632–2637, [hep-ex/9503003].

[80] **Tevatron New Physics Higgs Working Group, CDF and D0** Collaboration, *Updated Combination of CDF and D0 Searches for Standard Model Higgs Boson Production with up to 10.0 $fb^{-1}$ of Data*, arXiv:1207.0449.

[81] L. Evans and P. Bryant, *LHC Machine*, *JINST* **3** (2008) S08001.

[82] M. Lamont, *Status of the LHC*, *J.Phys.Conf.Ser.* **455** (2013) 012001.

[83] **ATLAS** Collaboration, G. Aad et al., *The ATLAS Experiment at the CERN Large Hadron Collider*, *JINST* **3** (2008) S08003.

[84] **CMS** Collaboration, S. Chatrchyan et al., *The CMS experiment at the CERN LHC*, *JINST* **3** (2008) S08004.

[85] J.-L. Caron, "Overall view of lhc experiments." http://cds.cern.ch/record/841555.

[86] N. D. Christensen and C. Duhr, *FeynRules - Feynman rules made easy*, *Comput.Phys.Commun.* **180** (2009) 1614–1641, [arXiv:0806.4194].

[87] C. Degrande, C. Duhr, B. Fuks, D. Grellscheid, O. Mattelaer, et al., *UFO - The Universal FeynRules Output*, *Comput.Phys.Commun.* **183** (2012) 1201–1214, [arXiv:1108.2040].

[88] T. Stelzer and W. Long, *Automatic generation of tree level helicity amplitudes*, *Comput.Phys.Commun.* **81** (1994) 357–371, [hep-ph/9401258].

[89] F. Maltoni and T. Stelzer, *MadEvent: Automatic event generation with MadGraph*, *JHEP* **0302** (2003) 027, [hep-ph/0208156].

[90] J. Alwall, P. Demin, S. de Visscher, R. Frederix, M. Herquet, et al., *MadGraph/MadEvent v4: The New Web Generation*, *JHEP* **0709** (2007) 028, [arXiv:0706.2334].

[91] J. Alwall, P. Artoisenet, S. de Visscher, C. Duhr, R. Frederix, et al., *New Developments in MadGraph/MadEvent*, *AIP Conf.Proc.* **1078** (2009) 84–89, [arXiv:0809.2410].

[92] J. Alwall, R. Frederix, S. Frixione, V. Hirschi, F. Maltoni, et al., *The automated computation of tree-level and next-to-leading order differential cross sections, and their matching to parton shower simulations*, arXiv:1405.0301.

[93] A. Pukhov, E. Boos, M. Dubinin, V. Edneral, V. Ilyin, et al., *CompHEP: A Package for evaluation of Feynman diagrams and integration over multiparticle phase space*, hep-ph/9908288. INP-MSU-98-41-542.

[94] **CompHEP** Collaboration, E. Boos et al., *CompHEP 4.4: Automatic computations from Lagrangians to events*, *Nucl.Instrum.Meth.* **A534** (2004) 250–259, [hep-ph/0403113].

[95] A. Pukhov, *CalcHEP 2.3: MSSM, structure functions, event generation, batchs, and generation of matrix elements for other packages*, hep-ph/0412191.

[96] A. Belyaev, N. D. Christensen, and A. Pukhov, *CalcHEP 3.4 for collider physics within and beyond the Standard Model*, *Comput.Phys.Commun.* **184** (2013) 1729–1769, [arXiv:1207.6082].

[97] T. Gleisberg, S. Hoeche, F. Krauss, A. Schalicke, S. Schumann, et al., *SHERPA 1. alpha: A Proof of concept version*, *JHEP* **0402** (2004) 056, [hep-ph/0311263].

[98] T. Gleisberg, S. Hoeche, F. Krauss, M. Schonherr, S. Schumann, et al., *Event generation with SHERPA 1.1*, *JHEP* **0902** (2009) 007, [arXiv:0811.4622].

[99] M. Moretti, T. Ohl, and J. Reuter, *O'Mega: An Optimizing matrix element generator*, hep-ph/0102195. IKDA-2001-06, LC-TOOL-2001-040.

[100] W. Kilian, T. Ohl, and J. Reuter, *WHIZARD: Simulating Multi-Particle Processes at LHC and ILC*, *Eur.Phys.J.* **C71** (2011) 1742, [arXiv:0708.4233].

[101] P. de Aquino, W. Link, F. Maltoni, O. Mattelaer, and T. Stelzer, *ALOHA: Automatic Libraries Of Helicity Amplitudes for Feynman diagram computations*, arXiv:1108.2041.

[102] J. Alwall, A. Ballestrero, P. Bartalini, S. Belov, E. Boos, et al., *A Standard format for Les Houches event files*, *Comput.Phys.Commun.* **176** (2007) 300–304, [hep-ph/0609017].

[103] T. Sjostrand, S. Mrenna, and P. Z. Skands, *PYTHIA 6.4 Physics and Manual*, *JHEP* **0605** (2006) 026, [hep-ph/0603175].

[104] T. Sjostrand, S. Mrenna, and P. Z. Skands, *A Brief Introduction to PYTHIA 8.1*, *Comput.Phys.Commun.* **178** (2008) 852–867, [arXiv:0710.3820].

[105] G. Corcella, I. Knowles, G. Marchesini, S. Moretti, K. Odagiri, et al., *HERWIG 6: An Event generator for hadron emission reactions with interfering gluons (including supersymmetric processes)*, *JHEP* **0101** (2001) 010, [hep-ph/0011363].

[106] M. Bahr, S. Gieseke, M. Gigg, D. Grellscheid, K. Hamilton, et al., *Herwig++ Physics and Manual*, *Eur.Phys.J.* **C58** (2008) 639–707, [arXiv:0803.0883].

[107] B. Andersson, G. Gustafson, G. Ingelman, and T. Sjostrand, *Parton Fragmentation and String Dynamics*, *Phys.Rept.* **97** (1983) 31–145.

[108] B. Andersson, *The Lund model*, *Camb.Monogr.Part.Phys.Nucl.Phys.Cosmol.* **7** (1997) 1–471.

[109] B. Webber, *A QCD Model for Jet Fragmentation Including Soft Gluon Interference*, *Nucl.Phys.* **B238** (1984) 492.

[110] S. Ovyn, X. Rouby, and V. Lemaitre, *DELPHES, a framework for fast simulation of a generic collider experiment*, arXiv:0903.2225.

[111] **DELPHES 3** Collaboration, J. de Favereau et al., *DELPHES 3, A modular framework for fast simulation of a generic collider experiment*, *JHEP* **1402** (2014) 057, [arXiv:1307.6346].

[112] C. John, "Pretty good simulation of high energy collisions." http://www.physics.ucdavis.edu/~conway/research/software/pgs/pgs4-general.htm.

[113] M. Cacciari, G. P. Salam, and G. Soyez, *FastJet user manual*, *Eur.Phys.J.* **C72** (2012) 1896, [arXiv:1111.6097].

[114] G. Salam, "Jets and jet substructure: some common jet algorithms." http://physicslearning.colorado.edu/tasi/tasi_2013/notes/june11/Salam2.pdf.

[115] E. Conte, B. Fuks, and G. Serret, *MadAnalysis 5, A User-Friendly Framework for Collider Phenomenology*, *Comput.Phys.Commun.* **184** (2013) 222–256, [arXiv:1206.1599].

[116] E. Conte and B. Fuks, *MadAnalysis 5: status and new developments*, arXiv:1309.7831.

[117] R. K. Ellis, W. J. Stirling, and B. Webber, *QCD and collider physics*, *Camb.Monogr.Part.Phys.Nucl.Phys.Cosmol.* **8** (1996) 1–435.

[118] G. Altarelli and G. Parisi, *Asymptotic Freedom in Parton Language*, *Nucl.Phys.* **B126** (1977) 298.

[119] T. Lee and M. Nauenberg, *Degenerate Systems and Mass Singularities*, *Phys.Rev.* **133** (1964) B1549–B1562.

[120] T. Kinoshita, *Mass singularities of Feynman amplitudes*, *J.Math.Phys.* **3** (1962) 650–677.

[121] S. Catani, F. Krauss, R. Kuhn, and B. Webber, *QCD matrix elements + parton showers*, *JHEP* **0111** (2001) 063, [hep-ph/0109231].

[122] L. Lonnblad, *Correcting the color dipole cascade model with fixed order matrix elements*, *JHEP* **0205** (2002) 046, [hep-ph/0112284].

[123] M. L. Mangano, M. Moretti, and R. Pittau, *Multijet matrix elements and shower evolution in hadronic collisions: $Wb\bar{b}$ + n jets as a case study*, *Nucl.Phys.* **B632** (2002) 343–362, [hep-ph/0108069].

[124] J. Alwall, S. Hoche, F. Krauss, N. Lavesson, L. Lonnblad, et al., *Comparative study of various algorithms for the merging of parton showers and matrix elements in hadronic collisions*, *Eur.Phys.J.* **C53** (2008) 473–500, [arXiv:0706.2569].

[125] S. Mrenna and P. Richardson, *Matching matrix elements and parton showers with HERWIG and PYTHIA*, *JHEP* **0405** (2004) 040, [hep-ph/0312274].

[126] J. Alwall, S. de Visscher, and F. Maltoni, *QCD radiation in the production of heavy colored particles at the LHC*, *JHEP* **0902** (2009) 017, [arXiv:0810.5350].

[127] S. Catani, Y. L. Dokshitzer, M. Seymour, and B. Webber, *Longitudinally invariant $K_t$ clustering algorithms for hadron hadron collisions*, *Nucl.Phys.* **B406** (1993) 187–224.

[128] O. Nachtmann, A. Reiter, and M. Wirbel, *Single Jet and Single Photon Production in Proton - Anti-proton Collisions and $e^+e^-$ Annihilation in a Supersymmetric Model*, *Z.Phys.* **C27** (1985) 577.

[129] A. Brignole, F. Feruglio, and F. Zwirner, *Signals of a superlight gravitino at $e^+e^-$ colliders when the other superparticles are heavy*, *Nucl.Phys.* **B516** (1998) 13–28, [hep-ph/9711516].

[130] A. Brignole, F. Feruglio, M. L. Mangano, and F. Zwirner, *Signals of a superlight gravitino at hadron colliders when the other superparticles are heavy*, *Nucl.Phys.* **B526** (1998) 136–152, [hep-ph/9801329].

[131] P. Fayet, *Lower Limit on the Mass of a Light Gravitino from $e^+e^-$ Annihilation Experiments*, *Phys.Lett.* **B175** (1986) 471.

[132] D. A. Dicus, S. Nandi, and J. Woodside, *A New source of single photons from $Z^0$ decay*, *Phys.Lett.* **B258** (1991) 231–235.

[133] J. L. Lopez, D. V. Nanopoulos, and A. Zichichi, *Supersymmetric photonic signals at LEP*, *Phys.Rev.Lett.* **77** (1996) 5168–5171, [hep-ph/9609524].

[134] J. L. Lopez, D. V. Nanopoulos, and A. Zichichi, *Single photon signals at LEP in supersymmetric models with a light gravitino*, *Phys.Rev.* **D55** (1997) 5813–5825, [hep-ph/9611437].

[135] S. Baek, S. C. Park, and J.-h. Song, *Kaluza-Klein gravitino production with a single photon at $e^+e^-$ colliders*, *Phys.Rev.* **D66** (2002) 056004, [hep-ph/0206008].

[136] S. Gopalakrishna and J. D. Wells, *Superlight gravitinos in electron photon collisions*, *Phys.Lett.* **B518** (2001) 123–127, [hep-ph/0108006].

[137] D. Dicus, S. Nandi, and J. Woodside, *Collider signals of a superlight gravitino*, *Phys.Rev.* **D41** (1990) 2347.

[138] M. Drees and J. Woodside, *Signals for a superlight gravitino at the LHC*, *To be publ. in Supersymmetry, Proc. of Conference: C90-1 0-04 (Aachen ECFA Workshop 1990:0681-683)* (1990).

[139] D. A. Dicus and S. Nandi, *New collider bound on light gravitino mass*, *Phys.Rev.* **D56** (1997) 4166–4169, [hep-ph/9611312].

[140] J. Kim, J. L. Lopez, D. V. Nanopoulos, R. Rangarajan, and A. Zichichi, *Light gravitino production at hadron colliders*, *Phys.Rev.* **D57** (1998) 373–382, [hep-ph/9707331].

[141] M. Klasen and G. Pignol, *New Results for Light Gravitinos at Hadron Colliders: Tevatron Limits and LHC Perspectives*, *Phys.Rev.* **D75** (2007) 115003, [hep-ph/0610160].

[142] **OPAL** Collaboration, G. Abbiendi et al., *Photonic events with missing energy in $e^+e^-$ collisions at $\sqrt{s}$ = 189 GeV*, *Eur.Phys.J.* **C18** (2000) 253–272, [hep-ex/0005002].

[143] **ALEPH** Collaboration, A. Heister et al., *Single photon and multiphoton production in $e^+e^-$ collisions at $\sqrt{s}$ up to 209 GeV*, *Eur.Phys.J.* **C28** (2003) 1–13.

[144] **L3** Collaboration, P. Achard et al., *Single photon and multiphoton events with missing energy in $e^+e^-$ collisions at LEP*, *Phys.Lett.* **B587** (2004) 16–32, [hep-ex/0402002].

[145] **DELPHI** Collaboration, J. Abdallah et al., *Photon events with missing energy in e+ e- collisions at s**(1/2) = 130-GeV to 209-GeV*, *Eur.Phys.J.* **C38** (2005) 395–411, [hep-ex/0406019].

[146] **LEP2 SUSY Working Group** Collaboration, "Single photon, 183-208 GeV." http://lepsusy.web.cern.ch/lepsusy/www/photons/single/single_public_summer04.html.

[147] **CDF** Collaboration, D. Acosta et al., *Limits on extra dimensions and new particle production in the exclusive photon and missing energy signature in $p\bar{p}$ collisions at $\sqrt{s} = 1.8$ TeV*, *Phys.Rev.Lett.* **89** (2002) 281801, [hep-ex/0205057].

[148] **CDF** Collaboration, T. Affolder et al., *Limits on gravitino production and new processes with large missing transverse energy in $p\bar{p}$ collisions at $\sqrt{s} = 1.8$ TeV*, *Phys.Rev.Lett.* **85** (2000) 1378–1383, [hep-ex/0003026].

[149] **ATLAS** Collaboration, *Search for New Phenomena in Monojet plus Missing Transverse Momentum Final States using 10 $fb^{-1}$ of pp Collisions at $\sqrt{s} =$ 8 TeV with the ATLAS detector at the LHC*, *ATLAS-CONF-2012-147* (2012).

[150] M. Bartelmann, "Neutrinos and structure formation in the universe." Proceedings C97-10-24.4, p. 149-158, 1997.

[151] J. L. Feng, M. Kamionkowski, and S. K. Lee, *Light Gravitinos at Colliders and Implications for Cosmology*, *Phys.Rev.* **D82** (2010) 015012, [arXiv:1004.4213].

[152] T. P. Walker, G. Steigman, D. N. Schramm, K. A. Olive, and H.-S. Kang, *Primordial nucleosynthesis redux*, *Astrophys.J.* **376** (1991) 51–69.

[153] **Planck** Collaboration, P. Ade et al., *Planck 2013 results. XVI. Cosmological parameters*, arXiv:1303.5076.

[154] T. Moroi, H. Murayama, and M. Yamaguchi, *Cosmological constraints on the light stable gravitino*, *Phys.Lett.* **B303** (1993) 289–294.

[155] T. Gherghetta, *Goldstino decoupling in spontaneously broken supergravity theories*, *Nucl.Phys.* **B485** (1997) 25–37, [hep-ph/9607448].

[156] J. Grifols, R. Mohapatra, and A. Riotto, *Astrophysical bounds on superlight gravitinos*, *Phys.Lett.* **B401** (1997) 283–286, [hep-ph/9610458].

[157] D. A. Dicus, R. N. Mohapatra, and V. L. Teplitz, *Supernova constraints on a superlight gravitino*, *Phys.Rev.* **D57** (1998) 578–582, [hep-ph/9708369].

[158] J. Grifols, R. Mohapatra, and A. Riotto, *New astrophysical constraints on the mass of the superlight gravitino*, *Phys.Lett.* **B400** (1997) 124–128, [hep-ph/9612253].

[159] A. Brignole, F. Feruglio, and F. Zwirner, *Four-fermion interactions and sgoldstino masses in models with a superlight gravitino*, *Phys.Lett.* **B438** (1998) 89–95, [hep-ph/9805282].

[160] M. Fukugita and N. Sakai, *Astrophysical constrains on broken supersymmetry*, *Phys.Lett.* **B114** (1982) 23.

[161] E. Cremmer, S. Ferrara, C. Kounnas, and D. V. Nanopoulos, *Naturally Vanishing Cosmological Constant in N=1 Supergravity*, *Phys.Lett.* **B133** (1983) 61.

[162] J. R. Ellis, K. Enqvist, and D. V. Nanopoulos, *A Very Light Gravitino in a No Scale Model*, *Phys.Lett.* **B147** (1984) 99.

[163] J. L. Lopez, D. V. Nanopoulos, and A. Zichichi, *The Simplest, string derivable, supergravity model and its experimental predictions*, *Phys.Rev.* **D49** (1994) 343–354, [hep-ph/9210280].

[164] T. Gherghetta and A. Pomarol, *Bulk fields and supersymmetry in a slice of AdS*, *Nucl.Phys.* **B586** (2000) 141–162, [hep-ph/0003129].

[165] T. Gherghetta and A. Pomarol, *A Warped supersymmetric standard model*, *Nucl.Phys.* **B602** (2001) 3–22, [hep-ph/0012378].

[166] K. Hagiwara, K. Mawatari, and Y. Takaesu, *HELAS and MadGraph with spin-3/2 particles*, *Eur.Phys.J.* **C71** (2011) 1529, [arXiv:1010.4255].

[167] K. Mawatari, B. Oexl, and Y. Takaesu, *Associated production of light gravitinos in $e^+e^-$ and $e^-\gamma$ collisions*, *Eur.Phys.J.* **C71** (2011) 1783, [arXiv:1106.5592].

[168] R. Argurio, K. De Causmaecker, G. Ferretti, A. Mariotti, K. Mawatari, et al., *Collider signatures of goldstini in gauge mediation*, *JHEP* **1206** (2012) 096, [arXiv:1112.5058].

[169] P. de Aquino, F. Maltoni, K. Mawatari, and B. Oexl, *Light Gravitino Production in Association with Gluinos at the LHC*, *JHEP* **1210** (2012) 008, [arXiv:1206.7098].

[170] J. D'Hondt, K. De Causmaecker, B. Fuks, A. Mariotti, K. Mawatari, et al., *Multilepton signals of gauge mediated supersymmetry breaking at the LHC*, arXiv:1310.0018.

[171] G. Ferretti, A. Mariotti, K. Mawatari, and C. Petersson, *Multiphoton signatures of goldstini at the LHC*, arXiv:1312.1698.

[172] K. Mawatari and B. Oexl, *Monophoton signals in light gravitino production at $e^+e^-$ colliders*, arXiv:1402.3223.

[173] P. Checchia, *Sensitivity to the gravitino mass from single photon spectrum at TESLA linear collider*, hep-ph/9911208.

[174] S. Gopalakrishna, M. Perelstein, and J. D. Wells, *Extra dimensions versus supersymmetric interpretation of missing energy events at a linear collider*, *eConf* **C010630** (2001) P311, [hep-ph/0110339].

[175] S. Choi, K. Hagiwara, H.-U. Martyn, K. Mawatari, and P. Zerwas, *Spin Analysis of Supersymmetric Particles*, *Eur.Phys.J.* **C51** (2007) 753–774, [hep-ph/0612301].

[176] **ILC** Collaboration, J. Brau et al., *ILC Reference Design Report: ILC Global Design Effort and World Wide Study*, arXiv:0712.1950.

[177] F. Cuypers, G. J. van Oldenborgh, and R. Ruckl, *Supersymmetric signals in electron - photon collisions*, *Nucl.Phys.* **B383** (1992) 45–57, [hep-ph/9205209].

[178] D. Choudhury and F. Cuypers, *Production of heavy selectrons in e- gamma collisions*, *Nucl.Phys.* **B451** (1995) 16–30, [hep-ph/9412245].

[179] K. Kiers, J. N. Ng, and G.-h. Wu, *Supersymmetric signatures at an e gamma collider*, *Phys.Lett.* **B381** (1996) 177–184, [hep-ph/9604338].

[180] V. D. Barger, T. Han, and J. Kelly, *Sparticle production in electron photon collisions*, *Phys.Lett.* **B419** (1998) 233–242, [hep-ph/9709366].

[181] A. Buckley, J. Butterworth, S. Gieseke, D. Grellscheid, S. Hoche, et al., *General-purpose event generators for LHC physics*, *Phys.Rept.* **504** (2011) 145–233, [arXiv:1101.2599].

[182] T. Plehn, D. Rainwater, and P. Z. Skands, *Squark and gluino production with jets*, *Phys.Lett.* **B645** (2007) 217–221, [hep-ph/0510144].

[183] J. Alwall, M.-P. Le, M. Lisanti, and J. G. Wacker, *Searching for Directly Decaying Gluinos at the Tevatron*, *Phys.Lett.* **B666** (2008) 34–37, [arXiv:0803.0019].

[184] J. Alwall, M.-P. Le, M. Lisanti, and J. G. Wacker, *Model-Independent Jets plus Missing Energy Searches*, *Phys.Rev.* **D79** (2009) 015005, [arXiv:0809.3264].

[185] T. Plehn and T. M. Tait, *Seeking Sgluons*, *J.Phys.G* **G36** (2009) 075001, [arXiv:0810.3919].

[186] P. de Aquino, K. Hagiwara, Q. Li, and F. Maltoni, *Simulating graviton production at hadron colliders*, *JHEP* **1106** (2011) 132, [arXiv:1101.5499].

[187] **ATLAS** Collaboration, G. Aad et al., *Search for squarks and gluinos using final states with jets and missing transverse momentum with the ATLAS detector in sqrt(s) = 7 TeV proton-proton collisions*, *Phys.Lett.* **B710** (2012) 67–85, [arXiv:1109.6572].

[188] Y. Kats, P. Meade, M. Reece, and D. Shih, *The Status of GMSB After 1/fb at the LHC*, *JHEP* **1202** (2012) 115, [arXiv:1110.6444].

[189] **ATLAS** Collaboration, *Search for squarks and gluinos with the ATLAS detector in final states with jets and missing transverse momentum and 20.3 $fb^{-1}$ of $\sqrt{s} = 8$ TeV proton-proton collision data*, *ATLAS-CONF-2013-047, ATLAS-COM-CONF-2013-049* (2013).

[190] **CMS** Collaboration, S. Chatrchyan et al., *Search for new physics in the multijet and missing transverse momentum final state in proton-proton collisions at $\sqrt{s}$ = 8 TeV*, arXiv:1402.4770.

[191] W. Beenakker, R. Hopker, M. Spira, and P. Zerwas, *Squark and gluino production at hadron colliders*, *Nucl.Phys.* **B492** (1997) 51–103, [hep-ph/9610490].

[192] **CMS** Collaboration, S. Chatrchyan et al., *Search for Supersymmetry at the LHC in Events with Jets and Missing Transverse Energy*, *Phys.Rev.Lett.* **107** (2011) 221804, [arXiv:1109.2352].

[193] M. Cacciari, G. P. Salam, and G. Soyez, *The Anti-k(t) jet clustering algorithm*, *JHEP* **0804** (2008) 063, [arXiv:0802.1189].

[194] **ATLAS** Collaboration, G. Aad et al., *Search for dark matter candidates and large extra dimensions in events with a photon and missing transverse momentum in pp collision data at $\sqrt{s} = 7$ TeV with the ATLAS detector*, *Phys.Rev.Lett.* **110** (2013) 011802, [arXiv:1209.4625].

[195] **CMS** Collaboration, S. Chatrchyan et al., *Search for Dark Matter and Large Extra Dimensions in pp Collisions Yielding a Photon and Missing Transverse Energy*, *Phys.Rev.Lett.* **108** (2012) 261803, [arXiv:1204.0821].

# Samenvatting

Het Standaard Model (SM) van de deeltjesfysica is een theorie die de fundamentele materiedeeltjes en hun onderlinge interacties beschrijft. Met de recente ontdekking van een nieuw boson dat geïdentificeerd kan worden met het Brout-Englert-Higgs boson van het SM, zijn alle deeltjes voorspeld door het SM ook experimenteel waargenomen.

Enerzijds vormt het nieuwe boson de sluitsteen van het SM, maar anderzijds versterkt het net de nood aan nieuwe fysica. In het SM is het boson namelijk onstabiel onder kwantumcorrecties. Binnenin het SM model kan dit enkel opgevangen worden door een onnatuurlijk precieze afstemming van de parameters, dit motiveert ons om op zoek te gaan naar uitbreidingen van het SM. Naast deze theoretische motivatie wijzen ook experimentele observaties in die richting. De materie zoals wij ze kennen vormt bijvoorbeeld minder dan 5% van de totale energiedichtheid in het universum. Bovendien bestaat ongeveer 25% van de totale energiedichtheid uit zogeheten donkere materie. Deze donkere materie zit niet vervat in de deeltjesinhoud van het SM.

Er bestaan veel verschillende uitbreidingen van het SM. In dit werk concentreren we ons op supersymmetrische (SUSY) theoriën, meer bepaald SUSY theoriën waarin het gravitino het lichtste SUSY deeltje (verder geschreven als LSP) is. Het gravitino is een deeltje met spin 3/2 en wordt ingevoerd wanneer de parameter die de SUSY transformaties parametriseert, ruimte-tijdsafhankelijk wordt. Dit is gelijkaardig aan de manier waarop ijkvelden ingevoerd worden bij het ijken van de symmetriën van het SM. Wanneer SUSY spontaan gebroken wordt absorbeert het gravitino het goldstino via het super-Higgs mechanisme en wordt zo massief. De massa van het gravitino is bijgevolg direct gerelateerd aan de schaal $F$ van SUSY breking. De spin 1/2 componenten van het gravitino nemen bovendien de sterkte van de interactie over van het goldstino zodat ze schalen met $1/F$. In scenario's waar SUSY op een lage energieschaal gebroken wordt, kunnen de interacties met het gravitino bijgevolg sterk genoeg worden om waargenomen te worden in botsingsexperimenten.

In dit werk bestudeerden we verschillende productiemechanismen voor lichte gravitino's en hun signaturen in toekomstige $e^+e^-$ versnellers en de Large Hadron Collider (LHC):

1. Mono-foton+$\not{E}$ signaal in $e^+e^-$ botsingen: We bestudeerden het mono-foton+$\not{E}$ signaal in toekomstige $e^+e^-$ versnellers ten gevolge van de directe productie van gravitino's in een scenario waar het gravitino en het neutralino respectievelijk het lichtste (LSP) en het op één na lichtste SUSY deeltje zijn (geschreven als NLSP). Er zijn twee belangrijke productieprocessen: gravitino paarproductie en neutralino-gravitino geassocieerde productie. Beiden geven aanleiding tot een mono-foton+$\not{E}$ signaal, het eerste door het uitstralen van een extra foton en het tweede door het verval van het neutralino. We onderzochten hoe de werkzame doorsnede en de hoekverdeling van beide processen afhangen van de parameters en toonden aan hoe de massa van het gravitino, het neutralino en het selektron afgeleid kunnen worden uit de energiedistributie en hoekverdeling van het foton in de eindtoestand.

2. Mono-elektron+$\not{E}_T$ signaal in $e^-\gamma$ botsingen: We onderzochten ook de productie

van een gravitino LSP samen met een selektron NLSP in $e^-\gamma$ botsingen waarbij het selectron onmiddellijk vervalt naar een elektron en een gravitino ( $e^-\gamma \to \tilde{e}^-\tilde{G} \to e^-\tilde{G}\tilde{G}$). Dit proces geeft aanleiding tot een mono-elektron+$\not{E}_T$ signaal. Uit een analyse gelijkaardig aan de analyse van het neutralino-gravitino productieproces, leidden we af dat de werkzame doorsnede voor de productie en de kinematische distributies van het elektron in de eindtoestand zowel afhankelijk zijn van de massa van het neutralino uitgewisseld via het $t$-kanaal als van de massa van het vervallende selektron.

3. Jets+$\not{E}_T$ signaal in $pp$ botsingen: We bestudeerden een jets+$\not{E}_T$ signaal in een scenario met gravitino LSP en gluino NLSP waarbij het gluino steeds onmiddellijk vervalt naar een gluon en een gravitino. We bekeken twee productieprocessen die aanleiding geven tot een jets+$\not{E}_T$ signaal: gluino-gravitino geassocieerde productie ($\tilde{g}\tilde{G}$) en paarproductie van gluino's ($\tilde{g}\tilde{g}$). Tot op eerste orde resulteren deze processen respectievelijk in een mono-jet+$\not{E}_T$ en een di-jet+$\not{E}_T$ signaal. We hielden echter ook rekening met eventuele extra jets. We simuleerden zowel het inclusieve signaal als de irreducibele achtergrond van het SM ($Z \to \nu\bar{\nu}$)+jets met behulp van het schema voor het samenvoegen van shower-$k_T$ matrix-element en parton shower (ME+PS) dat voorzien is in MadGraph.

De verdelingen van het jets+$\not{E}_T$ signaal kunnen informatie geven over de massa's van het gravitino en het gluino. Om dit te onderzoeken, kozen we drie referentiepunten die elk een andere eindtoestand illustreren. De referentiepunten onderscheiden zich van elkaar omdat de distributies van de $\tilde{g}\tilde{G}$ en $\tilde{g}\tilde{g}$ productieprocessen redelijk sterk verschillen en omdat de werkzame doorsnede voor $\tilde{g}\tilde{G}$ productie schaalt volgens $m_{3/2}^{-2}$. Aan de hand van de kinematische verdelingen en het aantal jets kan bijgevolg onderscheid gemaakt worden tussen de drie referentiescenario's enerzijds en het signaal en de achtergrond anderzijds.

4. Mono-foton+$\not{E}_T$ signaal in $pp$ botsingen: Ten slotte pasten we onze studie toe op een bestaande zoektocht voor nieuwe fysica in de LHC. Gebaseerd op de mono-foton+$\not{E}$ analyse van de 7 TeV data, zetten we een ondergrens op de massa van het gravitino LSP. In de limiet waar de neutralino massa heel hoog is, is enkel de paarproductie van gravitino's van belang. In dit geval onderzochten we de invloed van de massa's van de squarks. In de limiet waar de massa's van de SUSY deeltjes hoog zijn, sluiten we een gravitino massa onder $1 \times 10^{-13}$ GeV uit tot op 95% CL. Deze grens komt overeen met een ondergrens voor de schaal van SUSY breking rond 650 GeV. De limieten worden lager voor lichtere squarks.

We verwachten dat de productie van lichte gravitino's met massa $m_{3/2} \sim \mathcal{O}(10^{-14} - 10^{-9}$ GeV) onderzocht kan worden in de LHC en in een toekomstige $e^+e^-$ versneller. De eigenschappen van de signaturen hangen niet alleen sterk af van $m_{3/2}$ maar ook van de massa's van de andere SUSY deeltjes. We interpreteerden de zoektocht naar mono-foton+$\not{E}$ in de LHC run bij 7 TeV in het licht van onze theorie en zetten een limiet op de massa van het gravitino, en equivalent hiermee op de schaal van SUSY breking.

Deze limiet is sterker dan eerdere limieten in gelijkaardige onderzoeken van de LEP en Tevatron collaboraties.

We benadrukken tot slot dat we gedurende deze studies ook bijgedragen hebben tot de ontwikkeling en validatie van de simulatie software relevant voor het maken van de link tussen theoriën met gravitino's en versnellerexperimenten. Met deze software en de informatie verkregen in onze studies, kijken we uit naar verdere fenomenologische studies van theoreten en toekomstige experimentele analyses met betrekking tot de productie van gravitino's.